NATIONAL CENTRE FOR NUCLEAR RESEARCH

DOCTORAL THESIS

Expanded ν_e CC1π^+ sample selection and improved systematic treatments for neutrino oscillation parameter determination with T2K data

---

Author:
Yashwanth SANJEEV PRABHU

Supervisor:
Justyna ŁAGODA

Auxiliary supervisor:
Kamil SKWARCZYŃSKI

A thesis submitted in fulfillment of the requirements for the degree of Doctor of Philosophy

in the

High Energy Physics Division

NATIONAL CENTRE FOR NUCLEAR RESEARCH ŚWIERK

June 2024

Declaration of Authorship

I, Yashwanth SANJEEV PRABHU, declare that this thesis titled, "Expanded ν_e CC1π^+ sample selection and improved systematic treatments for neutrino oscillation parameter determination with T2K data" and the work presented in it are my own. I confirm that:

- This work was done wholly or mainly while in candidature for a research degree at the National Centre for Nuclear Research.
- Where any part of this thesis has previously been submitted for a degree or any other qualification at the National Centre for Nuclear Research or any other institution, this has been clearly stated.
- Where I have consulted the published work of others, this is always clearly attributed.
- Where I have quoted from the work of others, the source is always given. With the exception of such quotations, this thesis is entirely my own work.
- I have acknowledged all main sources of help.
- Where the thesis is based on work done by myself jointly with others, I have made clear exactly what was done by others and what I have contributed myself.

Signed:

Date:

NATIONAL CENTRE FOR NUCLEAR RESEARCH

Abstract

Expanded ν_e CC1π^+ sample selection and improved systematic treatments for neutrino oscillation parameter determination with T2K data

Yashwanth SANJEEV PRABHU

The thesis describes the development of a new electron neutrino (ν_e) event sample targeting charged-current single pion production interactions (CC1π^+) at T2K's far detector. The T2K experiment located in Japan studies neutrino oscillations with an accelerator-produced (anti)neutrino beam, an ensemble of near detectors, and Super-Kamiokande, the far detector. T2K's most ambitious objective is to measure the leptonic CP-violating phase, δ_{CP}, which could potentially explain the origin of the matter-antimatter asymmetry observed in the Universe. The appearance of electron (anti)neutrinos in the beam of muon (anti)neutrinos at the far detector provides sensitivity to measuring δ_{CP}. The new ν_e CC1π^+ sample is identified by tagging its electron-like and pion-like Cherenkov rings at the far detector. Combined with the existing single-ring ν_e CC1π^+ sample, which lacks a visible pion-like ring, the new sample increases T2K's second-most dominant ν_e interaction statistics by 27%. In order to support the new sample, systematic uncertainties related to the far detector have also been recalculated. Furthermore, resolutions of the kinematic parameters employed for binning at the far detector were studied in depth. This facilitated a re-evaluation of the kinematic binning of the ν_μ samples and the expanded ν_e CC1π^+ sample. An oscillation analysis was conducted with T2K's Markov Chain Monte Carlo fitter based on Bayesian inference, incorporating the expanded sample, the re-evaluated detector systematic uncertainties, and the updated binning, all of which represent the novelties described in this thesis. We report that CP-conserving values of $\delta_{CP} = 0, \pi$ are excluded at the 90% credible interval, and that a value of δ_{CP} attributing to maximal CP violation is preferred. Furthermore, the data also show a mild preference for the normal neutrino mass hierarchy and the upper octant of θ_{23} mixing angle. The improvements presented in this thesis will be included in T2K's official oscillation analysis for 2024. The thesis also presents sensitivity studies with the scenario of improved FD statistics for the ν_e CC1π^+ sample.

NATIONAL CENTRE FOR NUCLEAR RESEARCH

Streszczenie

Wyznaczanie parametrów oscylacji neutrin z użyciem danych T2K z rozszerzoną próbką ν_e CC$1\pi^+$ i ulepszonym traktowaniem niepewności systematycznych

Yashwanth SANJEEV PRABHU

Rozprawa przedstawia przygotowanie nowej próbki przypadków neutrin elektronowych (ν_e) wybierającej oddziaływania przez prądy naładowane z produkcją pojedynczego pionu (CC$1\pi^+$) w dalekim detektorze T2K. Zlokalizowany w Japonii eksperyment T2K bada oscylacje neutrin za pomocą wiązki (anty)neutrin wytwarzanej przy akceleratorze, zespołu bliskich detektorów i dalekiego detektora Super-Kamiokande. Najbardziej ambitnym celem T2K jest zmierzenie fazy naruszającej symetrię CP w sektorze leptonowym, δ_{CP}, która potencjalnie mogłaby wyjaśnić pochodzenie obserwowanej we Wszechświecie asymetrii materia-antymateria. Pojawianie się (anty)neutrin elektronowych w wiązce (anty)neutrin mionowych w dalekim detektorze jest kanałem czułym na parametr δ_{CP}. Nową próbkę ν_e CC$1\pi^+$ wybiera się poprzez znalezienie pierścieni czerenkowskich pochodzących od elektronu i pionu. W połączeniu z istniejącą próbką jednopierścieniową ν_e CC$1\pi^+$, w której nie wymaga się pierścienia od pionu, nowa próbka zwiększa statystykę dla drugiej dominującej w obszarze energii T2K reakcji ν_e o 27%. Aby wykorzystać nową próbkę, przeliczono również ponownie niepewności systematyczne związane z dalekim detektorem. Ponadto dogłębnie zbadano rozdzielczości zmiennych kinematycznych używanych do binowania próbek, w wyniku czego wprowadzono do analizy zmienione binowanie próbek ν_μ i rozszerzonej próbki ν_e CC$1\pi^+$. Przeprowadzono analizę oscylacyjną przy pomocy dopasowania łańcuchami Markowa używanego w T2K, włączając rozszerzoną próbkę, zmienione niepewności systematyczne detektora i zaktualizowane binowanie — wszystkie te zmiany opisano w rozprawie. Wyniki wskazują, że wartości zachowujące CP $\delta_{CP} = 0, \pi$ są wykluczone w przedziale wiarygodności 90%, a preferowana jest wartość δ_{CP} bliska maksymalnemu łamaniu CP. Ponadto dane wykazują niewielką preferencję dla normalnej hierarchii mas neutrin i górnego oktantu kąta mieszania θ_{23}. Rozprawa przedstawia również badania czułości przy założeniu zwiększonej statystyki dla próbki ν_e CC$1\pi^+$. Ulepszenia przedstawione w rozprawie zostaną włączone do tegorocznej oficjalnej analizy oscylacyjnej T2K.

Acknowledgements

I would like to express my deepest gratitude to my PhD supervisor Justyna Łagoda for being a beacon of support and guidance for the last four years. She is the best supervisor I could have asked for. Her constant feedback and scientific discussions have been instrumental in developing my scientific temper, and also making me much more confident in myself. I look forward to continuing to learn and grow under her guidance.

Secondly, I would like to thank Kamil Skwarczyński, my auxiliary supervisor who has since day one been both a source of inspiration and also someone who I could always rely on. Not only has he expanded my knowledge of physics and statistics, but he also taught me so many technical things which I will forever be grateful for. Thank you sensei!

I extend my gratitude to everyone in the Warsaw Neutrino Group, who helped, inspired and encouraged me during my four years at NCBJ. I will always be indebted to their support. I also take this opportunity to thank the entire Polish Neutrino Group and the fruitful meetings we have had over the years, both in Poland and during T2K collaboration meetings.

It has been a fascinating and rewarding journey being part of the T2K Collaboration. I am thankful to have met incredibly talented peers, and also greatly inspiring senior scientists who kept my scientific curiosity thriving. Special thanks to Roger Wendell, Yasuhiro Nakajima, Junjie Xia and the entire T2K-SK group for their support, and valuable discussions that were influential in my research. I extend my gratitude to Cristovao Vilela, who not only introduced me to modern ways of analysing physics but also gifted me with two long research visits at CERN, a place I consider the temple of sciences. I also thank Trevor Towstego and Lakshmi S. Mohan for all their help.

I would like to thank all the members of the MaCh3, Oscillation Analysis, and NIWG groups with whom I worked through these years, and also for the support they have shown to me. The feedback I received from them was also really important in streamlining this thesis. I also extend my thanks to Shunichi Mine and Thomas Mueller, with whom I did my first collaborative studies. Mine-san implanted in me the importance of looking at the smallest details of the detector's working with the utmost care and also taught me early on about in-depth scientific thinking.

I cannot stress enough the role of Michael Reh in this journey. He is one of the best and most fun human beings I have met during my PhD, and on top of it, a wonderful collaborator. I also thank Henry Wallace for bearing with my silly and frequent questions regarding coding, and for being kind to respond to them even when he was busy writing his thesis.

I take this opportunity also to thank the Kamioka Computing System (Sukap), Centrum Informatyczne Świerk (CIŚ), and Compute Canada for their computing resources that were crucial in performing all the analyses described in this thesis.

Many thanks to all my wonderful friends at NCBJ who are like a family to me. I cherish all the fun times I have had with them over these years. Special love to Margherita, my gym and party partner and best friend, to Hareesh, my first friend at NCBJ and the most humble and caring person I know, to Prasad, for being the younger but older brother to me and Giuliano for the crazy person that you are.

My parents are my pillars of strength. They gave me unwavering support since my school days to pursue my love for Physics, and I am where I am only because of them. I love you both. I also thank my entire extended family. It has not been easy staying away from them for such a long time, but they showed all the love and care through these years which was crucial. All my love goes to Devu and Pinki for being the best sisters in the world.

Finally, all of this would not have been possible without you, Krishna Priya. Thank you for being there through thick and thin, and for constantly believing in me more than I do myself!

Contents

Declaration of Authorship iii

Abstract v

Streszczenie vii

Acknowledgements ix

Introduction 1

1 Review of Neutrino Physics 5
1.1 The Standard Model and Neutrinos . . . 5
1.2 Neutrino Oscillations . . . 6
1.3 Oscillation Parameters: Present Status . . . 9
1.4 CP Violation in Neutrino Sector . . . 10
1.5 Neutrino Interactions . . . 12
1.5.1 Charged-Current Quasi-Elastic Interactions . . . 13
1.5.2 Single Pion Production . . . 14
1.5.3 2p2h . . . 15
1.5.4 DIS and Multi-Pion Production . . . 16
1.6 Final State Interactions . . . 17

2 The Tokai-to-Kamioka Experiment 19
2.1 Beamline . . . 19
2.2 Off-Axis Technique . . . 21
2.3 Near Detectors . . . 22
2.3.1 INGRID . . . 23
2.3.2 ND280 . . . 23
2.4 ND280 Samples . . . 24
2.5 Far Detector . . . 25
2.5.1 Cherenkov Radiation . . . 25
2.5.2 ID and OD . . . 27
2.5.3 Event Reconstruction . . . 27
2.5.4 SK-Gadolinium . . . 28
2.6 FD Samples . . . 28
2.7 T2K Oscillation Analysis Results from 2023 . . . 29

3 Development of a Multi-Ring ν_e CC1π^+ Sample at SK 33
3.1 The Selection Cut Variables . . . 34
3.2 Optimization Strategy . . . 35
3.3 Flow of Cuts . . . 36
3.3.1 FC, FV and Visible Energy Cuts . . . 37
3.3.2 Number of Reconstructed Rings and Decay Electrons . . . 40
3.3.3 The $e\pi/\pi\pi$ PID Cut . . . 41

3.3.4 The $e\pi/\pi^0$ PID Cut . . . 42
3.3.5 $E_{rec} < 1.25$ GeV Cut . . . 42
3.4 Event Rates . . . 45
3.5 Selection Efficiency Studies . . . 45
3.6 The Expanded ν_e CC1π^+ Sample . . . 48
3.7 E_{rec} Binning Studies . . . 48
3.7.1 Revised E_{rec} Binning Scheme . . . 53

4 Oscillation Analysis **55**
4.1 Overview . . . 55
4.2 Statistical Framework . . . 55
4.2.1 Bayesian Statistics . . . 56
4.2.2 The Likelihood Function . . . 56
4.2.3 Markov Chain Monte Carlo (MCMC) . . . 58
4.3 Fitter Diagnostics . . . 60
4.3.1 Far Detector Predictive Spectra . . . 60
4.3.2 Log-Likelihood Scans . . . 61
4.3.3 Autocorrelation and Trace Plots . . . 62
4.3.4 $\hat{R}$ Test . . . 65
4.3.5 Posterior Probability Distributions . . . 66

5 Systematic Uncertainties **69**
5.1 Flux Systematic Model . . . 69
5.2 Cross-Section Systematic Model . . . 70
5.2.1 CCQE . . . 71
5.2.2 SPP . . . 72
5.2.3 2p2h . . . 73
5.2.4 Multi-π and DIS . . . 75
5.2.5 FSI . . . 76
5.2.6 Others . . . 76
5.3 ND280 Detector Systematic Model . . . 77
5.4 Systematic Errors at SK . . . 77
5.4.1 Uncertainties on Fiducial Volume and Decay Electron Tagging . . . 78
5.4.2 Energy Scale Uncertainty . . . 78
5.4.3 The Atmospheric Fit . . . 79
5.4.4 Toy MC Procedure . . . 83
5.4.5 Pion Secondary Interactions and Photo-nuclear Effects . . . 86
5.4.6 The Final SK Detector Matrix . . . 88
5.5 Impact of PMT Reflectivity on ν_e CC1π^+ Reconstruction . . . 89

6 Results **93**
6.1 Opening Data and Comparisons with MC . . . 93
6.2 Asimov Fit Results . . . 96
6.3 Data Fit - Systematic Parameters . . . 98
6.4 Data Fit - Oscillation Parameters . . . 105
6.5 Comparison with T2K's Latest Analysis . . . 110

7 Future Sensitivity Study **113**
7.1 Data Excess in ν_e CC1π^+ Sample . . . 113
7.2 Constructing the Fake-Data Set . . . 114
7.3 Asimov Fit Results . . . 116

7.4 Impact of Oscillation Parameters on the ν_e CC1π^+ Sample 118

8 Summary **121**

A Additional Studies **123**
A.1 Impact of PMT Reflectivity on e/π^0 Separation 123
A.2 Additional Resolution Plots 124
A.3 Further Breakdown of Post-Fit Errors 125

B Posterior Distributions **127**
B.1 Cross-Section Parameters 127
B.2 SK Detector Parameters 135
B.3 Flux Parameters 141

Glossary **151**

Bibliography **153**

To my Parents

Introduction

> If I have seen further it is by standing on the shoulders of Giants.
>
> Isaac Newton

Ever since the dawn of humanity, we humans have been dazzled by the way the world works around us, be it everyday things like how birds fly, or even to the extent of how fundamental particles get mass through the Higgs mechanism. What started as a cognitive revolution about 70,000–30,000 years back in Homo sapiens, brought us to a place where we are capable of probing the tiniest building blocks of matter and feeling the faintest of gravitational vibrations from two distant galaxies merging.

On top of all this, as we ponder deep into the voids of the universe and slightly deeper into physics, a question arises. If science tells us that the Big Bang did create matter and antimatter equally, where did all that antimatter go? Why do we live in a universe which is isotropically matter-dominated? What phenomena at a cosmic scale caused this asymmetry?

Many have tried to answer this question, with Sakharov being credited with the most pedantic of solutions [1]. He proposed that for matter-antimatter asymmetry to take place, any of the three conditions need to be fulfilled:

- Baryon number violation.
- C-symmetry and CP symmetry violation.
- Thermal nonequilibrium.

Out of these, CP violation has been observed in multiple quark sector processes. However, the magnitude of CP violation in quarks is too small to explain the asymmetry. In the leptonic sector, CP violation is engraved within neutrino mixing and neutrino flavour oscillations can be used as a probe to measure it. This CP violation will occur as differences in neutrino-antineutrino oscillation and from the global data available so far, it can be two orders of magnitude as big as that in the quark sector. Thus, a huge push is underway in the physics community to measure the extent of CP violation in the leptonic sector by studying neutrino oscillations. This measurement of course requires the knowledge of all the other oscillation parameters, and multiple experiments have been able to measure some of these parameters very well in the last two decades.

As neutrino oscillation physics enters an era of precision, the goal to make the best out of the data collected in various neutrino oscillation experiments takes utmost importance. The Tokai-to-Kamioka (T2K) experiment [2] in Japan has been one of the two leading accelerator neutrino-based oscillation experiments since 2010. Along its way, T2K has achieved many milestones, for instance, T2K hinted at a non-zero θ_{13} mixing angle [3] followed by the first-ever observation of appearance channel [4], and in the most recent times, the strongest constraints on leptonic CP violation phase δ_{CP} [5].

The main motivation behind the works of this thesis is to improve T2K's capabilities to constrain neutrino oscillation parameters that the experiment is sensitive to. Oscillated ν_e events from T2K's ν_μ beam provide sensitivity to δ_{CP} , and the latter's measurements at T2K

are currently limited due to ν_e statistics. Furthermore, one of the most intriguing problems in T2K's analyses so far has been the event rate inconsistency observed in the low energy bin for the single-ring ν_e charged-current single pion production (CC1π^+) sample. This sample targetted ν_e CC1π^+ interactions where the π^+ was below its Cherenkov threshold, hence not capable of producing a ring at Super-Kamiokande detector but only leaving a delayed decay electron signature. The need for the π^+ to be below the Cherenkov threshold introduces π^+ production model dependencies, which at the time of writing is not very well understood.

By introducing the new multi-ring ν_e CC1π^+ sample that will be the main topic in this thesis, we aim to potentially improve, if not maintain T2K's sensitivity to δ_{CP} . Subsequently, by adding this sample the sharp π^+ momentum threshold dependence in ν_e CC1π^+ sample is removed and provides a potential resolution to the data-Monte Carlo discrepancy until a model that can better describe the π^+ production comes into existence. In addition, the kinematic binning of all the far detector samples was revisited and updated based on resolution studies. The SK detector uncertainties were also re-calculated with the inclusion of the new sample, all of which will be described in this thesis.

This thesis is organized in the following way:

Chapter 1 provides a concise review of the physics of neutrino oscillations and interactions. Current unknowns in neutrino oscillation physics, with special emphasis on CP violation in the leptonic sector, are described. Neutrino interactions most important in the context of this thesis are also discussed.

Chapter 2 introduces the T2K experiment. Each component of the T2K experiment, ranging from neutrino beam production, near detectors and the far detector are summarised. A brief introduction to how T2K performs its oscillation analysis is also presented.

Chapter 3 discusses the first key part of this analysis, where the Author develops a new far detector electron neutrino sample. Related studies such as selection efficiencies and binning optimisations are also included.

Chapter 4 switches to the oscillation analysis including the new sample and changes in the analysis introduced by the Author. A clear description of the Bayesian Markov Chain Monte Carlo (MCMC) framework used for the analysis is given. Some of the diagnostic tests related to Markov Chain convergence are also mentioned.

Chapter 5 outlines the various sources of systematic uncertainties that impact the oscillation analysis. Special emphasis is given to neutrino interaction systematic parameters that most dominantly impact the charged-current resonant pion production, which contributes the most to the sample developed in Chapter 3. The second half of the chapter introduces the systematic uncertainties of the Super-Kamiokande detector that govern the errors on T2K beam samples. The Author updated and recalculated the detector's systematic errors for this analysis. A study on how SK's photomultiplier tube (PMT) reflectivity impacts the expanded ν_e CC1π^+ sample is also presented.

Chapter 6 showcases the results of the oscillation analysis that the Author performed with the addition of the new sample, along with the improvements in the SK detector systematic parameters, and the new binning schemes. A comparison to T2K's official 2023 oscillation analysis is also portrayed to show the impact of this study on T2K's oscillation parameter sensitivities.

In Chapter 7, the Author describes the sensitivity studies assuming higher statistics for the expanded ν_e CC1π^+ sample, along with some additional tests done to support the results from the sensitivity study.

Chapter 8 will finally summarize all the results, present the latest world picture of neutrino oscillation physics, and discuss future prospects.

Various other studies directly related to the main topics discussed in the thesis were conducted by the Author. This is discussed concisely in the Appendix A. Due to the fact that the

main text cannot include all the plots from every parameter involved in the analysis, they are portrayed in Appendix B.

Best efforts have been made to keep the thesis as general as possible for a reader outside of T2K collaboration, with references to published and detailed T2K analyses provided in most instances. However, some technical details that support the main text are only available in T2K's internal technical notes and are restricted to T2K collaborators. A dictionary of all abbreviations used in the thesis has also been included in the end for the reader's convenience.

1

Review of Neutrino Physics

> It doesn't matter how beautiful your theory is, it doesn't matter how smart you are. If it doesn't agree with the experiment, it's wrong.
>
> *Richard P. Feynman*

1.1 The Standard Model and Neutrinos

One beautiful theory that has stood the test of time, and almost every experiment for that matter, is the Standard Model (SM) of particle physics [6–8]. The theory describes three of the four fundamental interactions that we observe in the universe, namely the strong, weak, and electromagnetic interactions using the machinery of quantum field theory. The SM neatly lays out a table (Fig. 1.1) of fundamental particles, where the quarks and leptons have spin $\frac{1}{2}$ and follow Fermi statistics. Of the particles that have integer spins (and hence bosons) in the SM, four of them are the carriers of the forces mentioned above. Finally, the fundamental field of the Higgs boson is what gives mass to the particles.

The fermions are further divided into quarks and leptons, both of which come in three generations of increasing mass. The number of bosons and their interactions with fermions and with themselves are uniquely determined as a result of the SM being based on the local gauge group $SU(3)_C \times SU(2)_L \times U(1)_Y$ gauge transformation. The $SU(3)_C$ part of this group gives rise to the eight massless gluons that govern the strong interaction experienced by quarks. The $SU(2)_L \times U(1)_Y$ sector describes the Weinberg-Salam electro-weak theory that governs the weak and electromagnetic interactions mediated by weak vector bosons $W^{\pm}$, Z^0 and photon γ respectively.

Neutrinos are neutral leptons that are coupled to their corresponding charged leptons as weak isospin doublets. In the SM framework, neutrinos are considered massless, possessing only left-handed chirality, and interacting only via weak interactions. Their story started in the early 20^{th} century when Chadwick found out that the β spectrum from the radioactive decay of uranium was continuous, unlike the α rays which were monoenergetic. Neutrinos, then unknown, were first proposed by Wolfgang Pauli in December of 1930 as a desperate measure to save the law of energy conservation, by stating that the missing energy in the β spectrum was, in fact, carried away by these tiny undetectable neutral particles. Three years later, Enrico Fermi brought forth his theory of β decay, where he first termed these particles neutrinos or "little neutral ones".

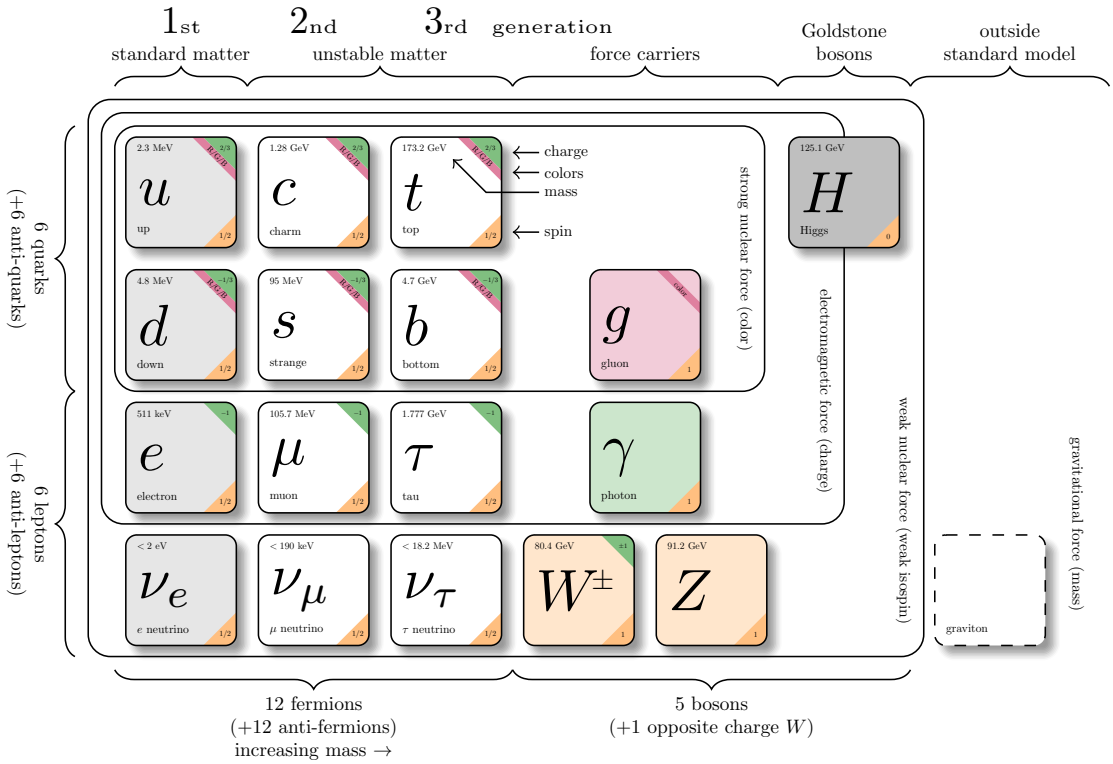

FIGURE 1.1: The Standard Model of Particle Physics [9].

It took another 23 years after Fermi's theory for the science community to come to a conclusion that these particles do exist, as they were finally detected by an experiment under the banner of Project Poltergeist, led by Cowan and Reines [10] in 1956. Using a liquid scintillator-based detector, they observed the positrons from the inverse beta decay process $\overline{\nu}_e + p \rightarrow n + e^+$, along with a delayed gamma signal from the neutron capture, where the anti-neutrinos came from the nearby Savannah River nuclear reactor.

The following decades saw multiple experiments designed to detect neutrinos emanating from various natural and human-made sources.

1.2 Neutrino Oscillations

In the late 1950s, Ray Davis' and John Bahcall's Homestake experiment [11] built specifically to measure the solar neutrinos observed a deficit in the solar neutrino flux. Solar neutrinos are created in thermonuclear reactions that take place in the Sun's core. The Standard Solar Model predicted about 8.1 ± 1.2 solar neutrino units (SNU, where 1 SNU = 1 neutrino detection per 10^{36} target atoms of the detector every second) while the Homestake experiment only observed 2.56 ± 0.25 SNU. This deficit of observed neutrino flux versus the predictions came to be known as the Solar neutrino problem.

After almost 20 years, two water Cherenkov detectors that were designed to search for proton decays, IMB and Kamiokande were studying atmospheric neutrinos since they were the background to proton decay searches. Atmospheric neutrinos are produced in the Earth's atmosphere due to the interactions of cosmic ray protons with the nuclei in the upper atmosphere. If this interaction produces a charged pion, the charged pion decays as:

$$\pi^{\pm} \rightarrow \mu^{\pm} + \overset{(-)}{\nu_{\mu}} \tag{1.1}$$

where the $\mu^{\pm}$ decays via

$$\mu^{\mp} \rightarrow \overset{(-)}{\nu_{\mu}} + e^{\mp} + \overset{(-)}{\nu_{e}} \tag{1.2}$$

In the GeV range, for every charged pion decay chain, one would expect two muon-type neutrinos ($\nu_{\mu} + \overline{\nu}_{\mu}$) and one electron-type neutrino (ν_e or $\overline{\nu}_e$), making the ratio of these two neutrino fluxes 2 : 1 at these detectors. However, both IMB and Kamiokande observed a deficit in the flux of muon neutrinos coming from below, which was then called the atmospheric neutrino problem.

Way before these anomalies were observed, Bruno Pontecorvo had put forward the theory of neutrino masses and mixing in 1957 inspired by the $K^0 \leftrightarrow \bar{K}^0$ oscillations in the quark sector. In the following years, he extensively worked on this [12–15] contemporarily with Z. Maki, M. Nakagawa and S. Sakata [16], leading to the theory of neutrino oscillations in three flavours as we know it today.

According to this theory, neutrino flavour states produced at the weak interaction vertices are a linear superposition of neutrino mass states, with the mass states being the true eigenstates of the energy Hamiltonian:

$$|\nu_{\ell}\rangle = \sum_{i=1,2,3} U_{\ell i} |\nu_i\rangle. \tag{1.3}$$

ν_{ℓ} represents the neutrino flavour state where $\ell = e, \mu, \tau$, and ν_i represents the neutrino mass states. The term $U_{\ell i}$ comes from the 3×3 Pontecorvo-Maki-Nakagawa-Sakata (PMNS) matrix, named after the pioneers behind the theory. This unitary matrix mitigates the mixing between the neutrino flavour states and the mass states and is constructed similarly to its quark-sector counterpart, the CKM matrix. The matrix is parametrized by three mixing angles θ_{12}, θ_{23} and θ_{13} along with the phase δ_{CP} that makes the matrix complex.

$$\begin{pmatrix} \nu_e \\ \nu_{\mu} \\ \nu_{\tau} \end{pmatrix} = \begin{pmatrix} 1 & 0 & 0 \\ 0 & c_{23} & s_{23} \\ 0 & -s_{23} & c_{23} \end{pmatrix} \begin{pmatrix} c_{13} & 0 & s_{13} e^{-i\delta_{CP}} \\ 0 & 1 & 0 \\ -s_{13} e^{i\delta_{CP}} & 0 & c_{13} \end{pmatrix} \begin{pmatrix} c_{12} & s_{12} & 0 \\ -s_{12} & c_{12} & 0 \\ 0 & 0 & 1 \end{pmatrix} \begin{pmatrix} \nu_1 \\ \nu_2 \\ \nu_3 \end{pmatrix} \tag{1.4}$$

Here, c_{ij}, s_{ij} stand for $\cos\theta_{ij}, \sin\theta_{ij}$ for each mixing angle. The phase δ_{CP} is called the charge conjugation-parity (CP) violating phase in the leptonic sector.

That the neutrino flavour states are a linear superposition of mass states tells us that a neutrino of flavour ν_{α} created at a spacetime point x_1 need not necessarily remain the same once it traverses to another spacetime point x_2. This is because mass states ν_i will travel at different phase velocities.

A flavour state generated at a weak interaction vertex, $|\nu_{\alpha}(x = 0)\rangle = U_{\alpha 1}|\nu_1\rangle + U_{\alpha 1}|\nu_2\rangle + U_{\alpha 3}|\nu_3\rangle$ will propagate through spacetime as

$$|\nu_{\alpha}(t)\rangle = U_{\alpha 1} e^{-ip_1 \cdot x} |\nu_1\rangle + U_{\alpha 2} e^{-ip_2 \cdot x} |\nu_2\rangle + U_{\alpha 3} e^{-ip_3 \cdot x} |\nu_3\rangle, \tag{1.5}$$

where $p_i \cdot x = E_i t - \mathbf{p_i} \cdot \mathbf{x}$. At this point, we invoke the unitarity of the PMNS matrix U to rewrite neutrino mass states as the superposition of the flavour states and simultaneously apply the following two approximations assuming neutrinos are relativistic and that they travelled a distance L through spacetime:

$$p_i \cdot x = E_i t - |p_i| L \sim (E_i - |p_i|) L, \tag{1.6}$$

and

$$p_i = \sqrt{E_i^2 - m_i^2} \sim E_i(1 - \frac{m_i^2}{E_i^2}). \tag{1.7}$$

To get the probability that ν_α oscillates to ν_β, or $P(\nu_\alpha \to \nu_\beta)$, we plug these two approximations back into Eqn. 1.5, and evaluate $|\langle \nu_\beta | \nu_\alpha(L) \rangle|^2$. Omitting the detailed derivations for the sake of brevity (detailed review can be found in [17–19]), we finally arrive at the well-known (anti)neutrino oscillation probability equation in a vacuum,

$$\begin{aligned} P(\overset{(-)}{\nu}_\alpha \to \overset{(-)}{\nu}_\beta) = \delta_{\alpha\beta} - 4\sum_{i>j} \mathcal{R}e(U^*_{\alpha i}U_{\beta i}U_{\alpha j}U^*_{\beta j}) \sin^2\left(\Delta m^2_{ij}\frac{L}{4E}\right) \\ \mp 2\sum_{i>j} \mathcal{I}m(U^*_{\alpha i}U_{\beta i}U_{\alpha j}U^*_{\beta j}) \sin^2\left(\Delta m^2_{ij}\frac{L}{2E}\right). \end{aligned} \tag{1.8}$$

The term $\Delta m^2_{ij} = m^2_i - m^2_j$ gives us the mass-squared differences between two neutrino mass states. In the three neutrino flavour framework, there are two independent mass-squared differences Δm^2_{21} and Δm^2_{32}. Together with the three mixing angles and the CP phase, they form six neutrino oscillation parameters. Mass hierarchy of a particular mass-squared difference Δm^2_{ij} is defined as normal hierarchy if $m^2_i > m^2_j$ and inverted hierarchy for vice versa.

Three things strike the eye immediately from the Eqn. 1.8:

- The oscillatory behaviour of the $\nu_\alpha \to \nu_\beta$ transition is governed by the ratio of L/E, where L is often referred to as the baseline.
- The probability is only sensitive to the mass-squared differences between the mass states and not the absolute neutrino masses.
- The probability is, by definition, different for neutrinos and antineutrinos, in case the imaginary term in Eqn. 1.8 is non-zero.

The atmospheric neutrino deficit could be explained by the oscillation of $\overset{(-)}{\nu}_\mu$ to $\overset{(-)}{\nu}_\tau$. The atmospheric neutrinos that travelled greater distances before reaching the detector, for example, the $\overset{(-)}{\nu}_\mu$ passing all the way through the earth, would have a higher probability of oscillating into $\overset{(-)}{\nu}_\tau$ than those produced directly above the detector, with a baseline of only $\sim$ 15 km. The distance that atmospheric neutrinos travel before detection can be linked to its zenith angle, and this angular dependence of the $\overset{(-)}{\nu}_\mu$ flux was first observed by the Super-Kamiokande experiment [20] in 1998, confirming the theory of neutrino oscillations.

However, to explain the solar neutrino problem, neutrino oscillations in vacuum were not enough. Electron neutrinos produced in the Sun's core have to travel through dense solar matter before leaving its surface. The presence of a high density of electrons in this matter causes these neutrinos to undergo coherent forward scattering, leading to a perturbed Hamiltonian. Depending on the neutrino energy and the density of electrons, the neutrino oscillation probabilities get enhanced. This effect is known as the Mikheyev-Smirnov-Wolfenstein (MSW) or the matter effect [21], which necessitates the correction of Eqn. 1.8 to include the matter-induced effects.

The perturbation ΔV due to the scattering is related to the electron density through

$$\Delta V = 2\sqrt{2}G_F E\rho_e \tag{1.9}$$

where G_F is the Fermi constant, E the neutrino energy, and ρ_e is the electron density in matter. This perturbation effectively modifies the mixing angle and mass-squared differences as follows:

$$\sin(2\theta_m) = \frac{\sin(2\theta)}{\sqrt{(\Delta V/\Delta m^2) - \cos(2\theta))^2 + \sin^2(2\theta)}} \tag{1.10}$$

and

$$\Delta m^2_m = \Delta m^2 \sqrt{(\Delta V/\Delta m^2) - \cos(2\theta))^2 + \sin^2(2\theta)} \tag{1.11}$$

As $\Delta V = 2\sqrt{2}G_F E\rho_e$ goes to infinity, $\sin^2(2\theta_m) \to 0$, terminating any oscillations in dense matter. Incidentally, when $\Delta V \to 0$, we get back vacuum oscillation parameters. For the special condition of $2\sqrt{2}G_F E\rho_e/\Delta m^2 \to \cos(2\theta)$, the mixing angle $\theta_m \to \pi/4$, enhancing the oscillations to its maximum in matter. This scenario is termed the MSW resonance.

In 2003, the SNO experiment [22] succeeded in solving the solar neutrino problem by measuring not just the incoming electron neutrino flux, but the flux of all three flavours of neutrinos ($\Phi(\nu_e) + \Phi(\nu_\mu) + \Phi(\nu_\tau)$), thanks to the measurement of NC events, after which the numbers matched the predictions well. The solar MSW effects also helped determine that $m_2 > m_1$, since matter effects help distinguish between mass-hierarchies.

Discoveries from both Super-Kamiokande and SNO received the Nobel Prize in 2015 for the confirmation of neutrino oscillations and through it the imminence of non-zero neutrino mass.

1.3 Oscillation Parameters: Present Status

Neutrino experiments that use different sources of neutrinos are designed with specific choices of L/E to give sensitivity to various neutrino oscillation parameters as shown in Table 1.1.

Neutrino sources/ /experiments	Baseline (L) [km]	Neutrino Energy (E) [MeV]	Sensitivity to oscillation parameters
Solar Neutrinos	10^{11}	$0.1 - 10$	Δm^2_{21}, θ_{12}
Atmospheric Neutrinos	$10 - 10^4$	$100 - 10000$	Δm^2_{32}, θ_{23}
Reactor Neutrinos - short baseline	1	1	Δm^2_{21}, θ_{13}
Reactor Neutrinos - long baseline	100	1	Δm^2_{21}, θ_{12}
Accelerator Neutrinos	100-1000	$500 - 5000$	Δm^2_{32}, θ_{23}, θ_{13}, δ_{CP}

TABLE 1.1: Types of neutrino experiments with their source of neutrinos along with their baseline (L), neutrino energy (E) and the oscillation parameters that they can probe.

Due to the relation between the neutrino sources and the parameters they can probe, Δm^2_{12} and θ_{12} are often called solar mass-squared differences and mixing angles respectively, while θ_{13} is commonly called the reactor mixing angle. The Δm^2_{32} and θ_{23} get the atmospheric prefix to them. Since this thesis covers the oscillation studies with an accelerator neutrino experiment, it's imperative to mention that accelerator neutrino experiments are state-of-the-art when it comes to studying δ_{CP} , on top of their sensitivities to atmospheric and reactor mixing parameters.

The solar neutrino sector has been very well measured, establishing through the MSW effect that $m_2 > m_1$. It is currently not known whether the third neutrino mass state is heavier than the second, or smaller than the first. The case where $m_3 > m_2 > m_1$ is referred to as normal hierarchy or ordering (NH/NO) while $m_2 > m_1 > m_3$ is called inverted hierarchy

or ordering (IH/IO). The atmospheric and accelerator neutrino experiments so far have not succeeded in resolving this mass hierarchy problem, making it one of the unknowns of the neutrino sector.

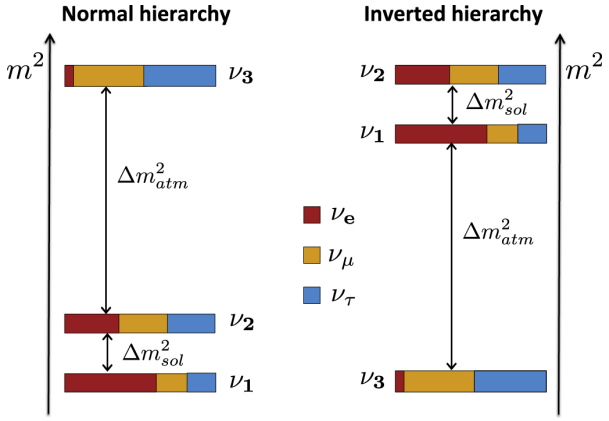

FIGURE 1.2: Neutrino mass hierarchy [23].

The mixing angle θ_{23} has been measured to be almost maximal (around 45°) but it's not yet known with precision whether it is exactly maximal (=45°), greater than 45° (upper octant, UO) or smaller than 45° (lower octant, LO). This is called the octant problem of θ_{23}. Many theories try to search for underlying symmetries in neutrino masses and mixing, and the resolution of θ_{23}'s octant will provide a very important input to such theories.

After a long period of uncertainty, reactor neutrino experiments Daya Bay [24] and RENO [25] independently measured a non-zero value of θ_{13} in 2012[1]. Shortly after that, the accelerator neutrino experiment T2K also recorded a consistent value of θ_{13}, opening the possibility of entering a whole new regime of CP violation measurements in the leptonic sector. Had the value of θ_{13} been very small, or even 0, the observation of CP violation would not have been possible in the neutrino sector.

1.4 CP Violation in Neutrino Sector

The transformation of $P(\nu_\alpha \rightarrow \nu_\beta) \rightarrow P(\overline{\nu}_\alpha \rightarrow \overline{\nu}_\beta)$ happens through the symmetry transformation of charge-conjugation (C) and parity (P). If a process is non-invariant upon CP transformation, it results in the violation of CP symmetry. CP violation within the SM has been observed in the weak interactions of the quark sector, raising the question of whether this happens in the leptonic sector too.

Heading back to Eqn. 1.8, for CP symmetry to break in the leptonic sector, the second term that differs in sign between neutrinos and antineutrinos needs to be non-zero. Accelerator neutrino experiments look for CP violation by studying the appearance of electron (anti)neutrinos from a beam of muon (anti)neutrinos, equivalently the $P(\nu_\mu \rightarrow \nu_e)$ and $P(\overline{\nu}_\mu \rightarrow \overline{\nu}_e)$ oscillations. In the context of these oscillations, the term that needs to be non-zero can be written as the Jarlskog invariant [26]:

$$J_{CP,I} = \frac{1}{8}\mathcal{I}m(U_{\mu 3}U_{e2}U^*_{\mu 2}U^*_{e3}). \tag{1.12}$$

When expanded in terms of the PMNS matrix 1.4, this term becomes:

$$J_{CP,I} \equiv \sin(\theta_{13})\cos^2(\theta_{13})\sin(\theta_{12})\cos(\theta_{12})\sin(\theta_{23})\cos(\theta_{23})\sin(\delta_{cp}). \tag{1.13}$$

[1]The first hint for a non-zero θ_{13} came from T2K [3].

The Jarlskog invariant determines how strongly the CP symmetry is violated.

Table 1.2 shows the values of neutrino oscillation parameters obtained from fit to global neutrino experiment data [27].

Oscillation parameter	Best fit	
	NH	IH
$\sin^2\theta_{12}$	$0.304^{+0.012}_{-0.012}$	$0.304^{+0.013}_{-0.012}$
$\sin^2\theta_{23}$	$450^{+0.019}_{-0.016}$	$570^{+0.016}_{-0.022}$
$\sin^2\theta_{13}$	$0.02246^{+0.000062}_{-0.000062}$	$0.02241^{+0.000074}_{-0.000062}$
Δm^2_{21} $[10^{-5}$ eV$^2]$	$7.42^{+0.21}_{-0.20}$	$7.42^{+0.21}_{-0.20}$
Δm^2_{31} $[10^{-3}$ eV$^2]$	$+2.510^{+0.027}_{-0.027}$	$-2.490^{+0.026}_{-0.028}$
δ_{CP}	230^{+36}_{-25}	278^{+22}_{-30}

TABLE 1.2: Neutrino oscillation parameters from the fit to global neutrino experimental data with constraints from Super-Kamiokande's atmospheric neutrino data [27].

Substituting the latest best-fit values of the mixing angles into Eqn. 1.13, we obtain

$$J_{CP,l} \approx 0.033 \sin(\delta_{CP}) \tag{1.14}$$

The universe as we know it is matter-dominated, and one of the ways this can happen is through the CP violation in the fundamental building blocks of the universe, as stated by Sakharov [1]. Assuming maximal CP violation by putting $\delta_{CP} = \pm\pi/2$ in Eqn. 1.14, we get $J_{CP,l} = \pm 3 \times 10^{-2}$, which is three orders of magnitude larger than the Jarlskog invariant in the quark sector, $J_{CP,q} = 3 \times 10^{-5}$. This makes the race to determine the CP phase truly exciting, not just for neutrino physicists, but the whole scientific community.

Neutrino experiments generally study oscillations in two ways. The first method is to observe how many neutrinos of a particular flavour produced at the source survived by the time it was detected, called the disappearance channel. The second way is to study the appearance of neutrinos with flavours different from those produced at the source, called the appearance channel. In the context of accelerator neutrinos, the neutrinos produced at the source are the muon (anti)neutrinos. They are created via the same charged pion decay chain as in atmospheric neutrinos. The disappearance and appearance channel probabilities for accelerator neutrinos are as follows:

$$\begin{aligned} P(\overset{(-)}{\nu}_\mu \to \overset{(-)}{\nu}_\mu) \approx 1 - 4\cos^2(\theta_{13})\sin^2(\theta_{23}) \\ \times (1 - \cos^2(\theta_{13})\sin^2(\theta_{23}))\sin^2\left(\frac{1.27\Delta m^2_{32}L}{E}\right), \end{aligned} \tag{1.15}$$

and

$$\begin{aligned} P(\overset{(-)}{\nu}_\mu \to \overset{(-)}{\nu}_e) \approx \sin^2(\theta_{23})\sin^2(2\theta_{13})\sin^2\left(\frac{1.27\Delta m^2_{32}L}{E}\right) \\ \mp 8 J_{CP,l}\frac{1.27\Delta m^2_{21}L}{E}\sin^2\left(\frac{1.27\Delta m^2_{32}L}{E}\right), \end{aligned} \tag{1.16}$$

where the factor 1.27 comes from taking into consideration values of fundamental constants c and $\hbar$ and measuring L in km and E in GeV. One has to pay attention that CP violation does not manifest in the disappearance channel and that the appearance channel is the only possible way to probe it. Studying the disappearance channel (Eqn. 1.15) provides constraints on all the oscillation parameters apart from δ_{CP} , helping tighten the constraints on δ_{CP} through the appearance channel measurements (Eqn. 1.16.)

1.5 Neutrino Interactions

Neutrinos can interact with fermions via weak interactions by the exchange of $W^{\pm}$ bosons, which is termed charged-current (CC) interactions, and through the exchange of Z^0 bosons, which is called neutral-current (NC) interactions. When it comes to studying neutrinos, it's crucial to have final-state particles that can be identified by the detectors, since neutrinos themselves are not directly detectable. It is therefore evident that the CC interactions are of paramount importance, as they result in the production of final state leptons of the same flavour as that of the parent neutrino, along with other particles which uniquely determine the nature of the neutrino interaction. Neutrino CC interactions can be broadly divided into three types[2] which dominate different neutrino energy regions:

- Quasi-Elastic (QE) scattering ($\nu_\ell + N \rightarrow \ell + N'$)
- Single pion production (SPP) ($\nu_\ell + N \rightarrow \ell + N' + \pi^{\pm,0}$)
- Deep-inelastic scattering (DIS) ($\nu_\ell + N \rightarrow \ell + N' + X$)

where ν_ℓ is the parent neutrino of flavour $\ell = e, \mu, \tau$, ℓ is the corresponding charged lepton, N is the target nucleon and N' the outgoing nucleon, $\pi^{\pm,0}$ is a charged or neutral pion, and X represent the hadrons collectively produced in DIS. The SPP is further divided into resonant (RES), non-resonant and coherent (COH) processes. All these interactions will be discussed in the following sections.

The CC (anti)neutrino interaction cross-section as a function of neutrino energy is shown in Fig. 1.3. For sub-GeV neutrino energies, QE is the most dominant interaction, followed by a subdominant contribution from the RES. DIS becomes prominent as neutrinos achieve energies above a few GeVs.

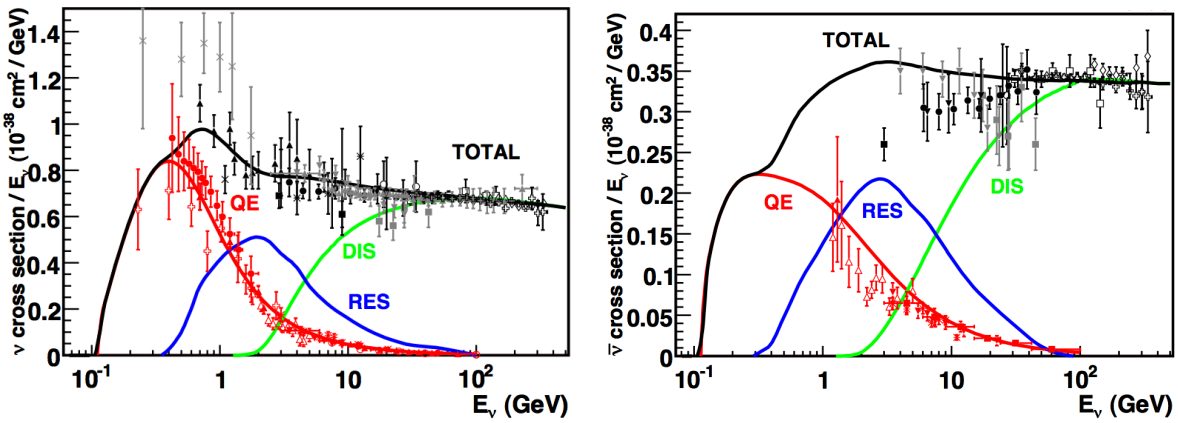

FIGURE 1.3: Interaction cross-sections as a function of (anti)neutrino energy [28]. Note that RES denotes the resonant pion production cross-section, which will be described in Section 1.5.2.

This thesis focuses on the T2K experiment, which will be introduced in the next chapter. T2K operates in the regime of sub-GeV neutrinos, hence the following sections will describe the CCQE and CCRES interactions more explicitly, along with that of the background processes.

[2]Elastic scattering on electrons is also possible, with the interaction being CC for ν_e and NC for all the flavours. However, these are neglected mainly due to much smaller cross-sections.

1.5.1 Charged-Current Quasi-Elastic Interactions

Neutrinos with sub-GeV energies interact with nucleons through the simplest of $W^{\pm}$-exchange processes as shown in the Feynman diagram 1.4, where the parent neutrino converts to a lepton of the same flavour whilst the parent nucleon converts to its isospin twin. This interaction is called the charged-current quasi-elastic (CCQE) interaction and is the most dominant neutrino interaction in experiments that work with neutrinos of sub-GeV like the T2K experiment.

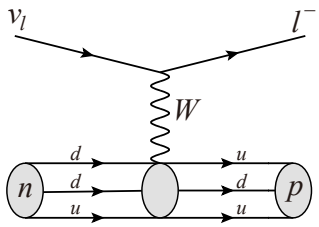

FIGURE 1.4: Tree-level Feynman diagram for a CCQE interaction

Albeit the simple structure, the interaction cross-section for this process is dependent not only on the parent neutrino's and nucleon's kinematics but also on the electric, magnetic, pseudoscalar and axial form factors of the parent nucleon. The electric and magnetic form factors are constrained well from electron scattering data [29]. The pseudoscalar form factor can be merged with the axial form factor, which is assumed to have a dipole form:

$$F_A(Q^2) = \frac{g_A}{\left(1 + \frac{Q^2}{(M_A^{QE})^2}\right)^2} \tag{1.17}$$

where Q^2 is the energy transferred from the neutrino to the parent nucleon, M_A^{QE} is the axial mass [30] corresponding to the QE interaction, and g_A is the normalisation factor known from neutron β decay as $= F_A(Q^2 = 0) = 1.2670 \pm 0.0035$. In this form factor parametrization, axial mass is the only remaining parameter which has to be measured by neutrino scattering experiments [31].

Detectors that require certain kinematic thresholds to be able to identify outgoing particles from an interaction, for example, the water Cherenkov detectors like Super-Kamiokande, cannot detect in most cases the outgoing proton due to their high Cherenkov threshold. Given the CCQE interaction is essentially a two-body process, the neutrino energy can be obtained exclusively from the outgoing lepton kinematics, assuming the neutrino interacted with a stationary nucleon as follows:

$$E_\nu^{rec,CCQE} = \frac{m_p^2 - (m_n - E_b^2)^2 - m_\ell^2 + 2(m_n - E_b)E_\ell}{2(m_n - E_b - E_\ell + p_\ell \cos(\theta_\ell))} \tag{1.18}$$

where $m_{p,n}$ are the proton and neutron masses, $p_\ell, E_\ell, \cos(\theta_\ell)$ are outgoing lepton momentum, energy and direction to the parent neutrino (beam in the case of T2K) and E_b is the nucleon binding energy.

However, the assumption that the target nucleon is stationary is only approximate and it is well-known that the nucleons bound inside the nucleus do undergo Fermi motion. This intra-nuclear Fermi motion is described by the spectral function (SF) model in NEUT [32], the neutrino event generator used by T2K. Another phenomenon that happens inside the nucleus is Pauli blocking. The interactions with low energy transfer get suppressed because neither can the nucleon be in an already occupied state nor can it exit the nucleus.

1.5.2 Single Pion Production

Within the energies where neutrinos can only probe nucleons as a whole, the second most dominant interaction that occurs is the single pion production (SPP), which constitutes of both (non)resonant and coherent pion productions. While there can be both neutral and charged current SPP, the former appears mostly as background while the latter is used as signal neutrino events.

Resonant Pion Production

This is the most dominant mode of SPP, which occurs when a neutrino scatters off a nucleon and raises it to one of its excited states. For energies below a few GeVs, the excited nucleon mostly attains the $\Delta(1232)$ resonance, which decays to a pion through interactions as follows:

$$\begin{aligned} \Delta^{++} &\rightarrow \pi^{+} + p \\ \Delta^{\pm} &\rightarrow \pi^{\pm} + n \\ \Delta^{+} &\rightarrow \pi^{0} + p \\ \Delta^{0} &\rightarrow \pi^{-} + p \\ \Delta^{0} &\rightarrow \pi^{0} + n \end{aligned} \tag{1.19}$$

The Feynman diagram for a neutrino interaction that undergoes SPP through Δ^{++} resonance state is shown in Fig. 1.5. Latest literature contains various models that can describe the RES SPP, for example, the Sato-Lee model [33] and the Rein-Sehgal (RS) model [34]. NEUT follows the RS model which uses two sequential steps to simulate a RES: a baryon resonance production ($\nu + N \rightarrow \ell + N^{*}$) followed by the decay of the resonance to a pion ($N^{*} \rightarrow \pi + N'$). Due to the presence of multiple resonances that can produce the same final state, interference terms are taken into account between the resonances. NEUT considers 18 such resonances below 2 GeV/c^2, where the cross-sections of each of them can be factorised as a function of form-factor dependent resonance production and that of pion-kinematics through Adler angles that only affect the hadronic system that escapes the nucleus as in Eqn. 1.20:

$$\frac{d^2\sigma}{dQ^2dW}\frac{d\sigma}{d\Omega} = \frac{d^2\sigma}{dQ^2dW}\frac{d\sigma}{d\cos\theta d\phi} \,. \tag{1.20}$$

The form factor for RES is obtained through Eqn 1.21, where the axial mass for RES SPP is represented by M_A^{RES}. The normalisation term coined as $C_5^A(Q^2 = 0) = F_A^{RES(Q^2=0)}$ is taken from Graczyk and Sobczyk [35]. Unlike its CCQE counterpart g_A, the normalisation factor $c_5^A(Q^2 = 0)$ has not been measured as precisely as the former [36].

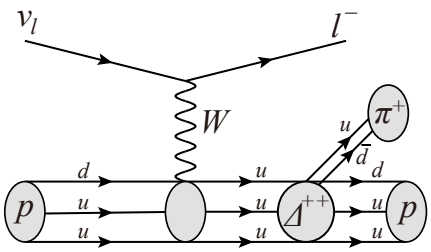

FIGURE 1.5: Tree-level Feynman diagram for a CC1π^+ interaction

$$F_A^{RES}(Q^2) = \frac{c_5^A(Q^2)}{\left(1 + \frac{Q^2}{(M_A^{RES})^2}\right)^2} \tag{1.21}$$

Non-Resonant and Coherent Pion Production

SPP can also happen without nucleon excitations to resonant states. These can happen through the isospin $I_{1/2}$ and $I_{3/2}$ channels. Most of the modern-day neutrino interaction generators only model the former as the contribution from the latter is found to be small from bubble chamber data [37, 38]. If the fraction of neutrino energy transferred to the nucleus is small, another SPP can occur, called the coherent pion production. In this interaction, the neutrino scatters on a nucleus as a whole, producing a pion but leaving the nucleus in the same state, as shown in Fig. 1.6.

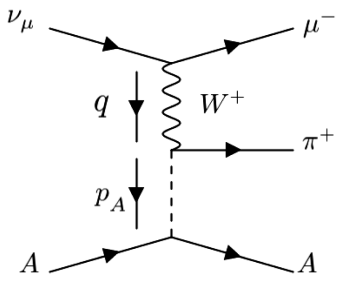

FIGURE 1.6: Feynman diagram for coherent pion production for a ν_μ [39]

As the thesis will focus mainly on the charged pion production, all the SPP interactions will hereafter be referred to as $CC1\pi^+$.

While neutrino energy from an SPP process can be reconstructed using both the outgoing lepton momentum and the pion momentum, the inadequacy of pion kinematics modelling and that of the pion's interactions inside the nucleus before leaving it, forces us to resort to an approximate estimation of neutrino energy by assuming the outgoing nucleon system as the Δ resonance. This reduces the SPP to a two-body process, and the neutrino energy can be reconstructed as:

$$E_\nu^{rec,CC1\pi} = \frac{2m_p E_\ell + m_\Delta^2 - m_p^2 - m_\ell^2}{2(m_p - E_\ell + p_\ell \cos\theta_\ell)} \,. \tag{1.22}$$

Eqn. 1.22 corresponds to Eqn. 1.18 with the only difference of proton mass being replaced by Δ resonance mass and $E_b \to 0$. The efficiency of this approximation will be portrayed in Chapter 3.

1.5.3 2p2h

Due to the presence of correlations between two nucleons in the nuclei, a neutrino interaction can result in the ejection of two nucleons instead of one. This interaction is called the two-particles-two-holes (2p2h) interaction and is depicted in Fig. 1.7. 2p2h can arise due to the meson exchange between two nucleons, most often the meson being a pion. The "correlated" nucleon can take part in the overall neutrino interaction via the meson propagator, and this process is called the meson exchange current (MEC) process.

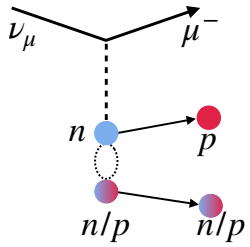

FIGURE 1.7: An illustration of ν_μ undergoing a 2p2h interaction with two possible nucleon-nucleon pairs.

As shown in the figure, the neutron can be correlated to either a proton (np) or with a neutron (nn), giving two possibilities in a 2p2h interaction. For the antineutrino case, this is replaced by the pp and pn pairs.

1.5.4 DIS and Multi-Pion Production

Neutrinos with energies of the order of a few GeVs can either produce multiple pions (so-called multi-π) or, if energetic enough, disintegrate a nucleon producing multiple hadrons (referred to as DIS, see Fig. 1.8). The line that separates these two processes is thin, and different generators implement the transitions between these two interactions differently. One of the ways to distinguish these processes in the generator is to categorise them based on the energy of the hadronic system W and use a different model to describe the two. In NEUT, this separation is made as:

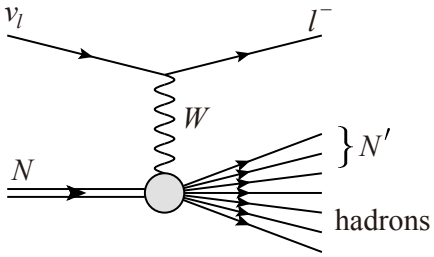

FIGURE 1.8: Feynman diagram for a CC DIS interaction.

- Multi-π for $W < 2$ GeV/c^2, and
- DIS (PYTHIA) for $W > 2$ GeV/c^2 [40].

This hard cut is necessary to avoid any double count of the same interactions if in case the DIS produces the same amount of pions. For the low W region, the Andreopoulos-Gallagher-Kehayias-Yang (AGKY) model [41] gives a description of the kinematics and multiplicities of the outgoing hadrons. Bodek and Yang (BY) [42] added a correction to the inclusive DIS cross-sections to better fit the data.

These two interactions form an important background in the CC $1\pi^+$ sample, as will be seen in Chapter 3.

1.6 Final State Interactions

All the interactions described so far follow the same trend, where a neutrino interacts with a nucleus, producing outgoing leptons and hadrons. Outgoing particles here refer to those produced at the interaction vertex and is all happening inside the nucleus. For these leptons and hadrons to be detected, they need to travel through the dense nuclear medium before exiting the nucleus. While doing so, these outgoing particles undergo various processes, collectively called final state interactions (FSI) and the particles that eventually escape the nucleus are termed the final state (FS) particles. Although all particles can undergo FSI, the effect is most prominent in hadrons, with pions being T2K's main concern. Pion FSI is very important to be understood in the context of this thesis, as the fate of the pion can very much alter the inference of the true neutrino interaction as can be seen from Fig. 1.9.

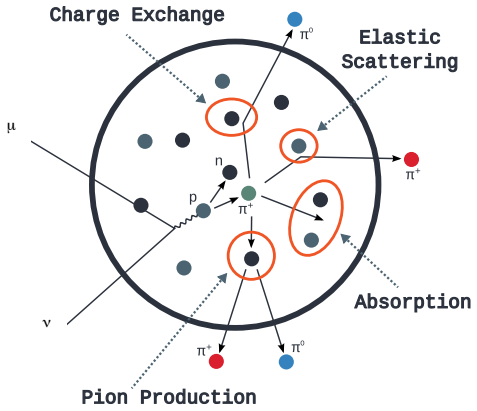

FIGURE 1.9: Possible FSI modes of a charged pion inside the nucleus [29].

The outgoing pion can undergo elastic scattering, pion absorption, charge exchange, and pion pair production, all of which lead to a very different set of FS particles (also called FS topology of a neutrino interaction event). If a π^+ from a CC $1\pi^+$ interaction gets absorbed by the nucleus, the resulting FS topology would just be an outgoing charged lepton, which mimics the CCQE interaction. Hence, a neutrino interaction which was truly a CC $1\pi^+$ gets identified as a CCQE interaction. Similarly, charge exchange in NC$1\pi^+$ events can convert them to NC$1\pi^0$ events, which can potentially become a background in $\nu_e/\overline{\nu_e}$ appearance analysis.

In NEUT, FSI is simulated through a cascade model. The pion FSI cascade simulation is as follows: the pion's initial kinematics are extracted from the pion production model and its position is modelled by a Woods-Saxon distribution tuned to electron scattering data [43]. Following this, the pion is propagated through steps of distance $R_N/100$ where R_N is 2.5 times the nuclear radius. For each of these steps, the probability that the pion undergoes a particular FSI mode is calculated based on its momentum:

- Oset et al. model [44] for $p_\pi < 400$ MeV/c,
- $\pi^\pm$-proton/deuteron scattering data [45] for $p_\pi > 500$ MeV/c,
- A mixture of the two models for the intermediate momentum.

The cascade is stopped when the pion either gets absorbed by the nucleus or when the propagation length is more than the nuclear radius (pion exits the nucleus).

Systematic uncertainties related to neutrino interactions and FSI and their treatment in this analysis will be discussed in detail in Chapter 5.

2

The Tokai-to-Kamioka Experiment

> We are very, very small, but we are profoundly capable of very, very big things.
>
> *Stephen Hawking*

The Tokai-to-Kamioka (T2K) experiment [2], located in Japan, is a long-baseline neutrino oscillation experiment designed to study the mixing and interactions of both neutrinos and antineutrinos. It utilizes an accelerator-produced beam of almost-pure $\nu_\mu(\overline{\nu}_\mu)$ generated at Japan Proton Accelerator Research Complex (J-PARC) at Tokai, on the eastern coast of Japan. This beam travels 280 meters to the near detector complex, which houses various subdetectors that precisely measure the neutrino beam properties. The neutrino beam then embarks on a 295-kilometer journey westward through the Earth to the Super-Kamiokande (SK) detector [46], the experiment's far detector (FD) and the final component. By the time the beam reaches SK, the neutrinos have travelled a sufficient distance to oscillate, making it possible to observe the $\nu_\mu(\overline{\nu}_\mu)$ disappearance and $\nu_\mu(\overline{\nu}_\mu) \rightarrow \nu_e(\overline{\nu}_e)$ appearance. This chapter delves deeper into each of these individual components, explaining their functionalities, and concludes with a concise overview of the employed analysis strategy.

Fig. 2.1 shows the cross-sectional view of the T2K experiment with its three main components.

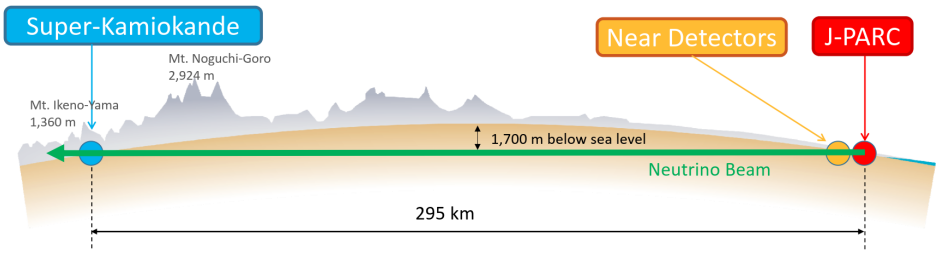

FIGURE 2.1: Cross-sectional view of the T2K experiment.

2.1 Beamline

J-PARC's ensemble of accelerators can accelerate the proton beam up to 30 GeV, which is then used to produce T2K's neutrino beam. The 30 GeV proton beam at J-PARC starts its voyage

as H^- ions which are accelerated to 400 MeV with a linear accelerator (LINAC). These H^- ions are then converted to protons using charge-stripping foils at the injection point into a Rapid Cycling synchrotron (RCS) which accelerates the protons to 3 GeV. Most of this beam is utilised by the Material and Life Science Experimental Facility (MLF) and the remaining fraction is then transferred to the main ring synchrotron (MR) where the 3 GeV protons are further stepped up to 30 GeV. While the hadron beamline facility extracts these protons using slow extraction mode, the neutrino beamline uses the fast extraction mode, where 8 bunches of the beam are extracted in a single turn and transferred to the neutrino facility. Each turn, or spill is $\sim 50\mu$s long, and the 8 bunches are 58 ns wide and equidistant. The knowledge of this timing is crucial to distinguish beam neutrinos from cosmic ray and atmospheric neutrino backgrounds at both the near and far detectors.

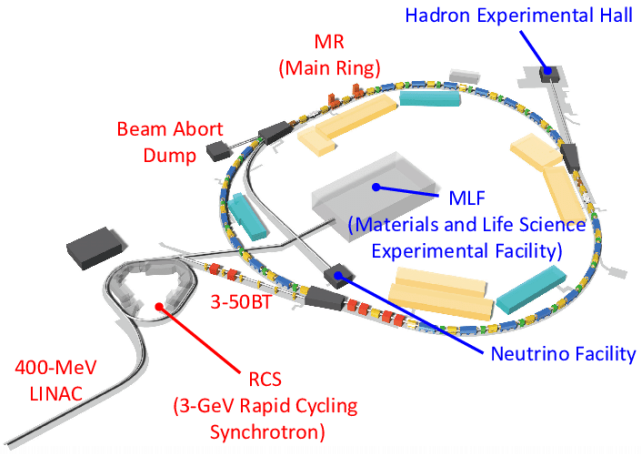

FIGURE 2.2: Illustration of J-PARC's accelerator facilities and related laboratories. Image from [47].

The extracted protons are then impinged on a graphite target that is 91.4 cm long and 2.6 cm wide, producing a bunch of secondary particles, mostly pions and kaons. These secondary particles pass through a system of three magnetic horns, whose polarity helps decide whether the beam will be predominantly ν_μ or $\overline{\nu}_\mu$. The case where positively charged secondaries are focused, leading to a ν_μ beam is called the forward horn current (FHC) mode, and the vice versa is referred to as the reverse horn current (RHC) mode. The graphite target is located inside the first magnetic horn, as shown in the Fig. 2.3.

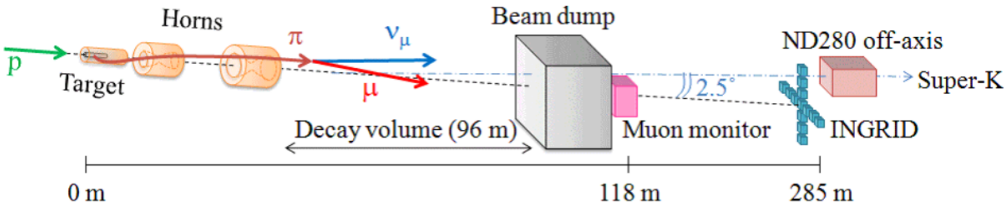

FIGURE 2.3: Illustration of the neutrino beamline, starting from its advent after the proton beam impinging on the graphite target.

Once the secondaries are focused according to the desired horn current, they travel through a 96 m-long decay volume. There, they decay into muons and muon neutrinos as shown in Eqns. 2.1 and 2.2:

$$\pi^{\pm} \rightarrow \mu^{\pm} + \overset{(-)}{\nu}_{\mu} \tag{2.1}$$

$$K^{\pm} \rightarrow \mu^{\pm} + \overset{(-)}{\nu}_{\mu} \tag{2.2}$$

It is necessary to dive a bit more into the secondary particles exiting the target. Pions decay almost entirely in a two-body process to produce $\mu^{\pm} + \overset{(-)}{\nu}_{\mu}$ (branching fraction of 99.9877% [48]). On the other hand, the two-body leptonic decay of kaons that is shown in Eqn. 2.2 only constitutes 63.55% of its branching fraction, with the remaining being distributed between $K^+ \rightarrow \pi^0 + \mu^+ + \nu_\mu$ (3.353%) and $K^+ \rightarrow \pi^0 + e^+ + \nu_e$ (5.07%). Table 2.1 shows the branching fractions of possible processes that contribute to the neutrino beam. The small fraction of $\overset{(-)}{\nu}_{e}$ produced by $K^{\pm}$ decay constitute the intrinsic ν_es, which are background to the $\overset{(-)}{\nu}_{\mu} \rightarrow \overset{(-)}{\nu}_{e}$ appearance studies.

Decay modes	Branching fraction [%]
$\pi^+ \rightarrow \mu^+\nu_\mu$	99.9877
$\pi^+ \rightarrow e^+\nu_e$	1.23×10^{-4}
$K^+ \rightarrow \mu^+\nu_\mu$	63.55
$K^+ \rightarrow \pi^0\mu^+\nu_\mu$	3.353
$K^+ \rightarrow \pi^0 e^+\nu_e$	5.07
$K^0_L \rightarrow \pi^-\mu^+\nu_\mu$	27.04
$K^0_L \rightarrow \pi^- e^+\nu_e$	40.55
$\mu^+ \rightarrow e^+\overline{\nu}_\mu\nu_e$	100

TABLE 2.1: Branching fraction of various processes that produce neutrinos in the FHC mode.

Additionally, it is important to say that the amount of positively charged secondary particles is higher than the negatively charged ones since both the carbon nuclei and the proton bear positive charges. Furthermore, some higher-energy secondary particles can pass through the magnetic horns without being deflected. The decays of these secondary particles constitute the "wrong-sign" component in the beam. For the FHC beam mode, they are the $\overline{\nu}_\mu$ and vice-versa for the RHC mode. The wrong-sign component is especially larger for the RHC beam mode due to the existence of more positively charged secondaries.

The beam dump at the end of the decay volume stops all the particles apart from neutrinos and high-energy muons. These high-energy muons are monitored with a muon monitor located right behind the beam dump to determine the stability and direction of the (anti)neutrino beam.

Finally, the accumulated amount of data is expressed as Protons on Target (POT) which indicates how many neutrino interactions can be expected at the detectors.

2.2 Off-Axis Technique

T2K is the first long-baseline neutrino experiment to introduce the "off-axis" technique. In this technique, the detectors are oriented a few degrees off-centre with respect to the direction of

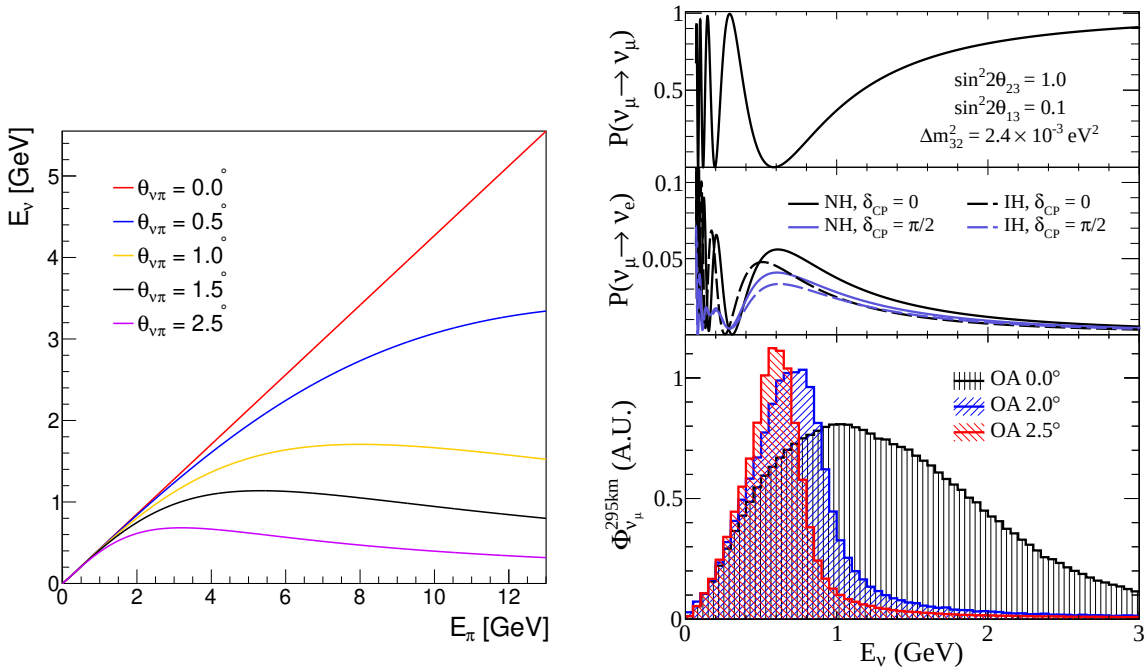

(A) (B)

FIGURE 2.4: (A) Relation between E_ν and E_π for different off-axis angles $\theta_{\nu\pi}$; Image from [49]. (B) neutrino oscillation probabilities as a function of E_ν for the baseline of 295 km, along with the flux of neutrinos incident at SK for different off-axis angles (without oscillations).

the beam. In T2K, one of its near detectors, the ND280, and the FD, SK are oriented 2.5° off-axis with respect to the beam centre, as depicted in Fig. 2.3.

The off-axis technique's importance can be demonstrated by looking into the two-body decay of charged pions. The energy of ν_μ from the π^+ decay in the laboratory frame is

$$E_\nu = \frac{m_\pi^2 - m_\mu^2}{2(E_\pi - p_\pi \cos\theta_{\nu\pi})} \tag{2.3}$$

where $m_{\pi,\mu}$ are pion and muon masses respectively, E_π and p_π are pion energy and momentum, and $\theta_{\nu\pi}$ is the angle between the π^+ and the outgoing ν_μ. As the angle $\theta_{\nu\pi}$ increases, the E_ν becomes almost independent of E_π as shown in Fig. 2.4a, making the E_ν spectra narrower as shown in the bottom plot of Fig. 2.4b.

With an off-axis angle of 2.5°, the flux at these detectors is strongly peaked at 0.6 GeV. For the distance of 295 km, at which SK is located, this energy corresponds to the maximum probability of oscillations for ν_μ (see Fig. 2.4b). Furthermore, at this energy range neutrinos interact most dominantly via CCQE followed by SPP interactions, whose energies can be reconstructed quite well as discussed in Chapter 1. Not only are the reconstruction of higher energy neutrino events hard, but they also produce NCπ^0 events which are a dominant background for ν_e appearance studies.

2.3 Near Detectors

The near detector complex is located 280 m downstream of the neutrino beam production target and is an underground pit that hosts most importantly the INGRID and ND280 detectors. These detectors are used in T2K's oscillation analysis and will be discussed in this section.

2.3.1 INGRID

Interactive Neutrino GRID (INGRID) is a detector system consisting of 14 identical scintillation modules, which are arranged in the shape of a cross, as shown in Fig. 2.5. INGRID is an on-axis detector with its centre aligned directly with that of the beam. In the past, two additional modules along with an upstream fully-scintillator plane-based proton module were used, mostly for cross-section studies, but they were decommissioned at the time of writing.

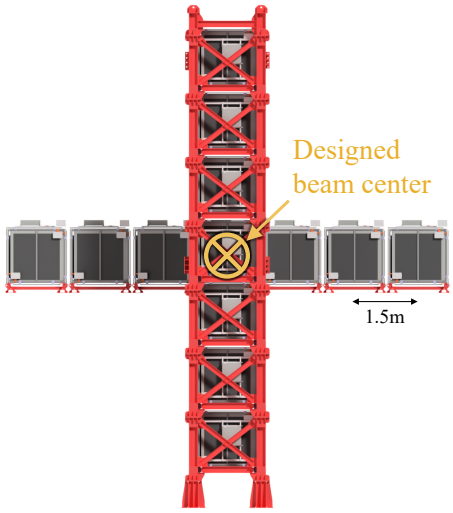

FIGURE 2.5: Front view of the INGRID detector.

Each INGRID module consists of 9 iron plates sandwiched between 11 tracking scintillator planes, which are shielded by veto scintillator planes that reject events outside the modules.

Since the neutrino energies depend strongly on the off-axis angle, it is important to measure the direction of the neutrino beam with high accuracy. The large flux of neutrinos incident on INGRID enables it to measure the beam direction (with a precision of 0.25 mrad [48]), profile and intensity on a day-to-day basis. INGRID's measurements are also used to tune the flux predictions at both the ND280 and the FD for each data taking period.

2.3.2 ND280

The ND280 detector, shown in Fig. 2.6 is a system of multiple different sub-detectors, and forms the most important element of the near detector complex. Housed inside the refurbished UA1 magnet that produces 0.2T dipole magnetic field, ND280 is stacked with an upstream π^0 detector (P0D), followed by two Fine-Grained detectors (FGDs) sandwiched between three time projection chambers (TPCs), and a downstream electromagnetic calorimeter (ds-ECal). The FGDs and TPCs are in combination called the tracker. Both the tracker and P0D are surrounded by the barrel ECals.

The first FGD, FGD1 consists of scintillator bars which are mainly ^{12}C targets. FGD2, in addition to the scintillator bars also houses water as a target. The FGDs are the main targets for neutrino interactions, and the presence of water (and hence ^{16}O nuclei) in FGD2 enables us to have a better understanding of neutrino interactions happening at the FD.

Neutrino events with interactions in the tracker detector are used in T2K's oscillation analysis. P0D was used to study neutral current neutrino interactions with water that produce π^0s, which are a major background in T2K's far detector. At the time of writing, the P0D

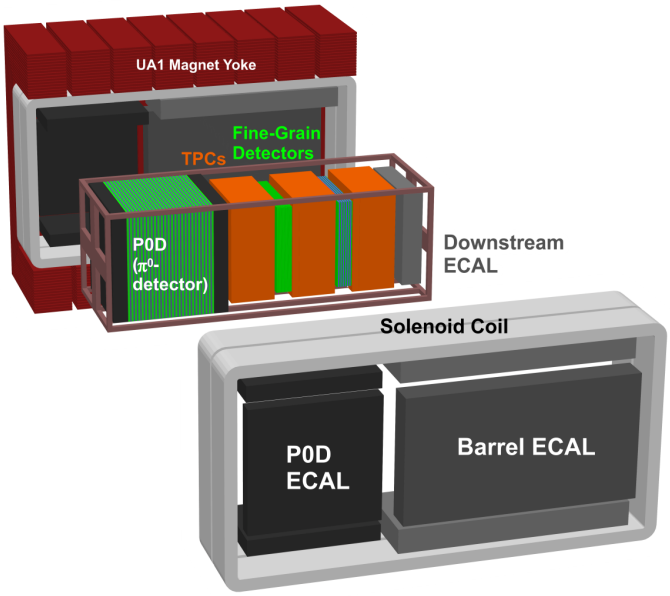

FIGURE 2.6: Exploded view of the ND280 detector.

detector was removed from the ND280 system and replaced with the new tracker detectors, namely Super FGDs and High-angle (HA) TPCs, both of which are irrelevant to this thesis.

2.4 ND280 Samples

ND280 samples are constructed in such a way they can represent the signal events observed at the FD, and also the most dominant backgrounds to these signal events. That the ND280 is magnetized means positively and negatively charged particles, and hence interactions of ν and $\overline{\nu}$ can be distinguished. This also enables ND280 to constrain the so-called wrong sign component (ν_μ) in the $\overline{\nu}$ beam mode. The samples are further split by tagging the outgoing proton and photon tracks. For instance, the CC0π-0p-0γ sample identifies events without any pions, protons or photons, directly representing the CCQE-like single-ring samples at the FD. The CC1$\pi^\pm$ samples are enriched in RES, while the CC-Other and CC-Photon samples mainly target DIS processes.

As mentioned before, T2K's neutrino beam also contains wrong-sign components, most dominantly in the RHC mode. Since SK is not a magnetized detector, it cannot differentiate between ν and $\overline{\nu}$ events, and hence cannot distinguish events from the wrong-sign neutrinos. To overcome this, samples that target the wrong-sign component in RHC mode are introduced in the ND280, which will help constrain the wrong-sign component at the FD.

FHC ν_μ CC-inclusive (FGD1 and FGD2)	RHC $\overline{\nu}_\mu$ CC-inclusive (FGD1 and FGD2)	RHC ν_μ CC-inclusive (FGD1 and FGD2)
CC0π-0p-0γ	CC0π	CC0π
CC0π-Np-0γ	CC1π^-	CC1π^-
CC1π^+-0γ	CC-Other	CC-Other
CC-Other-0γ		
CC-Photon		

TABLE 2.2: ND280 Samples used in T2K's oscillation analysis.

Each of the topologies shown in Table 2.2 is also distinguished based on which FDG the interaction takes place at. Therefore, there are 22 ND280 samples that are used in the analysis.

2.5 Far Detector

Super-Kamiokande (SK) is a 50-kiloton water Cherenkov detector located directly underneath the peak of Mt. Ikenoyama in the Mozumi mine in Gifu prefecture, Japan. The detector is shielded very well from cosmic ray muons below energies of 1.3 TeV by a 1000 m rock overburden.

The detector is enclosed in a stainless steel cylindrical tank. Within the tank, a cylindrical stainless steel support structure holds optically separated inner and outer detectors (ID and OD, see Fig. 2.7). The ID is instrumented with ∼11,000 ∼20-inch photo-multiplier tubes (PMTs) and the OD consists of ∼1900 ∼8-inch PMTs. The fiducial mass within the ID is 32 kton of water. While the ID is used to identify neutrino interactions happening inside SK's fiducial volume, the OD acts as a veto for tagging particles that exit the ID and also helps identify entering cosmic ray muons and products of radioactive decay within the rocks surrounding the detector.

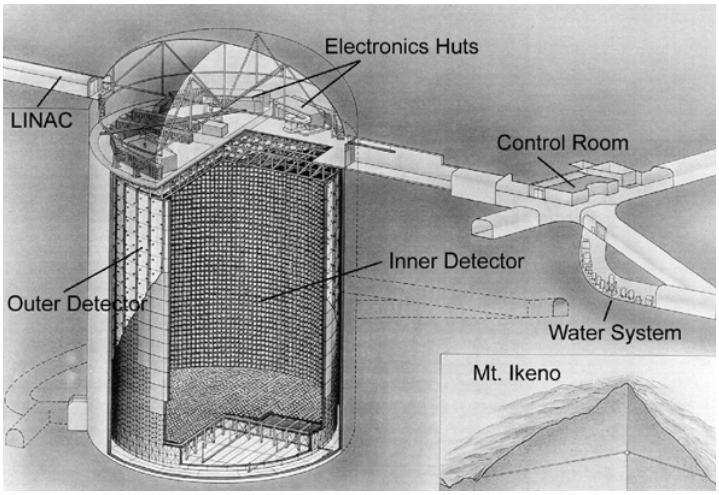

FIGURE 2.7: A schematic diagram of the SK detector site. The ID and OD are marked clearly. Image from [46].

SK's detector material was ultra-pure water until August 17, 2020, marked as the SK I-V period. Since then, at the time of writing, SK's otherwise pure water was doped first with a concentrated solution of $Gd_2(SO_4)_3 \cdot 8H_2O$ [50] to make the detector material 0.01% Gd by volume (referred to as SK-VI period) followed by a second stage addition of $Gd_2(SO_4)_3 \cdot 8H_2O$ [51] to increment the total Gd concentration to 0.03 % (SK-VII). This thesis makes use of SK data that corresponds to SK-IV, SK-V pure water phase and SK-VI period with 0.01% Gd salt doping.

2.5.1 Cherenkov Radiation

SK is one of the world's largest water Cherenkov detectors. The PMTs in SK observe the Cherenkov photons that are produced when charged particles move with a speed faster than the speed of light in water. In general, Cherenkov photons are emitted when charged particles move through any form of matter with a speed greater than c/n, where c is the speed of light, and n is the refractive index of that matter. The emission takes the shape of a cone, as shown in Fig. 2.8, where the opening angle θ of the cone is related to the speed of the charged particle β as

$$\cos\theta = \frac{ct/n}{\beta ct} = \frac{1}{n\beta}\,. \tag{2.4}$$

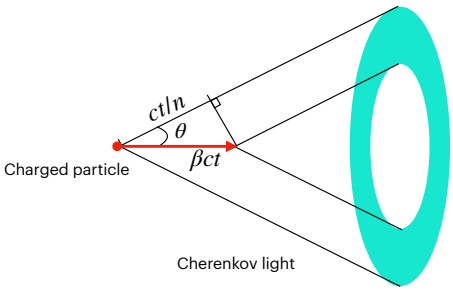

FIGURE 2.8: Schematic diagram of Cherenkov radiation, along with its projection in the form of a ring on a surface.

For pure water, particles with speeds $\beta \sim 1$ produce a characteristic Cherenkov cone with opening angle $\theta = 42^\circ$, since the refractive index of water is 1.33. The number of Cherenkov photons produced, N can be obtained from

$$\frac{d^2N}{dxd\lambda} = \frac{2\pi\alpha z^2}{\lambda^2}\left(1 - \frac{1}{(n\beta)^2}\right) \tag{2.5}$$

where x is the distance travelled by the charged particle, λ is the wavelength of the optical photon produced, α is the fine structure constant, and z is the particle's electric charge. The energy of a particle with small β can be calculated from the opening angle θ, while for high β particles, the number of detected photons provides the estimate of energy.

The projection of the Cherenkov radiation on a surface takes the shape of a ring for stopping particles and is used as the main source of particle identification (PID) method in Cherenkov detectors like SK. For example, electrons and muons can be distinguished by the fuzziness of their respective Cherenkov rings: due to electromagnetic showers, an electron produces a fuzzy ring, while a muon produces a rather sharp ring profile owing to its minimum ionizing characteristics. This simple, but extremely useful difference helps SK differentiate electrons and muons with less than 1% mis-PID at 1 GeV (see Fig. 2.9). As this thesis will be dealing with the multi-ring ν_e CC1π^+ events, it is also important to point out that charged pions also have sharp-edged rings like the muons.

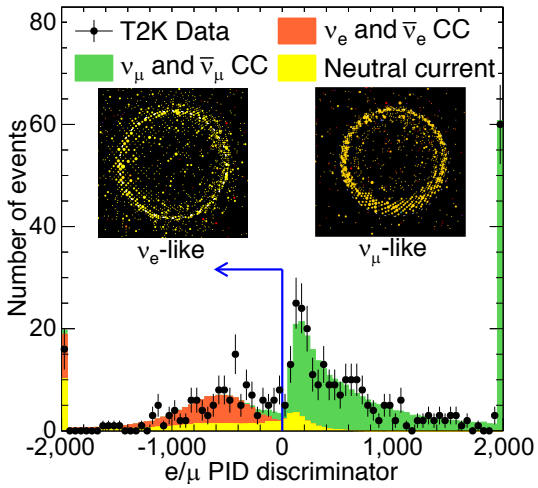

FIGURE 2.9: PID discrimination between e-like and μ-like rings at SK. The fuzziness(sharpness) of e (μ)-like ring can be very well noticed. Source: [52].

2.5.2 ID and OD

The cylindrical stainless steel scaffolding separates SK's detector volume into two concentric detector volumes, ID and OD as displayed in Fig 2.7. The areas of ID scaffolding between the inner PMTs are lined with black plastic sheets to minimize photons reflecting within the ID. The 11,146 ID PMT configuration provides a 40% photo-coverage. A schematic diagram marking the ID PMT's inner components is shown in Fig. 2.10. Incidentally, the OD is lined with a highly reflective Tyvek® sheet and the 1,885 OD PMTs are embedded to 50×50 cm^2 acrylic wavelength shifting plates to maximise light collection efficiency in a rather sparsely arranged OD PMT configuration.

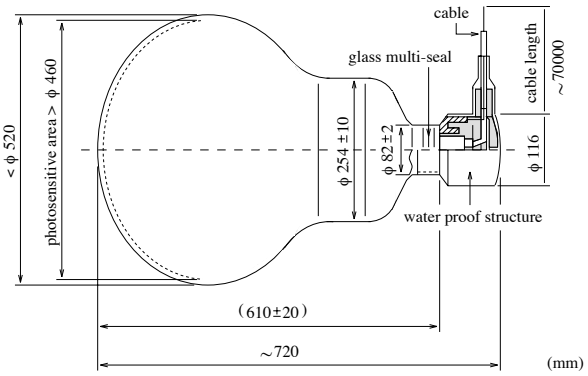

FIGURE 2.10: Schematic diagram of SK's ID PMT. Image from [46].

The ID is 33.8 m wide and 36.2 m tall. The OD is 2 m thick radially and at the top and bottom. The stainless steel scaffolding is roughly 50 cm thick and constitutes the "dead space" region.

The PMTs in the ID are used to detect the Cherenkov radiation produced by the charged particles travelling through water, and the information from them is used to reconstruct the event. The OD on the other hand are only used as a veto to reject cosmic ray muons and events that have significant activities happening outside of the ID. PMT hits from the OD are not used in PID or event reconstructions.

2.5.3 Event Reconstruction

At SK, an event is defined as a series of PMT hits clustered in time and satisfying one of the trigger requirements. Each event holds information about the charge and time information of PMT hits within a ~ 10 μs timing window around the trigger time. A maximum likelihood-based reconstruction framework is then used to reconstruct the event. This is done through four stages:

- **Vertex pre-fit**: At this step, the reconstruction algorithm estimates an approximate neutrino interaction vertex $\mathbf{x}$ and timing t using only the hit timing information from the event. This step is important for constructing subevents from the main event.
- **Subevent construction**: Very often, an event can have multiple PMT clustering separated in time. For example, the Cherenkov radiation from a muon can first register some hits, and after a delay, the decay electron from the muon also produces some PMT hits. Tagging these decay electrons is crucial in determining the FD samples. Therefore, the algorithm divides the event into multiple subevents separated in time using a peak-finding algorithm.

- **Single-Ring fit**: For each of these subevents, a set of parameters **f** are varied until they maximise the likelihood function for an electron, muon and charged pion-like ring. Although the final state topology of an event is taken from the first subevent, the single-ring fits are also applied to all the other subevents.

- **Multi-Ring fit**: The multi-ring fit is a direct extension of the single-ring fit, and is only performed for the first subevent. The fit starts with single-ring electron and pion fit results, and sequentially adds an electron/pion ring to the reconstruction hypothesis up to 6 rings. Each hypothesis is tested and the parameters for each ring that maximise the likelihood are determined.

An important feature of the multi-ring fit is that in the multi-ring fits, both the muon and pion hypotheses are tested using the pion hypothesis since the muon and pion rings look very similar, thereby saving the time required to perform the fits. In addition, a dedicated π^0 fit is also done by tagging the decay photons and reconstructing the parent π^0 kinematics. The reconstruction framework is quite complicated and beyond the scope of this thesis. A detailed description of it can be found in [53, 54].

Of the parameters **f** mentioned above, the most important ones in event selection include the various particle ($e, \mu, \pi^{\pm}, \pi^0$) hypothesis likelihoods, their kinematics, vertex and timing parameters and total number of rings and decay electrons. These variables will be discussed in Chapter 3.

2.5.4 SK-Gadolinium

SK, being not only a detector for neutrino oscillation-related studies but also astroparticle physics, had functioned as a pure water detector for over 25 years until it was doped with the Gd salt starting from SK-VI period. The primary purpose of adding Gd was for the relic neutrino searches. However, this can also benefit T2K's beam samples by selecting RHC events with more purity. Gd possesses a large neutron capture cross-section and a characteristic 8 MeV γ decay cascade. This feature allows the tagging of neutrons which are most likely produced in antineutrino interactions more efficiently [55].

Before the addition of Gd, the number of decay electrons was calculated as one less than the number of subevents in an event. However, the delayed de-excitation of the Gd nucleus that produces the γ cascade can also be confused with the delayed signal of a decay electron by the reconstruction framework. Hence, an improved decay electron reconstruction which efficiently distinguishes the true decay-electrons from the mid-ID neutron captures was applied to both the FD data and simulation used in this analysis.

2.6 FD Samples

CCQE is the golden interaction channel of T2K, followed by a sub-dominant contribution from the SPP channel. Neutrino energies can be estimated from both these processes solely as a function of the outgoing lepton's kinematics.

Neutrinos that undergo CCQE interactions produce a charged lepton in the final state, which is visible as a single lepton-like ring at SK. Therefore, there are single-ring e-like and μ-like samples at SK that target ν_e and ν_μ CCQE interactions respectively in both the FHC and RHC mode.

On the other hand, the SPP process can produce two different topologies. If the outgoing charged pion's momentum is below its Cherenkov threshold, SK will only identify the lepton-like ring and the delayed decay electron signal from the π-decay. If the pion momentum is well above its Cherenkov threshold, its ring can also be identified. SK has had a single-ring

FHC ν_e CC1π^+ sample since 2017, that represents the first type of SPP topology. Since its 2021 oscillation analysis, T2K introduced the FHC ν_μ CC1π^+ sample. Not only does this sample contain a single μ-like ring with tagged decay electrons from both the μ and π, but it also contains events that tagged both the μ- and π-like rings, making this sample T2K's first multi-ring sample at SK.

These samples are summarised in Table 2.3 and were used in T2K's 2023 oscillation analysis whose results will be discussed shortly after.

Sample	Target ν interaction
FHC 1Rμ	ν_μ CCQE
RHC 1Rμ	$\overline{\nu}_\mu$ CCQE
FHC ν_μ CC1π^+	ν_μ CC1π
FHC 1Re	ν_e CCQE
RHC 1Re	$\overline{\nu}_e$ CCQE
FHC single-ring ν_e CC1π^+	ν_e CC1π

TABLE 2.3: FD samples used in the oscillation analysis along with the neutrino interaction modes that they mostly constitute.

2.7 T2K Oscillation Analysis Results from 2023

T2K performs a three-flavour neutrino oscillation analysis using the ND280 samples described in section 2.4 and the FD samples from 2.6. Two data analysis strategies are used in T2K, both based on two different statistical approaches. The first strategy uses a Frequentist approach through a gradient descent algorithm with MINUIT [56], where a standalone ND fit is first performed that constrains the flux and cross-section parameters using the BANFF fitter [57]. These constraints are propagated as a covariance matrix to the FD-only fit that estimates the oscillation parameters and produces their best-fit values. This is done using the P-Theta fitter [58].

The second strategy incorporates a Markov Chain Monte Carlo (MCMC)-based framework named MaCh3 [59]. In this case, a simultaneous fit of ND and FD data is performed that constrains both the systematic parameters and estimates the oscillation parameters. MCMC is inherently Bayesian, and the results of this analysis are obtained as posterior probability distributions of all the parameters that go into the fit. MaCh3 is also capable of performing ND-only and FD-only fits, and the results of MaCh3 ND fit and BANFF ND fit are always cross-checked for compatibilities before performing the FD fits.

Both these analysis strategies aim to maximise a likelihood function (equivalently minimize the negative log-likelihood function) where the likelihood function is representative of T2K's ND and FD data and the simulation which is a function of oscillation parameters and all the model parameters, such as the flux and cross-section parameters, and the detector systematic parameters of ND and FD.

A detailed review of the frequentist oscillation analysis using P-Theta can be found in [58]. The oscillation analysis performed in this thesis uses the Bayesian MCMC approach and hence the MaCh3 fitter. A detailed description of the MCMC and the oscillation analysis itself will be provided in Chapter 4, followed by the results of the fits in Chapter 6 using the MaCh3 fitter.

T2K's latest oscillation analysis [60–63] was performed with 1.153×10^{21} FHC POT and 0.834×10^{21} RHC POT for ND280, 2.1428×10^{21} FHC POT and 1.6345×10^{21} RHC POT for the FD. Compared to the previous analysis, this analysis introduced the SK-VI period T2K data at FD, which corresponds to a 9% increase in FHC statistics. An updated treatment to the decay-electron variable was also implemented to account for the Gd-loaded phase of SK.

This was essential to avoid the reconstruction software wrongly identifying a delayed de-excitation Gd-nucleus signal after a neutron capture as a delayed decay-electron signature. In addition, the SK detector matrix was also updated to include correlations between single-ring and multi-ring samples that resulted in an overall reduction of errors as compared to the matrix used for T2K's previous oscillation analysis [64].

In addition, although T2K is sensitive to $\sin^2\theta_{13}$, it is far less than that of reactor neutrino experiments. Therefore, a Gaussian prior based on reactor neutrino result is applied as a prior constraint on $\sin^2\theta_{13}$. All the results shown in this thesis will quote oscillation parameter results with the constraints on $\sin^2\theta_{13}$ from the reactor experiments applied, unless stated otherwise.

The results of neutrino oscillation parameter measurement are usually represented as two-dimensional contours of $\sin^2\theta_{23}$–Δm^2_{32} (so-called disappearance parameters) and $\sin^2\theta_{13}$–δ_{CP} (appearance parameters) as shown in Fig. 2.11 and 2.12 respectively. The one-dimensional posterior distribution of δ_{CP} is shown in Fig. 2.13.

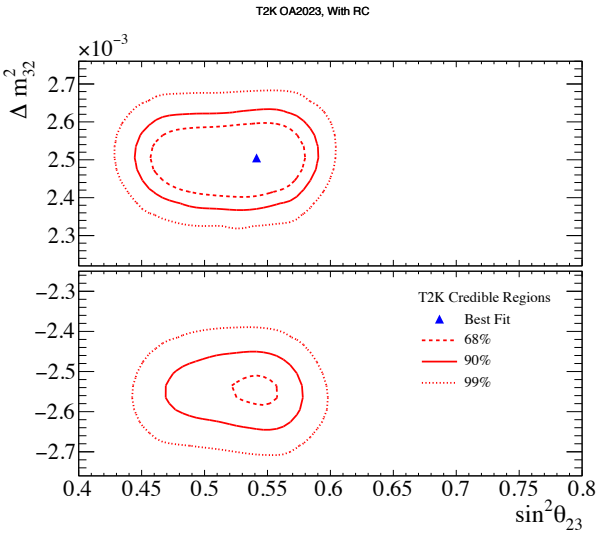

FIGURE 2.11: Two-dimensional disappearance contours showing MaCh3's results, marginalized over both neutrino mass hierarchies. $\sin^2\theta_{13}$ reactor constraint is applied.

These results show that T2K excludes CP conserving values of $\delta_{CP} = 0, \pm\pi$ at 90% credible interval. The fits also show a mild preference for the upper octant of θ_{23} and normal mass hierarchy.

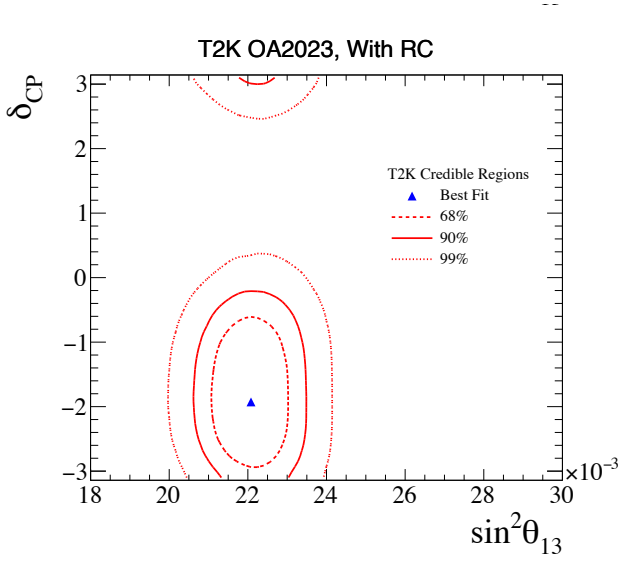

FIGURE 2.12: Two-dimensional appearance contours showing MaCh3's results, marginalized over both neutrino mass hierarchies. $\sin^2\theta_{13}$ reactor constraint is applied.

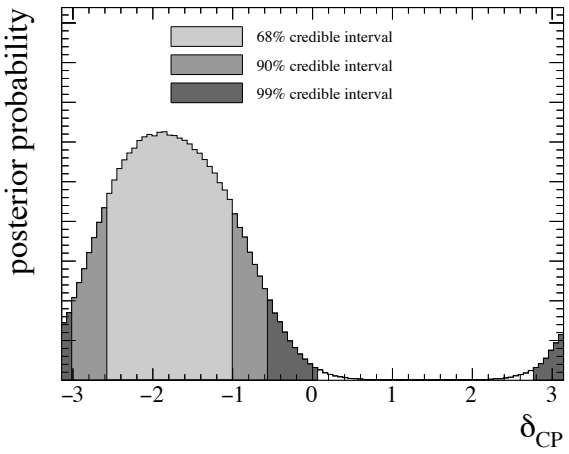

FIGURE 2.13: One-dimensional posterior probability distribution of δ_{CP}, marginalized over both neutrino mass hierarchies. $\sin^2\theta_{13}$ reactor constraint is applied.

3

Development of a Multi-Ring ν_e CC1π^+ Sample at SK

> Nothing in life is to be feared; it is only to be understood. Now is the time to understand more, so that we may fear less.
>
> Maria Skłodowska-Curie

Up until T2K's 2023 oscillation analysis that was described briefly in Section 2.7, six FD samples were used, that targeted both the most-dominant CCQE interactions and also the subdominant CC1π^+ interactions. As T2K enters a precision era, many efforts are underway to make the best used of data collected so far. With the introduction of the first multi-ring (FHC ν_μ CC1π^+) sample from T2K's 2021 analysis, it was decided that the single-ring FHC ν_e CC1π^+ sample should also be expanded to include its multi-ring counterpart. Being a ν_e appearance sample, it can possibly improve T2K's sensitivity to δ_{CP} .

The multi-ring ν_e CC1π^+ sample possesses the topology of 1e-like and 1π^+-like ring at SK, along with the delayed decay electron signal from the decay of π^+ as shown in Fig. 3.1. It should also be emphasised that this sample, along with the single-ring ν_e CC1π^+ and multi-ring ν_μ CC1π^+ sample exist only for the FHC mode. This is because, if the interaction were to be CC1π^-, the π^- will almost surely get absorbed by the positively charged nucleus, changing the event topology entirely.

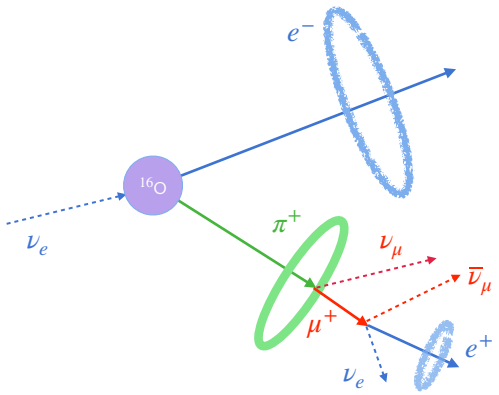

FIGURE 3.1: A schematic diagram of the multi-ring ν_e CC1π^+ sample with its topology of $1e + 1\pi^+$ Cherenkov rings and a decay electron marked.

The following sections will describe the development of selection cuts. The studies were performed entirely with T2K's FD Monte Carlo (MC) simulation that was scaled to represent T2K's collected data of 2.1428×10^{21} FHC POT and 1.6345×10^{21} RHC POT.

3.1 The Selection Cut Variables

All the FD samples undergo a data quality cut which requires the event to be within SK's fiducial volume (FV) and fully contained (FC) inside the ID, with little-to-no OD activity. These two conditions ensure that the entire event takes place well within a region where the event can be properly reconstructed and also rejects events that enter into the ID from an interaction happening outside.

Two variables are used to determine whether the event vertex lies within SK's FV. They are the *DWall* and *ToWall* variables defined as follows:

- *DWall*: The distance from the neutrino interaction vertex to the nearest ID wall.
- *ToWall*: The distance from the neutrino interaction vertex to the nearest ID wall measured along the direction of the outgoing particle(s).

These variables are picturized in Fig. 3.2. If an event contains multiple outgoing particles, the *ToWall* can be calculated for each of them.

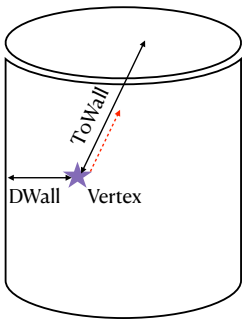

FIGURE 3.2: A schematic diagram showing the *DWall* and *ToWall* FV variables. The violet marking is the neutrino interaction vertex, while the red dashed arrow shows the direction of the outgoing charged particle for which the *ToWall* is calculated.

Another parameter on which the selection cut is applied is the visible energy of the event. Visible energy is defined differently for various particles. For electrons, this is taken as the reconstructed momentum, while for muons it is the energy above its Cherenkov threshold. For charged pions and protons, the visible energy is defined as the energy loss before any hard interaction occurs. If an event is multi-ring, visible energies of each particle type are summed together. Therefore, in the multi-ring ν_e CC1π^+ sample, visible energy is the sum of the e^--like ring's reconstructed momentum and the π^+-like ring's energy loss. Events with low visible energy are rejected since they are highly contaminated with the neutral current (NC) background.

Visible energy cut, together with the FC and FV conditions form what is called the FCFV cut.

The next set of reconstruction variables helps select events that most likely have the topology of multi-ring ν_e CC1π^+ sample, starting from the "N Rings" variable. From the various single- and multi-ring fits that SK's reconstruction algorithm performs, the best-fit number of

reconstructed rings (N Rings) is used to determine whether the event is single-ring or multi-ring. Additionally, to tag the delayed decay electron from the π^+ decay, the new version[1] of the decay electron tagging is used. The multi-ring ν_e CC1π^+ sample requires exactly two reconstructed Cherenkov rings and one decay electron.

The above requirement of Cherenkov rings and decay electrons also selects a big fraction of background events with similar topology but entirely different neutrino interactions. Events that can pass these selections are those with topologies of "$1\mu + 1\pi^+$" and "1μ + other", "$1\pi^0$" that produce two γ rings, multi-π and DIS background. To purify the multi-ring ν_e CC1π^+ sample from these backgrounds, two likelihood-ratio-based selection cuts were introduced. SK's reconstruction algorithm produces multiple single- and multi-ring event hypothesis likelihoods. Using them, likelihood ratios between two different hypotheses can be constructed. According to the Neyman-Pearson lemma [65], if there are two hypotheses H_0 and H_1, then a likelihood ratio test is the best way to compare the power of one hypothesis over the other.

Combinations of negative log-likelihood ratios (referred to as LLH hereafter) between the $1e + 1pi^+$ hypothesis and various background hypotheses were tested and it was found that the LLHs between "$1e + 1\pi^+$" and "$1\mu + 1\pi^+$" topologies and the two-dimensional space between the LLH between "$1e + 1\pi^+$" and "$1\pi^0$" topologies and the reconstructed π^0 mass provided the best signal-background separation powers. These cuts and their optimization will be described in the next sections.

Finally, being a ν_e appearance event, an upper cap of 1.25 GeV on the reconstructed neutrino energy E_{rec} is also applied. This cut is applied on all the e-like FD samples to reduce ν_e events coming from the intrinsic ν_e background which usually has higher neutrino energies.

3.2 Optimization Strategy

The two LLH-based selection cuts need to be optimized to maximise the background rejection and not lose signal events. Hereafter, these two cuts will be referred to as $e\pi/\pi\pi$ PID and $e\pi/\pi^0$ PID cuts. The goal of the optimization is to find a set of coefficients c_1, c_2 and c_3 such that

$$LLH(e\pi/\pi\pi) < c_1 \tag{3.1}$$

and

$$LLH(e\pi/\pi^0) < c_2 - c_3 \times m_{\pi^0} \tag{3.2}$$

give the best signal-background separation. The $e\pi/\pi\pi$ PID cut is one-dimensional, while the $e\pi/\pi^0$ PID cut is a two-dimensional line cut as can be seen from Eqns. 3.1 and 3.2. The metric that determines the background rejection capability of the cuts was chosen as the $S/\sqrt{S+B}$ metric. Here S denotes the number of signal events with true $1e + 1\pi^+$ topology, while B represents events with any other topology. c_1, c_2 and c_3 were varied simultaneously, and for each combination of those values, $S/\sqrt{S+B}$ was calculated.

This was essentially a three-dimensional grid search. The step sizes with which these coefficients varied were first set to be large to approach the best metric region fast. Subsequently, these step sizes were reduced so that a finer grid search was possible within that region. c_1 and c_2 step sizes were 10 units each while c_3 had a step size of 0.05 during the finer grid search. The values of these three coefficients that give the best performance were then found to be:

[1] Described in Chapter 2.

Cut Parameter	Optimal value
c_1	-300.0
c_2	170.0
c_3	0.75

TABLE 3.1: Cut parameter values obtained from $S/\sqrt{S+B}$ optimisation.

The $S/\sqrt{S+B}$ metric is a common metric used to perform signal-background separations, as it can very well pick up the optimal efficiency and purity for a given signal+background distribution. In general, the two entities behave destructively: if one chooses to maximise signal purity, it can lead to poor signal efficiency, and vice versa. Thus optimising the product of these two is more likely to find a middle ground such that the sample is sufficiently pure and has good efficiency. When performing the LLH cut optimization, the events had to pass the FCFV cut and had to possess two rings and one decay electron. The E_{rec} cut was not applied in this study. This was because the calculation of E_{rec} assumes the event to be most dominantly $1e1\pi^+$-like, and including that cut would introduce biases in the optimisation.

3.3 Flow of Cuts

This section will follow through the multi-ring ν_e CC1π^+ sample selection cuts that are applied to the T2K FD MC. The effect of oscillations is included in the plots, with assumed values of the parameters as given in Table 3.2.

Parameter	Value
$\sin^2\theta_{12}$	0.307
$\sin^2\theta_{13}$	0.0220
$\sin^2\theta_{23}$	0.561
Δm^2_{21}	7.53e-5
Δm^2_{32}	2.494e-3
δ_{CP}	-1.602
ρ_{earth}	2.6

TABLE 3.2: Values of the oscillation parameters and the constant matter density used to calculate the oscillation weights for each MC event. These parameter values are also used to generate the Asimov data set that will be discussed in the next chapters.

In the plots that will show the distributions of the selection cut variable, the MC events are broken down according to both the final state (FS) topologies extracted from the detector simulation and neutrino interaction modes as defined in NEUT. The breakdown of these is summarized in Table 3.3 and 3.4. In table 3.3, N_i tells the number of true outgoing particle of the type i tagged by the detector simulation. Furthermore, the $1e1\pi$ topology is split to $1e1\pi_{p>ChT}$ and $1e1\pi_{p<ChT}$ in the plots to differentiate between MC events with the π^+ momentum above(below) its Cherenkov thresholds.

FS event topology	Definition
$1e$	$N_{e^\pm} = 1, N_{\mu^\pm} = N_{\pi^0} = N_{\pi^\pm} = N_{\text{Oth. Had.}} = 0$
$1e1\pi$	$N_{e^\pm} = 1, N_{\pi^\pm} = 1, N_{\mu^\pm} = N_{\pi^0} = N_{\text{Oth. Had.}} = 0$
$1e$ + Other	$N_{e^\pm} = 1, N_{\mu^\pm} = 0$, Any no. of other visible particles
1μ	$N_{\mu^\pm} = 1, N_{e^\pm} = N_{\pi^0} = N_{\pi^\pm} = N_{\text{Oth. Had.}} = 0$
$1\mu1\pi$	$N_{\mu^\pm} = 1, N_{\pi^\pm} = 1, N_{e^\pm} = N_{\pi^0} = N_{\text{Oth. Had.}} = 0$
1μ + Other	$N_{\mu^\pm} = 1, N_{e^\pm} = 0$, Any no. of other visible particles
$1\pi^0$	$N_{\pi^0} = 1, N_{e^\pm} = N_{\mu^\pm} = N_{\pi^\pm} = N_{\text{Oth. Had.}} = 0$
$1\pi^\pm$	$N_{\pi^\pm} = 1, N_{e^\pm} = N_{\mu^\pm} = N_{\pi^0} = N_{\text{Oth. Had.}} = 0$
Had. bkg	Any other topology that doesn't belong to above topologies

TABLE 3.3: Definitions of various FS topologies that are used to differentiate between signal and background topologies in the selection variable distributions.

Interaction mode	Definition
ν_e CCQE	CCQE interactions of ν_e
ν_e CC1π^+	SPP interactions of ν_e
$\nu_e/\overline{\nu}_e$ CC	All other ν_e and $\overline{\nu}_e$ CC interactions
ν_μ CCQE	CCQE interactions of ν_μ
ν_μ CC1π^+	SPP interactions of ν_μ
$\nu_\mu/\overline{\nu}_\mu$ CC	All other ν_μ and $\overline{\nu}_\mu$ CC interactions
NC	All NC interactions

TABLE 3.4: Definitions of various interaction modes that are used to differentiate between signal and background interaction modes in the selection variable distributions.

3.3.1 FC, FV and Visible Energy Cuts

The FC condition ensures that the event is fully contained inside SK's ID. This is done by demanding the number of OD PMT hits to be less than 16.

For the multi-ring ν_e CC1π^+ 's *DWall* and *ToWall* calculation, the vertex was chosen to be the one from the best multi-ring hypothesis. The *DWall* cut was taken as 50 cm and the *ToWall* of both e and π^+ rings were taken as 150 cm. These values were obtained from the study described in [66] and were chosen such that the reconstructed neutrino energy error was consistent with zero, as shown in Fig. 3.3.

The distributions of FV parameters are shown in Fig. 3.4, 3.5 and 3.6.

The visible energy cut for FD e-like samples is applied at 100 MeV since the events below this are mostly dominated by NC background as can be seen in the plot broken down by interaction mode in Fig. 3.7 (right).

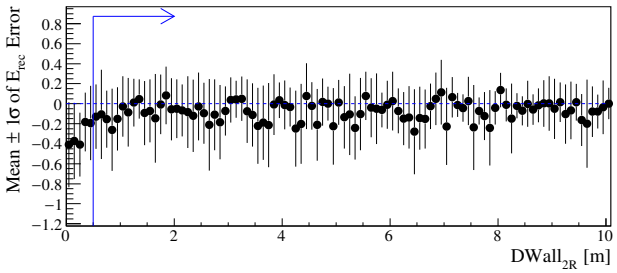

(a) DWall$_{2R}$

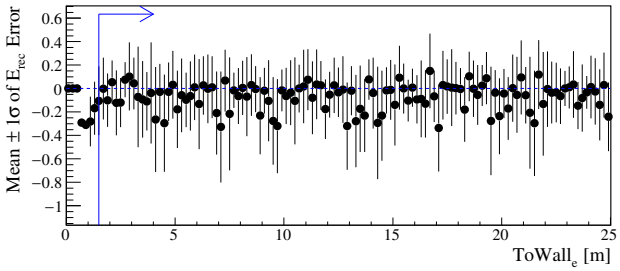

(b) ToWall$_e$

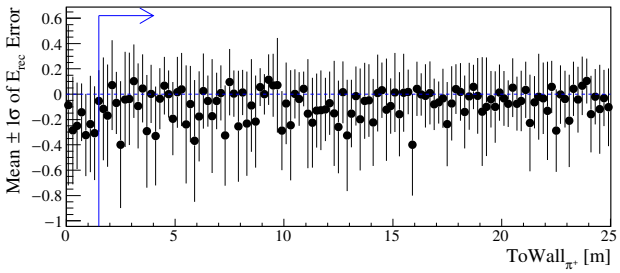

(c) ToWall$_{\pi^+}$

FIGURE 3.3: E_{rec} error as a function of *DWall* and $ToWall_{e,\pi}$, where E_{rec} error is defined as $(E_{rec} - E_{true})/E_{true}$ where E_{true} is the true neutrino energy. The cut values of these three parameters are taken from this study [66].

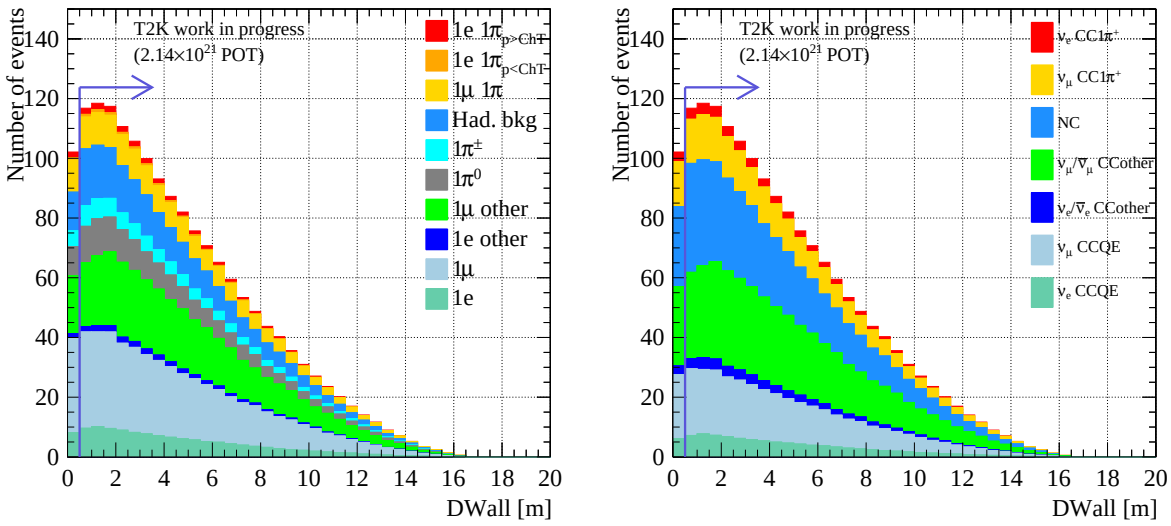

FIGURE 3.4: The distribution of *DWall*, along with the arrow that points towards the region selected by the cut. The plot on the left shows MC events broken down by FS topology and that on the right is broken down by interaction mode.

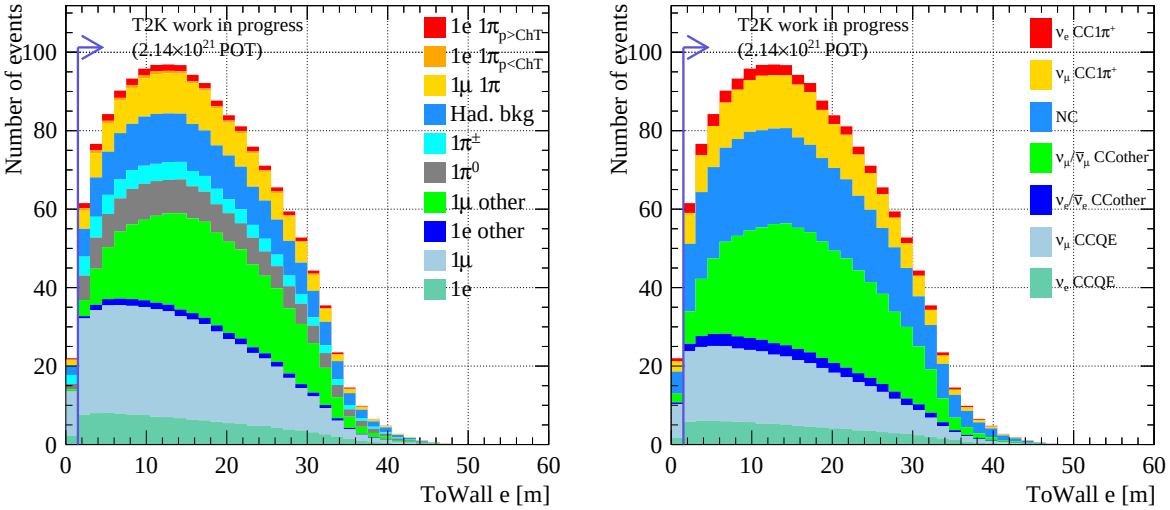

FIGURE 3.5: The distribution of *ToWall* for *e*-like ring from the multi-ring fit, along with the arrow that points towards the region selected by the cut. The plot on the left shows MC events broken down by FS topology and that on the right is broken down by interaction mode.

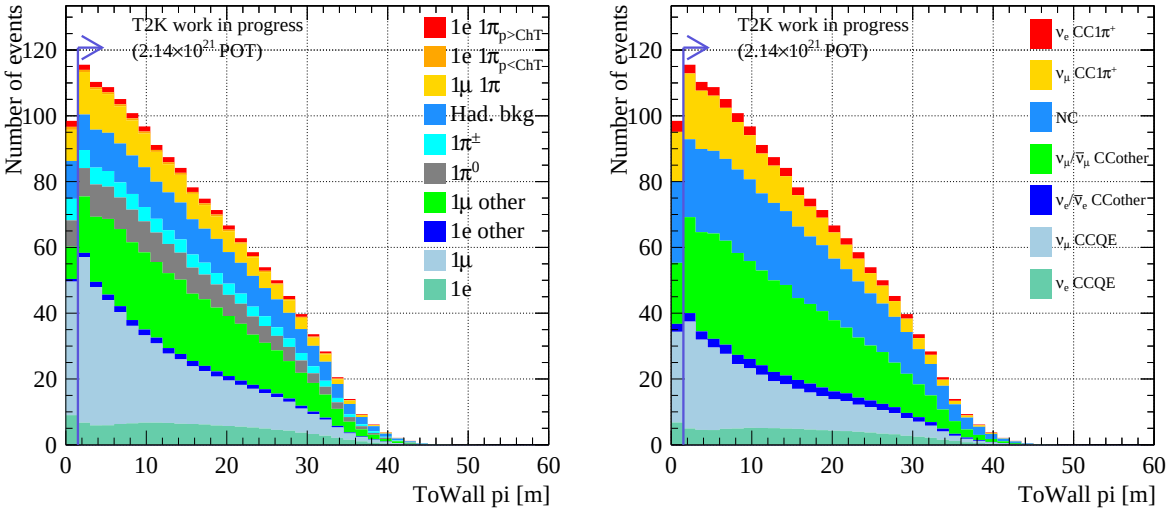

FIGURE 3.6: The distribution of *ToWall* for π^+-like ring from the multi-ring fit, along with the arrow that points towards the region selected by the cut. The plot on the left shows MC events broken down by FS topology and that on the right is broken down by interaction mode.

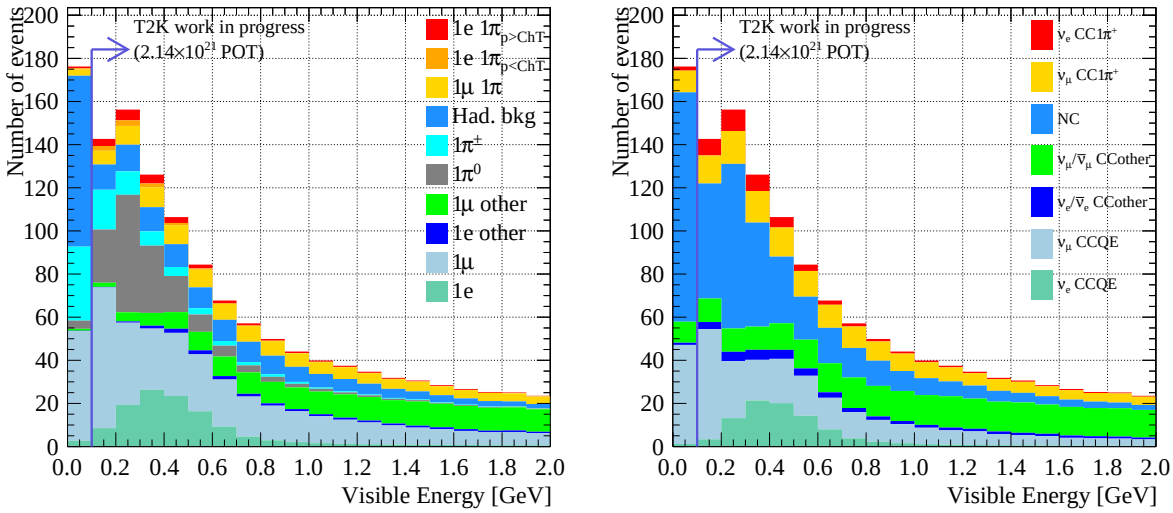

FIGURE 3.7: The distribution of visible energy, along with the arrow that points towards the region selected by the cut. The plot on the left shows MC events broken down by FS topology and that on the right is broken down by interaction mode.

3.3.2 Number of Reconstructed Rings and Decay Electrons

As described earlier, the signal topology of the multi-ring ν_e CC1π^+ sample contains an e-like and π^+-like ring, along with the π^+ decay's decay electron. The cuts on the number of rings and decay electrons are shown in Fig. 3.8 and 3.9 respectively. With the application of these two topological cuts, a large fraction of multi-π and DIS events were removed as expected. However, a significant number of signal events are also lost due to them being reconstructed with the wrong number of rings and no decay electrons. More information about that will be discussed in Section 3.5.

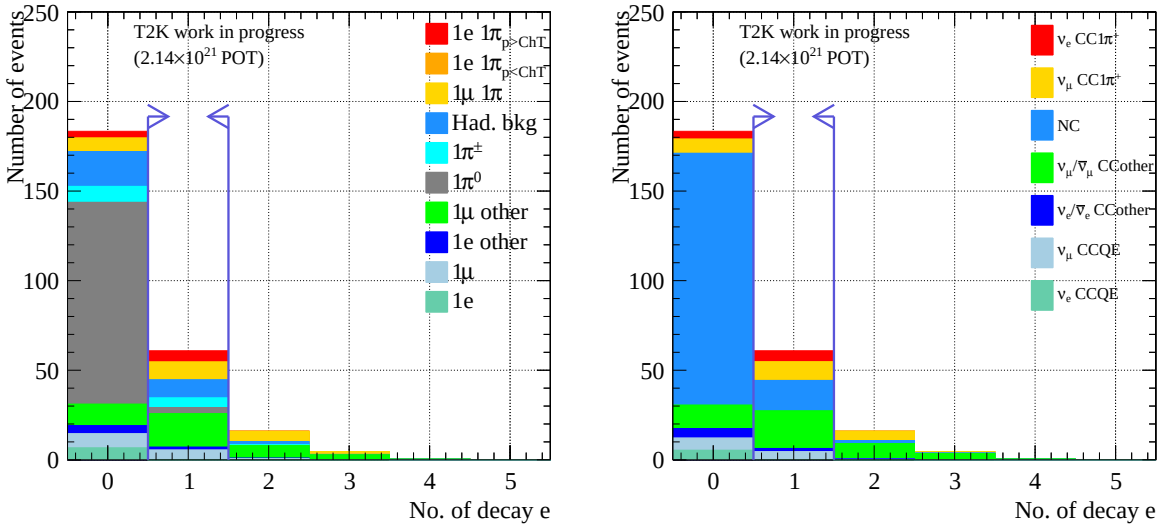

FIGURE 3.9: The distribution of the number of decay electrons, along with the arrows that denote which events are selected. The plot on the left shows MC events broken down by FS topology and that on the right is broken down by interaction mode.

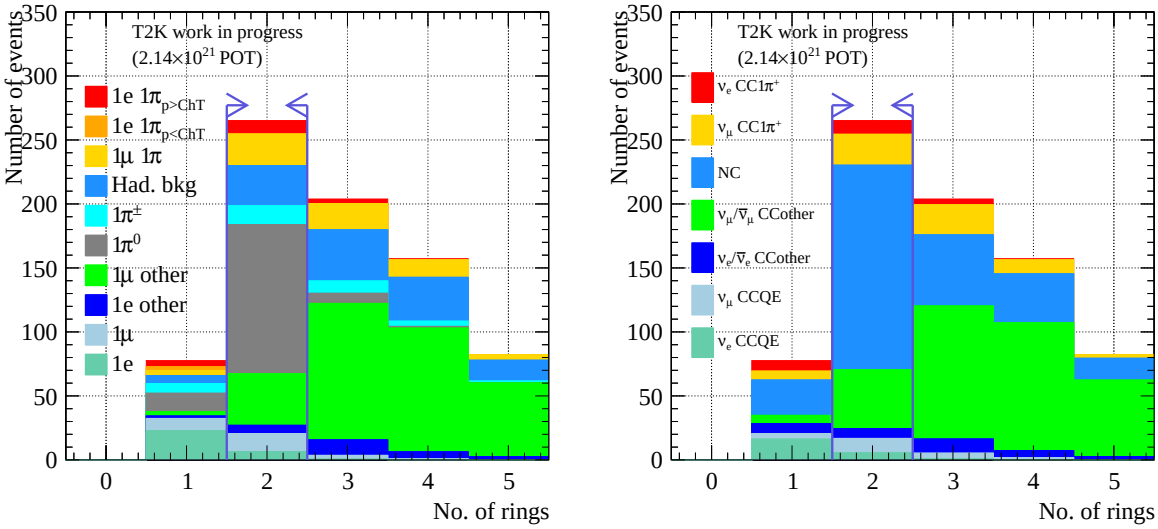

FIGURE 3.8: The distribution of the number of reconstructed rings, along with the arrows that denote which events are selected. The plot on the left shows MC events broken down by FS topology and that on the right is broken down by interaction mode.

3.3.3 The $e\pi/\pi\pi$ PID Cut

The optimized $e\pi/\pi\pi$ PID cut can reject multi-ring ν_μ CC events of various topologies, including that of the multi-ring ν_μ CC1π^+ sample. The distribution is shown in Fig. 3.10. While this cut efficiently removes most of the $1\mu + 1\pi$ topology events, it fails to reject $1\pi^0$ and hadronic background events, both of which are from NC interactions.

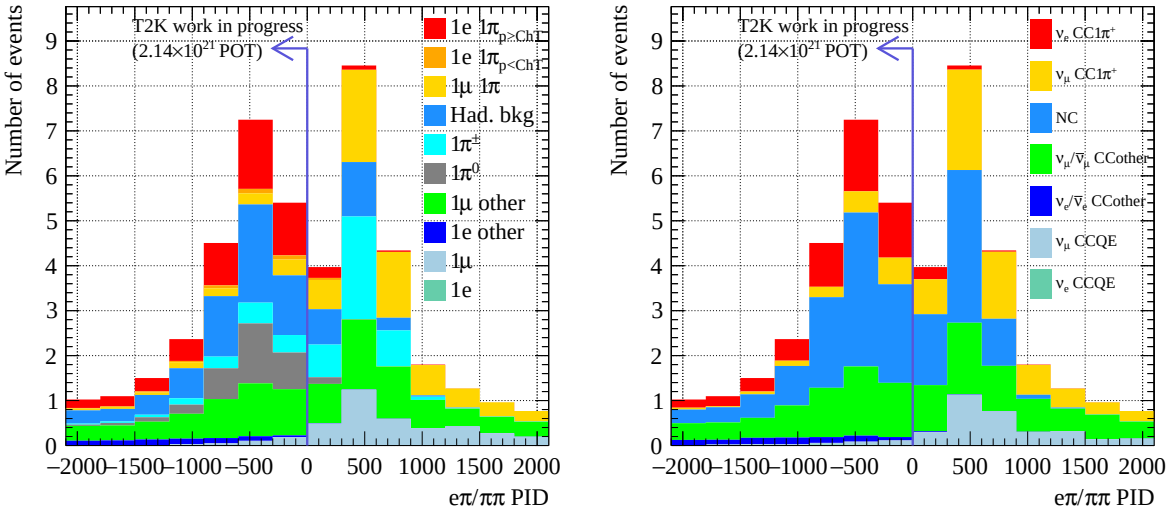

FIGURE 3.10: The distribution of $e\pi/\pi\pi$ PID variable, along with the arrow pointing towards events that pass the cut. The plot on the left shows MC events broken down by FS topology and that on the right is broken down by interaction mode.

3.3.4 The $e\pi/\pi^0$ PID Cut

As described before, this is a two-dimensional cut applied on $e\pi/\pi^0$ LLH - reconstructed π^0 mass distribution. This cut is aimed at rejecting a large number of NC backgrounds that passed all the other selection cuts until this cut.

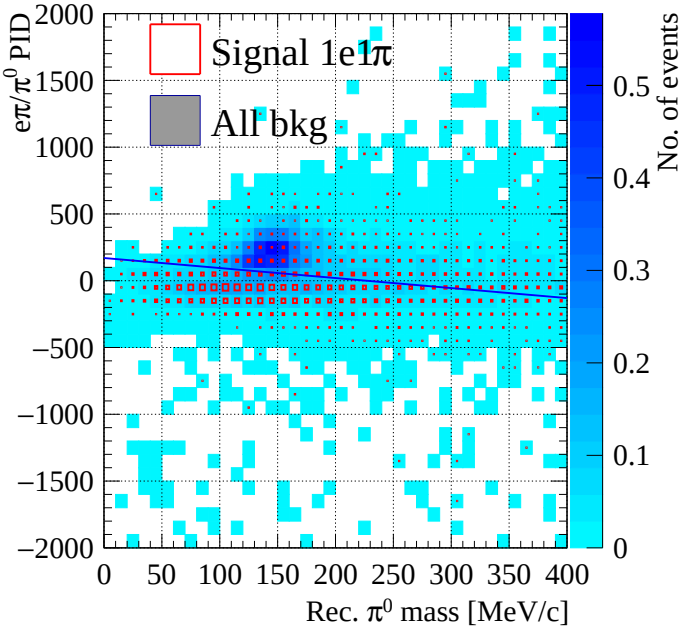

FIGURE 3.11: The two-dimensional distribution between reconstructed π^0 mass and the $e\pi/\pi^0$ LLH (although marked PID in y-axis). The red boxes represent the signal $1e + 1\pi^+$ topology, while the other palettes show all the background events. Events above the blue line are rejected.

Fig. 3.11 shows the characteristic clustering of events around the π^0 mass, denoting that those events are NC π^0 events. The optimized selection cut is able to remove most of that NC background.

3.3.5 $E_{rec} < 1.25$ GeV Cut

The last selection cut for the multi-ring ν_e CC1π^+ sample is the E_{rec} cut. This upper cap on E_{rec} removes the ν_e events coming from the intrinsic ν_e background in T2K's beam. To visualise this, an additional distribution where the MC is broken down by the type of neutrino in the beam is also provided in Fig. 3.12. The intrinsic ν_e are marked as "beam ν_e" in the figure. It is evident that although there are events with $1e + 1\pi^+$ signal topology after 1.25 GeV, very few of them are from the ν_e that truly come from $\nu_\mu \rightarrow \nu_e$ oscillation.

Event displays of two MC events that were selected as multi-ring ν_e CC1π^+ events are shown in Fig. 3.13.

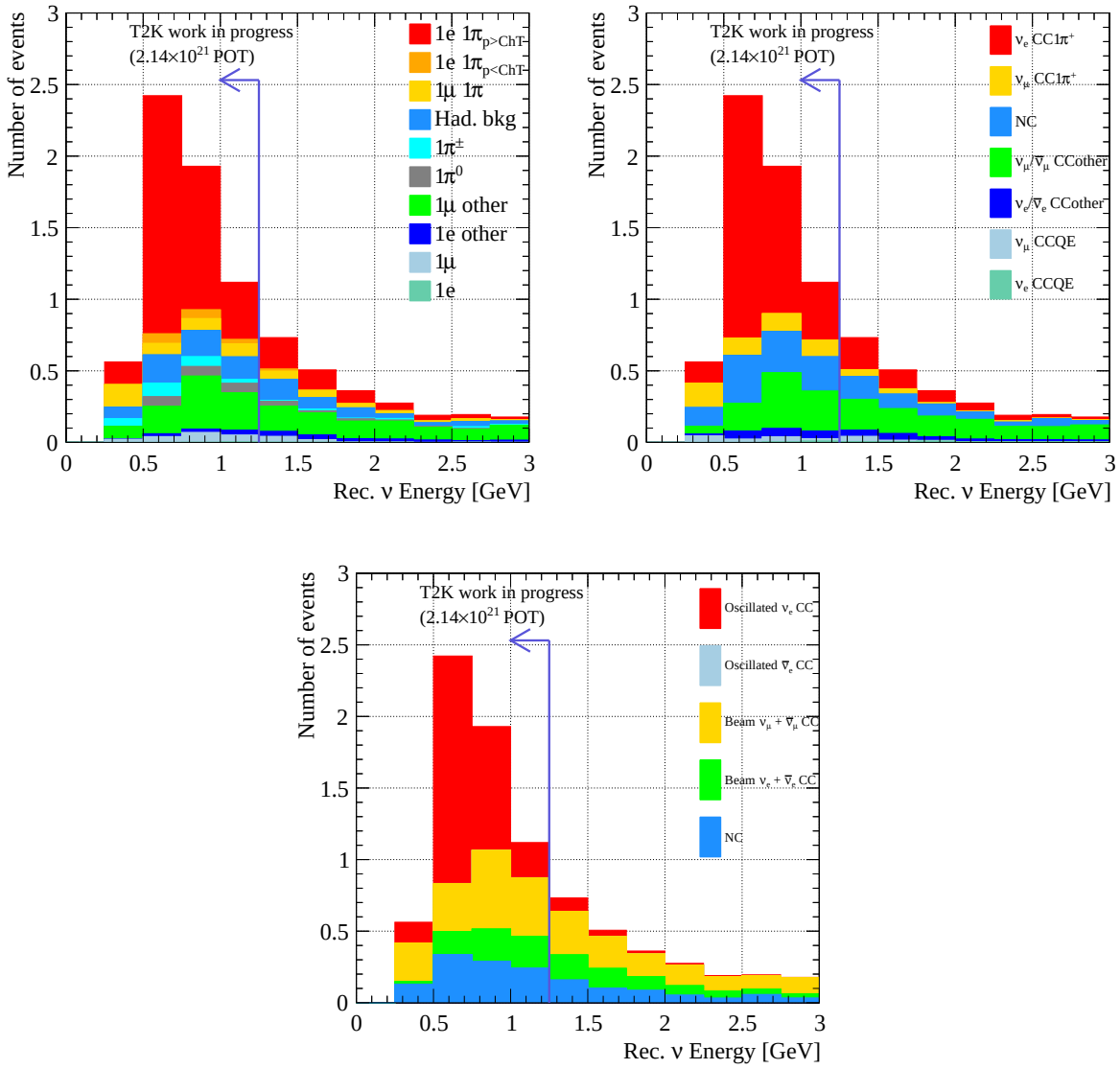

FIGURE 3.12: Distribution of E_{rec} estimated using the equation 1.22. The (left) right plot shows MC events broken down by (FS topology) interaction mode. The plot in the bottom panel shows the breakdown of the MC in terms of the neutrino type. Oscillated $\nu_e/\overline{\nu_e}$ CC refer to $\nu_\mu/\overline{\nu}_\mu$ neutrinos that underwent oscillations and CC interaction. Beam $\nu_e/\overline{\nu}_e$ are the intrinsic ν_e background in the beam.

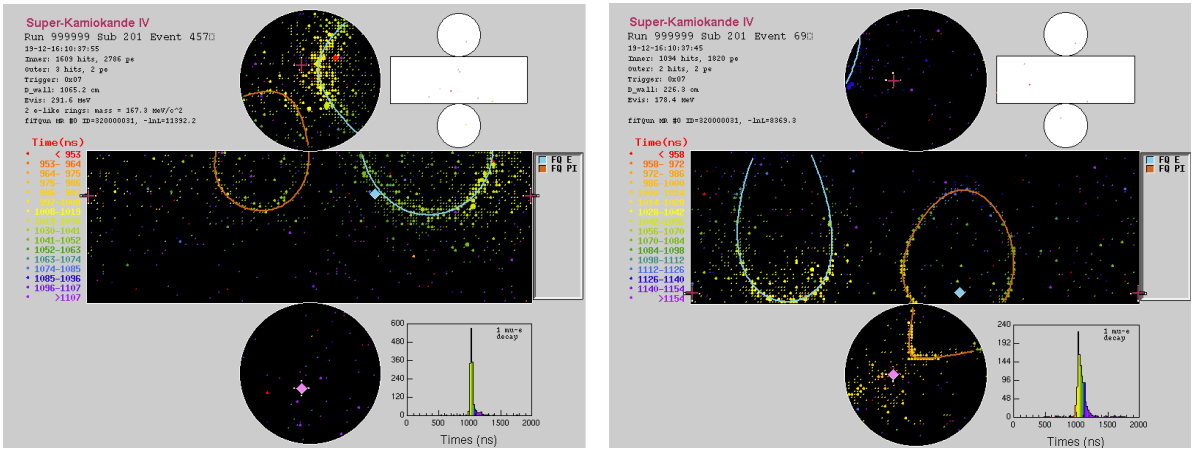

FIGURE 3.13: Event displays of two MC candidates that were selected as multi-ring ν_e CC1π^+ events, with the cyan ring marking the reconstructed e^- and the orange ring marking the reconstructed π^+.

Biases in using Δ approximation for E_{rec}:

It was mentioned before that the E_{rec} calculation for the ν_e CC1π^+ sample assumes the interaction goes through Δ resonance. However, there can also be contributions from nearby resonances that produce the signal topology, along with contributions from non-RES and coherent SPP interactions. Furthermore, background events that pass all the selections will also get assigned a wrong E_{rec}. To summarise the magnitude of E_{rec} bias in selected events, event rates as a function of $(E_{rec} - E_{true})/E_{true}$ was plotted, as shown in Fig 3.14. It can be seen that most of the events with true $1e + 1\pi^+$ topology do have minimal E_{rec} biases.

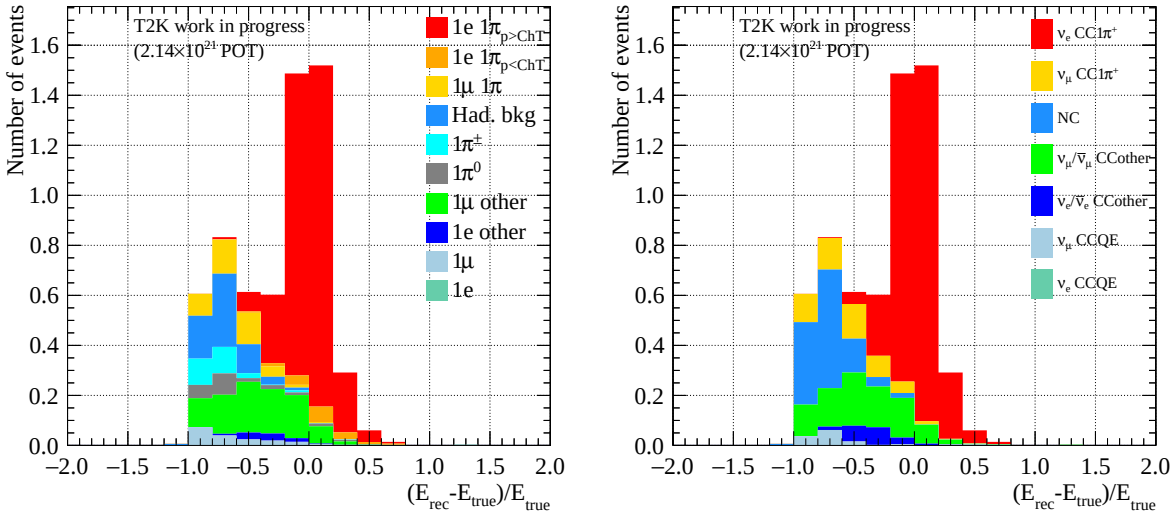

FIGURE 3.14: $(E_{rec} - E_{true})/E_{true}$ after applying all the multi-ring ν_e CC1π^+ selection cuts . The (left) right plot shows MC events broken down by (FS topology) interaction mode.

3.4 Event Rates

Event rates broken down by FS topology and interaction mode after each multi-ring ν_e CC1π^+ selection cut are tabulated in Tables 3.5 and 3.6.

Cut	$1e$	$1e1\pi^+_{p>CT}$	$1e1\pi^+_{p<CT}$	$1e$+Other	1μ	$1\mu1\pi^+$	1μ+Other	$1\pi^0$	$1\pi^\pm$	Had. bkg	MC Total
FC	132.15	30.27	12.20	31.39	468.94	169.38	398.41	160.91	87.08	232.73	1723.45
FC, FV, E_{vis}	29.83	19.77	3.79	28.41	27.65	67.36	321.02	140.52	37.22	132.41	807.99
No. of Rings	6.54	10.11	0.69	6.46	13.99	24.44	40.34	116.41	14.73	31.46	265.17
No. of Decay e	0.02	6.15	0.49	1.59	5.36	9.69	18.69	3.45	5.32	10.09	60.86
$e\pi/\pi\pi$ PID	0.02	5.76	0.45	1.58	0.39	1.30	9.37	3.29	1.42	7.78	31.35
$e\pi/\pi^0$ PID	0.01	3.86	0.21	0.28	0.24	0.62	2.23	0.29	0.31	1.15	9.19
$E_{rec} < 1.25$ GeV	0.00	3.23	0.16	0.08	0.18	0.41	0.91	0.20	0.24	0.63	6.05

TABLE 3.5: Reduction of MC events along ν_e CC1π^+ selection cuts broken down by FS topology. The far right column shows the total MC events that pass the selection. Signal events belong to the $1e1\pi^+_{p>CT}$ column.

Cut	ν_e CCQE	ν_e CC1π^+	$\nu_e/\overline{\nu}_e$ CC	ν_μ CCQE	ν_μ CC1π^+	$\nu_\mu/\overline{\nu}_\mu$ CC	NC	MC Total
FC	99.89	51.33	54.78	319.10	227.76	510.90	459.70	1723.46
FC, FV, E_{vis}	22.40	24.79	34.61	22.06	68.65	333.43	302.06	807.98
No. of Rings	5.41	10.77	7.62	11.36	24.16	46.17	159.67	265.17
No. of Decay e	0.14	6.25	1.87	4.31	10.33	20.89	17.08	60.86
$e\pi/\pi\pi$ PID	0.14	5.84	1.83	0.26	1.64	10.70	10.94	31.35
$e\pi/\pi^0$ PID	0.06	3.90	0.40	0.18	0.65	2.39	1.62	9.19
$E_{rec} < 1.25$ GeV	0.01	3.28	0.18	0.12	0.53	0.92	1.01	6.05

TABLE 3.6: Reduction of MC events along ν_e CC1π^+ selection cuts broken down by interaction mode. The far right column shows the total MC events that pass the selection. Signal events belong to the ν_e CC1π^+ column.

The purity of the selected samples in terms of FS topology is 53%, and 54% in terms of interaction mode. The most dominant backgrounds that still end up passing the ν_e CC1π^+ selection cuts are the 1μ+Other and hadronic background topology events, which are dominated by multi-π, DIS and NC interactions.

Although the purity is considerably small, it should be noted that the background events were reduced to only 0.4% after the initial number of background calculated from the FC, FV, E_{vis} cut while the remaining efficiency for the signal events is 16.6%.

3.5 Selection Efficiency Studies

When a new sample is introduced, its selection efficiency is studied as a function of true kinematic variables to know whether the sample has any model dependencies. If the selection is sensitive to certain regions of kinematic phase space where the knowledge of the interaction model is not great, it can lead to biases in the analysis. On the other hand, if the interaction systematic uncertainty can cover these regions, then there should not be a problem. Ideally, a sample should have a sufficiently high and flat efficiency throughout the phase space of the kinematic variable being studied. Usually, reconstruction biases manifest themselves as the efficiency dependence on the kinematic variables.

The selection efficiencies of the multi-ring ν_e CC1π^+ sample were studied as a function of true neutrino energy, true e and π^+ momenta, true cosine of the polar angle between the outgoing e and π^+ particles, true momentum transfer Q^2 and the true invariant hadronic mass of the system W. The selection efficiency is calculated as below:

$$\text{Selection efficiency} = \frac{1e1\pi^+ \text{ events that pass the selection}}{1e1\pi^+ \text{ events in true FCFV}} . \tag{3.3}$$

Here, 1e1π^+ events are the events which have the true signal topology of the multi-ring ν_e CC1π^+ sample, that is visible e- and π^+-like rings. True FCFV condition means that the event should be fully contained and within the true fiducial volume defined as $DWall_{true} > 50$cm. The selection efficiency plots give insight into which region of the kinematic phase space fail to reconstruct a true ν_e CC1π^+ event.

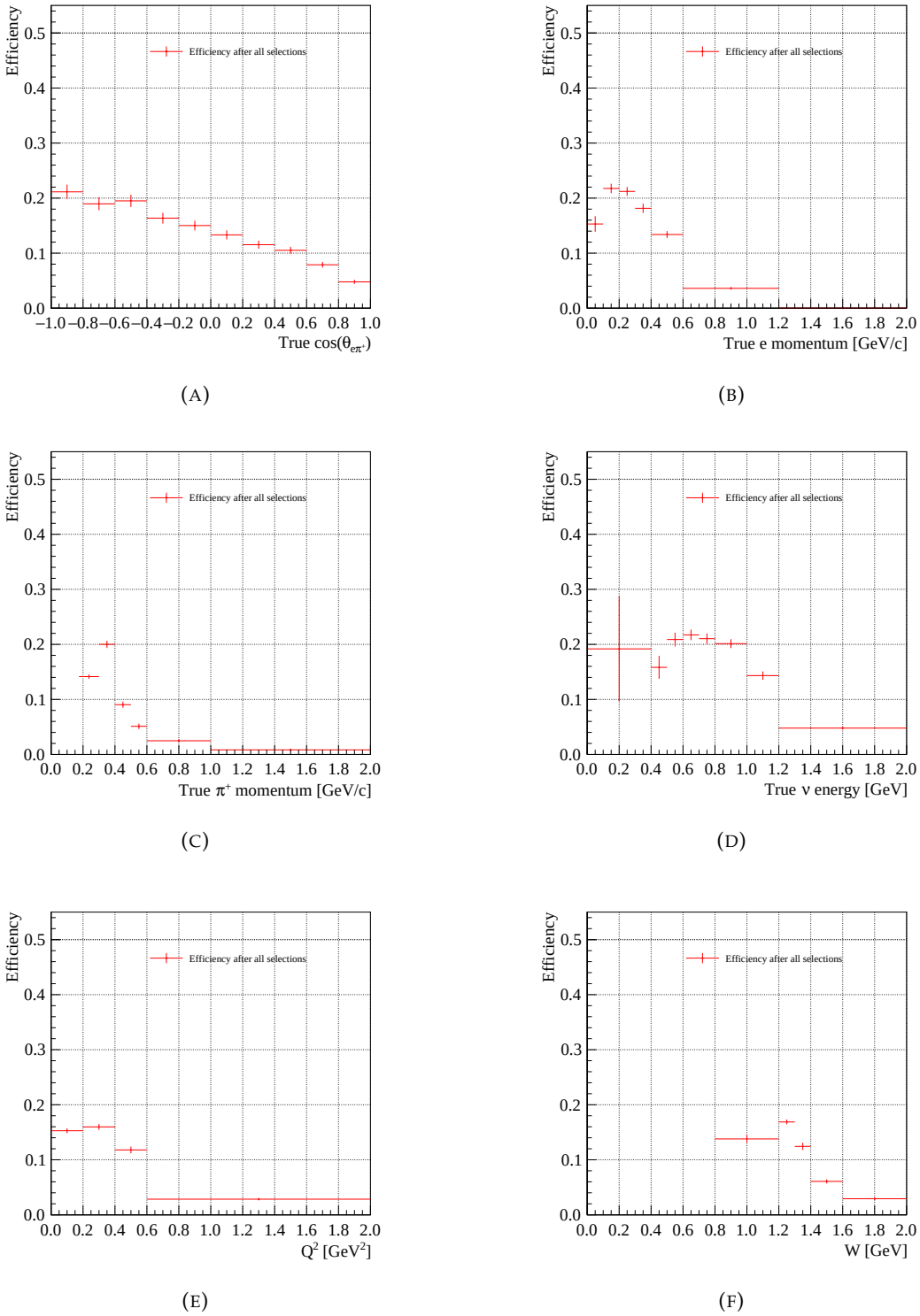

(A) (B) (C) (D) (E) (F)

FIGURE 3.15: Efficiencies calculated using equation 3.3 is shown in the plots above.

It is evident from the plots in Fig. 3.15 that the overall efficiency of the sample is low, and only around 20% at the peak for all the true kinematic variables. Fig. 3.15a shows that the efficiency has a systematic decline towards regions where the e and π^+ rings become collinear. This behaviour is understood because SK's reconstruction software cannot separate the rings from these two particles at such low polar angles, and hence they get merged as one fuzzy e-like ring.

The efficiency is considerably flat in true neutrino energy and Q^2. However, it has an evident decline at higher e and π^+ momenta and W. This is not well understood. Multiple tests were performed to understand why the sample possesses an efficiency dependence on these kinematic variables, with no test showing promising results. One of the most important test that was performed was to check if a particular selection cut was causing this. For this, one selection cut was removed at a time while keeping every other cut, and efficiencies were calculated for those selected events.

This test is summarised in Fig. 3.16 as a function of true π^+ momentum. It can be understood that the selection cuts themselves do not seem to impact the shape of the efficiency. From this, a conclusion was drawn that the reason for the efficiency dependence might have its roots in reconstruction or secondary interactions that end up changing the final state topology of the events.

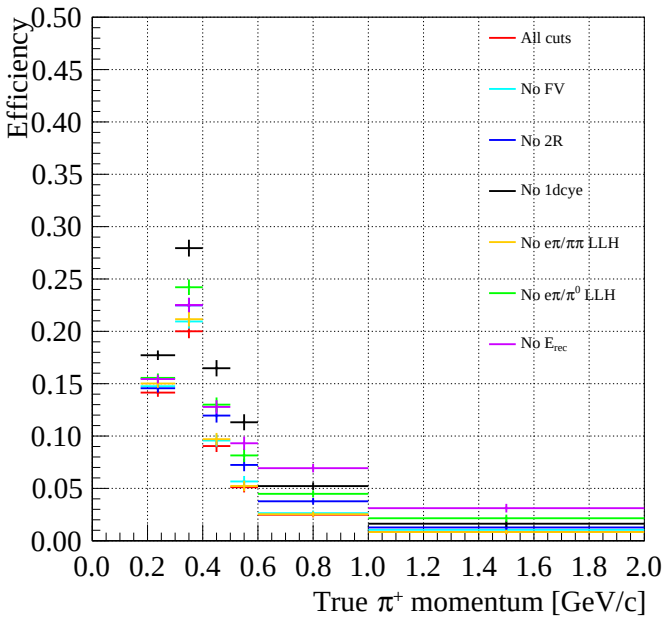

FIGURE 3.16: Efficiencies as a function of true π^+ momentum calculated after removing one selection cut at a time while keeping the others. This shows that no particular selection cut is causing the steep π^+ momentum dependence of efficiency.

Table 3.7 summarises the areas where a large fraction of true $1e + 1\pi^+$ topology events are lost due to reconstruction failure or because of selection cuts. It can be seen that of the available true $1e + 1\pi^+$ events, only 26% get reconstructed with exactly two rings and one decay electron. While the PID cuts and E_{rec} cut only reject a small fraction of true signal events, the reason why this sample loses most of its true signal events is that the reconstruction framework failed to tag exactly two rings and one decay electron.

<table>
<tr><td colspan="3">2 Rings
1 Decay e</td><td>2 Rings
Not 1 Decay e</td><td>1 Ring
1 Decay e</td><td>>2 Rings
1 Decay e</td><td>Not 2 Rings
Not 1 Decay e</td></tr>
<tr><td colspan="3">25.59%</td><td>14.20%</td><td>29.22%</td><td>7.68%</td><td>23.32%</td></tr>
<tr><td colspan="2">Passes $e\pi/\pi\pi$ PID</td><td>Fails</td><td rowspan="4"></td><td rowspan="4"></td><td rowspan="4"></td><td rowspan="4"></td></tr>
<tr><td colspan="2">23.79%</td><td>1.80%</td></tr>
<tr><td>Passes $e\pi/\pi^0$ PID</td><td>Fails</td><td rowspan="3"></td></tr>
<tr><td>16.42%</td><td>7.37%</td></tr>
<tr><td>$E_{rec} < 1.25$ GeV</td><td>Fails</td><td rowspan="2"></td><td rowspan="2"></td><td rowspan="2"></td><td rowspan="2"></td></tr>
<tr><td>13.93%</td><td>2.48%</td></tr>
</table>

TABLE 3.7: Breakdown of the percentage of true $1e + 1\pi^+$ events that remain after each selection cut. The column marked red shows the remaining $1e + 1\pi^+$ events after all selection cuts were applied. Note: The true $1e + 1\pi^+$ topology here includes π above and below Cherenkov threshold

Events that have one ring and one decay electron possess the topology of the single-ring ν_e CC1π^+ sample and hence can be retained by that sample. However, the events where true signal events were reconstructed with the other combinations of rings and decay electrons are truly lost due to faulty reconstruction. This is an area which can be improved in the future.

3.6 The Expanded ν_e CC1π^+ Sample

After discussions with various working groups within T2K, it was decided that the new sample should be merged with the existing single-ring ν_e CC1π^+ sample, since both these samples target the same SPP neutrino interaction. By doing so, the strong dependency on π^+ kinematic model is also removed.

The selection efficiency of the expanded ν_e CC1π^+ sample was also calculated and is shown in Fig. 3.17, along with an overlay of individual selection efficiencies of the single- and multi-ring ν_e CC1π^+ sample.

As claimed earlier, the drop of efficiency seen in the multi-ring sample around the collinear region can be seen as an increase of efficiency for the single-ring ν_e CC1π^+ sample in Fig. 3.17a. Combining the two samples thus bridges the reconstruction-related dependency for the time being until improvements can be made on the reconstruction level. While combining the samples does not necessarily flatten the efficiency dependency, it can be seen from Fig. 3.17c that the expanded sample no longer has a strong π^+ momentum cut-off as the individual samples. Every other distribution shows an overall total efficiency improvement, emphasising that the expanded sample is the best way to treat the ν_e CC1π^+ events.

3.7 E_{rec} Binning Studies

The far detector ν_e samples are binned in E_{rec}–θ_{lep} space and the ν_μ samples are binned in E_{rec} in the MCMC fitter. For the Frequentist fitter, they are binned in p_{lep}–θ_{lep} and E_{rec} respectively. Up until this analysis, an arbitrary choice of binning was employed in both the fitters. Ideally, the binning scheme should be motivated by how well the detector can resolve the kinematic parameters for their various ranges. In addition, having bins with very low statistics are also not good since they can cause biases in the analysis due to statistical fluctuations.

To create a binning scheme based on detector resolution, a two-dimensional distribution was constructed with $k_{rec} - k_{true}$ as a function of k_{rec}. Here k_{rec} and k_{true} are the reconstructed and true values of the kinematic parameter in consideration.

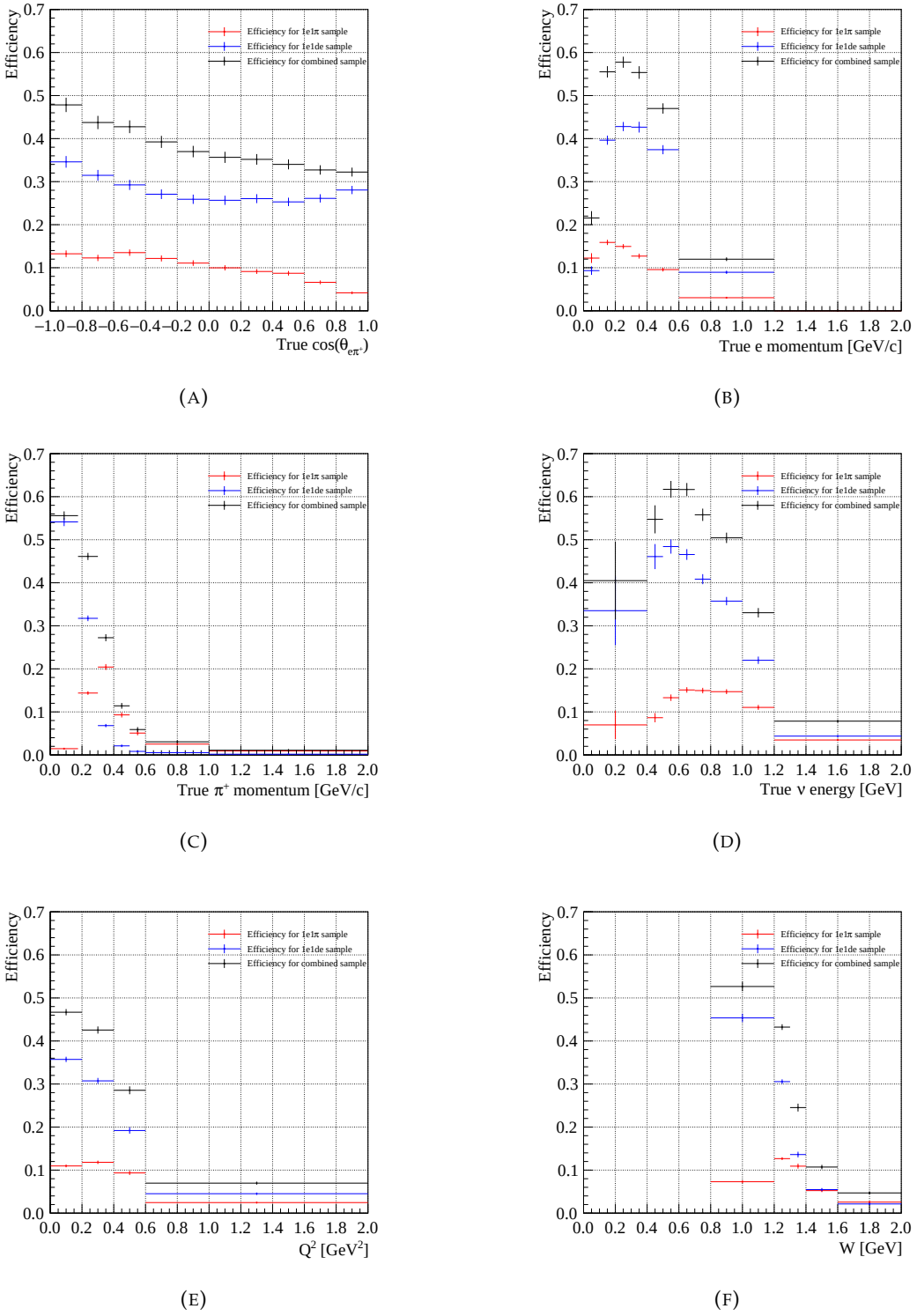

(A) (B)

(C) (D)

(E) (F)

FIGURE 3.17: Efficiencies of $1e1de$ (Blue), $1e1\pi^+$ (Red) and the expanded ν_e CC$1\pi^+$ sample (Black).

For this analysis, E_{rec} of all the 6 FD samples, and $\theta_{lep,rec}$ and $p_{lep,rec}$ of ν_e samples were studied. Due to the sheer number of plots that need to be looked at, only those of E_{rec} are shown in this section.

In the case of E_{rec} studies, E_{true} is calculated as a function of $p_{lep,true}$ and $\theta_{lep,true}$ as in Eqn. 1.18 and 1.22 for each FD sample rather than using the value directly from the NEUT-generated true neutrino energy.

From the two-dimensional distribution of $E_{rec} - E_{true}$ as a function of E_{rec}, a Gaussian is fitted for each slice of E_{rec}. Marked σ Reco. − True E_ν in the figures,[2] The error of the Mean is picked up from the Gaussian fit. This resolution metric is then used to decide the binning scheme. Since the x-axis represents the current binning used in T2K's analyses, a value of the resolution metric smaller than that of the E_{rec}'s bin-width in the particular bin means that a bin width smaller than the resolution is being employed, and hence needs to be widened.

For the ν_e samples, each E_{rec} bin is 50 MeV wide. For the ν_μ samples, the bins are defined as follows:

- 50 MeV bins for energy range 0–3 GeV
- 250 MeV bins for 3–4 GeV
- 500 MeV bins for 4–6 GeV
- 1 GeV bins for 6–10 GeV
- Single bin for 10–30 GeV

Fig. 3.18 and 3.19 show the two-dimensional distribution between $E_{rec} - E_{true}$ and E_{rec} (left) along with the resolution metric plot (right) for the FHC and RHC 1Re samples. As can be seen, all the bins except the ones with very low energy or high energy resolutions of more than 50 MeV. This happens because of the large spread in the Gaussian fit over a region that has low statistics. However, due to the overall agreement of resolution and bin-width, the current binning scheme can be claimed to be good enough.

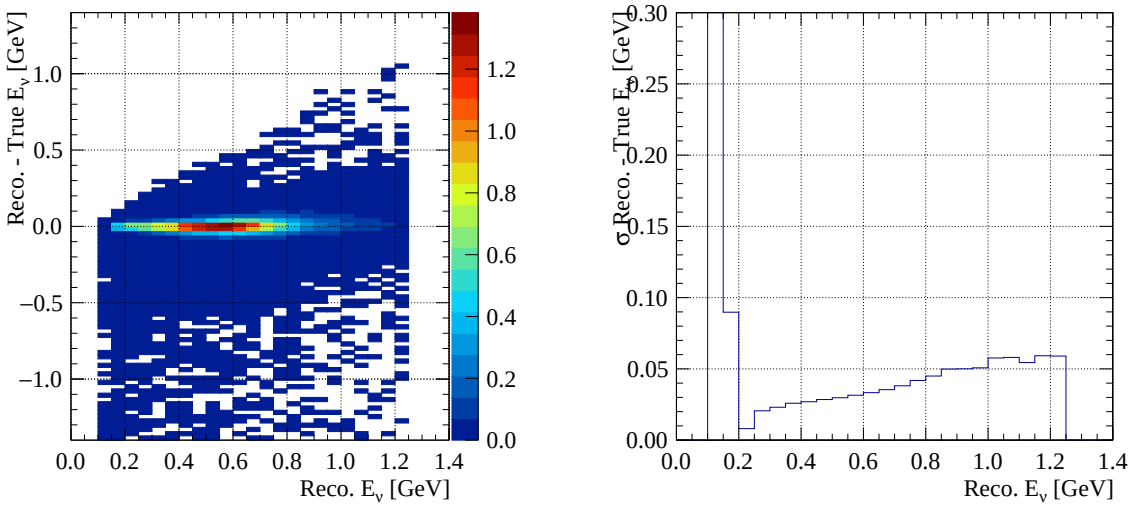

FIGURE 3.18: Rec. − True E_ν as a function of Rec. E_ν (left) and the spread (σ) in the Gaussian fit to the Rec. − True E_ν (right) for the FHC 1Re sample. The y-axis range in the right plot is truncated to avoid it being skewed by low-statistics bins with large Gaussian spread.

[2]The terms E_{rec}, E_{true} are also labelled as Reco., True E_ν in many Figures. Please note that they are the same.

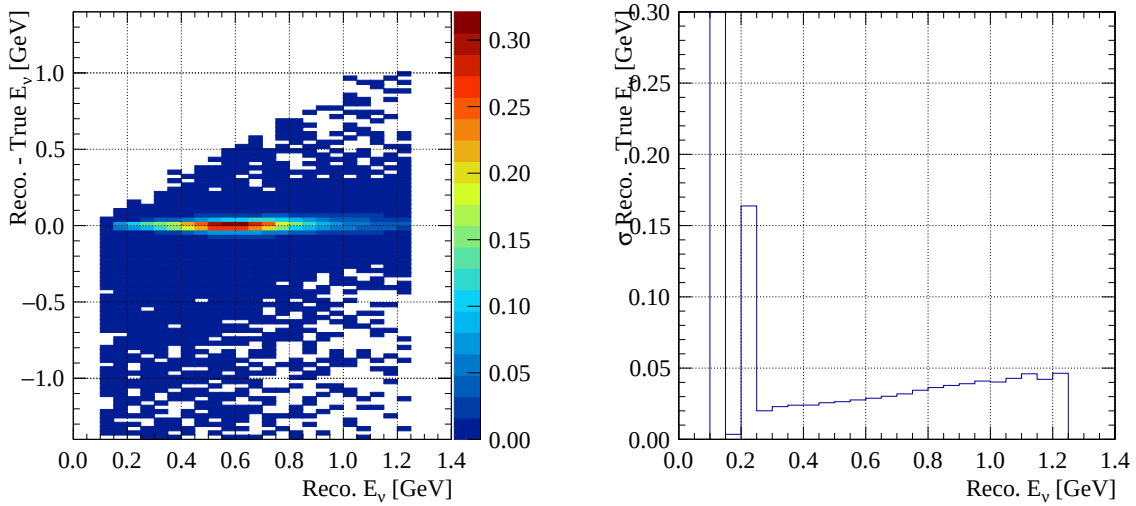

FIGURE 3.19: Rec. − True E_ν as a function of Rec. E_ν (left) and the spread (σ) in the Gaussian fit to the Rec. − True E_ν (right) for the RHC 1Re sample. The y-axis range in the right plot is truncated to avoid it being skewed by low-statistics bins with large Gaussian spread.

Fig. 3.20 shows the two-dimensional distribution between $E_{rec} - E_{true}$ and E_{rec} (left) along with the resolution metric plot (right) for the new expanded FHC ν_e CC1π^+ sample. Barring the first few that show a larger resolution than the bin width, all other resolutions are within the bin width. The first bins behave so because of the higher fraction of background events compared to the signal events. However, the sample does not contain any events below 0.3 GeV. Therefore, the bins ranging from 0–0.3 GeV were merged into a single bin. It was also decided to merge the bins from 1–1.25 GeV for the same reason.

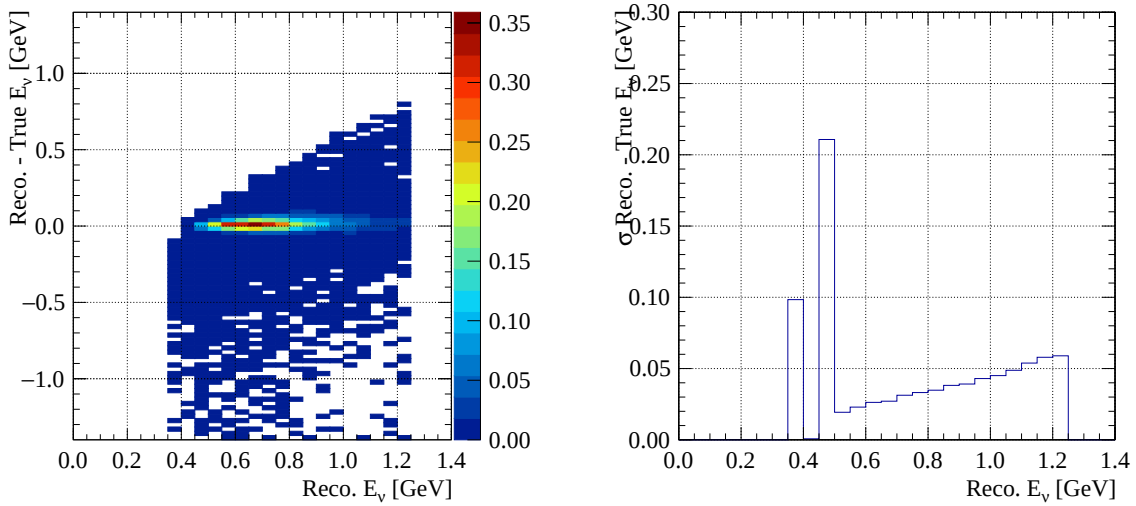

FIGURE 3.20: Rec. − True E_ν as a function of Rec. E_ν (left) and the spread (σ) in the Gaussian fit to the Rec. − True E_ν (right) for the FHC ν_e CC1π^+ sample.

The samples that have lesser agreement in resolution concerning the current binning scheme are the FHC, RHC 1Rμ and the FHC ν_μ CC1π^+ samples as visible in Fig. 3.21, 3.22 and 3.23 respectively.

The resolutions for these samples in the 0–3 GeV range are clearly of the order 75–150 MeV for the 1Rμ samples and from 100–200 MeV for the ν_μ CC1π^+ sample. Therefore, all of them need to be rebinned in that energy range. However, one needs to be careful when dealing with the 1Rμ sample as the region around 0.5–0.7 GeV, also known as the oscillation dip region provides the highest sensitivity to Δm^2_{32} and $\sin^2\theta_{23}$ parameters.

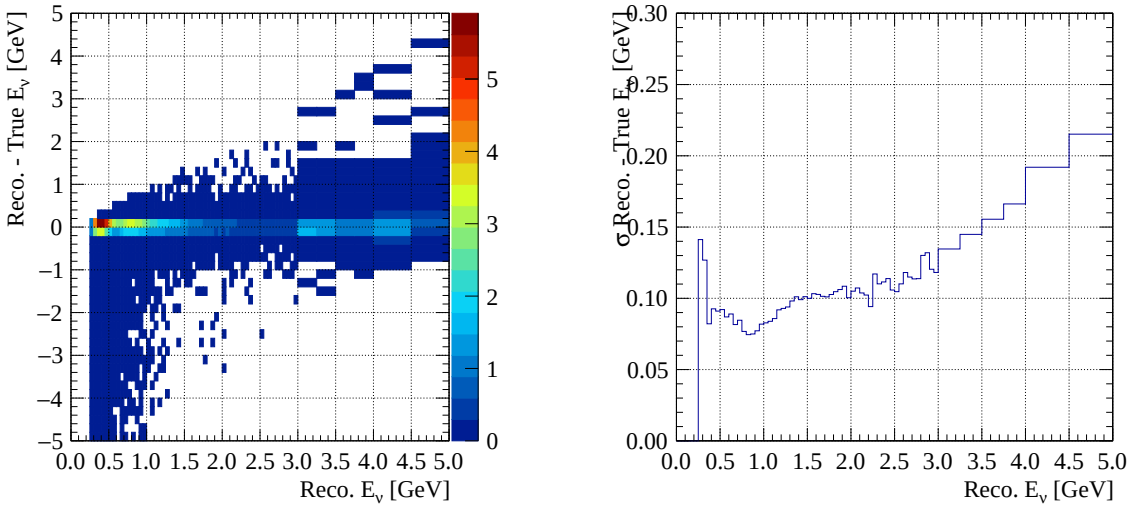

FIGURE 3.21: Rec. − True E_ν as a function of Rec. E_ν (left) and the spread (σ) in the Gaussian fit to the Rec. − True E_ν (right) for the FHC 1Rμ sample. The y-axis range in the right plot is truncated to avoid it being skewed by low-statistics bins with large Gaussian spread.

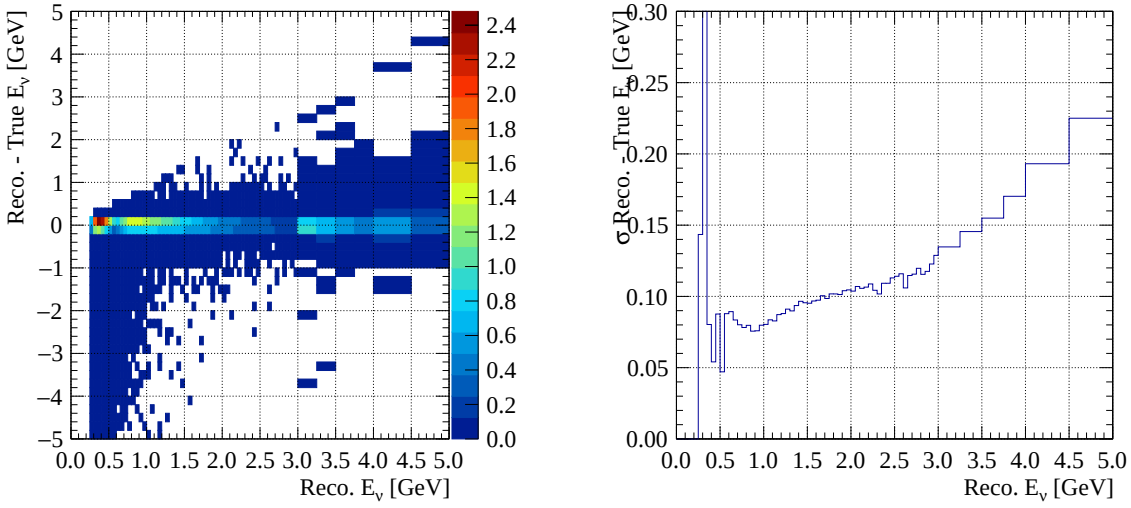

FIGURE 3.22: Rec. − True E_ν as a function of Rec. E_ν (left) and the spread (σ) in the Gaussian fit to the Rec. − True E_ν (right) for the RHC 1Rμ sample. The y-axis range in the right plot is truncated to avoid it being skewed by low-statistics bins with large Gaussian spread.

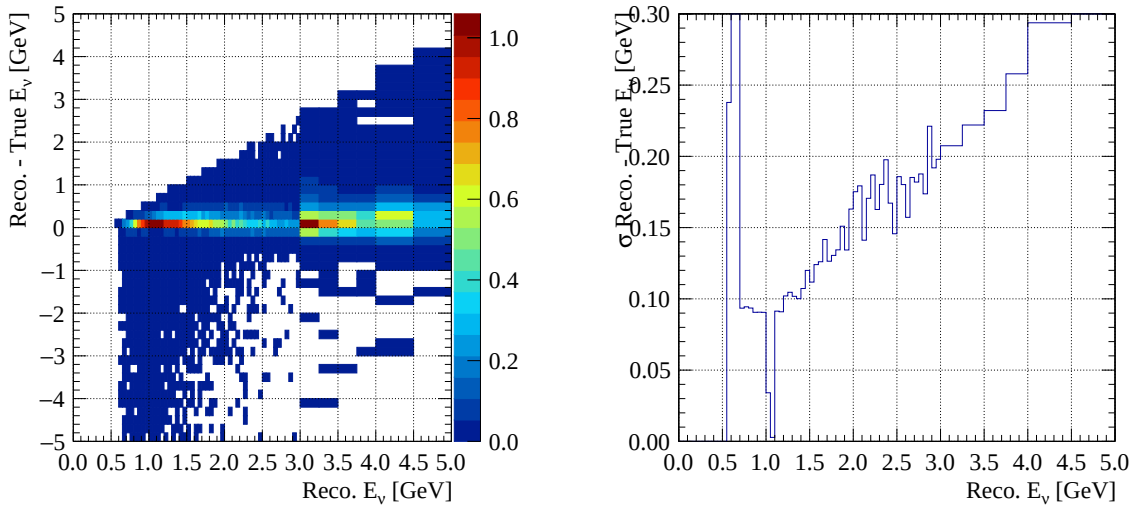

FIGURE 3.23: Rec. − True E_ν as a function of Rec. E_ν (left) and the spread (σ) in the Gaussian fit to the Rec. − True E_ν (right) for the FHC ν_μ CC1π^+ sample. The y-axis range in the right plot is truncated to avoid it being skewed by low-statistics bins with large Gaussian spread.

The $\theta_{lep,rec}$ and $p_{lep,rec}$ binning schemes used in the ν_e samples were kept unchanged since the binning used currently is well within the resolutions. These plots are added in A.2.

3.7.1 Revised E_{rec} Binning Scheme

For the oscillation analysis that will be performed in this thesis, the following binning schemes will be used, which were formulated after the resolution studies. The binnings of FHC and RHC CCQE-like 1Re samples remain unchanged.
For the expanded ν_e CC1π^+ sample, the binning scheme is as follows:

- Single bin for 0–0.3 GeV,
- 50 MeV bins from 0.3–1 GeV,
- Single bin for 1–1.25 GeV.

For the FHC and RHC 1Rμ samples, the updated binning scheme is:

- 100 MeV bins from 0–3 GeV,
- 250 MeV bins from 3–4 GeV,
- 500 MeV bins from 4–6 GeV,
- 1 GeV bins from 6–10 GeV,
- Single bin for 10–30 GeV.

Finally, the FHC ν_μ CC1π^+ sample is rebinned as:

- 100 MeV bins from 0–1.6 GeV,
- 200 MeV bins from 1.6–3 GeV,

- 250 MeV bins from 3–4 GeV,
- 500 MeV bins from 4–6 GeV,
- 1 GeV bins from 6–10 GeV,
- Single bin for 10–30 GeV.

4

Oscillation Analysis

You have to want to falsify the model.
If you love somebody, set them free

Andrew Gelman

4.1 Overview

T2K performs its oscillation analysis to obtain the neutrino oscillation parameters that the experiment is sensitive to. As a crude approximation, this "analysis" is a counting experiment, where data from both the ND280 and FD are compared to their MC predictions, from which oscillation parameters can be extracted. The main goal of this thesis is to study the impact of the new multi-ring ν_e CC1π^+ sample on the measurement of neutrino oscillation parameters. As discussed briefly in Chapter 2, T2K performs its neutrino analysis using both a frequentist statistics-based fitter and a Bayesian statistics-based fitter.

The frequentist fitter follows a sequential ND280 + FD fit, where the ND280 fit constrains the flux and cross-section parameters and provides a tuned FD prediction. These flux and cross-section constraints are propagated to the FD analysis as a covariance matrix and the FD fit gives constraints on the oscillation parameters. Both these fitters use a MINUIT-based algorithm.

The second fitter uses a Bayesian MCMC framework called MaCh3 [59] to simultaneously fit both ND and FD data samples to their respective MC to obtain posterior distribution functions of all the systematic and oscillation parameters. The parameters that ND is sensitive to are constrained within the joint fit. This framework can also be used to perform standalone ND[1] and FD fits. This chapter will describe the working of the joint ND+FD fit, which the Author performed to obtain the oscillation parameters that will be discussed in Chapter 6.

4.2 Statistical Framework

The outcome of any experiment is governed by numerous systematic uncertainties that can significantly alter the results if not treated properly. At T2K, careful treatment needs to be provided to the systematic errors arising from the beamline, the ND, the FD and underlying physics processes to obtain accurate predictions of event rates at its detectors. What sounded

[1] MaCh3's ND-only fit is done for validation purposes and for comparing the Bayesian results with the frequentist ND fit result. In addition, it is a valuable tool in assessing the impact of cross-section and flux systematics on the FD spectra.

like a simple counting experiment now becomes a multi-dimensional complex fit that requires powerful statistical machinery.

4.2.1 Bayesian Statistics

Any analysis framework based on Bayesian statistics is built with Bayes theorem at its core. As mentioned above, the expected number of events at a detector depends on many systematic parameters. A model comprising of these parameters $\vec{\theta}$ can be built, and the goal will then be to find a set of values for these model parameters that fit the data in the best way possible. To extract these parameters, we can make use of Bayes theorem.

The conditional probability distribution $p(\vec{\theta}|D)$, or the probability distribution of model parameters $\vec{\theta}$ given the measurement D is given by:

$$p(\vec{\theta}|D) = \frac{p(D|\vec{\theta})p(\vec{\theta})}{p(D)} \tag{4.1}$$

where $p(\vec{\theta})$ are the prior probability distributions (priors) of these parameters, $p(D)$ is the probability distribution of the observed measurement, and $p(D|\vec{\theta})$ is the probability distribution of the measurement D taken assuming a particular set of parameter values $\vec{\theta}$. $p(D|\vec{\theta})$ is also called the likelihood function (or just likelihood). This conditional probability distribution $p(\vec{\theta}|D)$, is also called the posterior probability distribution (also referred to as posteriors).

4.2.2 The Likelihood Function

We are interested in finding out the posterior probability distribution $p(\vec{\theta}|D)$. T2K's ND and FD data, together with their MC predictions are compared bin by bin for each sample. The number of events in each of these analysis bins follows a discrete Poisson distribution as a function of the expected number of MC events and the number of data events in that bin.

Exploiting Bayes theorem from Eqn. 4.1, all that we need to obtain the posterior distribution are the prior distributions of the model parameters $\vec{\theta}$ and the likelihood $p(D|\vec{\theta})$. The likelihood $p(D|\vec{\theta})$, which is essentially the product of Poisson distributions of all the analysis bins, can be expressed as:

$$p(D|\vec{\theta}) = \prod_i \frac{(N_i^{MC}(\vec{\theta}))^{N_i^{data}} e^{-N_i^{MC}(\vec{\theta})}}{N_i^{data}!} \tag{4.2}$$

where the i loops over all the analysis bins, $N_i^{MC}(\vec{\theta})$ are the number of MC events and N_i^{data} are the number of data events in the i$^{\text{th}}$ bin. The likelihood is hereafter referred to as $\mathcal{L}(\vec{\theta})$. Neyman-Pearson lemma [65] tells us that the most powerful way to test a hypothesis is to calculate the likelihood ratios between two hypotheses. Here, we take the null hypothesis $\mathcal{L}_0(\vec{\theta_0})$ as a set of parameters that give the same predicted number of events per bin as the number of data events in that bin.

Wilks' theorem [67] states that the distribution of a test statistic $-2\ln\kappa$ asymptotically reaches the $\Delta\chi^2$ distribution when the sample size goes to infinity. Here, κ is the likelihood ratio for a null hypothesis:

$$\Delta\chi^2 = -2\ln(\kappa) = -2\ln\left(\frac{\mathcal{L}(\vec{\theta})}{\mathcal{L}_0(\vec{\theta_0})}\right) \tag{4.3}$$

The term in Eqn. 4.3 only contains information about statistical effects on the number of events and can be written in short as $-2\ln\mathcal{L}_{stat}$. But we will have to take into account prior

knowledge of the systematic parameters which will be discussed concisely in Chapter 5. They are mainly of four types: cross-section parameters, flux parameters of both ND and FD, ND detector systematic parameters and SK detector systematic parameters. Since logarithmic functions are additive, the contribution of these systematic parameters can be added to the $\Delta\chi^2$ as:

$$\Delta\chi^2 = -2\ln\mathcal{L}_{stat} - 2\ln\mathcal{L}_{syst} \tag{4.4}$$

where contributions of systematic parameters, assumed to have Gaussian priors, take the generic form:

$$\sum_{i}^{syst}\sum_{j}^{syst}\Delta\theta_i(V_\theta^{-1})_{i,j}\Delta\theta_j\ . \tag{4.5}$$

Here i and j loop over all the systematic parameters $\vec{\theta}$, and $V_{\vec{\theta}}$ is the fractional covariance matrix that stores the correlations between various systematic parameters. These matrices act as constraints on the systematic parameters. Parameters that we do not have prior knowledge of, are given flat (or uniform) priors. For them, the term in Eqn. 4.5 will be zero, and hence they do not contribute to the $\Delta\chi^2$. Expanding all the families of systematic parameters and statistical terms in Eqn. 4.4, we can write the total log-likelihood used in the ND+FD joint fit as:

$$\begin{aligned}
-2\ln(\mathcal{L}) =& 2\sum_{i}^{ND280\ bins} N_i^{ND,P}(\vec{f},\vec{x},\vec{d}_{ND}) - N_i^{ND,D} + N_i^{ND,D}\ln\left(\frac{N_i^{ND,D}}{N_i^{ND,P}(\vec{f},\vec{x},\vec{d}_{ND})}\right) + \frac{(\beta_i-1)^2}{2\sigma_{\beta_i}^2} \\
&+ 2\sum_{i}^{SK\ bins} N_i^{SK,P}(\vec{f},\vec{x},\vec{d}_{SK},\vec{o}) - N_i^{SK,D} + N_i^{SK,D}\ln\left(\frac{N_i^{SK,D}}{N_i^{SK,P}(\vec{f},\vec{x},\vec{d}_{SK},\vec{o})}\right) \\
&+ \sum_{i}^{fluxpars}\sum_{j}^{fluxpars}\Delta f_i(V_f^{-1})_{i,j}\Delta f_j \\
&+ \sum_{i}^{xsecpars}\sum_{j}^{xsecpars}\Delta x_i(V_x^{-1})_{i,j}\Delta x_j \\
&+ \sum_{i}^{ND280det}\sum_{j}^{ND280det}\Delta d_{ND,i}(V_{d_{ND}}^{-1})_{i,j}\Delta d_{ND,j} \\
&+ \sum_{i}^{SKdet}\sum_{j}^{SKdet}\Delta d_{SK,i}(V_{d_{SK}}^{-1})_{i,j}\Delta d_{SK,j} \\
&+ \sum_{i}^{osc}\sum_{j}^{osc}\Delta o_i(V_o^{-1})_{i,j}\Delta o_j
\end{aligned} \tag{4.6}$$

where labels P and D stand for MC prediction and data respectively, while ND and SK represent ND280 and SK detectors. Oscillation parameters $\vec{o}$ appear as arguments in MC predictions at SK. $\vec{f}$ and $\vec{x}$ are flux and cross-section systematic parameters. The detector parameters are represented by $\vec{d}_{ND}$ and $\vec{d}_{SK}$. It is also important to understand the term $(\beta_i-1)^2)/2\sigma_{\beta_i}^2$. This is called the Barlow-Beeston [68] correction, which accounts for the MC statistical uncertainty at the ND280. β_i is a scaling parameter between the ideal (=true) MC and the generated MC in the i^{th} bin given by $\beta_i = N_{MC,i}^{ideal}/N_i^{MC}$, while the term $\sigma_{\beta_i}^2$ is the error of the parameter β_i.

More emphasis should be put on the oscillation parameters, as those are our parameters of

interest in this thesis. Priors are applied for neutrino oscillation parameters $\sin^2\theta_{12}$ and Δm^2_{21}, and also wherever applicable on $\sin^2\theta_{13}$ too with no correlations between these parameters in the prior. T2K has much lesser sensitivity to these parameters and hence constraints from external measurements are employed. Flat priors are given to δ_{CP}, $\sin^2\theta_{23}$ and Δm^2_{32} as these are the parameters we want to measure from the oscillation analysis. Additionally, equal priors (50% probability for each) are assigned to normal and inverted mass hierarchies, that are encoded as the sign of Δm^2_{32}.

4.2.3 Markov Chain Monte Carlo (MCMC)

The $\mathcal{L}$ presented in Eqn. 4.6 has a large dimensionality (over 800 parameters) and finding its minimum can be computationally expensive. To mitigate this, we make use of the MCMC algorithm. A Markov chain [69] is a stochastic process that helps us hover through the parameter space, where the probability of taking the next step[2] only depends on the current step, a property called "memorylessness" of the Markov chain. If the Markov chain is on step $\vec{\theta}_k$, the "transition" probability of going to the state $\vec{\theta}_{k+1}$ is given by

$$p(\vec{\theta}_{k+1}|\vec{\theta}_k, \vec{\theta}_{k-1}, ..., \vec{\theta}_0) = p(\vec{\theta}_{k+1}|\vec{\theta}_k). \tag{4.7}$$

As the Markov Chain takes more and more of these steps, a point is reached when the transition probability of going to any state becomes constant in time. This is when the chain is said to have converged to a stationary state. The stationary state can be interpreted as a region of parameter phase space close to the minimum $\Delta\chi^2$.

In the coming parts, we will discuss the mathematical formulation of the MCMC convergence process.

The essential point to understand here is that when the Markov chain has converged to a stationary state, the probability distribution of the stationary state will represent the posterior probability distribution, which is what we need to estimate. Speaking in the language of model parameters, the transition probability $p(\vec{\theta}'|\vec{\theta})$ of taking a step to $\vec{\theta}'$ given that the current step is at $\vec{\theta}$ can be written as a product of a proposal function $g(\vec{\theta}'|\vec{\theta})$ and the acceptance probability $A(\vec{\theta}', \vec{\theta})$:

$$p(\vec{\theta}'|\vec{\theta}) = g(\vec{\theta}'|\vec{\theta})A(\vec{\theta}', \vec{\theta}) \tag{4.8}$$

The acceptance probability $A(\vec{\theta}', \vec{\theta})$ is the probability of accepting a new state. From the principle of Detailed Balance, we can exploit the reversible nature of Markov chains in a stationary state to relate the transition probability between two steps $\vec{\theta}$ and $\vec{\theta}'$ to the posterior probability distributions as follows:

$$p(\vec{\theta}|D)p(\vec{\theta}'|\vec{\theta}) = p(\vec{\theta}'|D)p(\vec{\theta}|\vec{\theta}') \tag{4.9}$$

After substituting the Eqn. 4.8 into 4.9, one gets:

$$p(\vec{\theta}|D)g(\vec{\theta}'|\vec{\theta})A(\vec{\theta}', \vec{\theta}) = p(\vec{\theta}'|D)g(\vec{\theta}|\vec{\theta}')A(\vec{\theta}, \vec{\theta}') \tag{4.10}$$

which upon rearrangement gives the MCMC equation,

$$\frac{A(\vec{\theta}', \vec{\theta})}{A(\vec{\theta}, \vec{\theta}')} = \frac{p(\vec{\theta}'|D)g(\vec{\theta}|\vec{\theta}')}{p(\vec{\theta}|D)g(\vec{\theta}'|\vec{\theta})} \tag{4.11}$$

[2]Step here essentially means a set of values for the parameters ($\vec{\theta}$), and by changing step we are changing these parameter values.

The proposal function $g(\vec{\theta}|\vec{\theta}')$ can take any form, although the most commonly used are Gaussian or flat distributions. The step $\vec{\theta}$ can be related to $\vec{\theta}$ as $\vec{\theta}' = \vec{\theta} + rand_{proposal}(\vec{\theta})$. In MaCh3, $rand_{proposal}(\vec{\theta})$ is defined as the function that draws random numbers for each $\vec{\theta}$ from a Gaussian distribution with mean 0 and standard deviation as prior errors of the model parameters.

With the proposed step in hand, the acceptance probability then decides whether to take that step or not depending on the value of the likelihood ratios between the current and proposed steps. If a step is accepted, the state $\vec{\theta}$ contributes to the posterior probability distribution. In literature, there are multiple ways one can construct the acceptance probability. One of the most commonly used algorithms, which MaCh3 also incorporates is the Metropolis-Hastings [70] algorithm where the acceptance probability can be written as:

$$A(\vec{\theta}', \vec{\theta}) = min\left(1, \frac{p(\vec{\theta}'|D)g(\vec{\theta}|\vec{\theta}')}{p(\vec{\theta}|D)g(\vec{\theta}'|\vec{\theta})}\right) \tag{4.12}$$

which can be expanded using Bayes theorem 4.1 as

$$A(\vec{\theta}', \vec{\theta}) = min\left(1, \frac{p(D|\vec{\theta}')p(\vec{\theta}')g(\vec{\theta}|\vec{\theta}')}{p(D|\vec{\theta})p(\vec{\theta}')g(\vec{\theta}'|\vec{\theta})}\right) \tag{4.13}$$

where we can identify $p(D|\vec{\theta})$ as the likelihood $\mathcal{L}(\vec{\theta})$. The Detailed Balance principle 4.9 helps cancel the proposal functions and priors on the numerator and denominator, leaving us with,

$$A(\vec{\theta}', \vec{\theta}) = min\left(1, \frac{\mathcal{L}(\vec{\theta}')}{\mathcal{L}(\vec{\theta})}\right). \tag{4.14}$$

As it is easier to work with logarithms of likelihoods, we can rewrite Eqn 4.14 as

$$A(\vec{\theta}', \vec{\theta}) = min\left(1, e^{\ln \mathcal{L}(\vec{\theta}') - \ln \mathcal{L}(\vec{\theta})}\right). \tag{4.15}$$

The following ways are how the MCMC proceeds from here:

- If the proposed step has a higher likelihood, the acceptance probability will be equal to 1 and the step will be accepted.
- If the likelihood of the proposed step is smaller than the current step, we draw a random number x from a uniform distribution $0 \leq x \leq 1$. Now, two things are possible:
  1. If $A(\vec{\theta}', \vec{\theta}) > x$, we accept the step.
  2. If $A(\vec{\theta}', \vec{\theta}) < x$, we reject the proposed step $\vec{\theta}'$, and propose a new step.
  3. If the chain remains in the same state $\vec{\theta}$, that state contributes to the posterior probability distribution.

This is summarised well in the Fig. 4.1

The fact that we also allow for states of lower $\mathcal{L}$ to be accepted enables the MCMC to sufficiently explore a diverse parameter space instead of just heading towards the maximum $\mathcal{L}$ regions.

The proposed step $\vec{\theta}'$ can take into account correlations between various model parameters by performing correlated throws instead of randomly drawing values of the parameters. This is done using the Cholesky decomposition of the covariance matrix, where the function

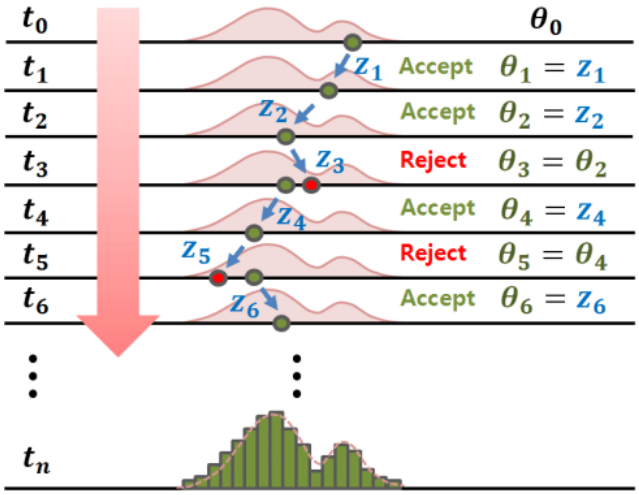

FIGURE 4.1: An illustration of how the MCMC algorithm works. Steps θ_i that are accepted contribute to the posterior distribution, eventually sampling the underlying distribution (peach coloured in the figure) quite well. Source: [71].

$rand_{proposal}(\vec{\theta})$ gets multiplied with the Cholesky matrix. This makes it possible for an increased acceptance rate of steps, which further makes convergence to a stationary state faster. The correlated throws further increase the "directionality" of the random walk in MCMC.

One can notice that the Markov chain approaches convergence when the log-likelihood ratios between the current and proposed steps become approximately constant after a certain accumulation of steps.

4.3 Fitter Diagnostics

Multiple tests are necessary before the interpretation of results from an MCMC analysis can be performed. Some of these tests are performed before running the MCMC. For instance, log-likelihood scans and Asimov fits[3] portray the impact of changes in the analysis on the oscillation parameters. Looking at predictive spectra can give insights into how systematic parameters affect the MC predictions. Some tests are performed on the Markov chains themselves which tell whether they have reached a stationary state or whether several Markov chains can be merged together. All of these will be discussed in the upcoming sections.

MaCh3 can perform both ND-only, FD-only and ND+FD joint fits. The Author performed the ND+FD joint fit and hence that will be discussed in detail, while a better description of ND fit can be found in [73]. However, ND-only fits are very useful for validations before performing the joint fit. This also helps estimate the sensitivity of both ND and FD samples to various systematic parameters. In the next section, one such study is discussed where an ND-only fit is used to predict FD sample spectra.

4.3.1 Far Detector Predictive Spectra

It is important to portray the impact of the ND fit on T2K's systematic parameters before performing the FD fit. Since we use a parametrized model of our systematics most of which can be constrained by ND280, we can see what the ND fit does to them, and how they help reduce the systematic uncertainties at the FD.

[3]The name Asimov appears here inspired by the short story Franchise, by Isaac Asimov [72] where instead of all the voters attending an election, a single voter most representative of the crowd was chosen.

Prior and posterior predictive distributions are useful to visualise how Bayesian analyses can help update the knowledge of model parameters after the fit. In the context of this thesis, these distributions are shown as the spread of an observable of interest H, owing to how loosely or tightly various systematic parameters were constrained.

Generating a new MC for different values of model parameters $\vec{\theta}$ is an extremely time and resource-consuming task. Instead, a reweighting approach is used, where a new MC is effectively created by applying a weight to the events of nominal MC that are representative of the differences between nominal and new values of $\vec{\theta}$. This reweighted MC is called a toy MC, and the term will be used extensively in the following sections.

To generate a prior predictive distribution of H, random throws are made from the ND flux and cross-section covariance matrix. The values of systematic parameters obtained from each throw is then used to reweight the FD MC. For n such throws, we get a variation of events per bin of the parameter H. This is formulated as:

$$p(H) = \int_{\vec{\theta}} p(H|\vec{\theta}) p(\vec{\theta}) d\vec{\theta}. \tag{4.16}$$

To see how the ND fit improves our knowledge of the flux and cross-section parameters, and constrains them, we now look at the posterior predictive distributions. To make these, a Markov Chain from the ND fit is used, and throws are made directly from the posterior distributions of $\vec{\theta}$, $p(\vec{\theta}|H)$. The posterior predictive distribution of an observable $p(H'|H)$ can be expressed as:

$$p(H'|H) = \int_{\vec{\theta}} p(H'|\vec{\theta}) p(\vec{\theta}|H) d\vec{\theta}. \tag{4.17}$$

One can immediately notice that this equation, although similar to Eqn. 4.16, has the difference that the "prior" knowledge of parameters $\vec{\theta}$ is now replaced by the "updated" knowledge of them from the MCMC.

Fig. 4.2 shows the reconstructed neutrino energy spectra with 1σ error bands constructed from the variation of number of events per bin caused by the systematic uncertainties for the expanded ν_e CC1π^+ sample. The plot shows the impact of systematic errors in each bin before the ND fit (Pre-ND), and after the ND fit (Post-ND). The impact of ND280 in reducing systematic errors at SK is strikingly evident. The ND fit not only reduces systematic errors but also alters the shape of the spectrum at SK.

4.3.2 Log-Likelihood Scans

As discussed in 1.4, T2K's δ_{CP} sensitivity comes mainly from the ν_e appearance samples. While the most dominant contributor to this sensitivity has been the FHC 1Re sample owing to its larger statistics, both FHC single-ring ν_e CC1π^+ and RHC 1Re samples have also contributed significantly over the years. The new multi-ring sample, combined with the single-ring ν_e CC1π^+ sample adds more FHC ν_e appearance statistics.

One of the tests that can be done to see how a change in the analysis can impact the sensitivity to the oscillation parameters is to look at the log-likelihood (LLH) scans. In this case, we are interested in seeing the impact of adding the multi-ring ν_e CC1π^+ sample on the oscillation parameters. To perform an LLH scan, we fix an MC with values of all the systematic parameters set to their prior values, and oscillation parameters set to a value of choice, say the best fit from the previous oscillation analyses. Let's call it the Asimov MC. We then generate toy MCs by varying the oscillation parameters and for each of these toys, we calculate the LLH between the toy MCs and the Asimov MC, where the Asimov MC (which is fixed) takes up the role of data.

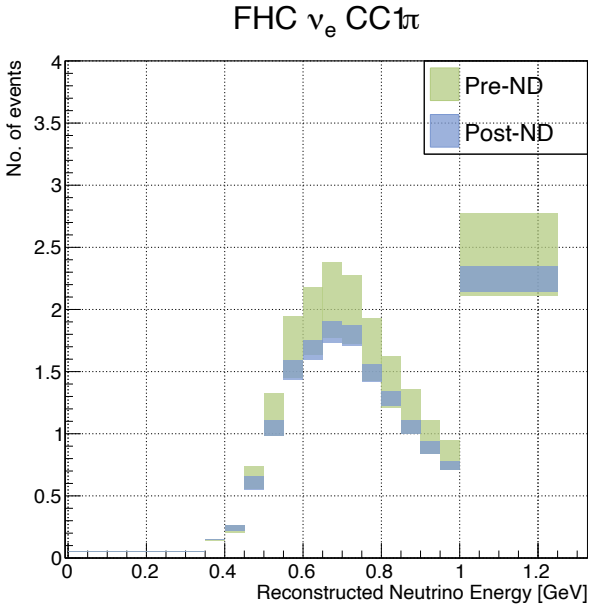

FIGURE 4.2: Reconstructed neutrino energy spectra for the expanded ν_e CC1π^+ sample showing the systematic errors before the ND fit (Pre-ND) and after the ND fit (Post-ND).

Whether the new analysis improves or worsens the sensitivity to oscillation parameters can be inferred from the change in the LLH distribution between the two analyses. In the case of adding the multi-ring ν_e CC1π^+ sample onto the existing single-ring sample, minute improvements can be seen in the appearance parameters θ_{13} and δ_{CP} . Fig. 4.3 shows the impact of all the SK samples on the LLH for each oscillation parameter, while Figure 4.4 shows the contribution coming only from the expanded ν_e CC1π^+ sample. In the latter, the impact of adding the multi-ring ν_e CC1π^+ is more profound. The reason why this sample also impacts the disappearance parameters[4] is due to the presence of background events (see Fig. 3.12) that receive improper treatment of reconstructed energy, but since the overall impact of the expanded ν_e CC1π^+ on the total LLH is small, this will not be an issue.

4.3.3 Autocorrelation and Trace Plots

It's important to keep track of whether the MCMC is exploring the phase space of parameters effectively, and converging to the stationary state after the accumulation of a certain number of steps. Apart from not accumulating enough steps, there are usually two issues a Markov chain can face: the first one is when we use the starting values of parameters that are far away from their true values. This then sets the chain to explore a region of low probability, making convergence slower. The second issue is when the proposed steps are highly correlated to each other, reducing the random exploration of the phase space, and hence missing out on reaching regions of low $\Delta\chi^2$. We can use both trace plots and autocorrelation plots as diagnostic tools to see the chain performances.

Not only are they useful for testing the performances of individual chains, but they can also be used to compare the performances of multiple chains together. This is very important because many times, multiple Markov chains are run in parallel[5], and are combined later.

[4] This will be further discussed in Chapter 7.

[5] We usually need tens of millions of Markov chain steps for exploring the entire parameter space and obtaining smooth posterior distributions. However, each step takes around ~0.15s. Thus we run several hundred chains in parallel and combine them later. In addition, we use GPU acceleration to reduce step time.

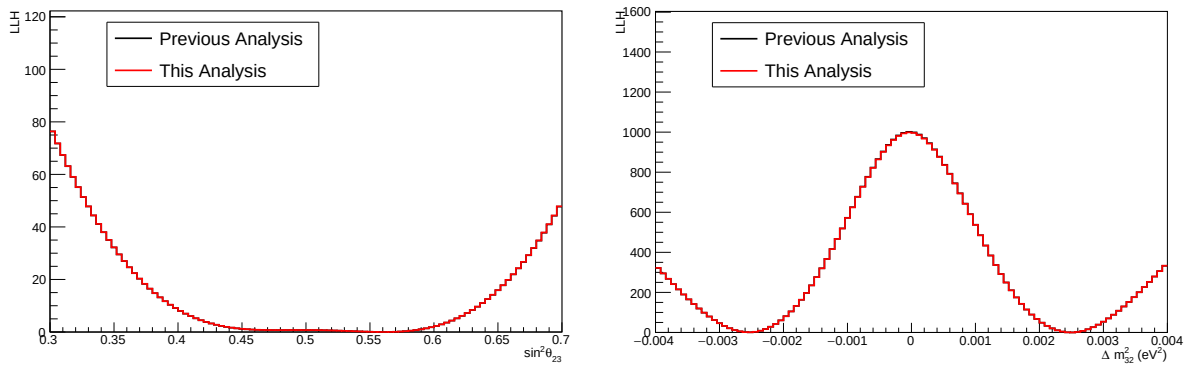

(A) $\sin^2\theta_{23}$ (B) Δm^2_{32}

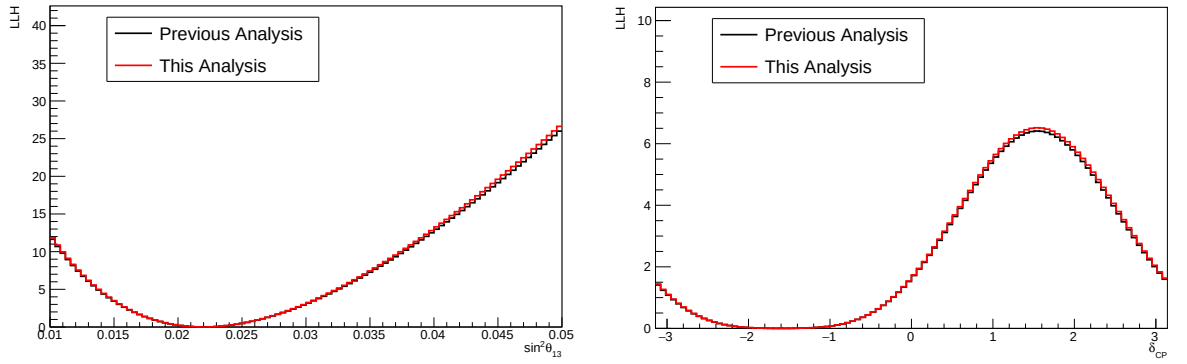

(C) $\sin^2\theta_{13}$ (D) δ_{CP}

FIGURE 4.3: Comparison between LLH scans of T2K's previous analysis (black histogram) with only single-ν_e CC1π^+ sample and this analysis (red histogram) with the addition of the multi-ring ν_e CC1π^+ sample as a function of oscillation parameters. The LLH here is the total LLH from all 6 SK samples. The addition of multi-ring ν_e CC1π^+ adds some sensitivity to the tail region of θ_{13} and the peak region of δ_{CP} .

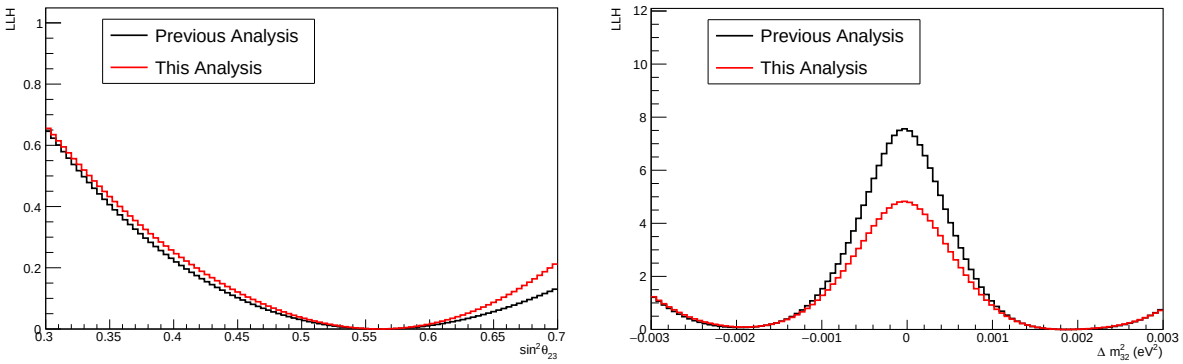

(A) $\sin^2\theta_{23}$ (B) Δm^2_{32}

(C) $\sin^2\theta_{13}$ (D) δ_{CP}

FIGURE 4.4: Comparison between LLH scans of single-ring ν_e CC1π^+ sample alone (previous analysis) and that of the expanded ν_e CC1π^+ sample (this analysis) as functions of oscillation parameters. The addition of multi-ring ν_e CC1π^+ impacts all the oscillation parameters, although it is understood that the disappearance parameters are affected due to the presence of relatively higher background events in the new sample.

For two Markov chains to be combined, they should all converge to the same stationary state. This can be also tested by looking at the trace and autocorrelation plots.

A trace plot visualizes a particular parameter's value at each step of the Markov Chain. When the chain approaches convergence, this value will tend to fluctuate around a central value. If multiple chains are being compared, they should all look similar eventually. This is shown in Fig. 4.5a, where the compatibility of four chains is tested for the M_A^{RES} parameter (axial mass for the RES interaction).

The autocorrelation plots tell us how correlated are two steps $\vec{\theta}$ and $\vec{\theta}'$ located n steps apart in the chain. To study the chain autocorrelation, a parameter called $Lag(n)$ is introduced which is defined as $Lag(n) = corr(\vec{\theta}_i, \vec{\theta}_{i-n})$, where i is the maximum considered distance.[6] The degree of randomness of the steps explored can be determined from $Lag(n)$, where it should fall to a low value after a certain number of steps. The autocorrelations for the M_A^{RES} parameter for four different chains are shown in Fig. 4.5, where they all fall below 0.2 after ∼15,000 steps.

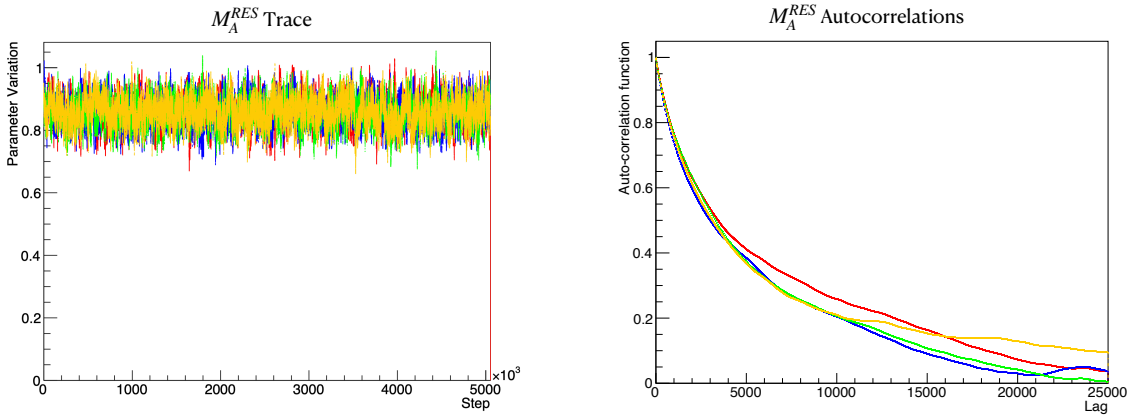

(A) Trace Plot (B) Autocorrelation plot

FIGURE 4.5: Trace (left) and autocorrelation (right) distributions of the M_A^{RES} parameters for four different chains marked with different colours. It can be seen that the fluctuations in the trace plot are very similar to each other for the four chains. The autocorrelation also falls and stabilises for all of these chains.

As discussed before, the probability distribution of a stationary state is what represents the posterior probability distribution. Hence we discard the initial steps of a chain when it is still in the process of stabilisation. The steps that have a stable trace (or post-burn-in steps) are what gets used in the oscillation analysis.

4.3.4 $\hat{R}$ Test

Whether independent Markov chains converged to the same stationary state can be qualitatively tested by performing the $\hat{R}$ test (also called Gelman-Rubin test) [74, 75]. This is a convergence diagnostic, performed on at least four chains at a time. According to this test, the $\hat{R}$ values are computed to check the similarity of each parameter's posteriors between the four chains. The estimator $\hat{R}$ should be less than 1.05 for all the parameters, failure to which would indicate the chains are incompatible and cannot be combined. The Fig. 4.6 shows $\hat{R}$ test done on 4 Markov chains run in parallel. There were two tests done, with procedures

[6] i in the Fig. 4.5b was taken as 25,000. The computation time of $Lag(n)$ significantly goes up with increasing i. i =25,000 was chosen since it proved to give satisfactory results.

laid out in [74] (marked Gelman 2013) and in [75] (marked Gelman 2021) which is an updated version of the former. It can be seen that both the tests show a value of $\hat{R} < 1.05$, meaning the four chains indeed converged to the same state and their steps can be combined.

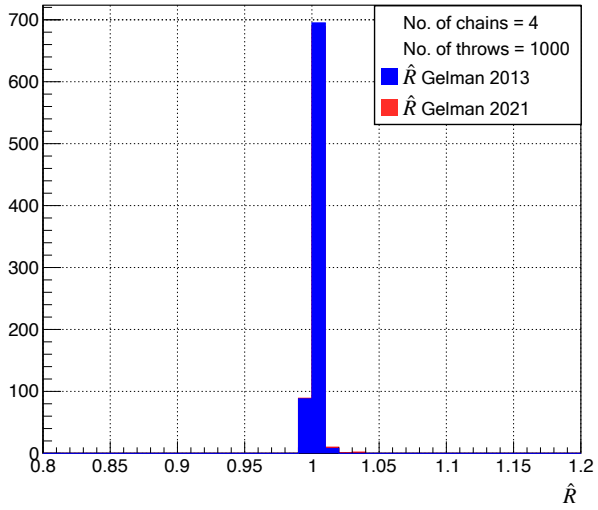

FIGURE 4.6: The $\hat{R}$ test performed on four different Markov chains. Since $\hat{R} < 1.05$, these chains can be combined. Each entry in the histogram corresponds to the $\hat{R}$ calculated for each of the ∼800 parameters.

4.3.5 Posterior Probability Distributions

The output of an MCMC that converged is a set of posterior probability distributions. This output is essentially an N-dimensional probability distribution (where N∼800) and we need to integrate all the nuisance parameters to obtain the "marginalized" posterior distribution of the parameter of interest, i.e., the oscillation parameters.

The posterior probabilities of oscillation parameters can be shown in one dimension or as a contour between two oscillation parameters. The contours are usually shown in the δ_{CP}–$\sin^2\theta_{13}$ (appearance parameter) space and in Δm^2_{32}–$\sin^2\theta_{23}$ (disappearance parameter) space. The highest posterior density (HPD) value of individual parameters is taken from these two-dimensional contours, while the credible intervals are constructed from the one-dimensional posterior distributions of these parameters (see Fig. 4.7).

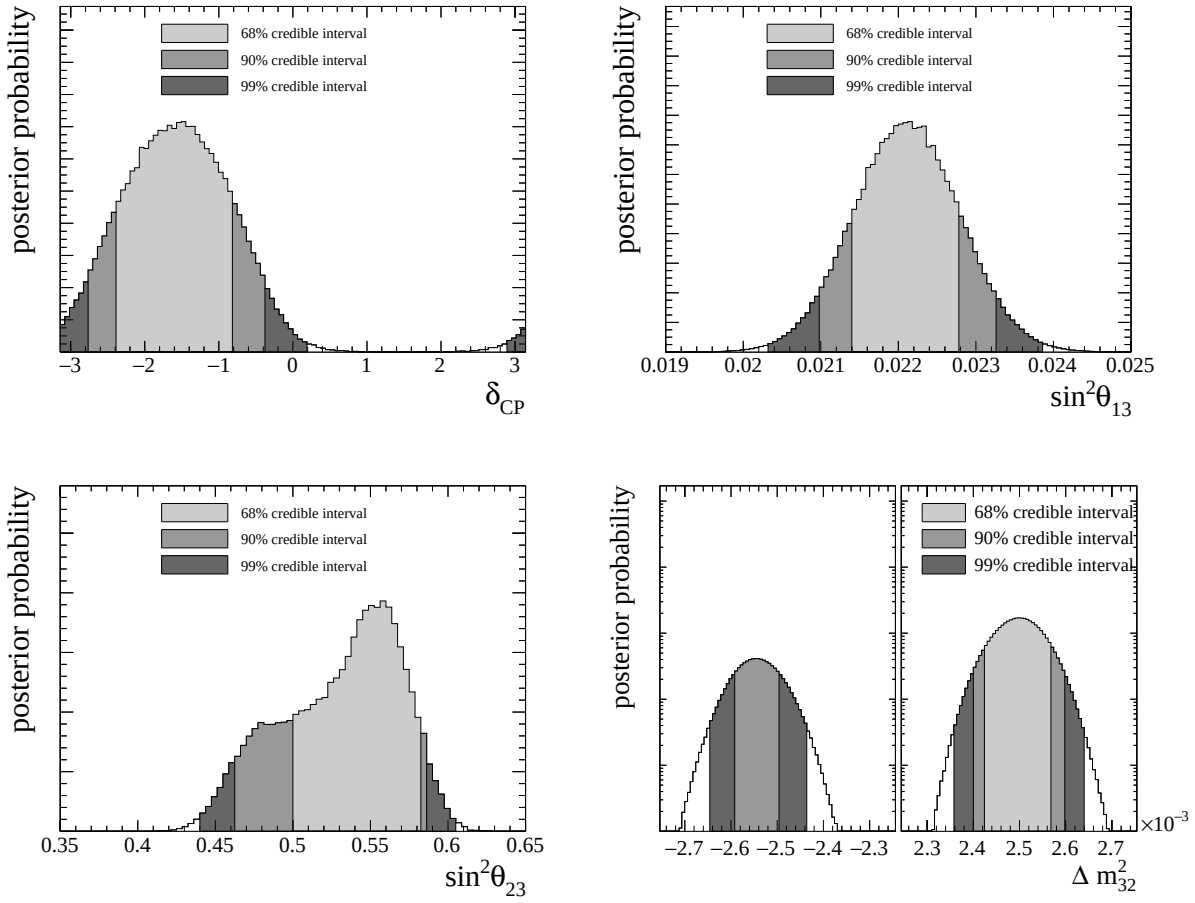

FIGURE 4.7: Posterior probability distribution of the oscillation parameters from an Asimov fit. The 68%, 90% and 99% credible intervals are also marked in each plots.

5

Systematic Uncertainties

> Progress in science is often built on wrong theories that are later corrected. It is better to be wrong than to be vague
>
> Freeman John Dyson

In particle physics experiments, and any scientific measurements for that matter, accurate estimation of both statistical and systematic uncertainties is crucial to ensure the validity of the result. While statistical uncertainties decrease with increasing data accumulation, systematic uncertainties present a significant challenge due to their diverse origins, difficulty in quantification, and often dependence on external models. The previous chapter introduced four key systematic parameter families impacting our measurement: flux, cross-section, ND280, and SK detector systematics. Building upon this framework, this chapter provides a concise review of each family, with a particular focus on the detailed estimation of SK detector systematic uncertainties, to which the author significantly contributed. The methodology employed and the main results obtained for estimating these uncertainties are discussed in detail.

5.1 Flux Systematic Model

The neutrino beam is the most crucial component in T2K's experimental setup, and a lot of factors such as the proton beam characteristics, horn current and magnetic field, horn's alignment to the graphite target, POT, and most importantly, the hadronic interactions that happen when the protons impinge the target dictates its production. The hadronic interaction modelling is one of the most dominant sources of uncertainties in T2K's flux prediction. Fig. 5.1 shows the total flux errors at the FD as a function of neutrino energy along with the systematic factors contributing to them.

The NA61/SHINE experiment [76] performs hadron production measurements on T2K's replica target. T2K uses this external data to reduce its flux uncertainties. Improvements in NA61/SHINE's latest results [77] from the replica target measurements (solid black histogram in the plots labelled as `21bv2`) compared to its previous result [78] (dashed black histogram labelled as `13av7.1`) lead to a reduction of flux error from 8% to 5%.

The flux uncertainties are parameterized for each neutrino flavour ($\nu_\mu, \overline{\nu}_\mu, \nu_e, \overline{\nu}_e$), for each beam mode (FHC, RHC) and for ND280 and SK detectors separately. These are further broken down to various true neutrino energy (E_ν^{true}) bins. There are a total of 50 flux parameters each

for ND280 and SK, and they act as normalisations for each E_ν^{true} bins. A detailed table of flux parameter binning is provided in B.2.

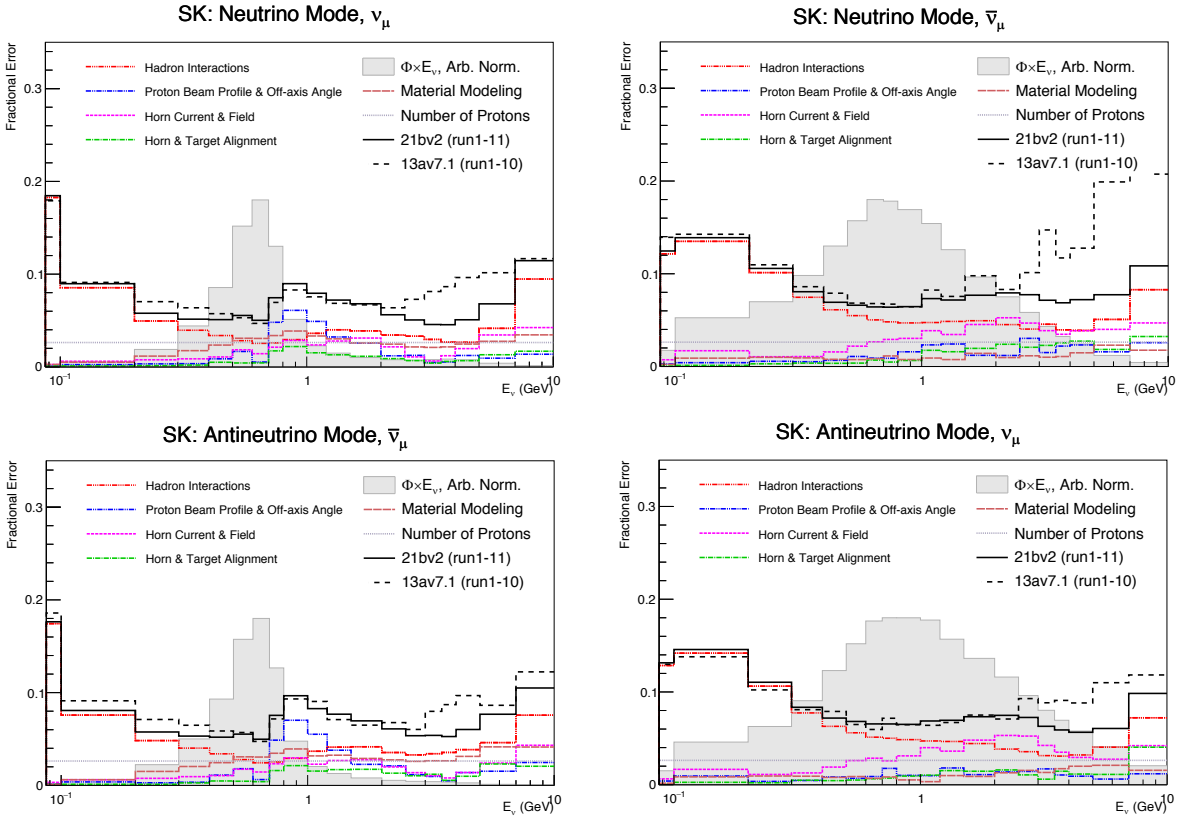

FIGURE 5.1: The total flux uncertainties broken down by its sources at the SK. The black solid histogram represents the total flux uncertainty with the latest NA61/SHINE tune, while the black dashed histogram represents that of the previous tune. The grey histogram shows the unoscillated $\nu_\mu/\overline{\nu}_\mu$ flux at SK.

5.2 Cross-Section Systematic Model

The oscillation analysis presented in this thesis depends on 75 cross-section parameters that describe different models which govern different neutrino interactions. They can either act as normalizations which increase or decrease the cross-section for a particular process or neutrino flavour while keeping the shape of kinematic distributions constant, or they can act as shape parameters which can alter the kinematic distributions but keep the overall cross-section constant.

These parameters can be grouped into interactions that contribute most dominantly to the signal events, and as the most important backgrounds to these events, along with other types of processes. Therefore, the following cross-section parameter groups exist:

- CCQE: The most dominant neutrino interaction channel (see Table 5.1),
- SPP: Second-most dominant neutrino interaction channel (see Table 5.2),
- 2p2h: Dominant background to CCQE processes (see Table 5.3),
- Multi-π, DIS: Dominant backgrounds to SPP processes (see Table 5.4),

- FSI: Impacts the final state topology of an event (see Table 5.5),
- Other: Lesser important interaction channels and effects (see Table 5.6).

The high statistics muon (anti)neutrino events at ND280 help constrain almost all of the cross-section parameters, except for a few. Those parameters are fixed in ND-only fits but allowed to vary in the ND+FD fits where they can be constrained. Incidentally, some parameters do not have any measurements performed or predictions from a model. They are assigned a flat prior, while every other measured/known parameter gets assigned a Gaussian prior distribution. All the cross-section parameters used in the analysis are accessible (or can be simulated) in the NEUT generator. In the case where some parameter is not implemented in NEUT, templates are generated from other generators (for instance: NuWro [79]), and can help alter the distributions produced in NEUT to emulate the parameter variations.

5.2.1 CCQE

The so-called "golden channel" of T2K contributes the highest statistics of events to T2K's oscillation analysis. Therefore naturally, this interaction channel is provided with the most model freedom. The CCQE axial mass M_A^{QE}, as described in Eqn. 1.17 is the most important CCQE cross-section parameter. It is also supported by three different normalisation factors High Q^2 Norm 1,2,3 for different Q^2 regions because the axial form factor parameterization is unable to describe sufficiently the current data for $Q^2 > 0.25\text{GeV}^2$.

The initial nucleon state in CCQE interactions is described by the Spectral Function (SF) model in NEUT. The SF model can be divided into mean field (MF) and short-range correlations (SRC) regions. As portrayed in Table 5.1, there are five normalisation parameters each for a particular nuclear shell and for ^{12}C and ^{16}O respectively for the MF region and one SRC normalisation parameter each for ^{12}C and ^{16}O. Additionally, five shape parameters affect the p_{miss} distributions for each shell and each nucleus, where p_{miss} is the initial state nucleon momentum arising from the nucleon's Fermi motion. These parameters have a negligible impact in the ND280-only analysis and are varied only in the ND280+FD analysis. A detailed description of these parameters can be found in [80].

To account for the Pauli blocking effects four parameters, one each for ^{12}C and ^{16}O for ν and $\overline{\nu}$ are used. The values of these parameters are directly proportional to that of the Fermi surface (± 1 unit change in these parameters leads to ± 30 MeV shift in the Fermi surface). This can result in the rejection of events upon the rise of the Fermi surface or vice versa.

To account for the FSI of leptons in SF formalism, the "Optical potential" parameter is included for both the carbon and oxygen nuclei as described in [81].

Proper consideration of the binding energy (E_b) is another essential factor in the oscillation analysis because failure to it can bias the FD samples' neutrino energy reconstruction. A correction to the binding energy is applied through

$$\Delta E_{\nu,T} = \delta_{\nu,T} + \alpha(a|\vec{q_3}| + b) \tag{5.1}$$

where $\delta_{\nu,T}$ are the binding energy parameters that depend on the type of neutrino ($\nu/\overline{\nu}$) and the nuclear target (^{12}C/^{16}O), α is a correction factor that can vary between 0 to 1. a and b are coefficients derived from a fit to external data [82]. It can be seen that this correction is dependent on momentum transfer $|\vec{q_3}|$. A higher $\Delta E_{\nu,T}$ means the lepton momentum p is reduced.

Parameter	Pre-fit value	Type	Description
M_A^{QE}	1.03 ± 0.06	Shape	CCQE axial mass
High Q^2 norm 1	1 ± 0.11	Norm	$0.25 < Q^2 < 0.5$
High Q^2 norm 2	1 ± 0.18	Norm	$0.5 < Q^2 < 1.0$
High Q^2 norm 3	1 ± 0.40	Norm	$Q^2 > 1.0$
S-Shell MF Norm ^{12}C	0 ± 0.45	Norm	
P-Shell MF Norm ^{12}C	0 ± 0.2	Norm	
S-Shell MF Norm ^{16}O	0 ± 0.75	Norm	
$P_{1/2}$-Shell MF Norm ^{16}O	0 ± 0.2	Norm	
$P_{3/2}$-Shell MF Norm ^{16}O	0 ± 0.45	Norm	
SRC norm ^{12}C	1 ± 2	Norm	
SRC norm ^{16}O	1 ± 2	Norm	
S-shell MF p_{miss} Shape ^{12}C	0 ± 1	Shape	Fixed at ND
P-shell MF p_{miss} Shape ^{12}C	0 ± 1	Shape	Fixed at ND
S-shell MF p_{miss} Shape ^{16}O	0 ± 1	Shape	Fixed at ND
$P_{1/2}$-shell MF p_{miss} Shape ^{16}O	0 ± 1	Shape	Fixed at ND
$P_{3/2}$-shell MF p_{miss} Shape ^{16}O	0 ± 1	Shape	Fixed at ND
Pauli blocking ^{12}C ν	0 ± 1	Shape	
Pauli blocking ^{12}C $\overline{\nu}$	0 ± 1	Shape	
Pauli blocking ^{16}O ν	0 ± 1	Shape	
Pauli blocking ^{16}O $\overline{\nu}$	0 ± 1	Shape	
Optical potential ^{12}C ν	0 ± 1	Shape	Flat prior
Optical potential ^{16}O ν	0 ± 1	Shape	Flat prior
CCQE E_b ^{12}C ν	2 ± 6	Shape	
CCQE E_b ^{12}C $\overline{\nu}$	0 ± 6	Shape	
CCQE E_b ^{16}O ν	4 ± 6	Shape	
CCQE E_b ^{12}C $\overline{\nu}$	0 ± 6	Shape	
α correction (q_3)	0 ± 1	Shape	Flat prior

TABLE 5.1: CCQE cross-section parameters used in the analysis along with their pre-fit value and descriptions.

5.2.2 SPP

SPPs are the second most dominant neutrino interactions and the most important one in the context of this thesis. At the FD, two samples are based on this channel: the ν_e CC1π^+ and ν_μ CC1π^+ samples. The M_A^{RES} parameter is the axial mass for the resonant parameter, and C_A^5 is the normalisation factor, both appearing in the RES form factor equation 1.21.

The SPP channel also contains isoscalar non-RES background events that require additional control. This is facilitated by two parameters Non-RES $I_{1/2}$ Low p_π and Non-RES $I_{1/2}$. The former targets all $\overline{\nu}$ SPP events with low pion momentum $p_\pi < 200$ MeV and is not constrained by the ND, while the latter covers all the other cases. Although not modelled in NEUT, isoscalar non-RES interactions can also happen through the $I_{3/2}$ channel. While there is ongoing work on adding the $I_{3/2}$ channel [83], it is hinted from bubble-chamber data that the contribution of this channel is small [84, 85]. Calculation of outgoing hadron kinematics and the four-momentum sharing between the π and N' in the $N* \rightarrow \pi N'$ can be done through three ways laid out by the Rein-Sehgal model [86]. The first method adopts a very simplistic isotropic ejection of the *pi* and N' back-to-back in the rest frame of the resonance $N*$. The second method uses a more sophisticated calculation of matrix elements for the $N \rightarrow \Delta$, where N is the initial nucleon and Δ is $\Delta(1232)$, with contributions from other resonances assumed to be minimal. This is very accurate for T2K's energies and hence proves

to be a much more realistic method compared to the first method. The third method is an expansion of the second, where nearby resonances of $\Delta(1232)$ are also utilised to calculate the combined matrix elements. The RS Δ Decay parameter facilitates the switching between these three models, and its impact on cross-section as a function of π and N momentum can be seen in the Fig. 5.2.

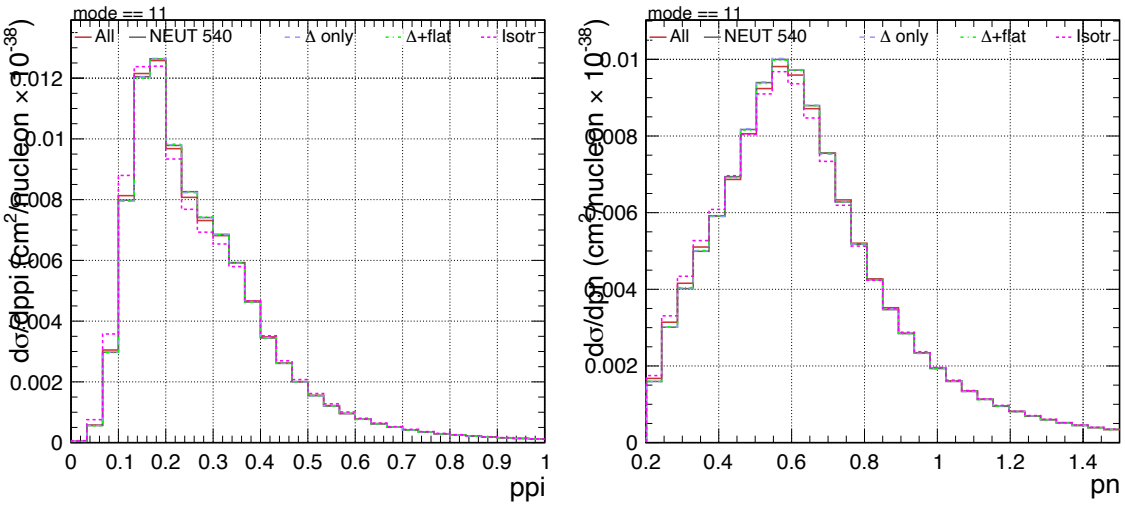

FIGURE 5.2: The impact of RS Δ Decay model on the cross-section for a hydrocarbon target without nuclear effects. Cross-section as a function of π (left) and neutron (right) momenta are shown. The colours represent different models. Source: [87].

Furthermore, the RES decays can also be of the type $N* \rightarrow \pi^0 N$, followed by $\pi^0 \rightarrow \gamma\gamma$ decays. Normalisation parameters for this process are provided for both ν_μ and $\overline{\nu}_\mu$.

Finally, four binding energy parameters are also employed for the RES channel. NEUT does not possess the freedom to vary the initial nuclear state and binding energy E_b for RES interactions, which is why the NuWro generator is used to study these nuclear effects. For a higher value of E_b, the lepton system needs to transfer more energy to the hadronic system for a kinematically allowed interaction to take place. Thus, for a fixed neutrino energy, the average energy transfer q_0 gets larger, resulting in a leftward shifted Q^2, as shown in Fig. 5.3. This is a use-case of NuWro templates as explained at the beginning of this section, which allows modifying NEUT-generated distributions to simulate the effects of E_b. For this analysis, the RES E_b prior values are set as 25 MeV, same as that in CCQE, but with a large conservative 1σ error of 25 MeV to cover 0 MeV (equal to no binding energy).

All the SPP model parameters are summarised in Table 5.2.

5.2.3 2p2h

Two normalisation parameters, one each for ν and $\overline{\nu}$ are used for 2p2h interactions, along with another parameter for ^{12}C to ^{16}O normalisation. To provide freedom of total pn versus nn pairs, the PNNN shape parameter is used to change the ratio between these two pairs.

In addition, shape parameters that control the Valencia model [88] for 2p2h interactions are used. There is one parameter of this type for each nuclear target ^{12}C to ^{16}O, and for each nn and pn pair. These parameters change the event ratio between two regions of the $|\vec{q}_3| - q_0$ kinematic phase space, where q_0 is the energy transferred to the hadronic system.

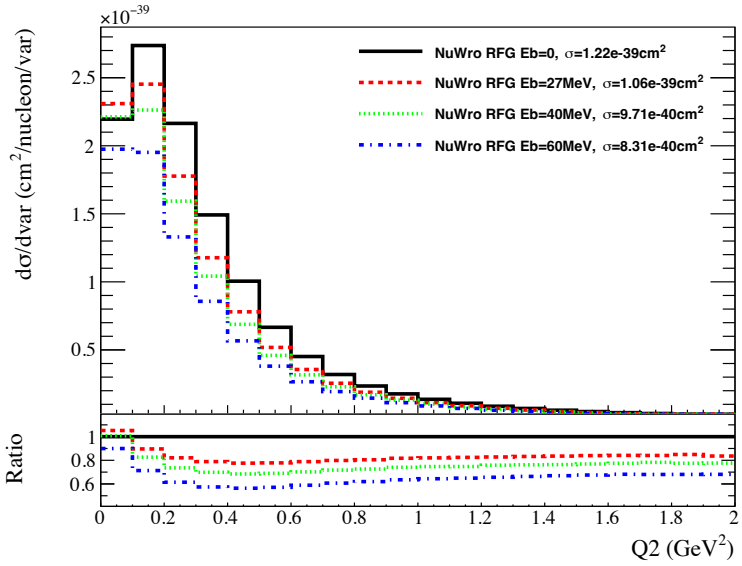

FIGURE 5.3: ND280 flux-integrated differential cross-section for $\nu_\mu + p \rightarrow \mu^- + \pi^+ + p$ interaction on carbon as a function of Q^2 for a few variations of E_b. The ratio plot at the bottom shows the relative ratio of these cross-sections to that of the $E_b = 0$ case. Source: [87]

Parameter	Pre-fit value	Type	Description
C_A^5	1.06 ± 0.1	Shape	RES Form factor norm.
M_A^{RES}	0.91 ± 0.1	Shape	Axial mass for RES
Non-RES $I_{1/2}$	1.21 ± 0.27	Shape	
Non-RES $I_{1/2}$ Low p_π	1.3 ± 1.3	Shape	Fixed at ND
RS Δ Decay	1 ± 1	Shape	Flat prior
SPP π^0 norm ν_μ	1 ± 0.3	Norm	
SPP π^0 norm $\overline{\nu}_\mu$	1 ± 0.3	Norm	
RES E_b ^{12}C ν	25 ± 25	Shape	
RES E_b ^{12}C $\overline{\nu}$	25 ± 25	Shape	
RES E_b ^{16}O ν	25 ± 25	Shape	
RES E_b ^{12}C $\overline{\nu}$	25 ± 25	Shape	

TABLE 5.2: SPP cross-section parameters used in the analysis along with their pre-fit value and descriptions.

Considerable shape differences[1] exist in the neutrino energy dependence of 2p2h cross-sections when comparing the Valencia model to other models in the literature. To account for this, two shape parameters below and above $E_\nu = 600$ MeV (set arbitrarily) are used for both ν and $\overline{\nu}$. The 2p2h systematic parameters are summarised in Table 5.3.

Parameter	Pre-fit value	Type	Description
2p2h norm ν	1 ± 1	Norm	Flat prior
2p2h norm $\overline{\nu}$	1 ± 1	Norm	Flat prior
2p2h norm ^{12}C to ^{16}O	1 ± 0.2	Norm	
PNNN shape	0 ± 0.33	Shape	
2p2h shape ^{12}C nn	0 ± 3	Shape	
2p2h shape ^{12}C np	0 ± 3	Shape	
2p2h shape ^{16}O nn	0 ± 3	Shape	
2p2h shape ^{16}O np	0 ± 3	Shape	
2p2h Edep low E_ν	1 ± 1	Shape	Fixed at ND
2p2h Edep high E_ν	1 ± 1	Shape	Fixed at ND
2p2h Edep low $E_{\overline{\nu}}$	1 ± 1	Shape	Fixed at ND
2p2h Edep high $E_{\overline{\nu}}$	1 ± 1	Shape	Fixed at ND

TABLE 5.3: 2p2h cross-section parameters used in the analysis along with their pre-fit value and descriptions.

5.2.4 Multi-π and DIS

Multi-π and DIS processes are an important background for the SPP samples and also have a subleading impact on CCQE-like samples. There are four Multi-π parameters, with functionalities as follows: The Multi-π BY Vector and Axial parameters are related to the Bodek-Yang parameterization. These act as a correction to the cross-section as a function of Q^2. The Multi-π Multi TotXsec is directly related to the π multiplicity. The Multi-π Multi Shape parameter varies the invariant hadronic mass and also the π multiplicity according to the AKGY model.

There is one BY correction parameter for the DIS events. In addition, there are normalisation parameters between DIS and Multi-π for both ν and $\overline{\nu}$ events. Finally, the CC Misc parameter impacts the normalisation for the other channels such as CC1K, CC1η and CC1γ.

Parameter	Pre-fit value	Type	Description
Multi-π Multi TotXsec	0 ± 1	Shape	
Multi-π BY Vector	0 ± 1	Shape	
Multi-π BY Axial	0 ± 1	Shape	
Multi-π Multi Shape	0 ± 1	Shape	Fixed at ND
CC BY DIS	0 ± 1	Shape	Flat prior
CC DIS Multi-π Norm ν	1 ± 0.035	Norm	
CC DIS Multi-π Norm $\overline{\nu}$	1 ± 0.065	Norm	
CC Misc	1 ± 1	Norm	

TABLE 5.4: Multi-π and DIS cross-section parameters used in the analysis along with their pre-fit value and descriptions.

[1] However, these differences are not very sensitive at T2K due to its narrow band ν beam.

5.2.5 FSI

FSI parameters are provided for all the possible modes of FSI described in 1.6. In addition, the QE and charge exchange (Cex) modes are also split into pion momentum regions. The FSI parameters are equally important both for CCQE-like and CC $1\pi^+$-like samples because they can mitigate the migration of events with one final state topology to another. For example, an increase in π FSI Prod. parameter can convert a true CCQE-like sample at FD to a CC $1\pi^+$-like sample. At the same time, an opposite migration will happen when π FSI Abs. is increased. An additional Nucleon FSI parameter is also included.

Parameter	Pre-fit value	Type	Description
π FSI QE low E	1.069 ± 0.313	Shape	For $p_\pi < 500$
π FSI QE high E	1.824 ± 0.859	Shape	For $p_\pi > 500$
π FSI Prod.	1.002 ± 0.101	Shape	
π FSI Abs.	1.404 ± 0.432	Shape	
π FSI Cex low E	0.697 ± 0.305	Shape	For $p_\pi < 500$
π FSI Cex high E	1.8 ± 0.288	Shape	For $p_\pi > 500$
Nucleon FSI	0 ± 0.3	Shape	

TABLE 5.5: FSI cross-section parameters used in the analysis along with their pre-fit value and descriptions

5.2.6 Others

The remaining interaction channels contribute very little to the overall neutrino events but are still accounted for through the normalisation parameters listed in Table 5.6. CC Coh ^{12}C and ^{16}O affect the CC coherent scattering for the respective nuclear targets. There are two parameters in the NC channel, namely NC Coh and NC 1γ. They are fixed at ND280-only analysis due to low statistics and hence low sensitivity. The contribution of NC Other channels are different for near and far detectors, and hence they are kept as two different parameters. There are two Coulomb correction parameters (CC norm $\nu/\overline{\nu}$ in the Table) that only affect CC events in the 300 - 600 MeV neutrino energy range. Last but not least, there are also relative normalisations of $\nu_e(\overline{\nu}_e)$ cross-sections with respect to that of $\nu_\mu(\overline{\nu}_\mu)$.

Parameter	Pre-fit value	Type	Description
CC Coh ^{12}C	1 ± 0.3	Norm	
CC Coh ^{16}O	1 ± 0.3	Norm	
NC Coh	1 ± 0.3	Norm	Fixed at ND
NC 1γ	1 ± 1	Norm	Fixed at ND
NC other near	1 ± 0.3	Norm	
NC other far	1 ± 0.3	Norm	
CC norm ν	1 ± 0.2	Norm	
CC norm $\overline{\nu}$	1 ± 0.1	Norm	
ν_e/ν_μ	1 ± 0.0282843	Norm	
$\overline{\nu}_e/\overline{\nu}_\mu$	1 ± 0.0282843	Norm	

TABLE 5.6: Other cross-section parameters used in the analysis along with their pre-fit value and descriptions.

5.3 ND280 Detector Systematic Model

A detailed description of ND280 detector uncertainty can be found in [73], and is beyond the scope of this thesis. ND280 detector systematics arise from different sources. The first kind deals with migrations of events between samples or bins occurring when modifying the reconstructed observables like p_μ. The second type corresponds to variables that are impacted by detection and reconstruction efficiency. The third type deals with the overall normalisation of events caused by certain detector parameters. Due to computational heaviness, ND280 detector systematic uncertainty is propagated as a covariance matrix, rather than being constrained in the fit. This matrix is binned in p_μ–$\cos\theta_\mu$ space, hence each matrix element corresponds to a particular lepton momentum and direction region. The covariances between different matrix elements are captured by comparing the differences in the number of events through a toy MC procedure with ND280 detector systematic parameters varied simultaneously.

ND280 detector systematic parameters are strongly correlated to the flux and cross-section parameters, and hence they can inflate the latters' uncertainties that are propagated to the FD. However, studies in [73] showed that the impact of ND280 detector parameters on FD predictions is very small.

5.4 Systematic Errors at SK

This thesis describes the analysis developments done at the FD that is the SK detector. It is necessary to take a deep dive into various systematic error sources and their estimations to comprehend the results presented in Chapter 6.

At the most basic level, the process of generating the far detector MC simulation can be explained as a three-stage process. Neutrino interactions based on the T2K beam flux model are generated, which are then propagated to the SK detector simulation, where the neutrino's interactions with water and the subsequent detector responses are simulated. The output of this, which is most importantly the time and charge information from each PMT in SK is used to reconstruct the kinematics of the parent neutrino and the outgoing particles from its interaction.

From the point of view of physics, this three-stage process can give rise to a large number of systematic uncertainties. SK is a huge and extremely complex detector. Multiple intricate detector processes require proper modelling to make the detector model as realistic as possible so that the simulated events will best match the data. However, it's almost impossible to have full control over these intricate processes. These mis-modellings will ultimately cause reconstruction biases, leading to data-MC discrepancies.

To tackle this, SK performs rigorous and regular calibration of the detector, where the detector simulation gets tuned to the calibrated data. Even after careful calibrations and tuning, there will still be some processes that miss considerations. However, the T2K beam events are too low in statistics to create any control sample to extract these detector errors. Incidentally, the fact that T2K uses SK as its FD allows atmospheric neutrino events recorded at SK in T2K's energy range and topology type to be used as the control samples. These control samples mentioned in Table 5.7 are created by applying T2K-like selection cuts on the atmospheric data and MC, and a fit is performed using them to obtain the SK detector errors. Hence this fit is sometimes referred to as the "atmospheric fit". The upcoming sections will describe some of the systematic parameters constrained by SK calibration data, and finally a detailed description of the atmospheric fit.

Atmospheric Fit Samples
Single-ring e-like 0 Decay electron
Single-ring e-like 1 Decay electron
Single-ring μ-like 0 Decay electron
Single-ring μ-like 1 Decay electron
Single-ring μ-like 2+ Decay electron
Multi-ring μ-like 0 Decay electron
Multi-ring μ-like 1 Decay electron
Multi-ring μ-like 2+ Decay electron

TABLE 5.7: Summary of the T2K beam-like samples from the SK atmospheric samples.

5.4.1 Uncertainties on Fiducial Volume and Decay Electron Tagging

High statistics cosmic ray "stopping" muons are used as control samples for estimating uncertainties on FV and decay electron tagging. The stopping muons are called so because they comprise of muons that enter SK from outside the ID, and lose their energy to below the Cherenkov threshold as they travel through the water. These tracks "originate" at the ID wall, and hence have true $DWall = 0$. The difference in vertex distributions of stopping muon data and MC then provides uncertainties on the FV cut variables $DWall$ and $ToWall$. The same control sample is used to estimate the uncertainty in decay electron tagging, which is also a crucial parameter used in all the T2K FD samples. All these events are expected to have at least one decay electron through the $\mu \rightarrow e$ decay, and the tagging efficiency can be calculated using:

$$\eta_{tag} = \frac{N_{1dcye}}{N_{0dcye} + N_{1dcye}} \tag{5.2}$$

A fake rate is then assigned as

$$\eta_{fake} = \frac{N_{2dcye}}{N_{1dcye} + N_{2dcye}} \tag{5.3}$$

where N_{kdcye} represents the number of stopping muon events having k reconstructed decay electrons. The tagging efficiency and fake rate uncertainties are calculated by comparing the differences in these values between the data and MC. It is then found that the tagging efficiency uncertainty is $\sigma_{tag} = 1\%$ and fake rate uncertainty is $\sigma_{fake} = 0.2\%$.

The uncertainties in event rates due to decay electron tagging for each sample are then evaluated as follows:

$$\sigma_{\text{decay-e}} = \sqrt{(P_{\text{true decay-e}} \times \sigma_{tag})^2 + ((1 - P_{\text{true decay-e}}))} \times \frac{N_{sample}^{Nodcyecut}}{N_{sample}}, \tag{5.4}$$

where $P_{\text{true decay-e}}$ is defined as the fraction of events with at least one true decay electron after all the selection cuts in that sample applied except for the decay electron cut. $N_{sample}^{Nodcyecut}$ is the number of events in the sample without applying the decay electron cut, and N_{sample} is the total number of events in that sample.

5.4.2 Energy Scale Uncertainty

The importance of accurate estimation of neutrino energy in measuring neutrino oscillation parameters has already been stressed. Factors such as water quality and temperature can

affect SK detector parameters such as water transparency, PMT efficiency etc. This can cause biases in reconstruction which strongly relies on these parameters as discussed in Chapter 2. The bias between the measured energy for the data and that predicted in the MC is represented by the energy scale uncertainty. Rigorous calibration is done at SK to estimate the energy scale uncertainty. Four different control samples that span four different kinematic ranges are used:

- Decay electrons from stopping muons: These cover the low-energy region (30–50 MeV/c).
- Atmospheric neutral current π^0 events: Used for the medium-energy region (150–300 MeV/c).
- Sub-GeV and multi-GeV stopping muons: These probe the higher-energy regions (200––440 MeV/c) and (1.5–8 GeV/c).

These four samples' largest energy scale uncertainty is conservatively taken as the global energy scale error. This was estimated to be 2.1% as described in [89]. This uncertainty is then added uncorrelated to the SK detector covariance matrix, which will be discussed in the upcoming sections.

5.4.3 The Atmospheric Fit

Any biases in the detector modelling will be seen as biases in event reconstruction variables like the PID parameters and the ring counting (RC) parameter. A reconstruction variable x can be parametrized using a set of smear (α) and shift (β) parameters such that for a particular value of α and β, the substitution

$$x \rightarrow \alpha x + \beta, \tag{5.5}$$

results in best data-MC agreement. This re-parametrization is done for all the PID parameters and the Ring counting parameter (see Table 5.8), for 8 FS topologies relevant to T2K samples' signal and background topologies (Table 5.10), and 5 visible energy regions (Table 5.9). This is done because the detector response can be different for different topologies and energies.

PID parameter	Functionality
Ring counting parameter	Likelihood parameter that determines the number of reconstructed rings in an event
e/μ PID	Separating e-like and μ-like rings
e/π^0 PID	Separating ν_e CCQE-like and NCπ^0 events
μ/π^+ PID	Separating μ-like and π^+-like rings
$\pi\pi/e$ PID	Separating multi-ring ν_μ CC1π^+ events from single-ring events
$\pi\pi/2R$ PID	Separating multi-ring ν_μ CC1π^+ events from other multi-ring events
$E^{loss}_{\pi\pi}$ parameter	Separating multi-ring ν_μ CC1π^+ events from NC events

TABLE 5.8: Reconstructed variables that are used in FD sample selections.

Bin	Visible Energy [MeV]
0	$30-300$
1	$300-700$
2	$700-1330$
3	$1330-3000$
4	$3000-5000$

TABLE 5.9: Visible energy binning used for the atmospheric fit MCMC.

FS topology	Description
$1e$	1Re signal topology
1μ	1Rμ signal topology
$1e$ + Other	Multi-ring ν_e signal topology + bkg. for the rest
$1\mu + 1\pi^+$	ν_μ CC1π^+ signal topology
1μ + Other	Multi-ring background
$1\pi^0$	1Re background
$1\pi^\pm$	1Rμ background
Other	All other topologies (mostly hadrons)

TABLE 5.10: Final state topologies used in the atmospheric fit MCMC and their relation with beam samples. Note: this is slightly different from Table 3.3 with the $1e + 1\pi$ topology merged with $1e$ + Other topology.

Hybrid χ^2 Maps

Certain FS topologies are either significant signal components of the FD samples or constitute the most dominant background. For example, NCπ^0 events with only one visible decay photon are a major background to the $1Re$ samples, while $1\mu + 1\pi^+$ topology is the dominant signal FS for multi-ring ν_μ CC1π^+ sample.

Special control samples called hybrid samples are constructed to obtain prior constraints on the shift and smear parameters dependent on these FS topologies.

These hybrid samples are constructed in the following manner:

- If the topology of interest is $A + B$ where A, B are the true visible particles, we select a T2K beam MC event with that topology.
- We then find a reconstructed atmospheric data/MC ring of the particle type A.
- The T2K beam event is rotated spatially to align with the kinematics of this matched atmospheric data/MC ring A.
- The particle B is then re-simulated in the detector using this modified vertex and direction.
- The PMT hits of the reconstructed B ring are then added to the atmospheric event A, thus creating a hybrid data/MC sample, depending on the source of A.

A χ^2 map is then generated by calculating $\Delta\chi^2$ between data and MC for a wide range of α, β values as follows:

$$\Delta\chi^2 = \sum_{bins} \frac{[N_{data} - N_{MC}]^2}{\sigma^2_{data} + \sigma^2_{MC}} \tag{5.6}$$

For this analysis, χ^2 maps adding prior constraints on the α, β parameters were generated using both the hybrid π^0 and the hybrid $\mu\pi$ samples. These maps are shown in Fig. 5.4 and 5.5.

MCMC

A total of 560 parameters exists taking into account the number of topologies, visible energy bins and variables that impact the selections, in addition to a big number of nuisance parameters arising from flux, cross-section and oscillation parameters. A binned-likelihood

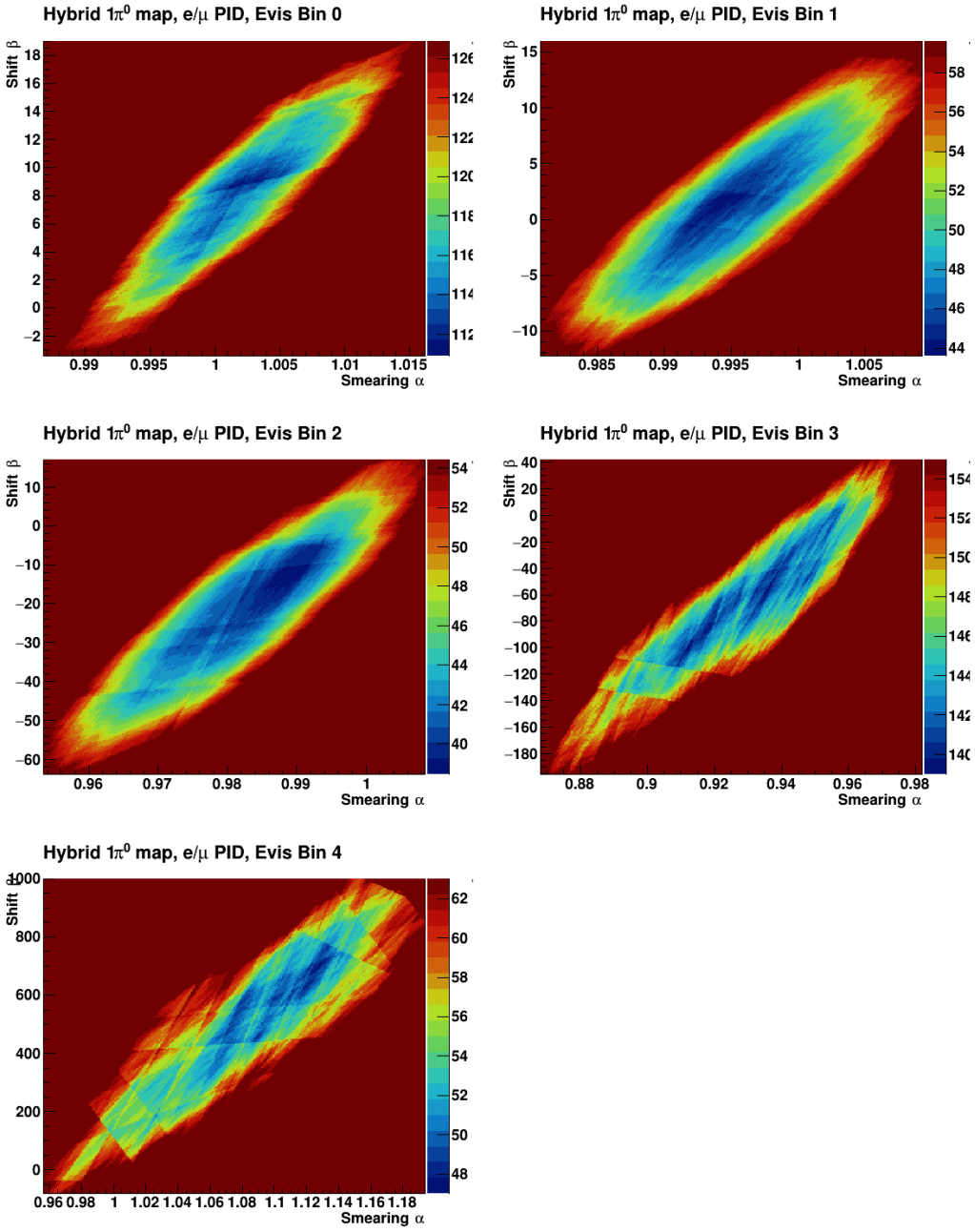

FIGURE 5.4: χ^2 maps for the $e\mu$ PID parameter generated using the hybrid $\pi 0$ sample. The colour axis was truncated to show only $[\chi^2_{min}, \chi^2_{min} + 16]$ for visualisation purposes.

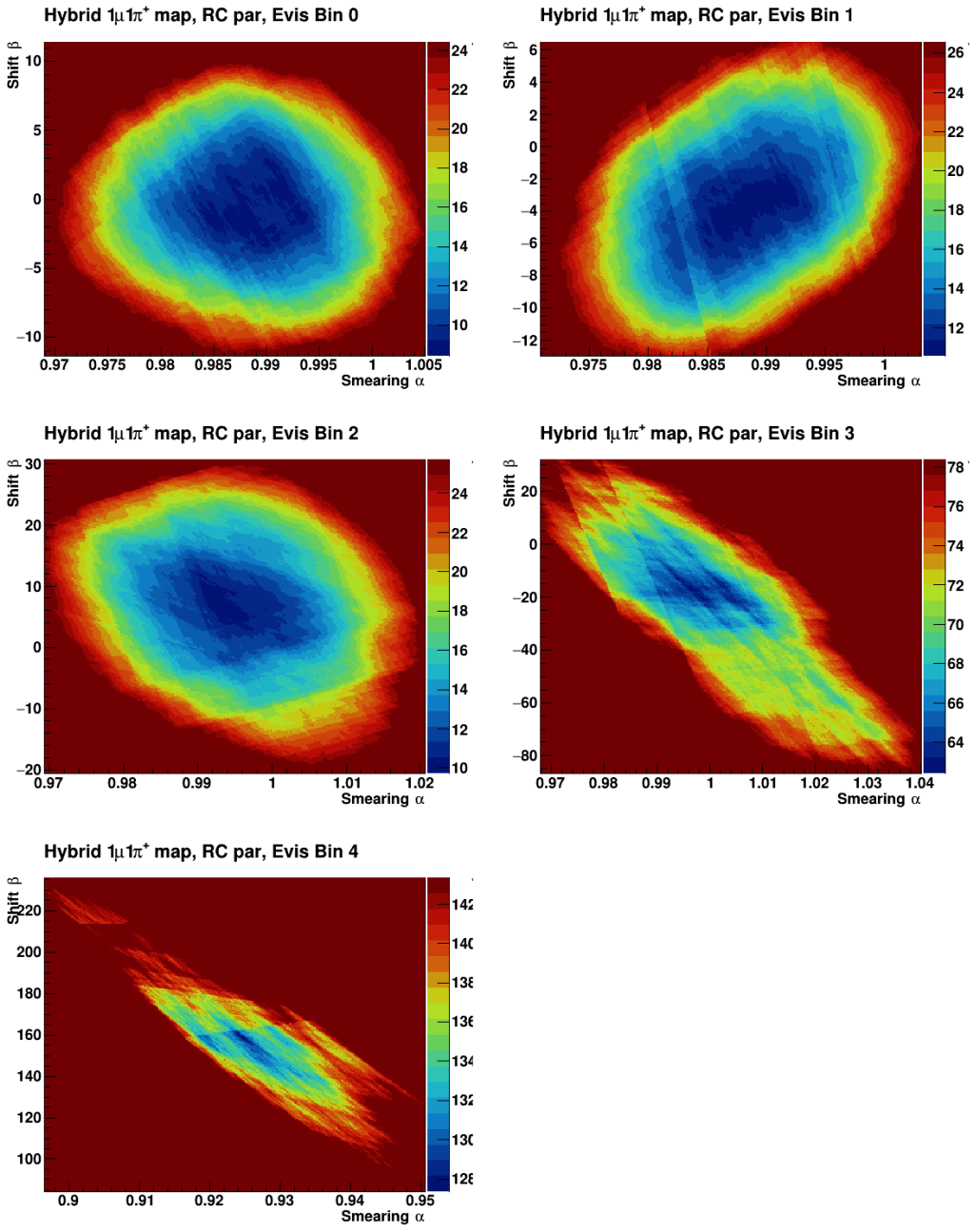

FIGURE 5.5: χ^2 maps of Ring counting parameter generated using the hybrid $\mu\pi$ sample. The colour axis was truncated to show only $[\chi^2_{min}, \chi^2_{min} + 16]$ for visualisation purposes.

function between the data and MC is constructed using these parameters, along with additional prior constraints from the hybrid samples, and other external constraints on the nuisance parameters, thereby taking the form:

$$-ln[\mathcal{L}(\alpha,\beta,\gamma,\theta,\epsilon|\mathbf{h}^{Data})] = -\sum_{i,k,l,m}\left[N^{Data}_{i,k,l,m} ln\left(\frac{N^{MC}_{i,k,l,m}}{\Sigma_n N^{MC}_{i,k,l,n}}\right)\right] + \frac{1}{2}\sum_{i,k,c}\chi^2_{i,k,c}(\alpha_{i,k,c},\beta_{i,k,c}) + \sum_{i,j}\Delta_i(\epsilon,\theta,\gamma)V^{-}1_{ij}\Delta_j(\epsilon,\theta,\gamma), \tag{5.7}$$

where $\mathbf{h}^{Data}$ are histograms binned in the reconstructed selection variables that are filled with atmospheric data events, α and β are the smear and shift parameters, γ represent the flux and cross-section parameters, θ are oscillation parameters and finally ϵ are all the other associated systematic parameters. The index i runs over all the 7 PID/Ring-counting parameters described in Table 5.8. Indices k and l are looped over the 5 visible energy bins (see table 5.9) and 8 atmospheric beam-like samples mentioned in Table 5.7, and finally m and n are looped over the histogram bins. The index j that appears in the last term on the right side loops over the 8 FS topologies described in Table 5.10. Note that this index is not present in the first and second terms since the contributions of all the FS topologies are summed before evaluating those terms.

The χ^2 term in the middle is the hybrid-χ^2 penalty term, where c goes over the different χ^2 maps and the last term is the penalty term arising from the flux, cross-section, oscillation and other systematic uncertainties which are nuisance parameters in the SK detector error estimation.

We then use a Bayesian MCMC framework to sample the posterior distributions of these parameters of which α, β are of the most significance. The posteriors of α, β parameters are thus marginalized over all the other nuisance parameters.

5.4.4 Toy MC Procedure

Each T2K beam MC event that undergoes one of the FD sample selections gets assigned a bin number that is defined in Table B.1 based on:

- what sample the event gets selected as,
- what the sample's E_{rec} is,
- what is the true neutrino interaction of the MC event is.

At this point, a nominal E_{rec} vector is generated by performing the T2K FD sample selections on the nominal or unchanged T2K beam MC and filling the nominal event rates into the bins mentioned in Table B.1. After this, random values of α and β are drawn from their posterior distributions. The beam MC is then shifted and smeared with these values, creating a "toy MC". The FD selections are applied again on this modified MC, and the events are again assigned to the bins. Due to the change in MC, an event that belonged to one bin in the nominal MC can migrate to another bin. Along with the shifts and smears, the fiducial volume and decay electron uncertainties are also applied to the events. This process is repeated n times, producing a matrix of dimension $n_{throws} \times n_{E_{rec}bins}$ tracking the variations in the E_{rec} bins for each throw. The nominal E_{rec} vector is then subtracted and divided from this matrix, and a covariance matrix is then constructed using:

$$cov(x,y) = \frac{1}{n}\sum_{i}^{n}(x_i - x_{nom})(y_i - y_{nom}) \tag{5.8}$$

where the subscript *nom* refers to the nominal event rates in the bins x and y. The SK detector covariance matrix so calculated is shown in Fig. 5.7

The most important change in the SK detector matrix in this thesis compared to that used in T2K's latest oscillation analysis is the inclusion of the multi-ring ν_e CC1π^+ sample in the Toy MC procedure. Since the multi-ring sample was combined with the existing single-ring ν_e CC1π^+ sample, it is assigned the same E_{rec} bins in the detector covariance matrix.

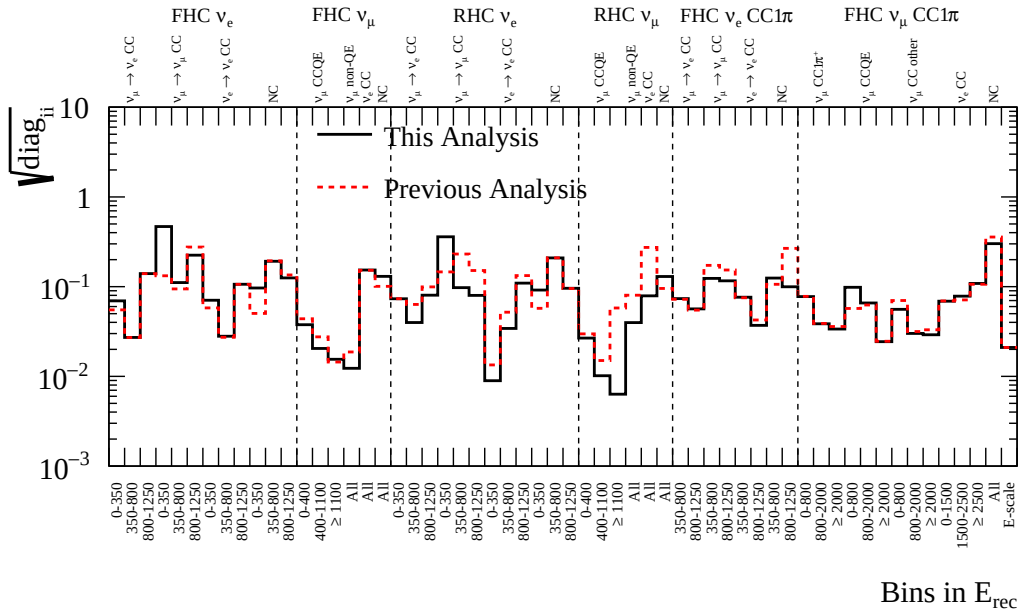

FIGURE 5.6: Comparison of $\sqrt{diagonal}$ elements between the SK detector matrix used in T2K's latest analysis (dashed red line) and this analysis with the inclusion of the multi-ring ν_e CC1π^+ sample (black solid line).

There is a considerable reduction of errors, especially in the bins belonging to background events for the ν_e CC1π^+ sample when comparing the matrix without the multi-ring ν_e CC1π^+ sample (labelled Previous Analysis) and with the multi-ring ν_e CC1π^+ sample (labelled This Analysis), as seen in Fig. 5.6. This can possibly be because of the positive correlations between multi-ring ν_e CC1π^+ and ν_μ CC1π^+ samples. There is also a general trend observed as a reduction of errors in all the samples except some bins, none of them being signal components of any sample. Therefore, it can be said that the addition of the multi-ring ν_e CC1π^+ sample helped add additional constraints in SK detector systematic errors[2].

[2]Some of the reduction in the errors are also attributed to corrections made by the Author in the Toy Matrix generation framework.

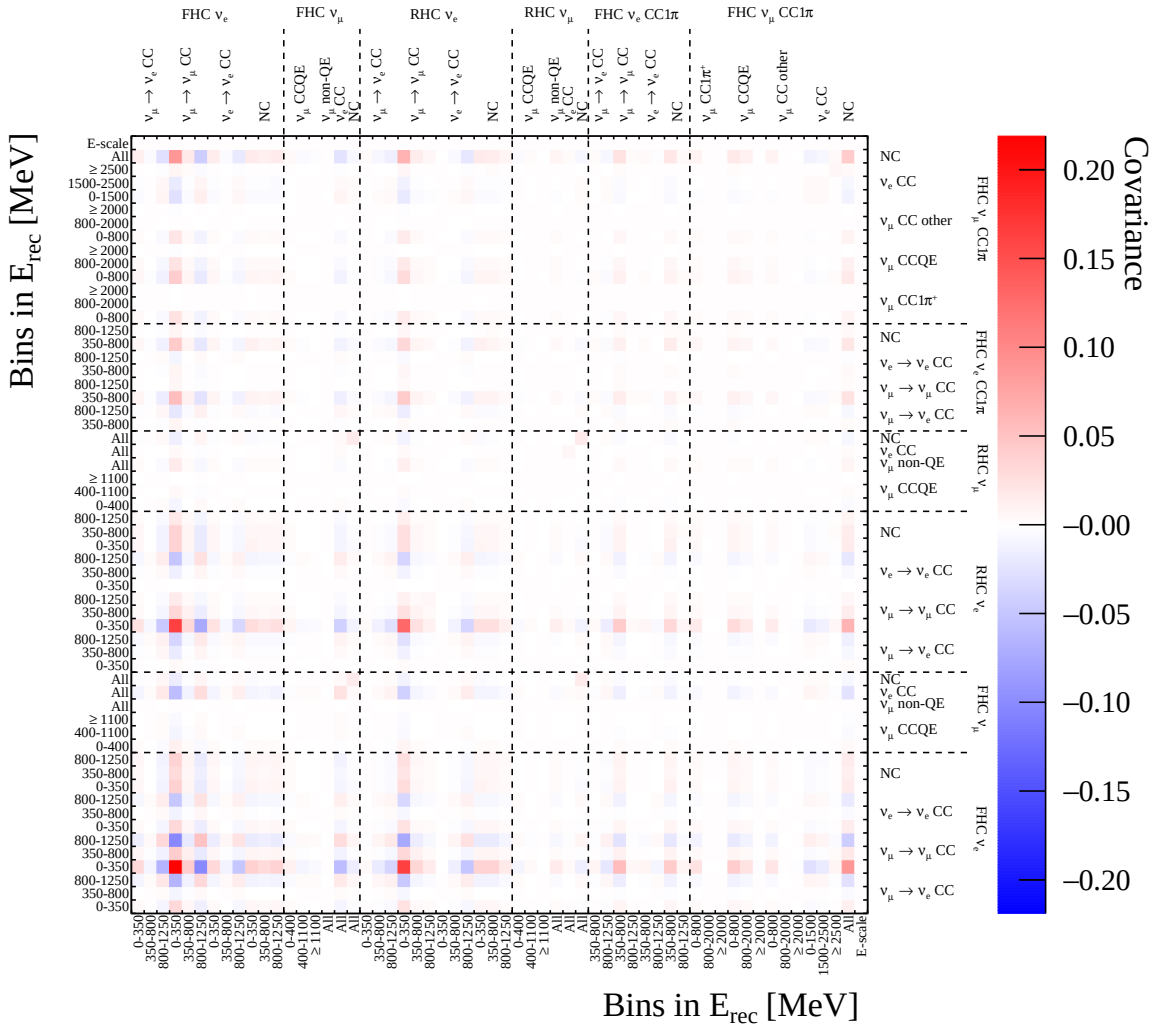

FIGURE 5.7: SK detector covariance matrix generated from the toy MC procedure with the posteriors of α and β from the atmospheric MCMC.

5.4.5 Pion Secondary Interactions and Photo-nuclear Effects

Other important sources of error at SK are the pion secondary interactions (SI) and photo-nuclear effects (PN). Pions that escape the oxygen nucleus can re-interact in the detector medium, essentially allowing the pion to undergo elastic and quasi-elastic scattering, absorption, single and double charge exchange, multi-pion production, pion decay, and other processes. A failure to properly tag the pion can cause a wrong deduction of the underlying neutrino interaction. This can bias the entire neutrino energy calculation procedure, and hence oscillation studies too.

At SK, NEUT is used to simulate pion FSI and SI using a cascade model. For a pion that is produced in a neutrino interaction, at each step of the cascade the pion momentum is evaluated and is passed to NEUT, where the interaction probability of the pion with multiple target materials in the detector is calculated. This NEUT cascade model is tuned to external pion-nucleus scattering data.

The SI parameters are analogous to the FSI parameters described in the table 5.5. For a given throw of SI parameters the SI weight $w_{SI}(f_{SI})$ for the event is calculated as

$$w_{SI}(f_{SI}) = \prod_i \frac{\sigma_i^{Throw}(p_i, f_{SI})}{\sigma^{Nominal}(p_i)}, \tag{5.9}$$

where the index i loops over all the pion SI for the particular event, and p_i is the pion momentum at each pion SI vertex. $\sigma^{Nominal}(p_i)$ is the nominal cross-section of the interaction, and $\sigma_i^{Throw}(p_i, f_{SI})$ is the cross-section of the interaction for a given set of FSI parameters. These variations are then applied to the FD samples binned in the same way as that described in the toy MC. This generates the pion SI covariance matrix.

The photons from a π^0 decay can excite a nucleus that can result in nuclear emissions. This further increases the single photon background at SK, which is one of the most dominant backgrounds in ν_e CCQE samples. This photo-nuclear effect is applied as a large uncertainty of 100% for all events where photons from π^0 get absorbed.

The SI+PN covariances (Fig. 5.8) are much smaller than the SK detector covariances from the atmospheric fit (Fig. 5.7), but still its impact on e-like samples and the multi-ring ν_μ CC1π^+ sample is evident.

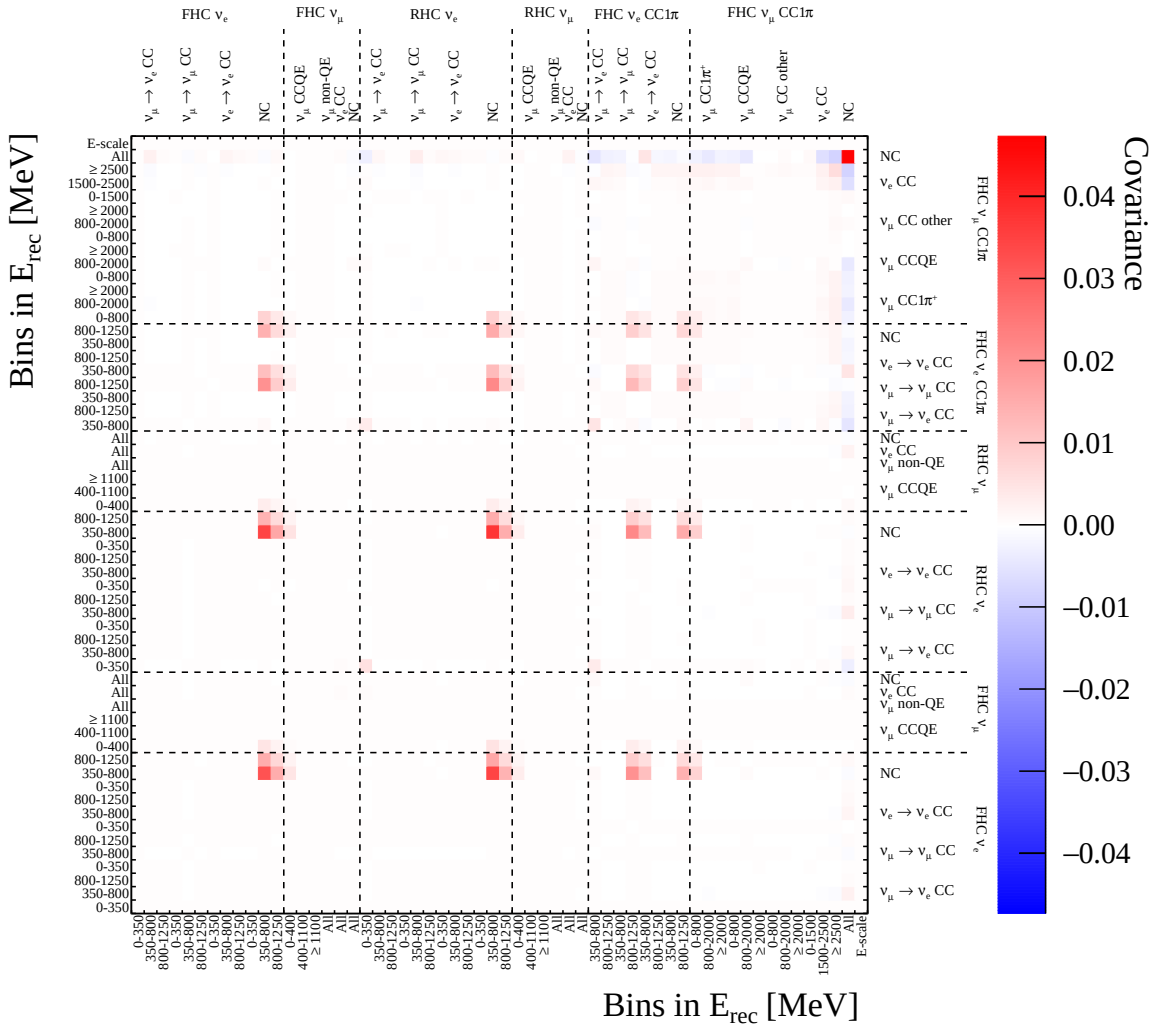

FIGURE 5.8: The SI+PN covariance matrix. The impact on ν_e samples is very evident, along with mild covariances between the multi-ring ν_μ sample and single ring samples.

5.4.6 The Final SK Detector Matrix

The SI+PN covariance matrix (Fig. 5.8) is added in quadrature to the SK detector matrix from the atmospheric fit (Fig. 5.7) to obtain the final SK detector matrix.

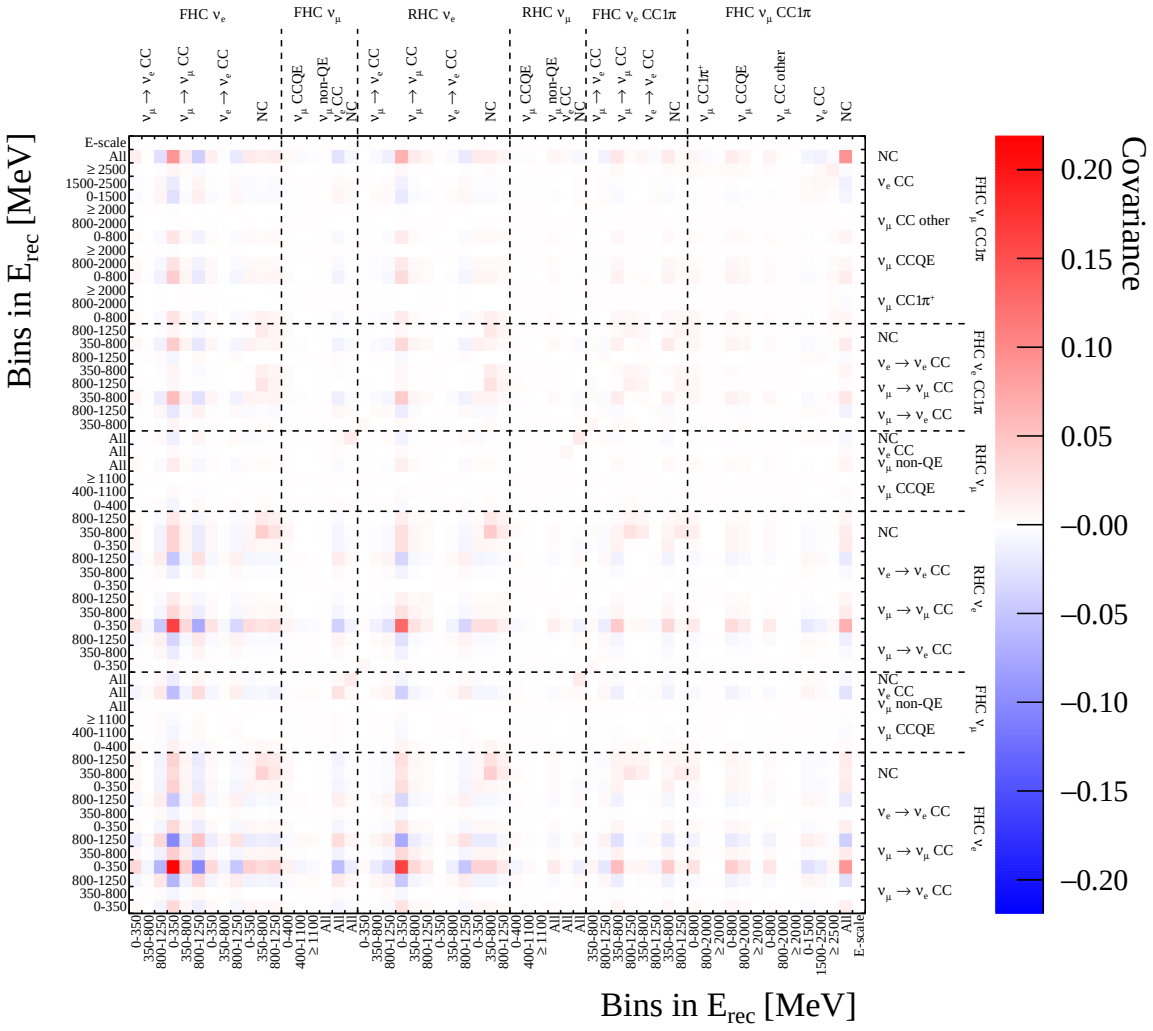

FIGURE 5.9: The final SK detector covariance matrix used in the oscillation analysis.

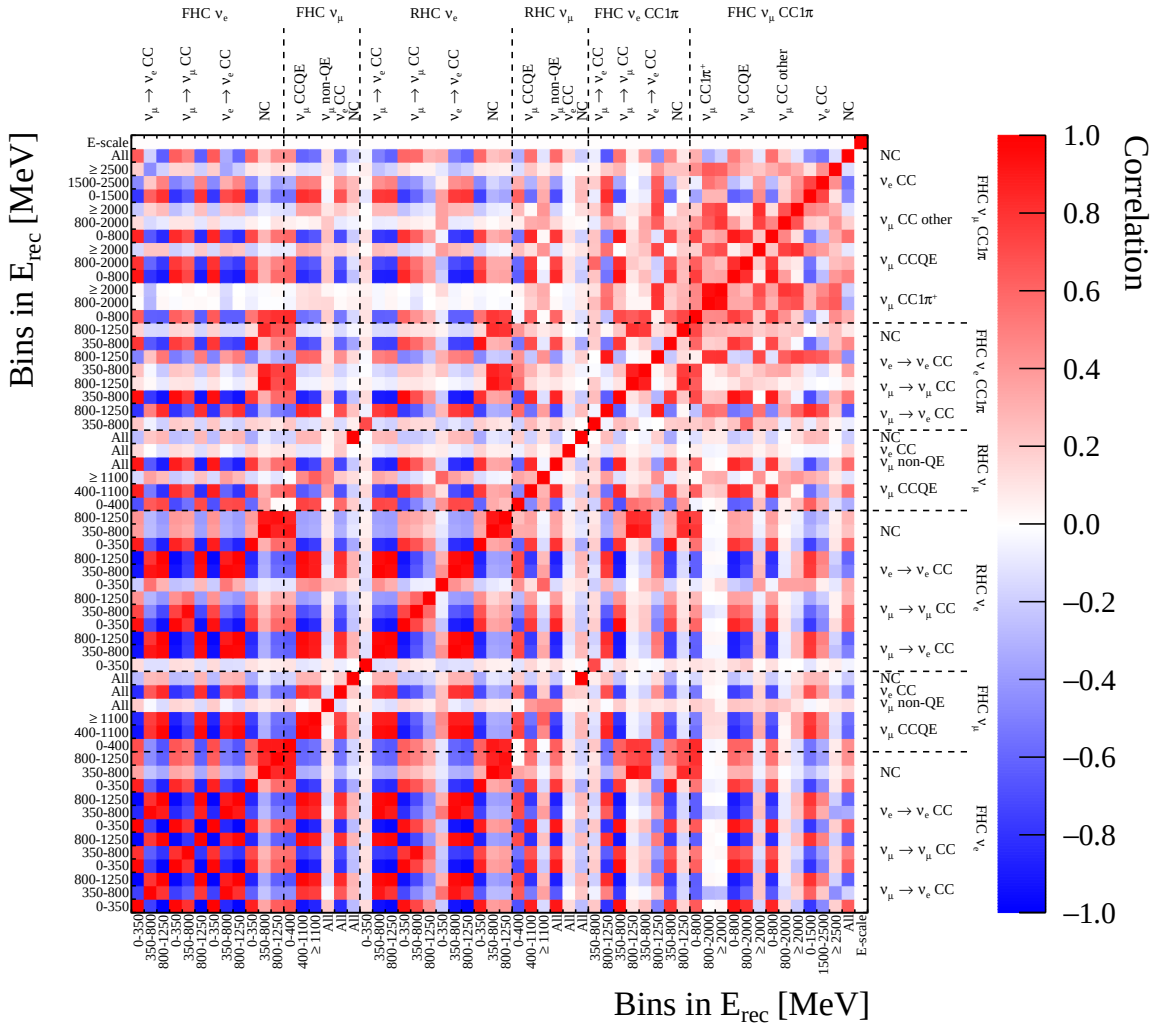

FIGURE 5.10: The final SK detector correlation matrix used in the oscillation analysis.

5.5 Impact of PMT Reflectivity on ν_e CC1π^+ Reconstruction

Among many underlying effects that impact the described detector errors is the reflectivity of the PMT photocathode. The author performed a study on the impact of this reflectivity on e/π^0 separation A.1, which is important in ν_e appearance analyses. Additionally, a similar study was done to test the impact of the reflectivity on ν_e CC1π^+ reconstruction and is discussed below.

Starting from the surface to the internal parts of the PMT, the photons can face absorption, transmission and reflection from four different materials: water, the PMT's glass, the bialkali photocathode and vacuum. While the refractive indices of water, glass and vacuum are well-known, that of the bialkali cathode is estimated through SK's calibration studies [90]. This is done by injecting a collimated laser beam of various wavelengths from the top of the SK tank. The timing and spatial distribution of these photons are then studied with respect to an MC to extract the refractive indices of the cathode for multiple wavelengths.

For the SK-V period, it was found that the dark noise subtraction was not performed when estimating the reflectivity parameters. This resulted in a change of reflectivity parameters ranging from 3–22%, with the refractive indices of the lowest wavelengths undergoing the

most changes. This provided an opportunity to study what such a big impact on reflectivity parameters would translate to reconstruction biases.

10,000 ν_e CC1π^+ events that follow T2K's kinematics were simulated using the SK detector simulation with the reflectivity parameters before and after the dark noise subtraction. After reconstruction, single and multi-ring ν_e CC1π^+ selections were applied on them.

Fig. 5.11 shows the comparison of event reduction along the various selection cuts for both single and multi-ring ν_e CC1π^+ sample for events reconstructed with reflectivity parameters before and after the dark noise subtraction. The last bin in these plots shows the total ν_e CC1π^+ events after all the selection cuts. It can be seen that a large change in reflectivity only translates to a very small change in event rate differences at each cut level.

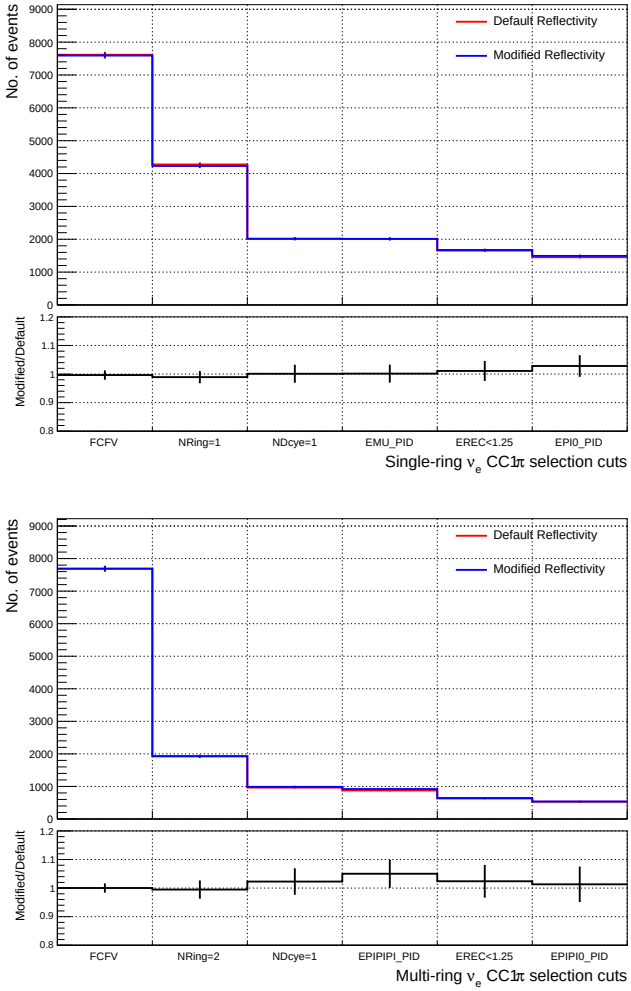

FIGURE 5.11: Number of single (top) and multi-ring (bottom) ν_e CC1π^+ events after each selection cut. The last bin shows the final number of selected events. Default (Modified) reflectivity represents events reconstructed with reflectivity parameters before (after) dark noise subtraction.

Fig. 5.12 compares the reconstructed electron momentum and neutrino energy of all the selected ν_e CC1π^+ events. The small changes observed due to changes in reflectivity parameters are within the statistical errors in each bin. A raw event-rate comparison is also shown in Table 5.11.

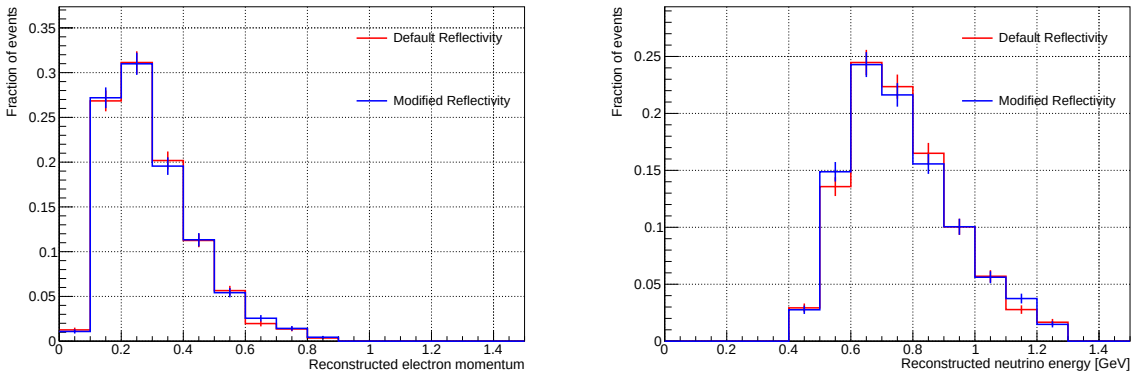

FIGURE 5.12: Reconstructed electron momentum (left) and neutrino energy (right) of the combined ν_e CC1π^+ sample. Default (Modified) reflectivity represents events reconstructed with reflectivity parameters before (after) dark noise subtraction.

Sample	Event Rates		Ratio
	Default Reflectivity	Modified Reflectivity	
Single-ring ν_e CC1π^+	1452.000 ± 38.105	1493.000 ± 38.639	1.028 ± 0.038
Multi-ring ν_e CC1π^+	530.000 ± 23.022	537.000 ± 23.173	1.013 ± 0.062

TABLE 5.11: Comparison of event rates for both the ν_e CC1π^+ samples generated with reflectivity parameters before (default) and after (modified) dark noise subtraction. The ratio here is taken between the event rate of modified reflectivity to the default reflectivity.

It can be concluded that the impact of a large change in reflectivity parameters does not have an evident impact on the reconstruction of ν_e CC1π^+ events, and the ratio of event rates as quoted in both the plots and the table are consistent with unity.

6

Results

> Among creations, I am the beginning, the middle and also the end, O Arjuna; among sciences, I am the Science of the Self and I am the logic in all arguments.
>
> *Bhagavad Gita 10.32*

This chapter synopsizes the results of the oscillation analysis using the Bayesian MCMC framework with 1.153×10^{21} FHC POT and 0.834×10^{21} RHC POT for ND280, 2.1428×10^{21} FHC POT and 1.6345×10^{21} RHC POT for the FD. Firstly, the result of applying the new multi-ring ν_e CC1π^+ selections on FHC FD data is discussed. The next section describes Asimov fit studies to validate the robustness of the fitter before performing a data fit. Finally, the last sections of this chapter show the results of the data fit, where a short overview of the constraints on systematic parameters is first provided, followed by a detailed description of the constraints on the oscillation parameters.

6.1 Opening Data and Comparisons with MC

The selection cut developments described in Chapter 3 were studied solely with the FD MC, making this analysis a blind analysis. After rigorous tests ranging from efficiency and resolution studies to re-evaluating the SK detector matrix, the multi-ring ν_e CC1π^+ selections were finally applied to the FD FHC data. For an MC prediction of ~ 6 events, 4 data events were selected. Data-MC comparisons for some of the cut variables used in the selections are portrayed in Fig. 6.1.

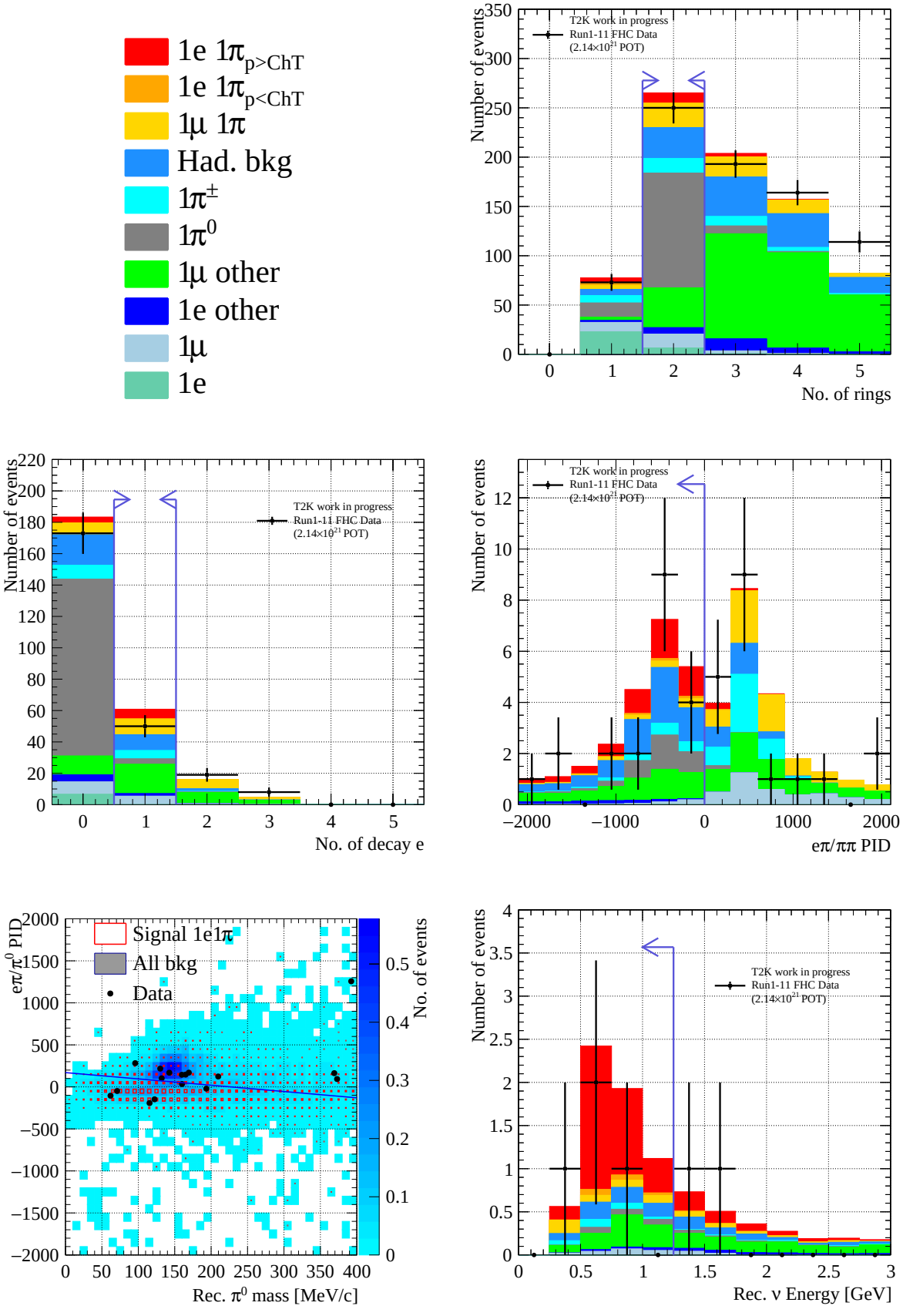

FIGURE 6.1: Data-MC comparisons at each selection cut for the multi-ring ν_e CC1π^+ sample. The arrow shows the region accepted by the cut. In the 2D π^0 rejection cut, black points are data events, red hollow boxes show signal $1e + 1\pi$ topology MC while the coloured boxes show all other backgrounds and all events above the cut line are rejected.

The reconstructed neutrino energy distribution of the single-ring ν_e CC1π^+ sample is shown in Fig. 6.2 along with that of the multi-ring sample. As discussed in Chapter 3, a significant fraction of MC events with π^+ momentum above its Cherenkov threshold (labelled as 1e1$\pi_{p>ChT}$ in the plot) exists in the single-ring sample.

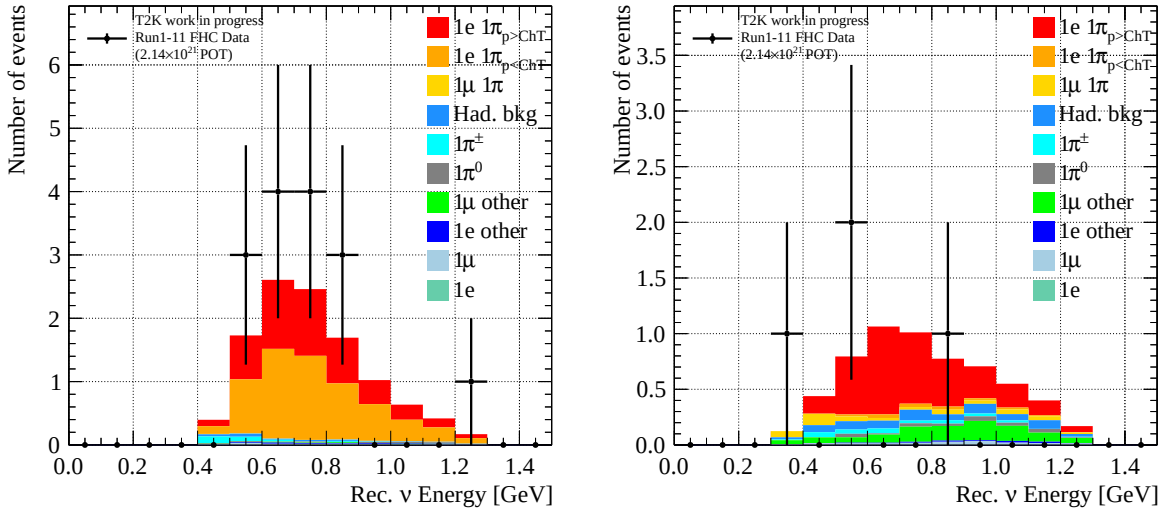

FIGURE 6.2: Data-MC comparison in reconstructed neutrino energy for the single-ring (left) and multi-ring (right)ν_e CC1π^+ samples after all selections.

When both these samples are combined, the reconstructed neutrino energy distribution sample takes the form shown in Fig. 6.3. The direct consequence of combining these two samples is removing any biases arising from the model dependencies of the π^+ kinematics.

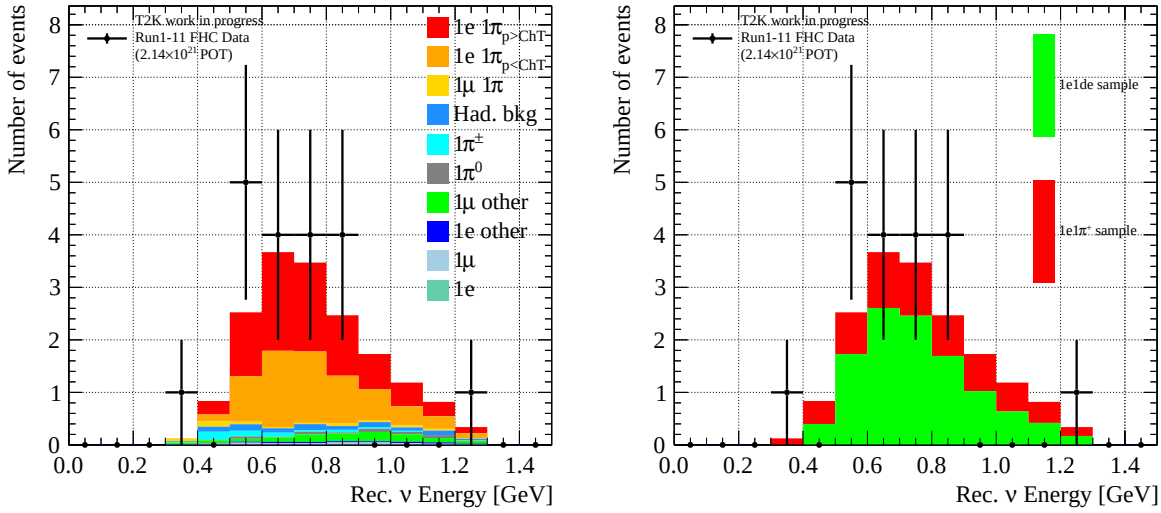

FIGURE 6.3: Data-MC comparisons for the combined ν_e CC1π^+ sample. The left plot shows the MC distributions broken down by FS categories, whilst the right plot shows the MC contribution of single- and multi-ring ν_e CC1π^+ samples (labelled 1e1de and 1e1π^+ in the plots respectively).

6.2 Asimov Fit Results

Asimov fits are necessary before performing data fits to ensure the robustness of a fitter. In addition, they also provide means to calculate the experiment's sensitivity to various parameters. Ideally, the post-fit values of parameters after the Asimov fit should be equal to their prior values. The FD Asimov fit uses ND280 data and an FD Asimov "fake-data". The Asimov "fake-data" is constructed by setting all the systematic parameters to their Post-BANFF best-fit values, and the oscillation parameters to the Asimov parameters described in Table 6.1. The prior values and uncertainties of the oscillation parameters that are used both in the Asimov fit and later in the data fit are also mentioned in the same table. Due to the presence of ND280 data, all the flux and cross-section parameters will be pulled or shifted away from their prior values in the FD Asimov fit. Nevertheless, the oscillation parameters should retain their prior values. The result of the MCMC is an N-dimensional posterior distribution, from which nuisance parameters are integrated (or marginalized) to obtain the one- and two-dimensional posterior distributions that are usually presented in the plots. If two parameters are strongly (anti)correlated, one of those parameters may be pulled away from its prior.

Oscillation Parameters	Prior	Asimov Value
δ_{CP}	$[-\pi, \pi]$	-1.601
Δm^2_{32} ($\times 10^{-3}$ eV^2)	$[2.3, 2.7]$	2.494
$\sin^2\theta_{23}$	$[0.0, 1.0]$	0.561
$\sin^2\theta_{13}$ (without RC)	$[0.007557, 0.052786]$	0.0220
$\sin^2\theta_{13}$ (with RC)	0.0220 ± 0.0007	0.0220
$\sin^2\theta_{12}$	$0.307^{+0.013}_{-0.012}$	0.307
Δm^2_{21} ($\times 10^{-5}$ eV^2)	(7.53 ± 0.18)	7.53

TABLE 6.1: The prior values and uncertainties of oscillation parameters that were used in this analysis. The first four parameters are given flat priors in the fit while the others have Gaussian distributions.

For instance, by looking at Fig 6.4, it is understandable that $\sin^2\theta_{23}$ and $\sin^2\theta_{13}$ are highly anti-correlated, moving each other's post-fit central values beyond 3σ of their prior values as in Fig 6.5. This owes to the fact that T2K's constraints on $\sin^2\theta_{13}$ are weak, and these strong (anti)correlations impact $\sin^2\theta_{23}$ measurements. This is also seen in the two-dimensional contour $\sin^2\theta_{23}$–Δm^2_{32} where the $\sin^2\theta_{23}$'s best-fit value lies in the lower octant while its Asimov point is in the upper octant. To break this degeneracy, external constraints from reactor neutrino experiments (referred to as reactor constraint or RC hereafter) on $\sin^2\theta_{13}$ are applied. By doing so, the T2K best-fit point of $\sin^2\theta_{23}$ moves back to the upper octant closer to its Asimov point. This very much portrays the importance of RC in obtaining T2K's oscillation parameter results.

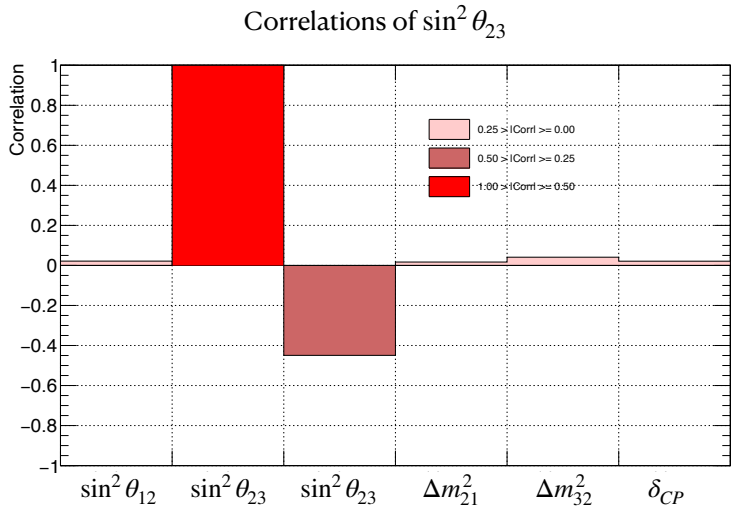

FIGURE 6.4: Post-fit correlations of $\sin^2\theta_{23}$ with all other oscillation parameters. The anti-correlation with $\sin^2\theta_{13}$ is quite evident.

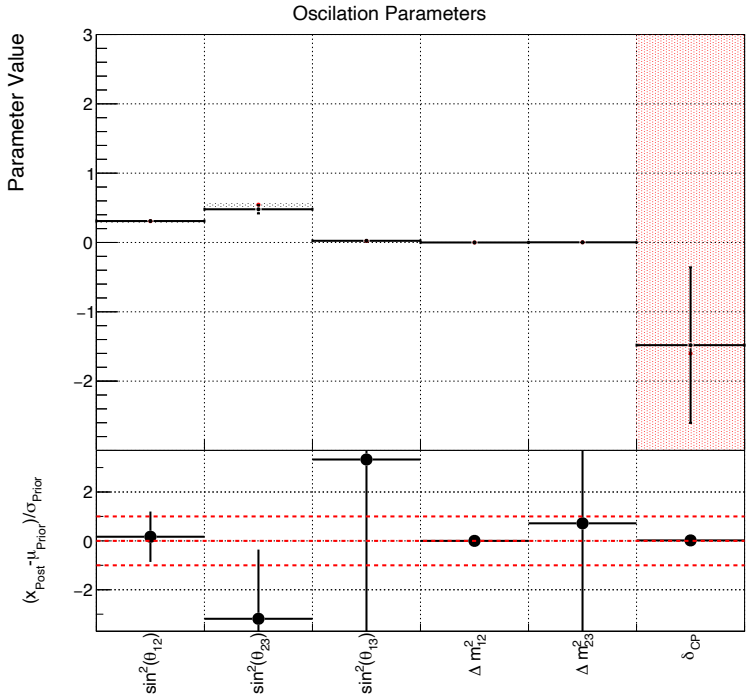

FIGURE 6.5: Pre-fit and post-fit central values of oscillation parameters after the Asimov fit. The grey band represents the pre-fit error, while the black point shows the post-fit central values and their errors. The ratio plot in the lower pad shows how far the parameters move in the post-fit compared to their prior values.

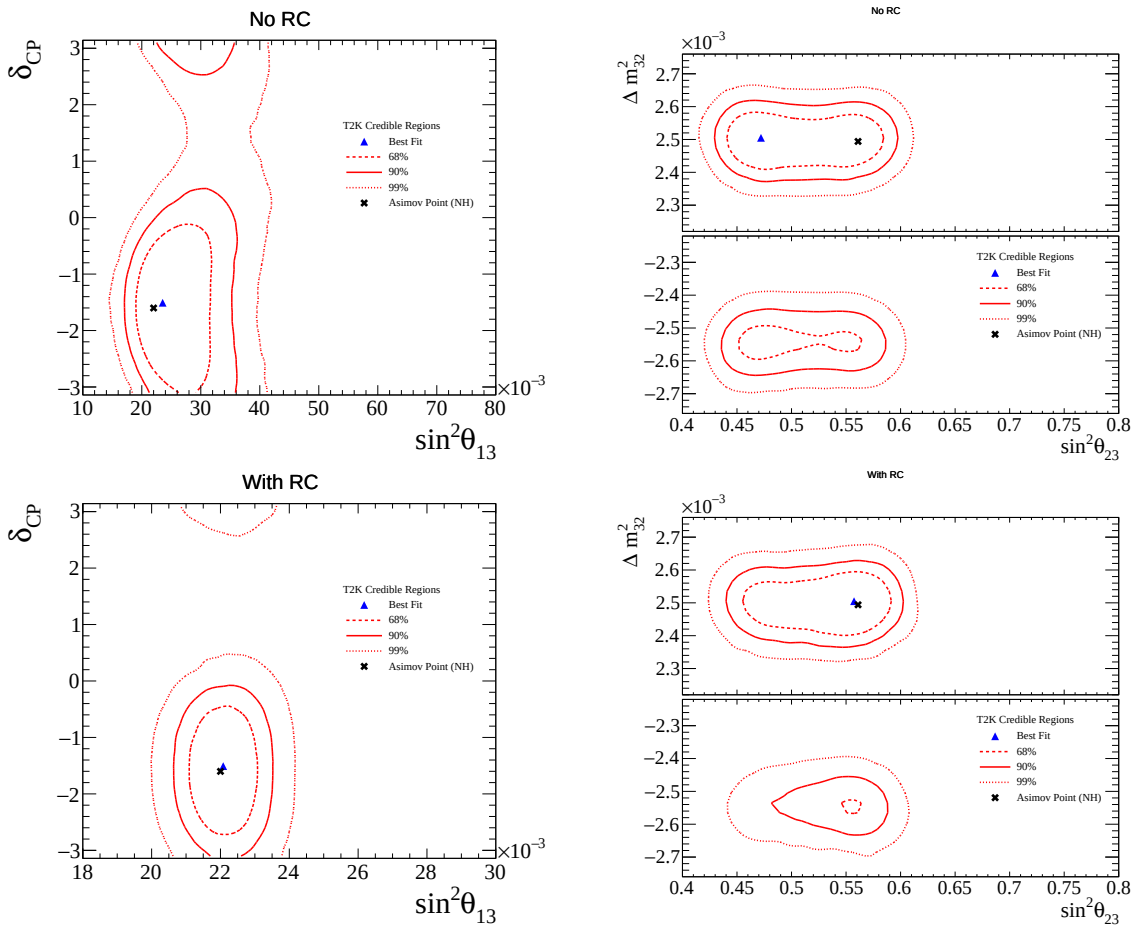

FIGURE 6.6: 2D appearance (left) and disappearance (right) contours from the Asimov fit. The contours in the top panel are without the reactor constraint, and those in the bottom panel are with the reactor constraint (RC).

The Asimov contours portray that the fitter behaves as it should, and is good to perform a data fit. The following sections will describe the data fit results in detail.

6.3 Data Fit - Systematic Parameters

Data fit was performed using both ND and FD data with all the 22 ND samples and 6 FD samples described in Chapter 2 with the addition of the multi-ring ν_e CC1π^+ sample. The fit also incorporates the new SK detector matrix and updated ν_μ and ν_e CC1π^+ sample binning. For the sake of brevity, only prior and post-fit uncertainties parameters of interest are shown. A complete set of posterior distributions for all the systematic parameters is included in Appendix B.

Fig. 6.7 shows the pre-fit and post-fit values after the data fit for the SPP parameters that impact the ν_e CC1π^+ sample directly. It can be seen that the C_5^A parameter has been pulled away by almost 2σ from its prior value. The SPP axial mass M_A^{RES} is also pulled to a lower value compared to the prior but is still within the prior's $\pm 1\sigma$. Non-res $I_{1/2}$ Low P_π, a parameter not constrained by the ND, has been pulled down by almost 1σ, while the trend is the opposite for the Non-res $I_{1/2}$ parameter. The RS Δ Decay parameter remains closer to its prior value, which implies that the data fit still prefers Δ-like decay over an isotropic decay. The SPP π^0 normalisation factor for the ν is pulled to a higher value by 1σ, but the same is not the case for the $\overline{\nu}$, where the constraint is fairly weaker.

A strong pull towards binding energy equal to 0 is observed for all the RES Binding Energy parameters. This is because the prior values of these parameters are set to a large conservative value of 25 MeV, while the values the MC generated were at 0. The results on all the SPP parameters are very consistent with the previous results in [87].

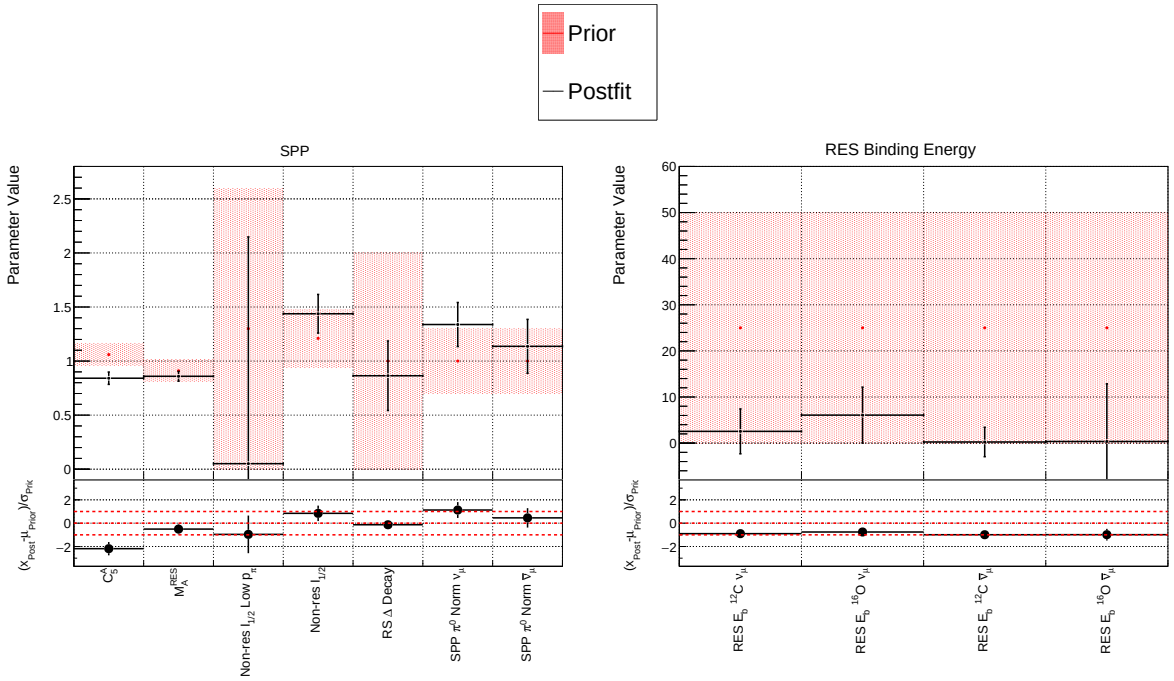

FIGURE 6.7: Pre-fit and Post-fit values of SPP cross-section and binding energy parameters.

One-dimensional posterior distributions for SPP cross-section parameters along with the ^{16}O RES E_b parameters are shown in Fig. 6.8. All of them demonstrate a nice Gaussian behaviour except for those parameters on a boundary.

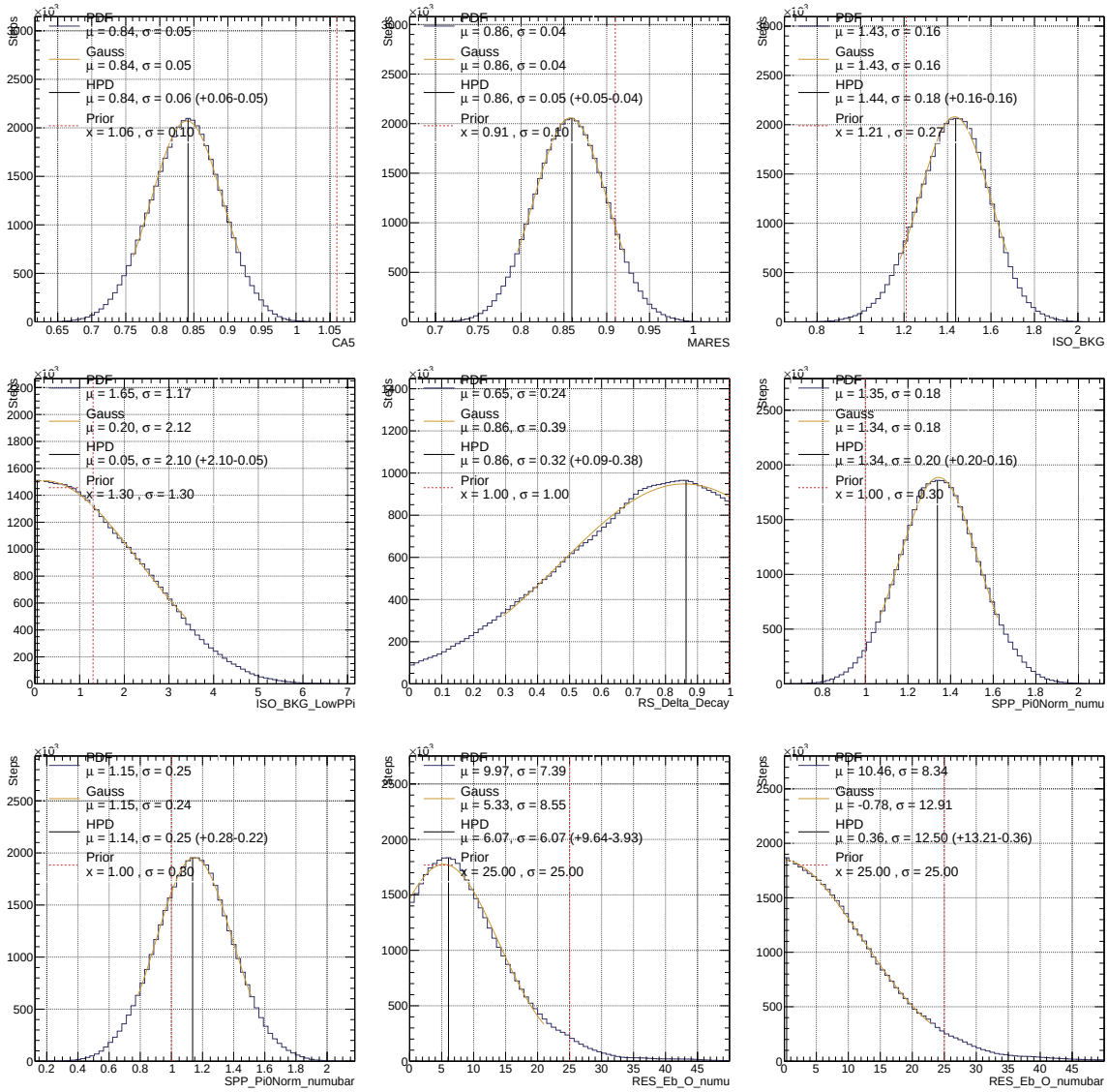

FIGURE 6.8: Posterior distributions of SPP cross-section parameters from the data fit.

The results of all other cross-section parameters are portrayed in Fig. 6.9. A detailed description of each parameter's behaviour can be found in [87] and [73].

Fig. 6.10 depicts some of the ND and SK flux parameters after the data fit. Some strong pulls away from the prior are observed in the ND flux parameters as seen in the top panel of the plots. However, we see the same behaviour for the corresponding ones at SK in the bottom panel. This is expected since SK flux parameters are almost entirely constrained by ND280 due to their high correlation with ND flux parameters.

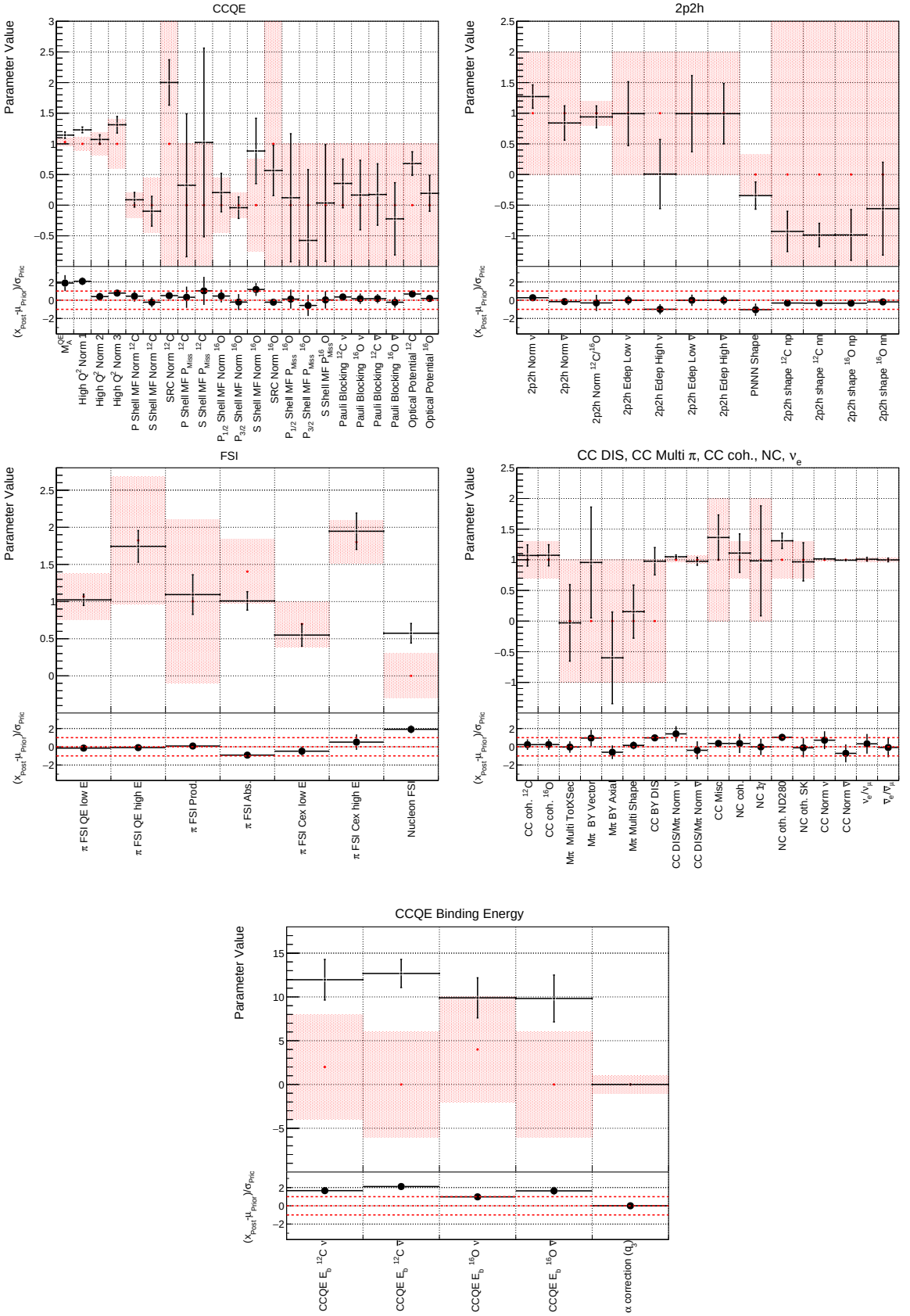

FIGURE 6.9: Pre-fit and the post-fit values of all other cross-section parameters grouped by the interaction types.

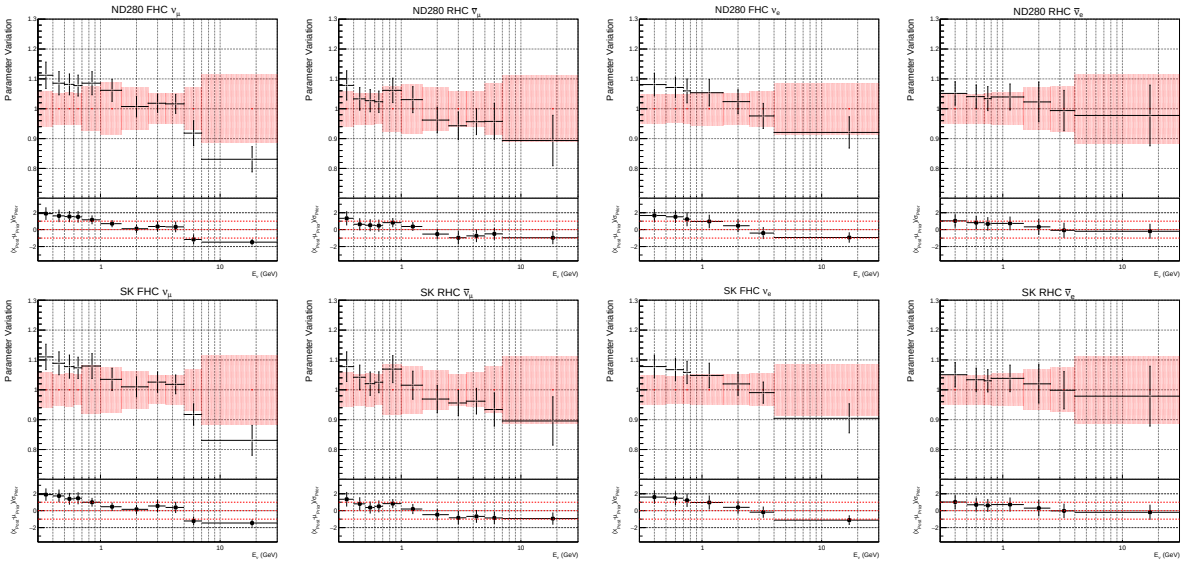

FIGURE 6.10: Pre-fit and Post-fit values of some ND and SK flux parameters from the data fit.

As discussed in Chapter 5, T2K's FD samples are not good at constraining SK detector parameters, which is one of the reasons why SK detector systematic errors are evaluated through the SK atmospheric MCMC procedure. Nevertheless, all the SK detector parameters that account for the 6 FD samples have post-fit values within $\pm 1\sigma$ of the prior central values, as can be seen from Fig. 6.11. The description of these parameters can be found in Table B.1.

The energy scale uncertainty (described in Section 5.4.2) is applied to the lepton momentum during the fit. Hence, its name as displayed in Fig. 6.12 is "momentum scale". This parameter has a slightly non-Gaussian behaviour but is still within the vicinity of its prior value.

The correlation matrix in 6.13 shows the full post-fit (anti)correlations between all the SK detector parameters, energy scale (marked momentum scale in the plot) and oscillation parameters. It is evident that none of the SK detector parameters share any strong correlations with the oscillation parameters, which is crucial to obtaining an unbiased result. A very weak (anti)correlation indeed exists with $\sin^2\theta_{13}$ but it is bypassed when applying RC. The correlations between post-fit and pre-fit SK detector parameters are very similar, as can be observed when comparing the matrices in Fig. 6.13 and 5.9, emphasising again why we require the atmospheric fit to constrain SK detector errors.

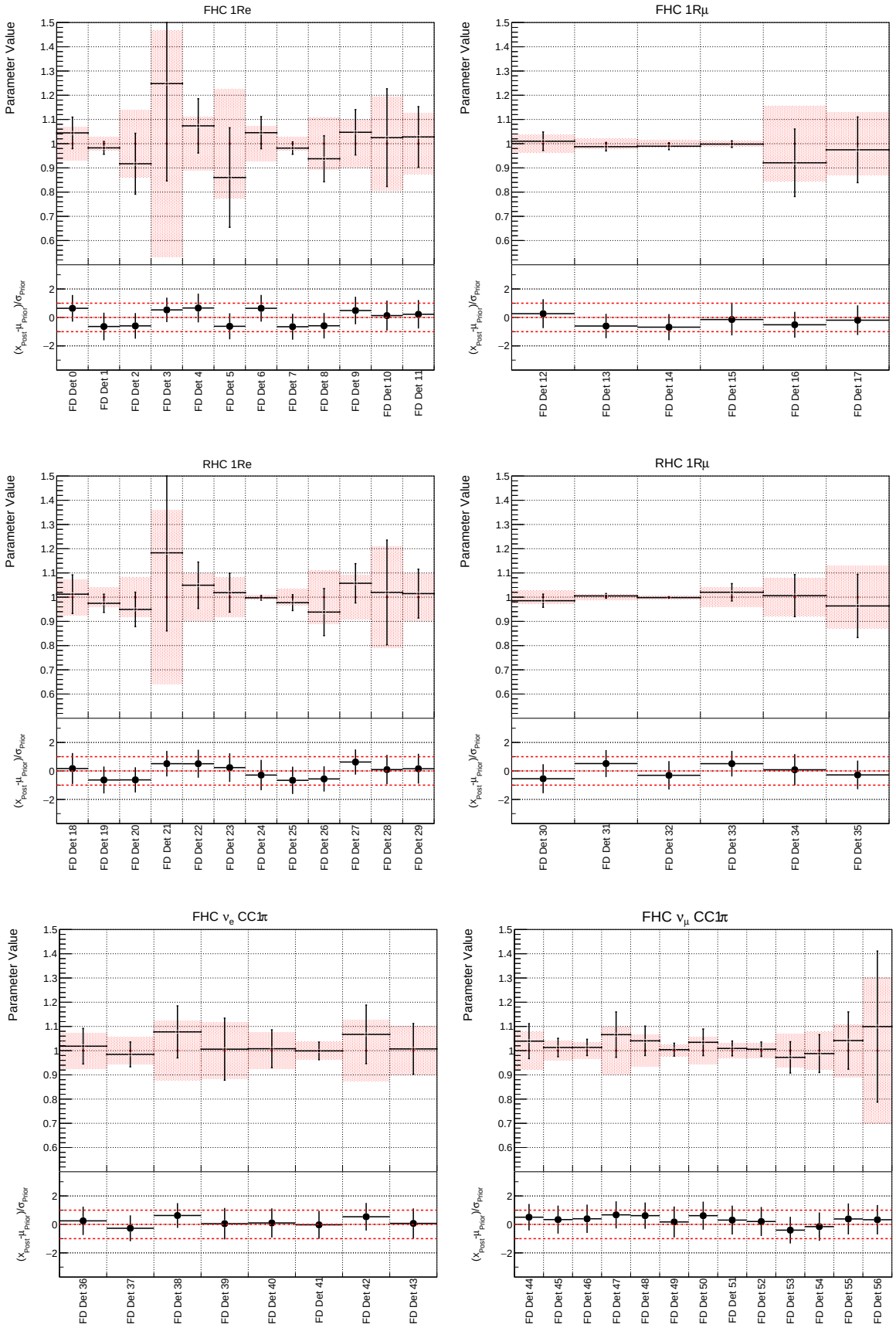

FIGURE 6.11: Pre-fit and the post-fit values of SK detector parameters grouped by the FD samples that they apply to.

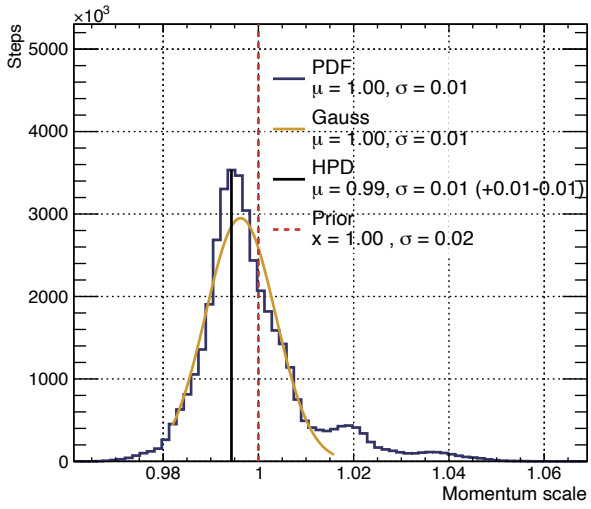

FIGURE 6.12: Posterior distribution of the momentum scale parameter from the data fit.

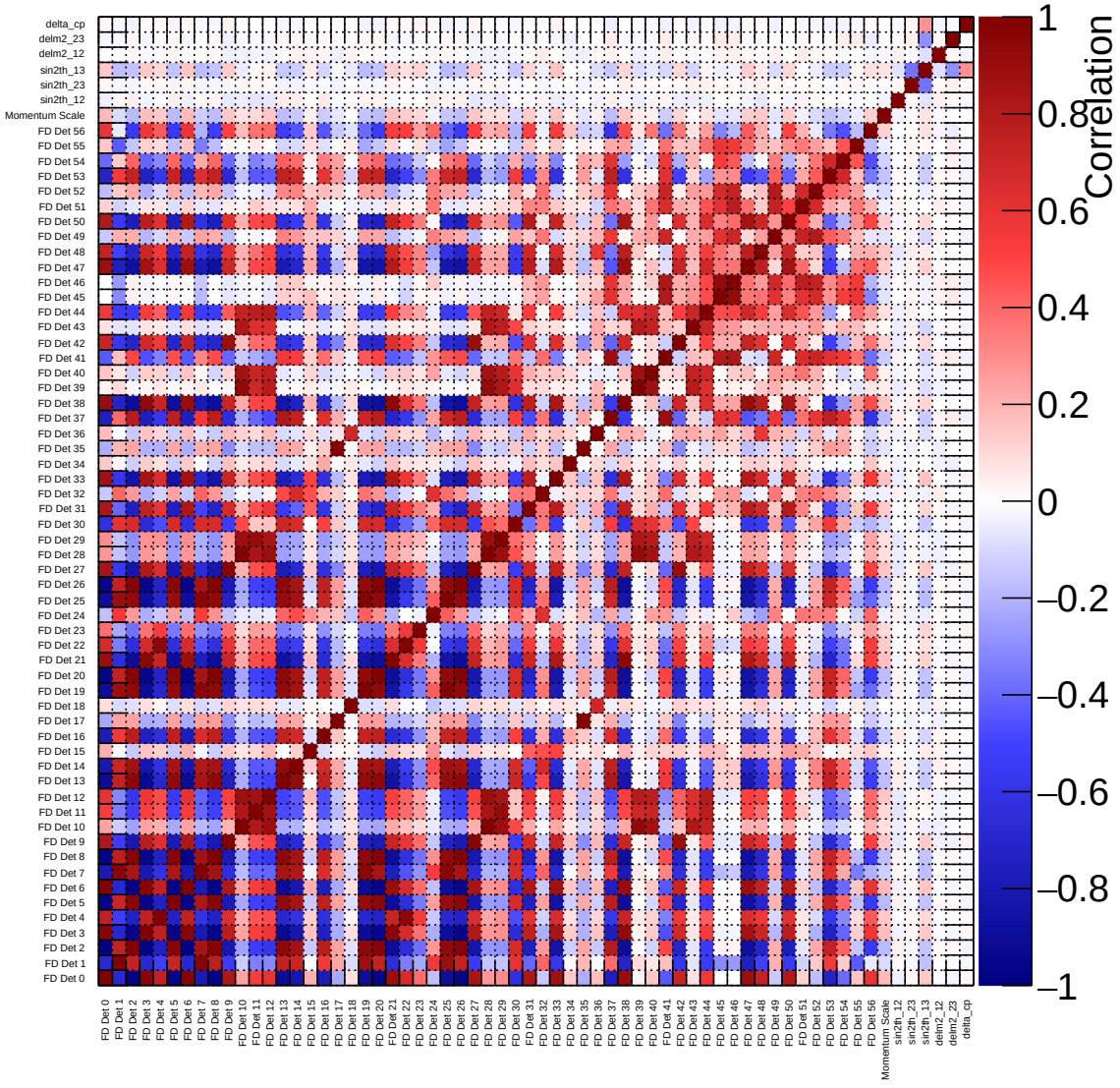

FIGURE 6.13: Post-fit correlations between SK detector matrix parameters, SK energy scale and the oscillation parameters.

Table 6.2 quotes the reduction of systematic errors for all the FD samples with the constraints provided by ND. The table is broken down to show the contribution of errors from different sources of uncertainty. For the pre-ND fit uncertainty, values of all the parameters are sampled from the prior covariance matrix.

Fit	FHC 1Rμ	RHC 1Rμ	FHC ν_μ CC1π	FHC 1Re	RHC 1Re	FHC ν_e CC1π
Pre-ND fit	14.80%	13.63%	11.77%	16.26%	13.22%	13.61%
Post-ND fit	2.74%	2.62%	2.40%	3.85%	3.11%	4.11%
Post-ND fit + SKDet SI/PN only	2.75%	2.63%	2.98%	4.00%	3.31%	5.45%
Post-ND fit + SKDet Det. only	3.07%	2.77%	3.28%	4.67%	4.84%	4.84%
Post-ND fit + SKDet total	3.11%	2.78%	3.88%	4.78%	4.94%	6.08%

TABLE 6.2: Errors on event rates (RMS/Mean) before and after a joint fit of ND and FD data.

The posterior predictive spectra of the expanded ν_e CC1π^+ sample, overlaid with data events is shown in Fig. 6.14. The plot shows the pre-ND fit error bands (labelled PreND) and also post-ND fit error bands without (PostND woSKDet) and with throws from the SK detector matrix (PostND wSKDet). It can be seen that the SK detector matrix increases the ND post-fit error by a small amount, but is still much smaller the pre-ND fit error bands.

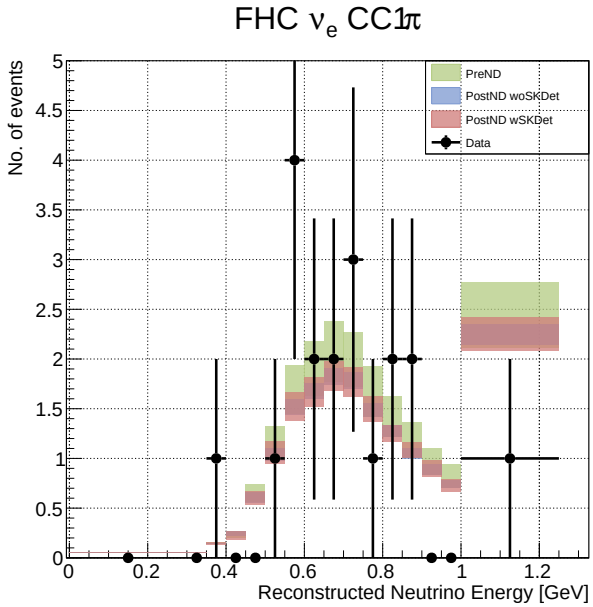

FIGURE 6.14: ν_e CC1π^+ pre-ND fit and post-ND fit predictions (without and with SK detector uncertainties) along with data. The reduction of errors seen in Table 6.2 is evident in this figure.

6.4 Data Fit - Oscillation Parameters

As discussed in Section 6.2 (see also Fig. 6.15), using T2K's data alone cannot lift the degeneracies between θ_{23}, θ_{13} and δ_{CP} parameters, unless reactor constraint on θ_{13} (RC) is used. Therefore, the results and discussions shown hereafter will always be with the RC applied. Furthermore, T2K performed simulated data studies to test the robustness of its results when using alternate model predictions as described in [5]. As a result of that study, it was determined that smearing of 1.35×10^{-5} eV^2 needs to be applied on the uncertainty of Δm^2_{32}, increasing its uncertainty from 5.3×10^{-5} eV^2 to 5.7×10^{-5} eV^2. In all the results shown, this

smearing is also applied unless stated otherwise. All the one-dimensional posterior distributions are normalized to unity.

A depiction of how RC tightens the $\sin^2\theta_{13}$–δ_{CP} contour is shown in Fig. 6.15. The violet band shows the RC ($\sin^2\theta_{13} = 0.0220 \pm 0.0007$) obtained from the PDG 2019 world average [91].

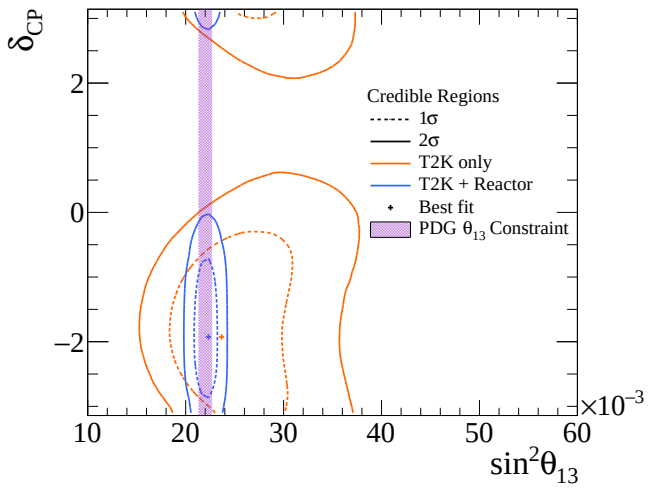

FIGURE 6.15: The impact of RC on the 2D $\sin^2\theta_{13}$–δ_{CP} contours.

The data-MC event rate comparisons after the fit are shown in Table 6.3, where the MC is reweighted to the highest posterior density (HPD) points of all the systematic and oscillation parameters.

Sample	Data	Best fit MC
FHC 1Rμ	357	374.50
RHC 1Rμ	137	142.56
FHC ν_μ CC1π	140	132.41
FHC 1Re	102	95.87
RHC 1Re	16	17.18
FHC ν_e CC1π	19	17.94

TABLE 6.3: Event rate comparison between Data and MC reweighted to the HPD points after the data fit.

The Bayesian posterior predictive p-values (PPPs) were calculated for the total FD samples through bin-by-bin (or, Shape-based) and total event rate (Rate-based) χ^2 calculations to test the compatibility between the FD data and the best-fit model, also referred to as goodness-of-fit (GOF). The PPPs were determined through the approach laid out by Gelman [92, 93] and are quoted in Table 6.4.

	Shape-Based	Rate-Based
p-value	0.1520	0.1960

TABLE 6.4: Bayesian PPPs, quoted separately for shape-based and rate-based χ^2 calculation.

The shape-based PPP test yields a p-value of 15.2% while the rate-based PPP test produces a p-value of 19.6%, both of which pass the p-value $> 5\%$ criteria used by T2K.

With the data-best fit MC compatibility well established, we can now proceed to look at the oscillation parameters. In Bayesian statistics, credible intervals (C.I.) give the probability that the true value of a parameter being measured falls within a certain interval. In the following figures, posterior probability distributions and contours of all the oscillation parameters are shown with both the % C.I. and $n\sigma$ C.I representations for the reader's flexibility.

Fig. 6.16 and 6.18 show the appearance and disappearance parameter contours. The 1D posterior distributions of δ_{CP}, $\sin^2\theta_{23}$ and Δm^2_{32} are shown in Figs. 6.17, 6.19 and 6.20, respectively.

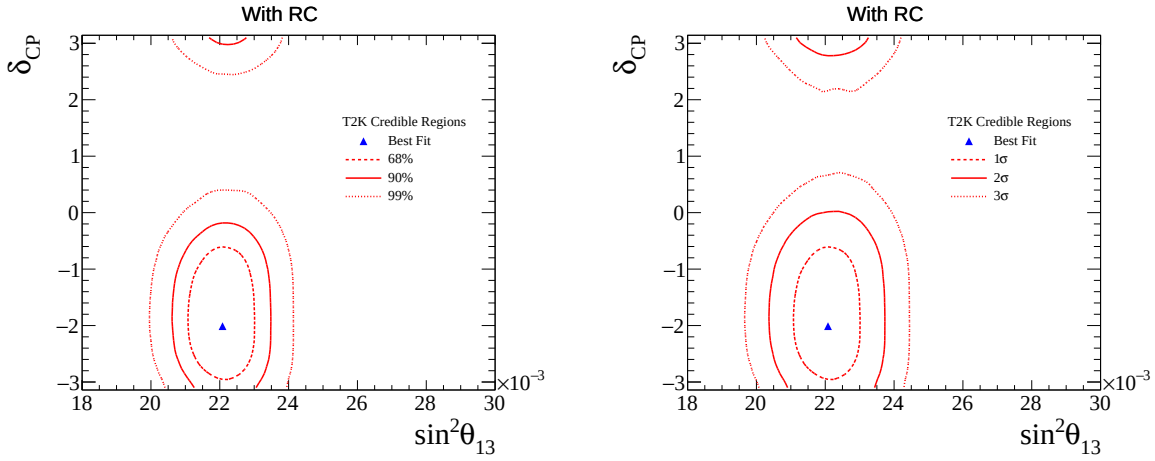

FIGURE 6.16: 2D δ_{CP}–$\sin^2\theta_{13}$ appearance parameters contours marginalized over both mass hierarchies. The plot on the left shows credible regions in %, while the right plot shows $n\sigma$ credible regions. RC is applied.

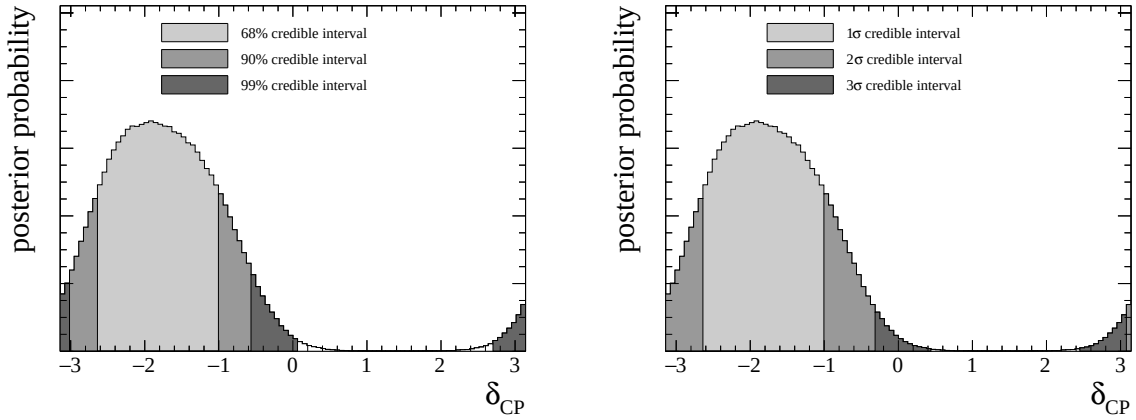

FIGURE 6.17: 1D posterior distribution along with C.I in % (left) and in $n\sigma$ (right) for δ_{CP}, marginalized over both mass hierarchies. RC is applied.

CP conserving values of $\delta_{CP} = 0, \pm\pi$ are outside the 90% C.I, with the HPD pointing towards a region that prefers maximal CP violation.

The disappearance contours in Fig. 6.18 show that there is a weak preference for upper octant of θ_{23}, although the lower octant is still allowed inside the 68% C.I. Similarly, from Fig. 6.20, it can be seen that the HPD points towards $\Delta m^2_{32} > 0$, or the normal hierarchy.

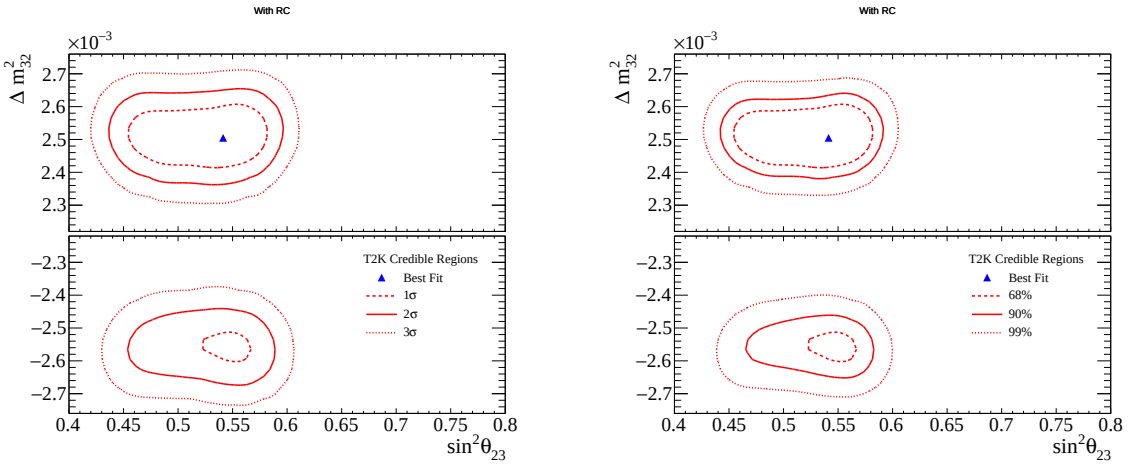

FIGURE 6.18: 2D Δm^2_{32}–$\sin^2\theta_{23}$ disappearance parameters contours marginalized over both mass hierarchies. RC is applied.

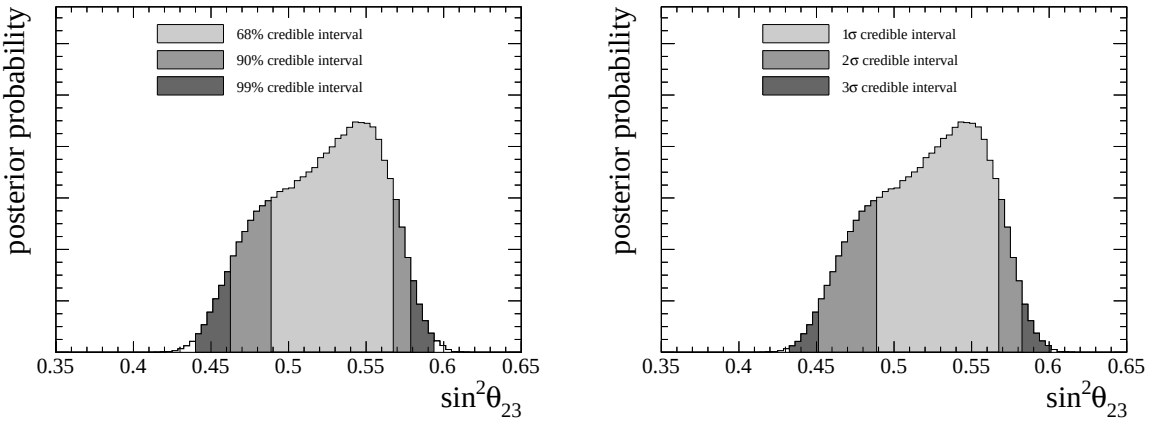

FIGURE 6.19: 1D posterior distribution along with C.I in % (left) and in $n\sigma$ (right) for $\sin^2\theta_{23}$, marginalized over both mass hierarchies. RC is applied.

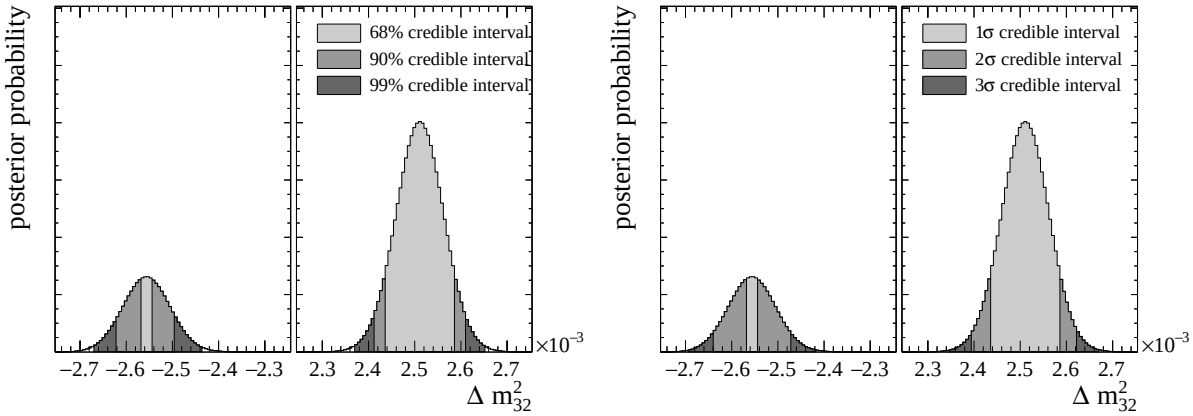

FIGURE 6.20: 1D posterior distribution along with C.I in % (left) and in $n\sigma$ (right) for Δm^2_{32}, marginalized over both mass hierarchies. RC is applied.

With the Bayesian prowess of MCMC, useful inferences can also be drawn about model preferences based on conditional probabilities. A neutrino mass hierarchy–θ_{23} octant conditional probability comparison is shown in Table 6.5 for the case without RC and in Table 6.6 for that with RC.

	LO	UO	Sum
NH	0.27	0.36	0.63
IH	0.17	0.20	0.37
Sum	0.44	0.56	1.00

TABLE 6.5: Comparisons of probabilities for various combination of mass hierarchy and θ_{23} octant from the data fit without RC.

	LO	UO	Sum
NH	0.23	0.53	0.76
IH	0.05	0.19	0.24
Sum	0.28	0.72	1.00

TABLE 6.6: Comparisons of probabilities for various combination of mass hierarchy and θ_{23} octant from the data fit with RC.

From Table 6.6, it can be stated that with RC, there is a 76% probability for normal mass hierarchy and 72% probability for the upper octant of θ_{23} from the result of the data fit.

Furthermore, these probabilities can be used to calculate the Bayes factor. Bayes factor is a quantitative way through which one can deduce whether a particular hypothesis is preferred over another. In other words, it is the ratio between the probability of one hypothesis and the probability of the other. For an MCMC that has converged, the Bayes factor is obtained as the ratio of MCMC steps that accumulate in the former's region to that of the latter. In the case of T2K's results, Bayes factors for both neutrino mass hierarchy and θ_{23} octant can be calculated.

In the data fit without RC, the Bayes factor
— for $\Delta m^2_{32} > 0$ or $\Delta m^2_{32} < 0$ (NH/IH) was found to be $\mathfrak{B}(NH/IH) = 1.70$
— and for $\sin^2\theta_{23} > 0.5$ or $\sin^2\theta_{23} < 0.5$ (UO/LO) was $\mathfrak{B}(UO/LO) = 1.27$.
With reactor constraints, these values become $\mathfrak{B}(NH/IH) = 3.17$ and $\mathfrak{B}(UO/LO) = 2.57$. The Bayes factors can also be interpreted with Jeffrey's scales [94]. According to this, the numbers quoted above are both classified as "barely worth mentioning".

The best-fit values of appearance and disappearance oscillation parameters are extracted from the mode of their respective 2D contours. The $n\sigma$ C.I. are calculated from their individual 1D posterior distributions.

Parameter	δ_{CP} [rad.]	$\sin^2\theta_{23}$	$\sin^2\theta_{13}$	Δm^2_{32} [$\times 10^{-3}$ eV^2]
2D Best Fit Value	-2.01	0.54	0.022	2.51
68%(1σ) C.I Range	[-2.60,-1.01]	[0.49,0.57]	[0.021,0.023]	[-2.57,-2.54] $\cup$ [2.44,2.59]
95.4%(2σ) C.I Range	[-π,-0.34] $\cup$ [3.06, π]	[0.45,0.58]	[0.021,0.024]	[-2.64,-2.47] $\cup$ [2.39,2.62]
99.73%(3σ) C.I Range	[-π,0.38] $\cup$ [2.43,π]	[0.43,0.60]	[0.020,0.024]	[-2.69,-2.42] $\cup$ [2.35,2.67]

TABLE 6.7: Best fit values of oscillation parameters from the data fit, with RC applied.

The CP violation phase can also be represented in a PMNS model independent formalism through the Jarlskog invariant. There are two equally valid choices of δ_{CP} priors that can be used to calculate J_{CP}, namely a prior flat in δ_{CP} or a prior flat in $\sin\delta_{CP}$. The posterior distributions of J_{CP} can be different for the choice of this prior.

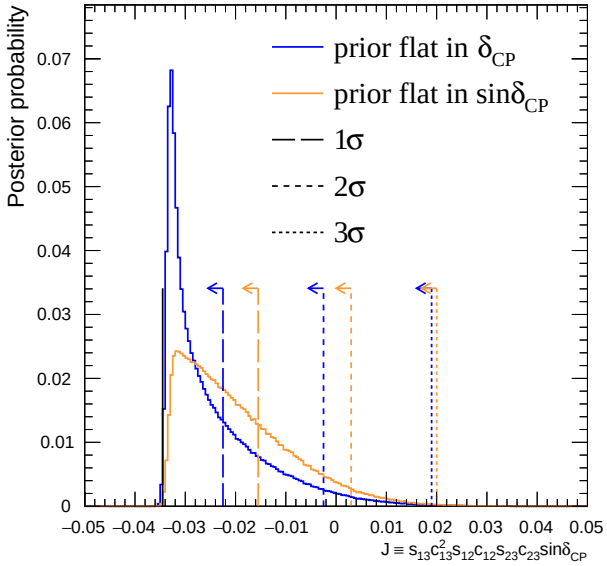

FIGURE 6.21: 1D posterior probability distribution of the Jarlskog invariant with posteriors derived from the two choices of priors overlaid. RC is applied.

CP conserving value of $J_{CP} = 0$ is outside the 90% C.I. when using a prior flat in δ_{CP} while the prior that is flat in $\sin\delta_{CP}$ includes $J_{CP} = 0$ within the 90% C.I. Regardless of it, the HPD in both the cases are directed towards maximum CP violation in the leptonic sector.

6.5 Comparison with T2K's Latest Analysis

It is important to reiterate that a dedicated far-detector sample binning study had never been performed before. All the samples were studied with an arbitrary choice of kinematic bins before this analysis. By adopting a physics-driven choice of binning described in Section 3.7, the problem of kinematic bins being smaller than the detector resolution of that parameter was avoided. By the numbers, the 1Rμ samples had a reduction of reconstructed neutrino energy bins from 71 to 42 and 71 to 36 for the ν_μ CC1π^+ sample.

Fig. 6.22 and 6.23 show the appearance and disappearance contour comparisons between the analysis described in this thesis (labelled This Analysis) and the result from T2K's latest official oscillation analysis [60] (labelled OA2023 in the plots).

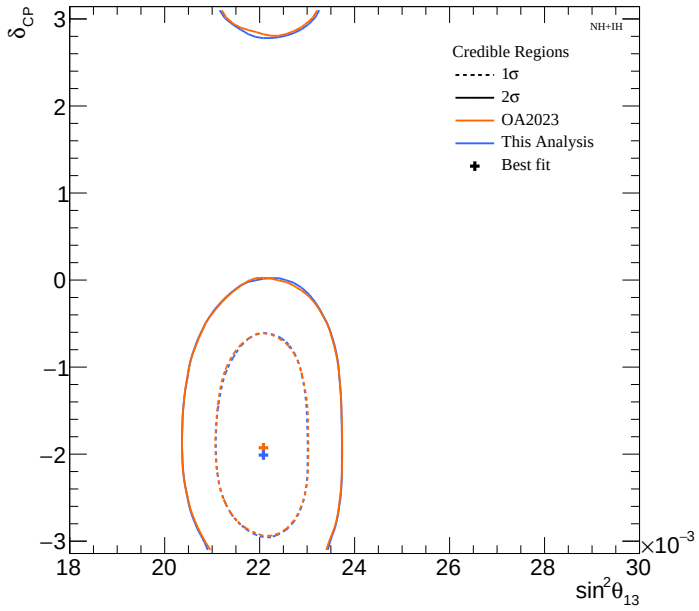

FIGURE 6.22: 2D appearance contour comparisons between T2K's latest official result (in orange) and this analysis (in blue). 1σ and 2σ C.I. are drawn and RC is applied.

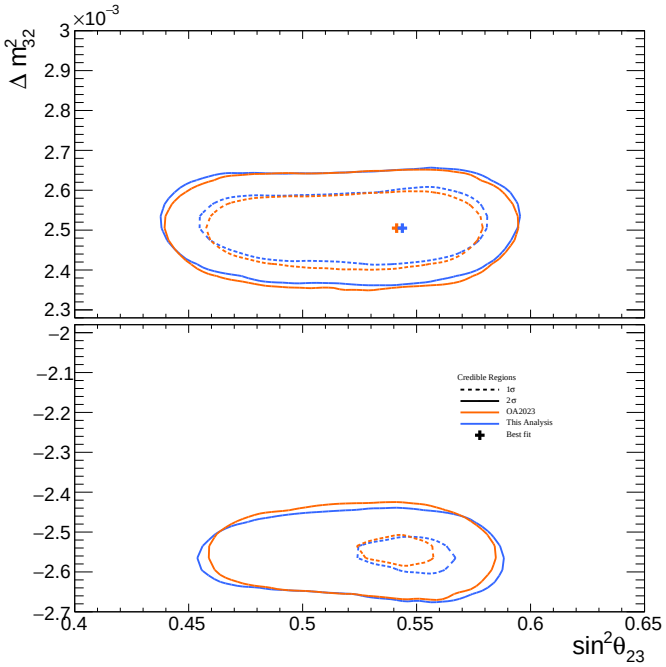

FIGURE 6.23: 2D appearance contour comparisons between T2K's latest official result (in orange) and this analysis (in blue). 1σ and 2σ C.I. are drawn and RC is applied.

The Bayes factors between the two analyses are shown in Table 6.8. For UO/LO, the Bayes factor remains the same. Although there is a small drop in that of the NH/IH for this analysis, the conclusion is still "Barely worth mentioning" across both analyses.

Bayes factor	T2K's latest result	This Analysis
$\mathfrak{B}(NH/IH)$	3.35	3.17
$\mathfrak{B}(UO/LO)$	2.57	2.57

TABLE 6.8: Comparision of Bayes factors of neutrino mass hierarchy and θ_{23} octant between T2K's latest result [63] and This Analysis. Calculated with RC applied

A very important conclusion that can be drawn from these contours is that T2K's oscillation analysis results are not much dependent on the choice of FD sample binning, and hence not vulnerable to potential reconstruction or modelling biases coming from it. Furthermore, the new multi-ring ν_e CC1π^+ sample's addition into the analysis removes the strong selection dependence on π^+ momentum because of the Cherenkov threshold for the ν_e CC1π^+ sample. It also improves the overall ν_e CC1π^+ selection efficiencies. These changes do not alter the results much. The best-fit points from the two analyses lay very close to each other within fractional differences. It can be said that T2K's oscillation parameter estimations are very robust, and are expected to improve with more statistics accumulated in the coming years of data taking.

7

Future Sensitivity Study

Dream, Dream Dream,
Dreams transform into thoughts,
And thoughts result in action.

A.P.J Abdul Kalam

7.1 Data Excess in ν_e CC1π^+ Sample

Before the introduction of the multi-ring ν_e CC1π^+ sample, a low-momentum data excess was observed in the single-ring ν_e CC1π^+ sample (see Fig. 7.2a). However, due to the low statistics of the sample, it was unsure whether any form of detector or interaction mis-modelling caused this excess, or also just a fluctuation in data.

Recently, this trend was also observed in the SK atmospheric single-ring ν_e CC1π^+ sample that was used in the SK+T2K joint analysis [95]. This sample, unlike the T2K counterpart, was high in statistics and a mere statistical fluctuation could not explain the observed excess.

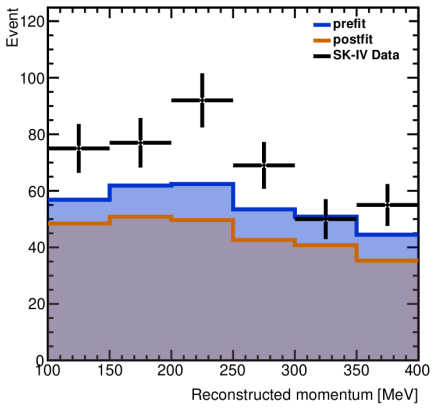

FIGURE 7.1: Data-MC comparison for the low-momentum sub-GeV atmospheric ν_e CC1π^+ sample. The shaded bands show pre-fit and post-fit errors. The sample includes both up-going and down-going atmospheric neutrinos. Plot from [96].

With the inclusion of the multi-ring ν_e CC1π^+ sample that removes the dependence over pion kinematics modelling, the extent of this excess was reduced although not very significantly. The low electron momentum data points tend to be higher than the MC prediction in that region even in the expanded sample as shown in Fig. 7.2b.

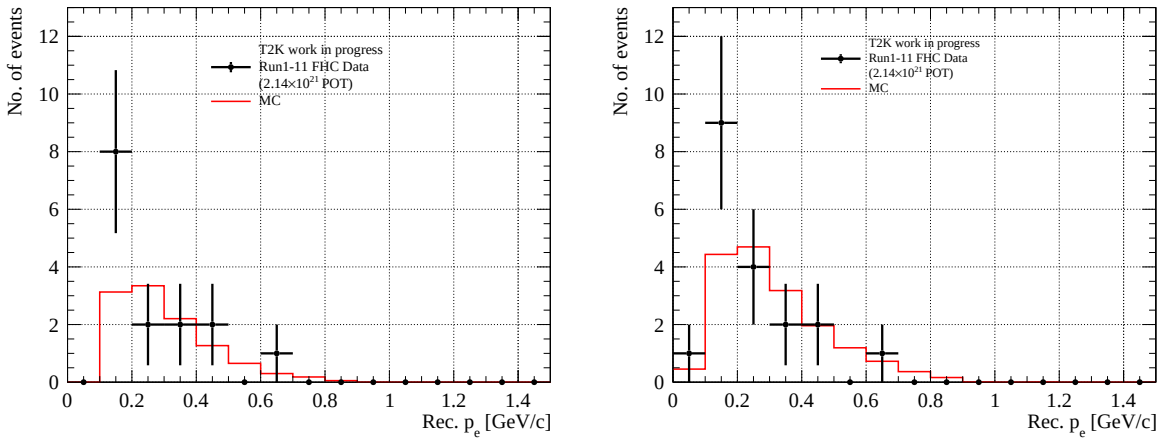

(A) FHC single-ring ν_e CC1π^+ sample

(B) Expanded FHC ν_e CC1π^+ sample

FIGURE 7.2: Data-MC comparison of reconstructed electron momentum distributions.

After confirming this trend in both the experiments results, and the ν_e CC1π^+ sample being a ν_e appearance at T2K, a special task force was formed in T2K called the CC1π task force whose aim is to study the low e momentum data excess in various contexts, ranging from cross-section modelling to detector systematics. The Author performed two studies, the first of which is described in Section 5.5, and an Asimov fit using a modified MC prediction that will be explained in the next section, both of which are relevant within the CC1π task force plans.

Furthermore, it was shown in Section 3.5 that the multi-ring ν_e CC1π^+ sample suffers from low selection efficiency. This is triggered mainly by the reconstruction software's failure to reconstruct the correct number of rings and decay electrons.

7.2 Constructing the Fake-Data Set

Assuming that due to possible improvements in the future, both the low e momentum discrepancy and the low selection efficiency issue are fixed, we constructed a fake data set by artificially increasing the nominal ν_e CC1π^+ event rates by 30% uniformly (see Table 7.1 for event rate comparison). This number was conservatively chosen to cover both the data-MC excess observed in the single-ring ν_e CC1π^+ sample and the low selection efficiency seen in the multi-ring ν_e CC1π^+ sample.

Sample	Event Rate
Default ν_e CC1π^+	16.53
30% increased ν_e CC1π^+	23.18

TABLE 7.1: Comparison of event rates for the default ν_e CC1π^+ sample and for the sample whose statistics was increased by 30%

Before the Asimov fit, an LLH scan was performed to see the impact of this 30% statistics increase on oscillation parameters. The LLH scans are generated by varying one oscillation parameter at a time while keeping the others fixed. Therefore, these distributions are not representative of the true correlations between oscillation parameters, but it is still informative whether the fake data does impact the likelihood term as it should.

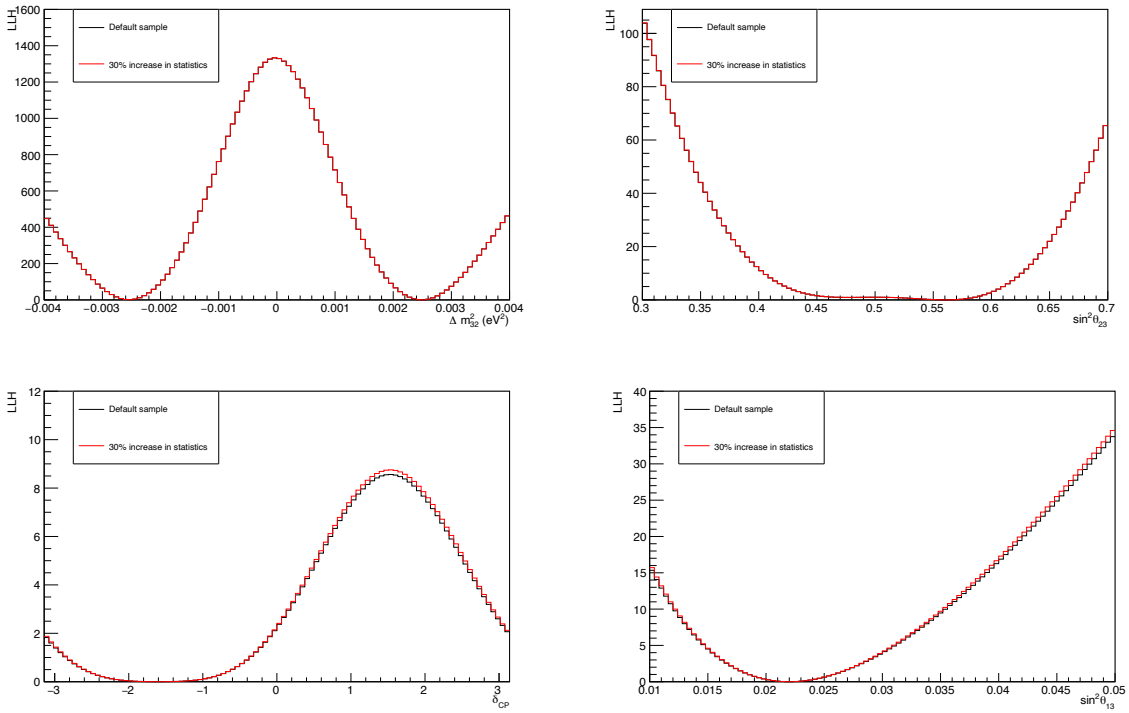

FIGURE 7.3: Oscillation parameter LLH scan (all FD samples) comparisons between the default ν_e CC1π^+ sample and the 30% statistics enhanced ν_e CC1π^+ sample.

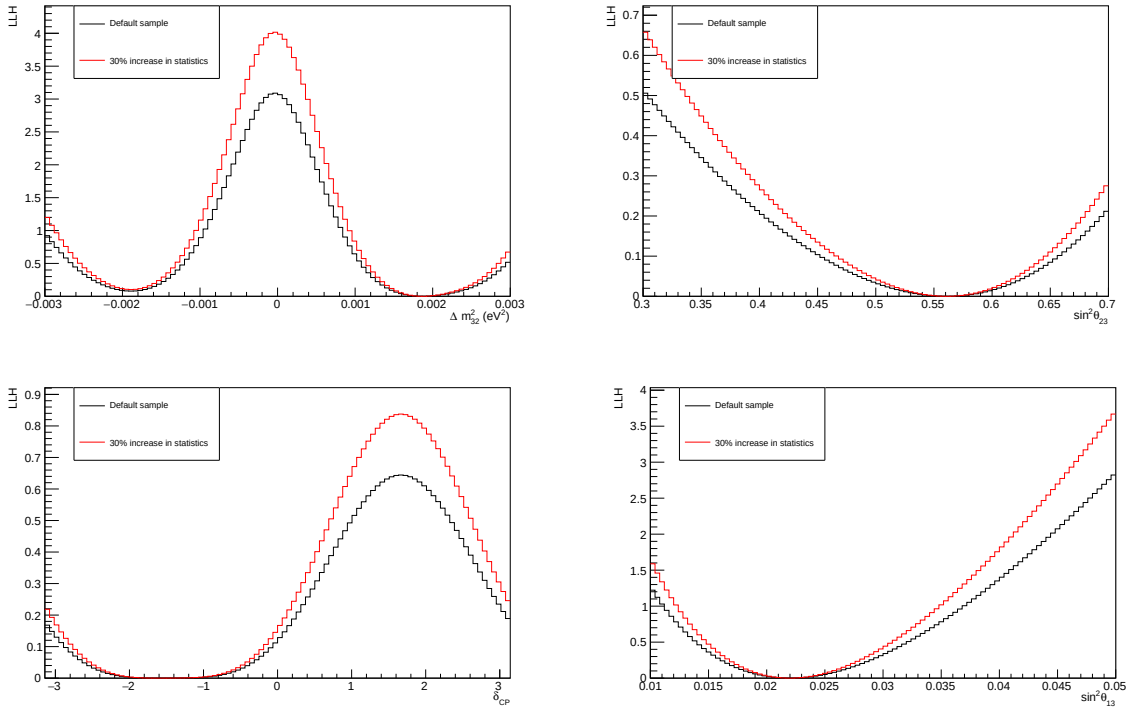

FIGURE 7.4: Oscillation parameter LLH scan (only ν_e CC1π^+ samples) comparisons between the default ν_e CC1π^+ sample and the 30% statistics enhanced ν_e CC1π^+ sample.

It can be seen in Fig. 7.3 and 7.4 that the increased statistics of the ν_e CC1π^+ sample does impact the appearance parameters. The results of an Asimov fit, which also takes into account correlations between the oscillation parameters, are discussed in the next section.

7.3 Asimov Fit Results

Asimov fits were performed with ND280 data and two sets of FD fake data as follows:

- Default ν_e CC1π^+ sample,
- ν_e CC1π^+ sample with statistics enhanced uniformly by 30%.

For a 30% uniform increase in ν_e CC1π^+ statistics, it can be seen that the impact on appearance parameters is minimal (Fig. 7.5). Incidentally, a notable improvement is observed in the disappearance parameters (Fig. 7.6). While the reason behind this behaviour is not very well understood, it can be attributed to the effects of correlation between the oscillation parameters.

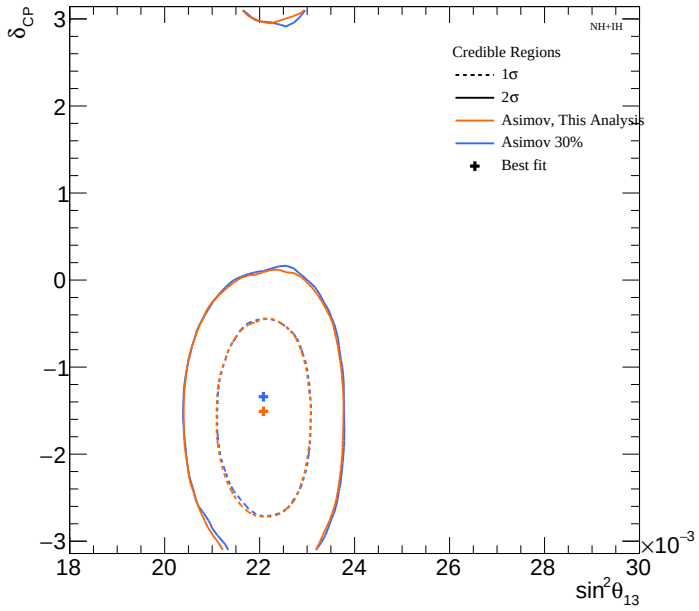

FIGURE 7.5: Appearance parameter contour comparison

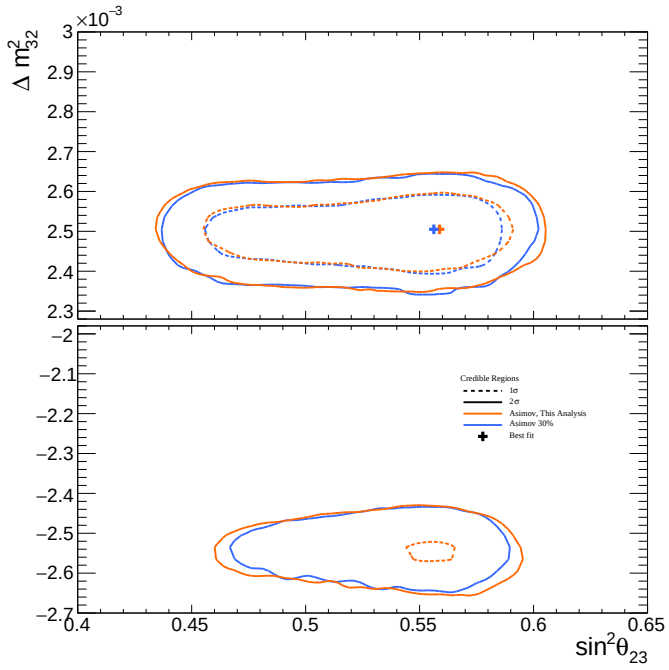

FIGURE 7.6: Disappearance parameter contour comparison

It is better to look at a model-independent parameter like J_{CP}, since all the mixing angles and δ_{CP} are involved in its calculation, thereby including correlations between all the parameters. From the posterior distributions of J_{CP}, we can observe that both the Asimov data sets are consistent. In addition, the 30% statistically enhanced Asimov produces a minor improvement in the HPD.

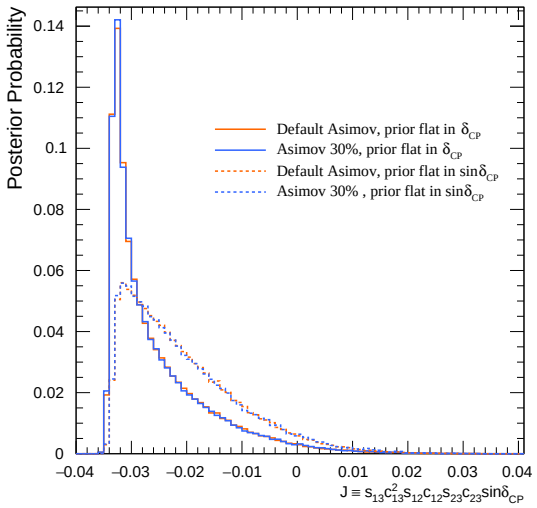

FIGURE 7.7: The comparison between posterior probabilities of the Jarlskog invariant for the default ν_e CC1π^+ sample, and the sample whose statistics was increased by 30%. Both choices of δ_{CP} priors are also shown.

7.4 Impact of Oscillation Parameters on the ν_e CC1π^+ Sample

We also investigated the impact of varying the oscillation parameters on the ν_e CC1π^+ sample's reconstructed neutrino energy spectra, in efforts to understand the behaviours observed earlier in Fig. 4.4 depicting LLH scans and also for that in Fig. 7.4.

When studying the impact of one oscillation parameter, all others were kept fixed. The parameters were varied $\pm$ 10, $\pm$20% from their Asimov values and their reconstructed neutrino energy spectra were overlaid. They are portrayed in Fig. 7.8.

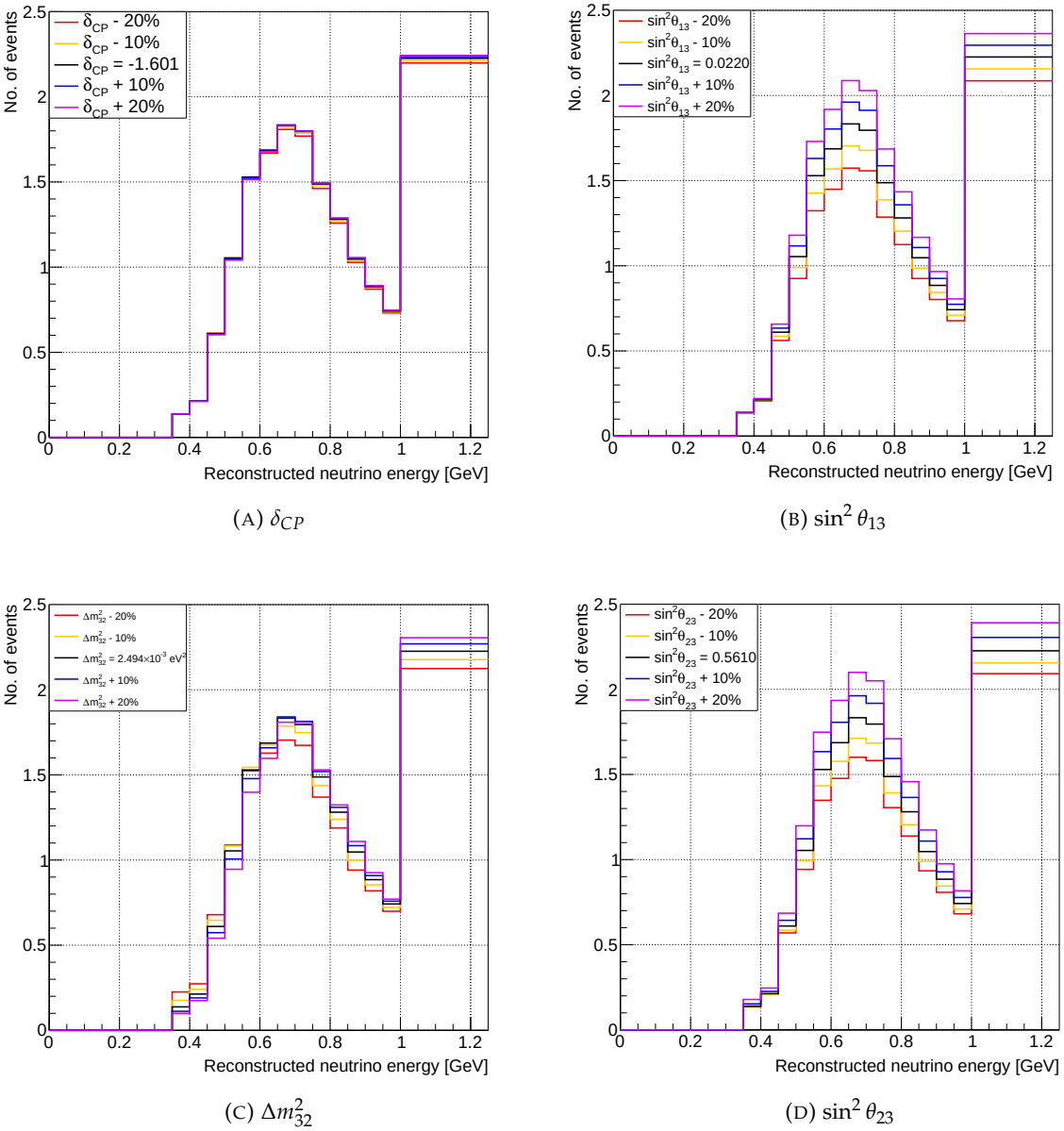

(A) δ_{CP} (B) $\sin^2\theta_{13}$

(C) Δm^2_{32} (D) $\sin^2\theta_{23}$

FIGURE 7.8: Impact of varying the oscillation parameters on the ν_e CC1π^+ sample's reconstructed neutrino energy spectra. The different coloured histograms mark the percentage variation of these parameters as labelled in their respective legends.

From these distributions, we see that the variations of -20% to $+20\%$ in $\sin^2\theta_{13}$ and $\sin^2\theta_{23}$ result only in overall normalisation changes in each reconstructed neutrino energy bins. The same order of changes in δ_{CP} do not produce huge differences in the ν_e CC1π^+'s spectra. However, it can be noticed that the impact of δ_{CP} is mostly experienced in energies above 0.6 GeV, which is interesting.

The impact of the ν_e CC1π^+ on the Δm^2_{32}'s LLH is hinted by how this parameter changes the shape of the ν_e CC1π^+ spectra in the bottom left plot in Fig. 7.8.

8

Summary

> There are two possible outcomes: if the result confirms the hypothesis, then you've made a measurement. If the result is contrary to the hypothesis, then you've made a discovery.
>
> *Enrico Fermi*

This thesis brought forward multiple advancements in T2K's oscillation analysis studies. Notably, it is the first T2K study to incorporate the multi-ring ν_e CC1π^+ sample. When combined with the existing single-ring ν_e CC1π^+ sample, the multi-ring ν_e CC1π^+ sample removes the strong dependence on the π^+ momentum threshold required for its Cherenkov ring detection at SK, effectively eliminating any dependency on the π^+ kinematics model. Additionally, it moderately enhances the statistical power of the ν_e appearance analysis, which is sensitive to δ_{CP}, by lifting the total ν_e CC1π^+ statistics by 27%. The combined sample also leads to an improved post-fit data-MC agreement compared to using only the single-ring sample. The inclusion of the multi-ring sample illustrated the best use of T2K's data collected so far, as the experiment continues to gather more data in the coming years.

With the inclusion of the multi-ring sample, the SK detector uncertainty matrix was also updated, and correlations between single and multi-ring samples were added. This resulted in an overall reduction in the errors of SK detector parameters.

Before the studies performed in this thesis, the SK samples used a general kinematic binning scheme for oscillation analysis. The binning optimisation performed by studying the E_{rec} resolution incorporated the effects of resolution, making the kinematic binning used in this analysis more physics-motivated and robust than before.

Taking all these developments into account, the oscillation analysis that was performed indicates a preference for maximal CP violation. Values of δ_{CP} that conserve CP, such as 0 and $\pm\pi$, fall outside the 90% credible intervals, with the highest posterior probability near $\delta_{CP} = -\pi/2$. Furthermore, the analysis shows a slight preference for normal hierarchy and the upper octant of θ_{23}. We also report 15.2% shape-based and 19.6% rate-based Bayesian posterior predictive p-values, which pass the p-value $> 5\%$ criteria used by T2K. In addition, these results align perfectly with T2K's latest [60] and also previous results [64], demonstrating consistency across analyses.

The data-MC discrepancy observed in both Super-Kamiokande (SK) atmospheric and T2K beam single-ring ν_e CC1π^+ samples has been a significant topic of investigation recently. The Author conducted a study to assess the impact of uncertainties in SK's photomultiplier tube (PMT) reflectivity parameters on the reconstruction of ν_e CC1π^+ events. The study

found that the impact was minimal, thereby ruling out PMT reflectivity as a source of the discrepancy. Additionally, the Author carried out a sensitivity study using increased statistics of the ν_e CC1π^+ sample. This study underscored the importance of understanding and resolving the data-MC discrepancy, as doing so could help T2K better constrain oscillation parameters. A notable improvement in the disappearance parameter constraints was observed in this study, which can be attributed to the effects of correlation between the oscillation parameters.

T2K's oscillation analyses represent a collaborative effort involving many researchers, from those at J-PARC to far detector (FD) analysts. The Author is the main FD analyser for the Bayesian Markov Chain Monte Carlo (MCMC) framework and the developer of the new multi-ring sample. Most of the studies described were performed directly by the Author, with additional assistance from collaborators in generating the SK detector matrix. Furthermore, the Author made significant contributions to software development for both the FD and OA frameworks. These advancements have improved the usability of the frameworks, enhanced the reproducibility of results, and accelerated the overall analysis process, benefiting the entire collaboration.

The latest upgrades to T2K's beam, ND280, and Gadolinium doping at SK will enhance T2K's sensitivity to oscillation parameters. An increase in beam power[1] will provide higher statistics at FD, which will be particularly advantageous for the enhanced ν_e CC1π^+ sample. Recent joint fits between experiments such as T2K-NOνA [97] and SK-T2K [98] have demonstrated how complementarities between different experiments can further constrain oscillation parameters. The new sample can be employed in the next iteration of joint fits to add more ν_e statistics in these cross-experiment data analyses.

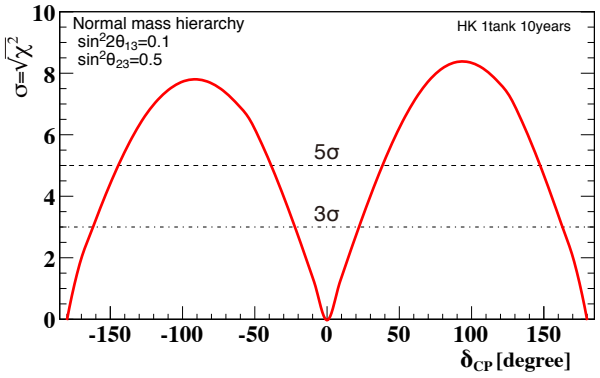

FIGURE 8.1: Hyper-Kamiokande experiment's expected significance to exclude the CP conserving value $\sin\delta_{CP} = 0$ assuming normal hierarchy and 10 years of data taking and that mass-hierarchy problem has been resolved [99].

Japan's next-generation water Cherenkov detector, the Hyper-Kamiokande (HK) experiment, which will have eight times the fiducial volume of SK, is currently under construction. Insights gained from the new ν_e CC1π^+ sample and detector systematic studies can be seamlessly integrated into HK, which is projected to begin operations in 2027. The HK detector is expected to have the physics capability to exclude many values of the CP-violating phase δ_{CP} with a significance of 5σ, as shown in Fig. 8.1, within just a few years of operation.

[1] The T2K beam power reached 800kW in June 2024.

A

Additional Studies

A.1 Impact of PMT Reflectivity on e/π^0 Separation

A study was performed to check the impact of SK's PMT's photocathode reflectivity on separating e-like and NCπ^0-like events, in particular in T2K's ν_e event selections. As discussed, T2K studies δ_{CP} by studying $\nu_e/\overline{\nu}_e$ appearance from the $\nu_\mu/\overline{\nu}_\mu$ beam at T2K's FD. Therefore, it is of utmost importance to select a clean sample of signal ν_e events with the least background contamination.

NCπ^0 events are one of the most dominant backgrounds in T2K's ν_e selections. When the reconstruction software fails to identify the two γ rings coming from $\pi^0 \rightarrow \gamma\gamma$ decay, the event can get misidentified as a ν_e-like event. This can lead to improper measurement of event rates and reconstructed neutrino energy, and hence inaccuracy in estimating oscillation parameters. It has been observed that at higher energies there is a data-MC discrepancy in the e/π^0 separation.

This discrepancy is suspected to be coming from improper detector modelling, of which, the refractive index of the photocathode is a possibility. The default reflectivity table for SK-V period was not calculated with dark noise subtraction. After dark noise subtraction, the relative changes between these two reflectivity parameters ranged from ∼3-22% for different wavelengths of light, with the lowest wavelengths having the most impact.

To study the impact of this change in reflectivity parameters, two samples of e^- and π^0s events with T2K kinematics were generated in SK detector simulation using two different sets of reflectivity parameters. Here, all the e^- events were extracted from T2K's $\nu_\mu \rightarrow \nu_e$ (appearance) MC that had exactly one true e as the FS topology. For the π^0 events, all the events that had exactly two γ rings from the π^0 decay as the FS topology were selected from the $\nu_\mu \rightarrow \nu_\mu$ (disappearance) MC. These events were then reconstructed to perform T2K ν_e selection.

Shown in Fig. A.1 are the remaining efficiencies after each cut for both e^- and π^0s events. Remaining efficiency is given by the ratio of events at each cut level to the total number of events in true fiducial volume of SK. X-axis represents the T2K ν_e selection cuts.

The ratio between events generated using reflectivity parameters with and without dark noise subtraction is consistent with unity.
This shows that the impact of reflectivity parameters on the performance of reconstruction software is minimal within the scope of e/π^0 separation in T2K's ν_e selections.

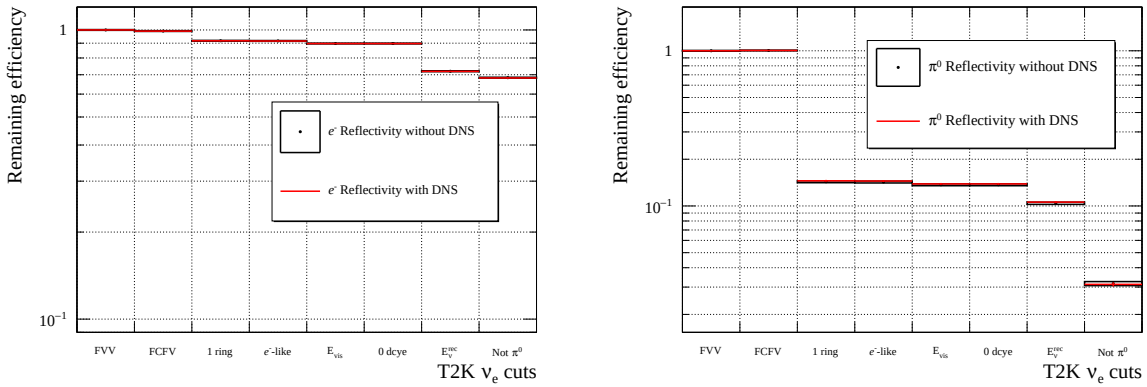

FIGURE A.1: On left: e^- events and on right: π^0 events. Here, the red (black) histogram corresponds to events generated using reflectivity parameters with (without) dark noise subtraction.

A.2 Additional Resolution Plots

The ν_e appearance samples are binned in E_{rec}–θ_{lep} in the Bayesian analysis, and in p_{lep}–θ_{lep} for the frequentist analysis. The resolutions of electron momentum and the polar angle θ_{lep} (in degrees) with respect to the beam direction are shown in Fig. A.2 and A.3.

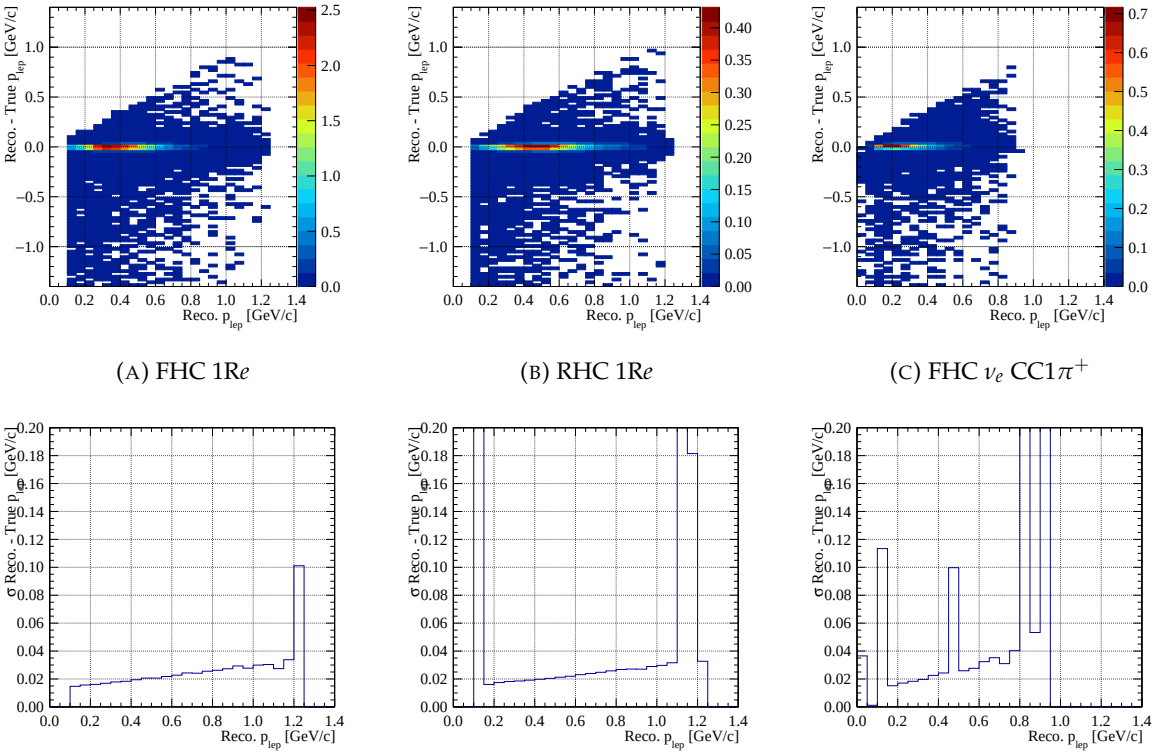

(A) FHC 1Re (B) RHC 1Re (C) FHC ν_e CC1π^+

FIGURE A.2: Rec. − True p_{lep} as a function of Rec. p_{lep} (top panel) and the spread (σ) in the Gaussian fit to the Rec. − True p_{lep} (bottom panel) for the ν_e appearance samples. The y-axis range in the resolution plots is truncated to avoid it being skewed by low-statistics bins with large Gaussian spread.

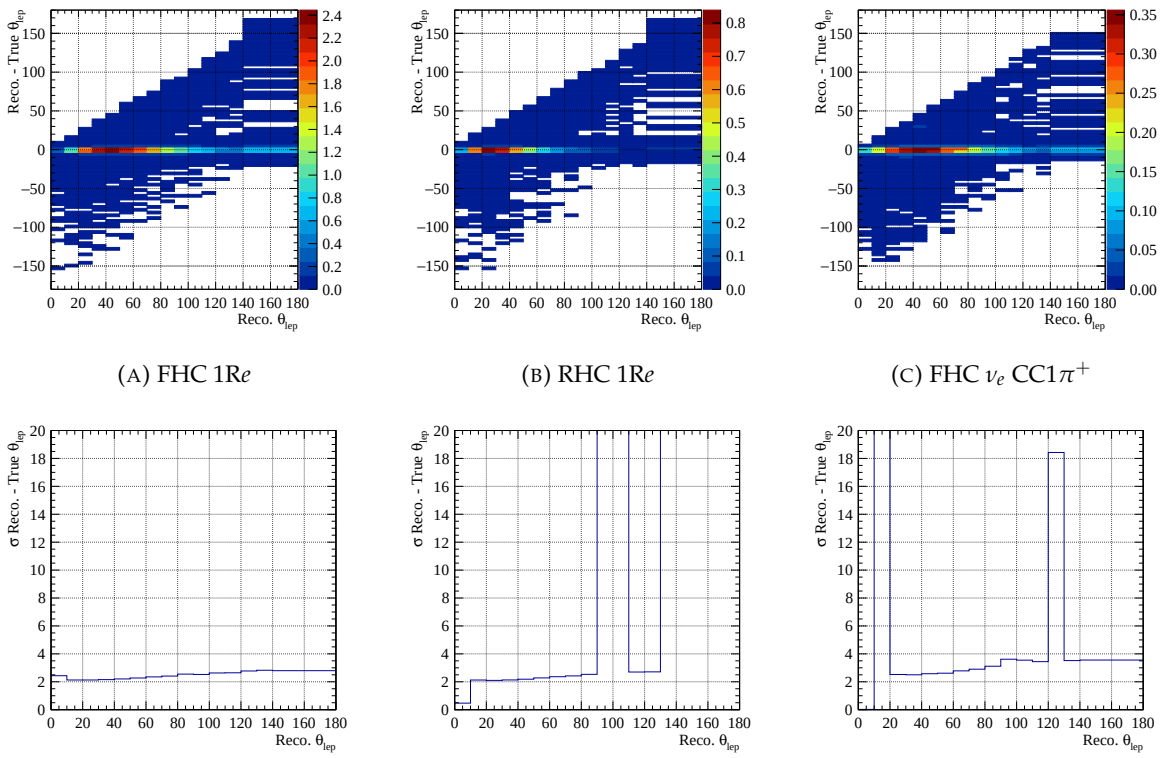

(A) FHC 1Re (B) RHC 1Re (C) FHC ν_e CC1π^+

FIGURE A.3: Rec. − True θ_{lep} as a function of Rec. θ_{lep} (top panel) and the spread (σ) in the Gaussian fit to the Rec. − True θ_{lep} (bottom panel) for the ν_e appearance samples. The y-axis range in the resolution plots is truncated to avoid it being skewed by low-statistics bins with large Gaussian spread.

A.3 Further Breakdown of Post-Fit Errors

The Table A.1 provides an expanded breakdown of post-fit errors. Here, errors due to individual systematic components are shown. For example "Post-ND (Flux only)" errors were obtained by keeping cross-section and SK detector parameters fixed and only varying the flux parameters, thereby giving us errors coming only from a certain family of systematic parameters. The same strategy holds for other rows too.

Fit	FHC 1Rμ	RHC 1Rμ	FHC ν_μ CC1π	FHC 1Re	RHC 1Re	FHC ν_e CC1π
Pre-ND fit	14.80%	13.63%	11.77%	16.26%	13.22%	13.61%
Post-ND (Flux only)	2.73%	2.82%	2.75%	2.83%	2.95%	2.81%
Post-ND (Xsec. only)	3.69%	3.45%	3.15%	4.67%	3.70%	4.59%
Post-ND fit (Flux + Xsec.)	2.74%	2.62%	2.40%	3.85%	3.11%	4.11%
Post-ND fit + SKDet SI/PN only	2.75%	2.63%	2.98%	4.00%	3.31%	5.45%
Post-ND fit + SKDet Det. only	3.07%	2.77%	3.28%	4.67%	4.84%	4.84%
Post-ND fit + SKDet total	3.11%	2.78%	3.88%	4.78%	4.94%	6.08%

TABLE A.1: Errors on event rates (RMS/Mean) before and after a joint fit of ND and FD data.

B

Posterior Distributions

This section includes the posterior distributions of all the cross-section parameters, SK detector parameters and flux parameters. The tables that describe what each SK detector parameter and flux parameter represent are also provided for the user's convenience.

B.1 Cross-Section Parameters

The posterior distributions of all the cross-section parameters tabulated in Tables 5.1, 5.2, 5.3, 5.4, and 5.5.

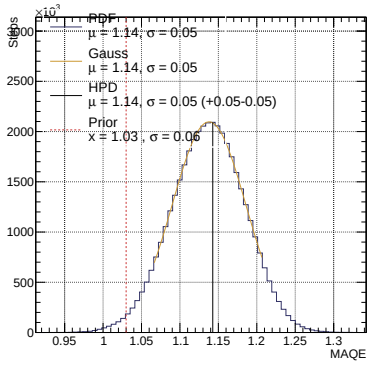
PDF
μ = 1.14, σ = 0.05
Gauss
μ = 1.14, σ = 0.05
HPD
μ = 1.14, σ = 0.05 (+0.05-0.05)
Prior
x = 1.03 , σ = 0.06
Steps
MAQE

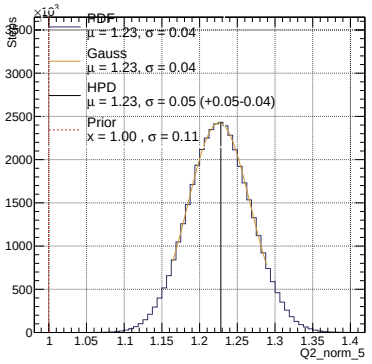
PDF
μ = 1.23, σ = 0.04
Gauss
μ = 1.23, σ = 0.04
HPD
μ = 1.23, σ = 0.05 (+0.05-0.04)
Prior
x = 1.00 , σ = 0.11
Steps
Q2_norm_5

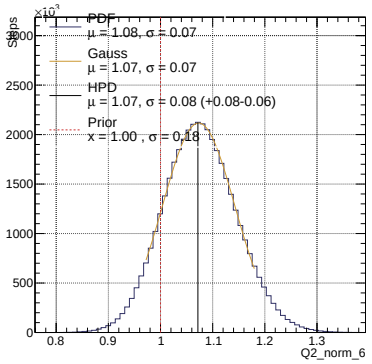
PDF
μ = 1.08, σ = 0.07
Gauss
μ = 1.07, σ = 0.07
HPD
μ = 1.07, σ = 0.08 (+0.08-0.06)
Prior
x = 1.00 , σ = 0.18
Steps
Q2_norm_6

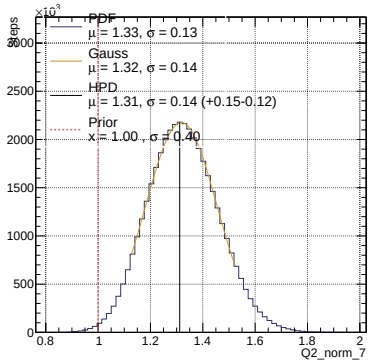
PDF
μ = 1.33, σ = 0.13
Gauss
μ = 1.32, σ = 0.14
HPD
μ = 1.31, σ = 0.14 (+0.15-0.12)
Prior
x = 1.00 , σ = 0.40
Steps
Q2_norm_7

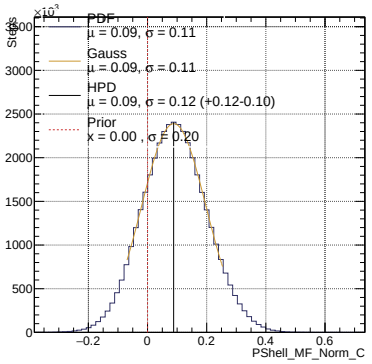
PDF
μ = 0.09, σ = 0.11
Gauss
μ = 0.09, σ = 0.11
HPD
μ = 0.09, σ = 0.12 (+0.12-0.10)
Prior
x = 0.00 , σ = 0.20
Steps
PShell_MF_Norm_C

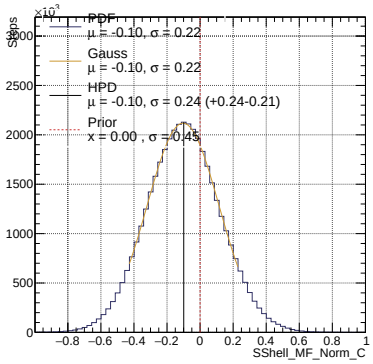
PDF
μ = -0.10, σ = 0.22
Gauss
μ = -0.10, σ = 0.22
HPD
μ = -0.10, σ = 0.24 (+0.24-0.21)
Prior
x = 0.00 , σ = 0.45
Steps
SShell_MF_Norm_C

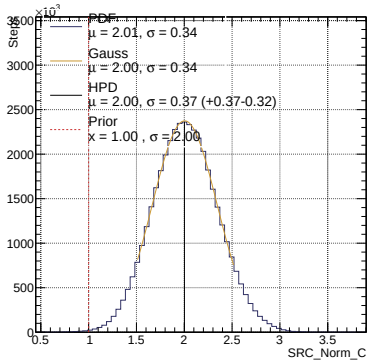
PDF
μ = 2.01, σ = 0.34
Gauss
μ = 2.00, σ = 0.34
HPD
μ = 2.00, σ = 0.37 (+0.37-0.32)
Prior
x = 1.00 , σ = 2.00
Steps
SRC_Norm_C

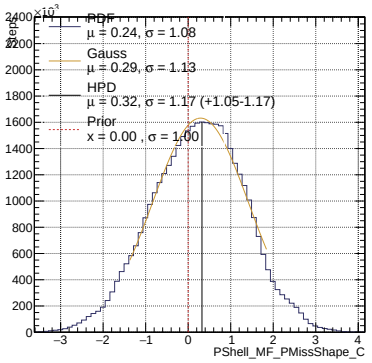
PDF
μ = 0.24, σ = 1.08
Gauss
μ = 0.29, σ = 1.13
HPD
μ = 0.32, σ = 1.17 (+1.05-1.17)
Prior
x = 0.00 , σ = 1.00
Steps
PShell_MF_PMissShape_C

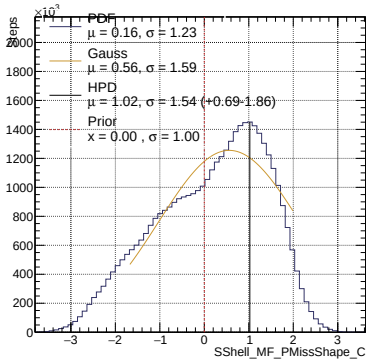
PDF
μ = 0.16, σ = 1.23
Gauss
μ = 0.56, σ = 1.59
HPD
μ = 1.02, σ = 1.54 (+0.69-1.86)
Prior
x = 0.00 , σ = 1.00
Steps
SShell_MF_PMissShape_C

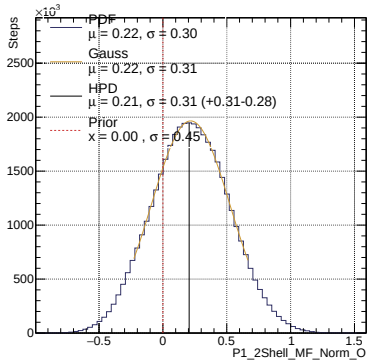
PDF
μ = 0.22, σ = 0.30
Gauss
μ = 0.22, σ = 0.31
HPD
μ = 0.21, σ = 0.31 (+0.31-0.28)
Prior
x = 0.00 , σ = 0.45
Steps
P1_2Shell_MF_Norm_O

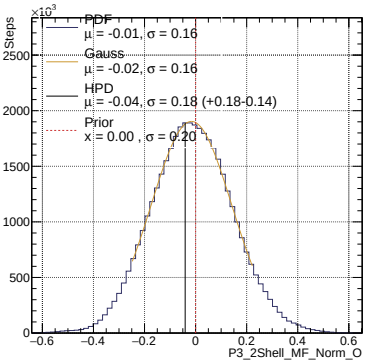
PDF
μ = -0.01, σ = 0.16
Gauss
μ = -0.02, σ = 0.16
HPD
μ = -0.04, σ = 0.18 (+0.18-0.14)
Prior
x = 0.00 , σ = 0.20
Steps
P3_2Shell_MF_Norm_O

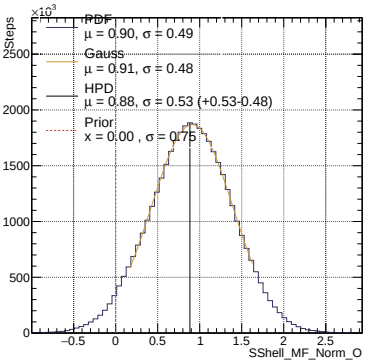
PDF
μ = 0.90, σ = 0.49
Gauss
μ = 0.91, σ = 0.48
HPD
μ = 0.88, σ = 0.53 (+0.53-0.48)
Prior
x = 0.00 , σ = 0.75
Steps
SShell_MF_Norm_O

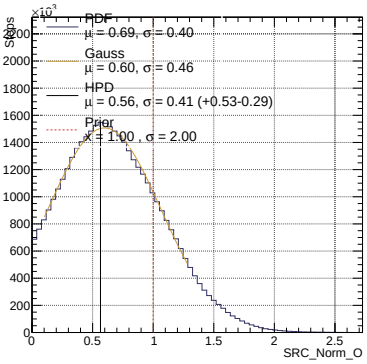
PDF
μ = 0.69, σ = 0.40
Gauss
μ = 0.60, σ = 0.46
HPD
μ = 0.56, σ = 0.41 (+0.53-0.29)
Prior
x = 1.00 , σ = 2.00
Steps
SRC_Norm_O

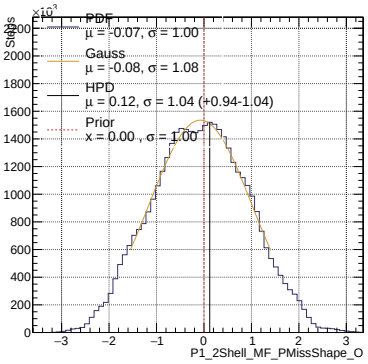
PDF
μ = -0.07, σ = 1.00
Gauss
μ = -0.08, σ = 1.08
HPD
μ = 0.12, σ = 1.04 (+0.94-1.04)
Prior
x = 0.00 , σ = 1.00
Steps
P1_2Shell_MF_PMissShape_O

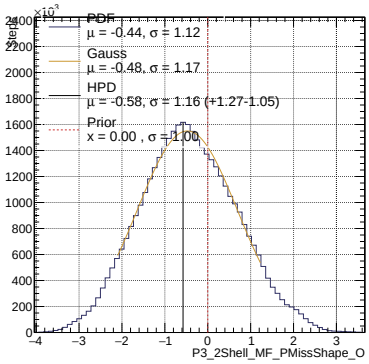
PDF
μ = -0.44, σ = 1.12
Gauss
μ = -0.48, σ = 1.17
HPD
μ = -0.58, σ = 1.16 (+1.27-1.05)
Prior
x = 0.00 , σ = 1.00
Steps
P3_2Shell_MF_PMissShape_O

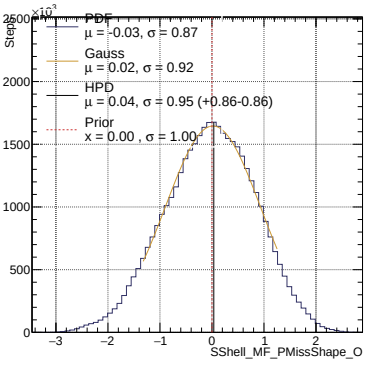
PDF
μ = -0.03, σ = 0.87
Gauss
μ = 0.02, σ = 0.92
HPD
μ = 0.04, σ = 0.95 (+0.86-0.86)
Prior
x = 0.00 , σ = 1.00
Steps
SShell_MF_PMissShape_O

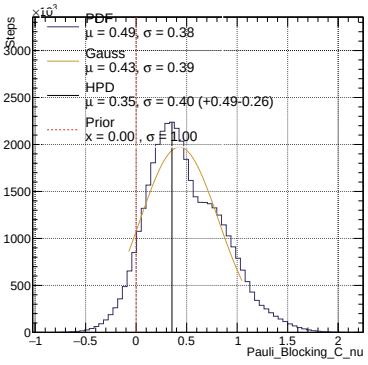
PDF
μ = 0.49, σ = 0.38
Gauss
μ = 0.43, σ = 0.39
HPD
μ = 0.35, σ = 0.40 (+0.49-0.26)
Prior
x = 0.00 , σ = 1.00
Steps
Pauli_Blocking_C_nu

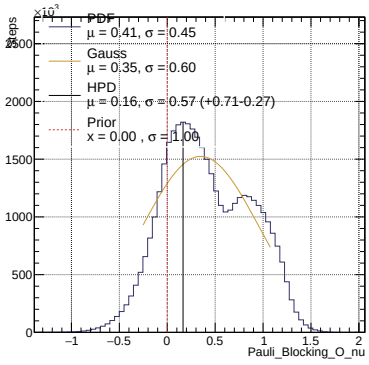
PDF
μ = 0.41, σ = 0.45
Gauss
μ = 0.35, σ = 0.60
HPD
μ = 0.16, σ = 0.57 (+0.71-0.27)
Prior
x = 0.00 , σ = 1.00
Steps
Pauli_Blocking_O_nu

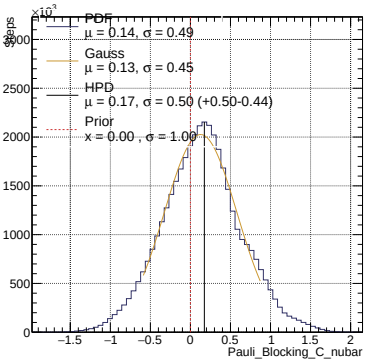
PDF
μ = 0.14, σ = 0.49
Gauss
μ = 0.13, σ = 0.45
HPD
μ = 0.17, σ = 0.50 (+0.50-0.44)
Prior
x = 0.00 , σ = 1.00
Steps
Pauli_Blocking_C_nubar

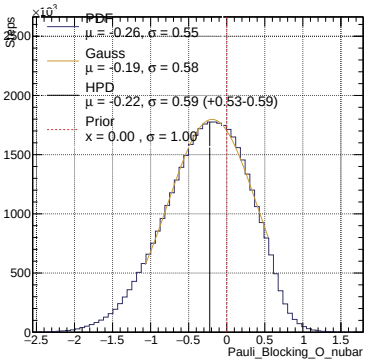
PDF
μ = -0.26, σ = 0.55
Gauss
μ = -0.19, σ = 0.58
HPD
μ = -0.22, σ = 0.59 (+0.53-0.59)
Prior
x = 0.00 , σ = 1.00
Steps
Pauli_Blocking_O_nubar

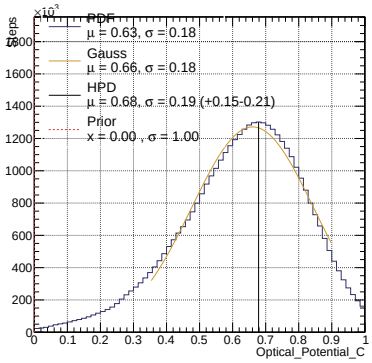
PDF
μ = 0.63, σ = 0.18
Gauss
μ = 0.66, σ = 0.18
HPD
μ = 0.68, σ = 0.19 (+0.15-0.21)
Prior
x = 0.00 , σ = 1.00
Steps
Optical_Potential_C

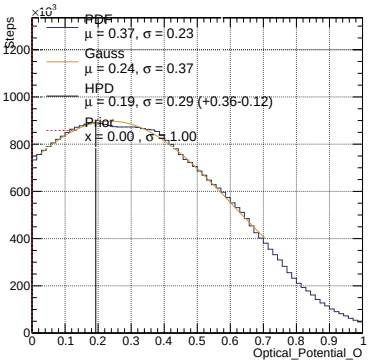
PDF
μ = 0.37, σ = 0.23
Gauss
μ = 0.24, σ = 0.37
HPD
μ = 0.19, σ = 0.29 (+0.36-0.12)
Prior
x = 0.00 , σ = 1.00
Steps
Optical_Potential_O

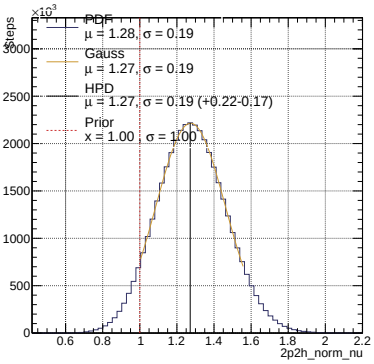
PDF
μ = 1.28, σ = 0.19
Gauss
μ = 1.27, σ = 0.19
HPD
μ = 1.27, σ = 0.19 (+0.22-0.17)
Prior
x = 1.00 , σ = 1.00
Steps
2p2h_norm_nu

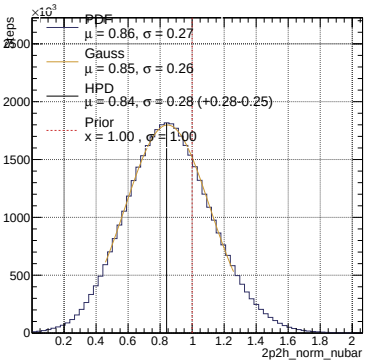
PDF
μ = 0.86, σ = 0.27
Gauss
μ = 0.85, σ = 0.26
HPD
μ = 0.84, σ = 0.28 (+0.28-0.25)
Prior
x = 1.00 , σ = 1.00
Steps
2p2h_norm_nubar

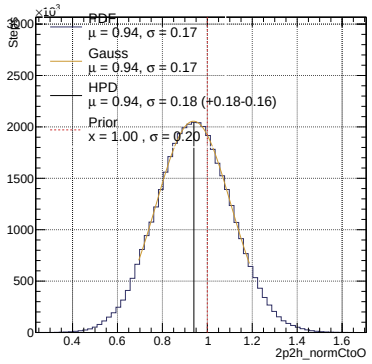
PDF
μ = 0.94, σ = 0.17
Gauss
μ = 0.94, σ = 0.17
HPD
μ = 0.94, σ = 0.18 (+0.18-0.16)
Prior
x = 1.00 , σ = 0.20
Steps
2p2h_normCtoO

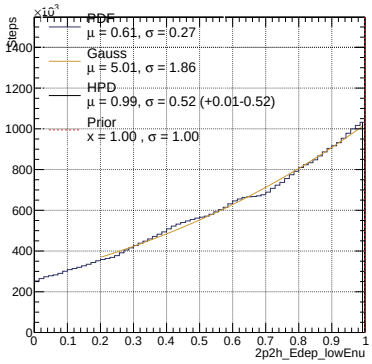
PDF
μ = 0.61, σ = 0.27
Gauss
μ = 5.01, σ = 1.86
HPD
μ = 0.99, σ = 0.52 (+0.01-0.52)
Prior
x = 1.00 , σ = 1.00
Steps
2p2h_Edep_lowEnu

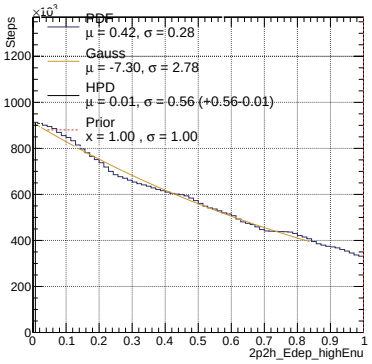
PDF
μ = 0.42, σ = 0.28
Gauss
μ = -7.30, σ = 2.78
HPD
μ = 0.01, σ = 0.56 (+0.56-0.01)
Prior
x = 1.00 , σ = 1.00
Steps
2p2h_Edep_highEnu

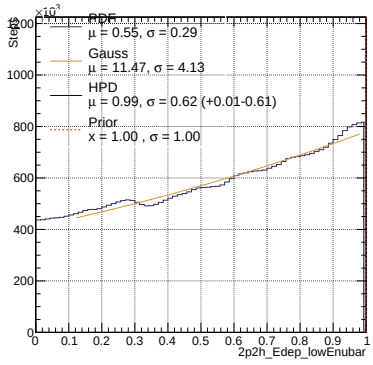
PDF
μ = 0.55, σ = 0.29
Gauss
μ = 11.47, σ = 4.13
HPD
μ = 0.99, σ = 0.62 (+0.01-0.61)
Prior
x = 1.00 , σ = 1.00
Steps
2p2h_Edep_lowEnubar

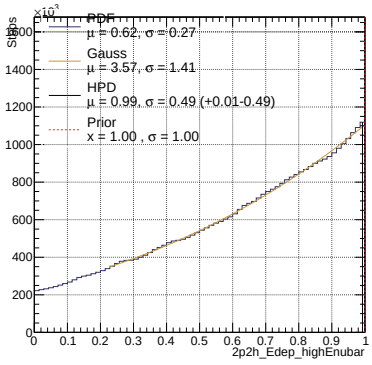
PDF
μ = 0.62, σ = 0.27
Gauss
μ = 3.57, σ = 1.41
HPD
μ = 0.99, σ = 0.49 (+0.01-0.49)
Prior
x = 1.00 , σ = 1.00
Steps
2p2h_Edep_highEnubar

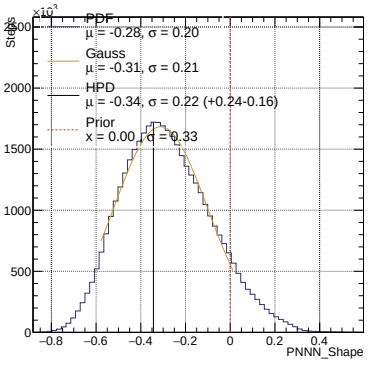
PDF
μ = -0.28, σ = 0.20
Gauss
μ = -0.31, σ = 0.21
HPD
μ = -0.34, σ = 0.22 (+0.24-0.16)
Prior
x = 0.00 , σ = 0.33
Steps
PNNN_Shape

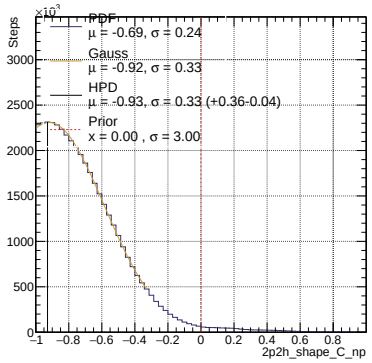
PDF
μ = -0.69, σ = 0.24
Gauss
μ = -0.92, σ = 0.33
HPD
μ = -0.93, σ = 0.33 (+0.36-0.04)
Prior
x = 0.00 , σ = 3.00
Steps
2p2h_shape_C_np

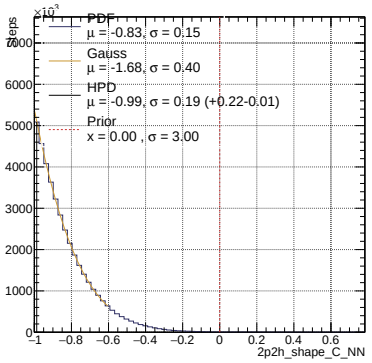
PDF
μ = -0.83, σ = 0.15
Gauss
μ = -1.68, σ = 0.40
HPD
μ = -0.99, σ = 0.19 (+0.22-0.01)
Prior
x = 0.00 , σ = 3.00
Steps
2p2h_shape_C_NN

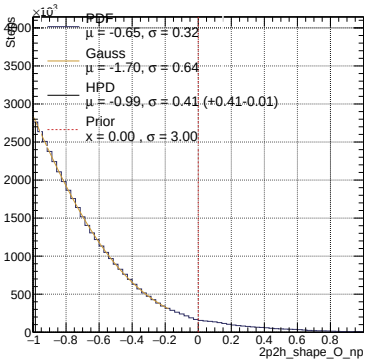
PDF
μ = -0.65, σ = 0.32
Gauss
μ = -1.70, σ = 0.64
HPD
μ = -0.99, σ = 0.41 (+0.41-0.01)
Prior
x = 0.00 , σ = 3.00
Steps
2p2h_shape_O_np

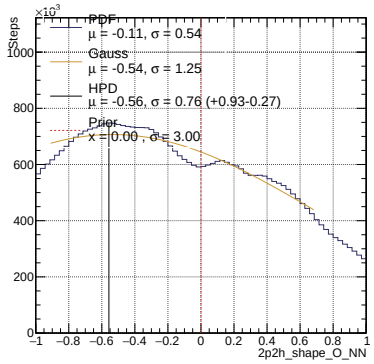
PDF
μ = -0.11, σ = 0.54
Gauss
μ = -0.54, σ = 1.25
HPD
μ = -0.56, σ = 0.76 (+0.93-0.27)
Prior
x = 0.00 , σ = 3.00
Steps
2p2h_shape_O_NN

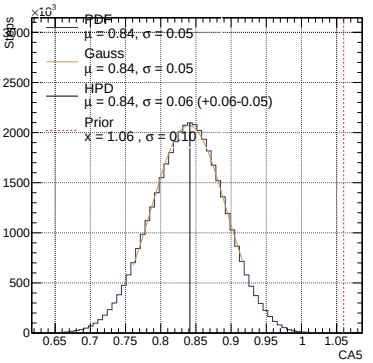
PDF
μ = 0.84, σ = 0.05
Gauss
μ = 0.84, σ = 0.05
HPD
μ = 0.84, σ = 0.06 (+0.06-0.05)
Prior
x = 1.06 , σ = 0.10
Steps
CA5

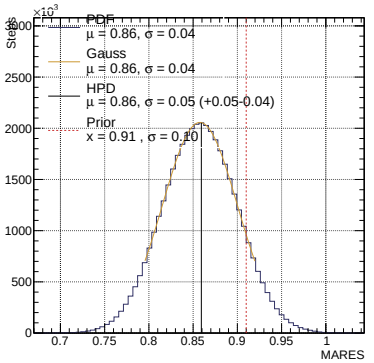
PDF
μ = 0.86, σ = 0.04
Gauss
μ = 0.86, σ = 0.04
HPD
μ = 0.86, σ = 0.05 (+0.05-0.04)
Prior
x = 0.91 , σ = 0.10
Steps
MARES

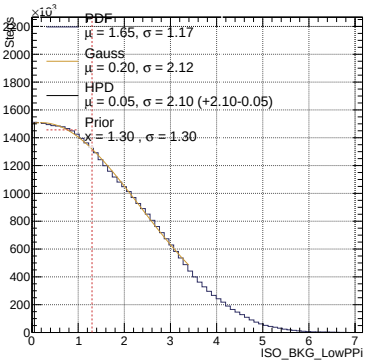
PDF
μ = 1.65, σ = 1.17
Gauss
μ = 0.20, σ = 2.12
HPD
μ = 0.05, σ = 2.10 (+2.10-0.05)
Prior
x = 1.30 , σ = 1.30
Steps
ISO_BKG_LowPPi

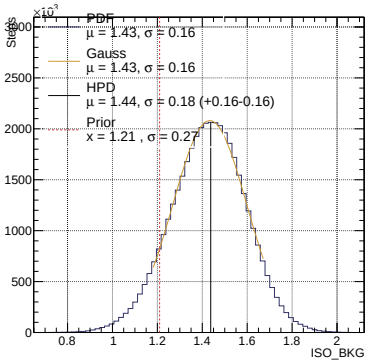
PDF
μ = 1.43, σ = 0.16
Gauss
μ = 1.43, σ = 0.16
HPD
μ = 1.44, σ = 0.18 (+0.16-0.16)
Prior
x = 1.21 , σ = 0.27
Steps
ISO_BKG

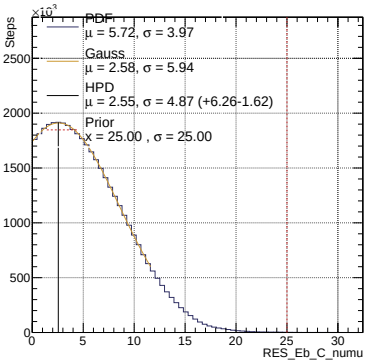
PDF
μ = 5.72, σ = 3.97
Gauss
μ = 2.58, σ = 5.94
HPD
μ = 2.55, σ = 4.87 (+6.26-1.62)
Prior
x = 25.00 , σ = 25.00
Steps
RES_Eb_C_numu

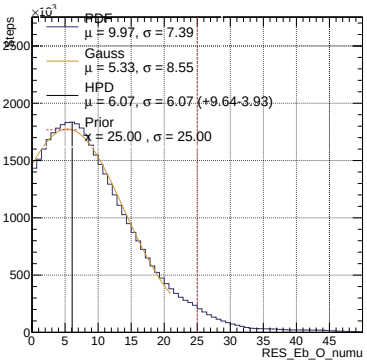
PDF
μ = 9.97, σ = 7.39
Gauss
μ = 5.33, σ = 8.55
HPD
μ = 6.07, σ = 6.07 (+9.64-3.93)
Prior
x = 25.00 , σ = 25.00
Steps
RES_Eb_O_numu

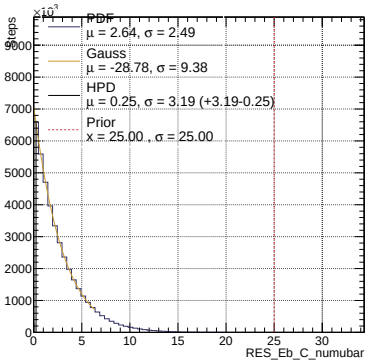
PDF
μ = 2.64, σ = 2.49
Gauss
μ = -28.78, σ = 9.38
HPD
μ = 0.25, σ = 3.19 (+3.19-0.25)
Prior
x = 25.00 , σ = 25.00
Steps
RES_Eb_C_numubar

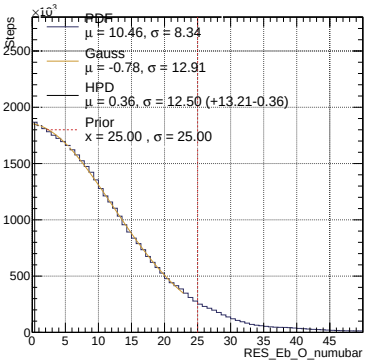
PDF
μ = 10.46, σ = 8.34
Gauss
μ = -0.78, σ = 12.91
HPD
μ = 0.36, σ = 12.50 (+13.21-0.36)
Prior
x = 25.00 , σ = 25.00
Steps
RES_Eb_O_numubar

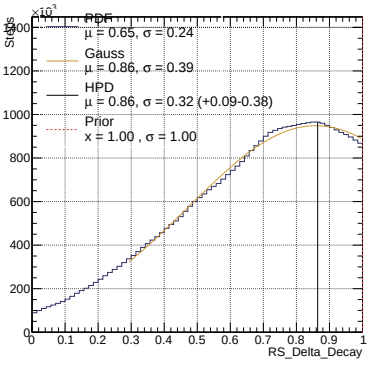
PDF
μ = 0.65, σ = 0.24
Gauss
μ = 0.86, σ = 0.39
HPD
μ = 0.86, σ = 0.32 (+0.09-0.38)
Prior
x = 1.00 , σ = 1.00
Steps
RS_Delta_Decay

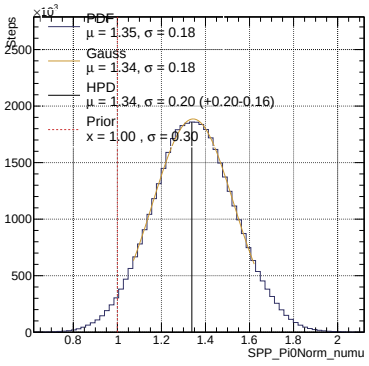
PDF
μ = 1.35, σ = 0.18
Gauss
μ = 1.34, σ = 0.18
HPD
μ = 1.34, σ = 0.20 (+0.20-0.16)
Prior
x = 1.00 , σ = 0.30
Steps
SPP_Pi0Norm_numu

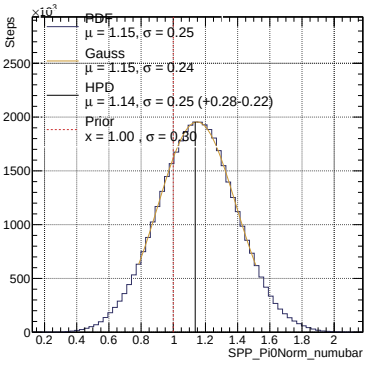
PDF
μ = 1.15, σ = 0.25
Gauss
μ = 1.15, σ = 0.24
HPD
μ = 1.14, σ = 0.25 (+0.28-0.22)
Prior
x = 1.00 , σ = 0.30
Steps
SPP_Pi0Norm_numubar

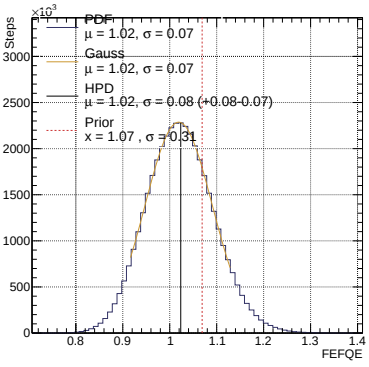
PDF
μ = 1.02, σ = 0.07
Gauss
μ = 1.02, σ = 0.07
HPD
μ = 1.02, σ = 0.08 (+0.08-0.07)
Prior
x = 1.07 , σ = 0.31
Steps
FEFQE

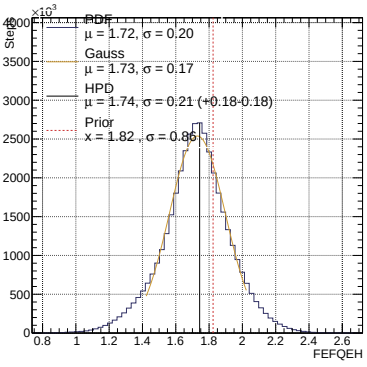
PDF
μ = 1.72, σ = 0.20
Gauss
μ = 1.73, σ = 0.17
HPD
μ = 1.74, σ = 0.21 (+0.18-0.18)
Prior
x = 1.82 , σ = 0.86
Steps
FEFQEH

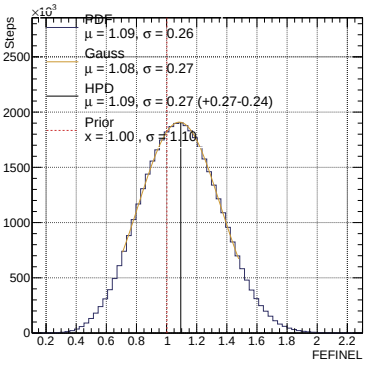
PDF
μ = 1.09, σ = 0.26
Gauss
μ = 1.08, σ = 0.27
HPD
μ = 1.09, σ = 0.27 (+0.27-0.24)
Prior
x = 1.00 , σ = 1.10
Steps
FEFINEL

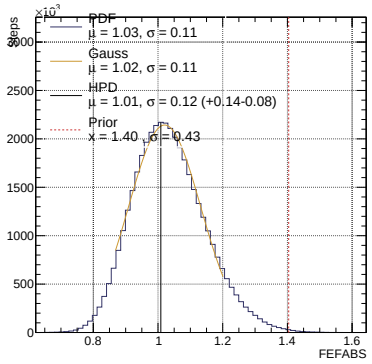
PDF
μ = 1.03, σ = 0.11
Gauss
μ = 1.02, σ = 0.11
HPD
μ = 1.01, σ = 0.12 (+0.14-0.08)
Prior
x = 1.40 , σ = 0.43
Steps
FEFABS

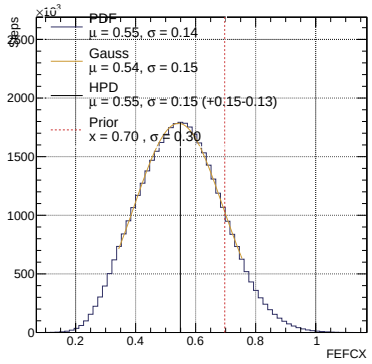
PDF
μ = 0.55, σ = 0.14
Gauss
μ = 0.54, σ = 0.15
HPD
μ = 0.55, σ = 0.15 (+0.15-0.13)
Prior
x = 0.70 , σ = 0.30
Steps
FEFCX

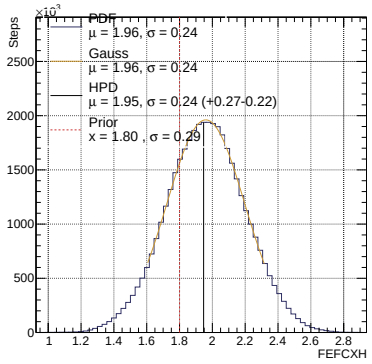
PDF
μ = 1.96, σ = 0.24
Gauss
μ = 1.96, σ = 0.24
HPD
μ = 1.95, σ = 0.24 (+0.27-0.22)
Prior
x = 1.80 , σ = 0.29
Steps
FEFCXH

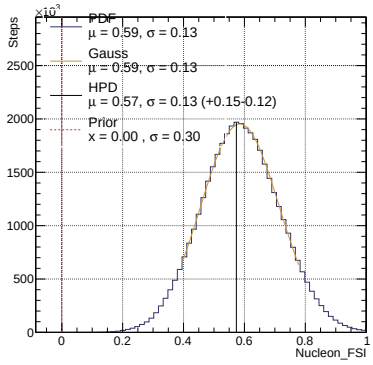
PDF
μ = 0.59, σ = 0.13
Gauss
μ = 0.59, σ = 0.13
HPD
μ = 0.57, σ = 0.13 (+0.15-0.12)
Prior
x = 0.00 , σ = 0.30
Steps
Nucleon_FSI

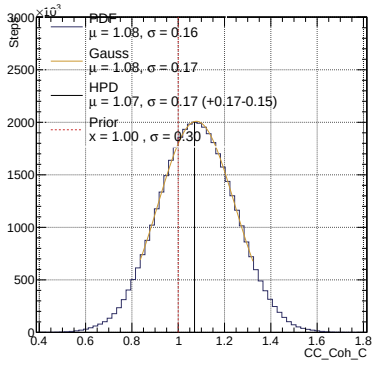
PDF
μ = 1.08, σ = 0.16
Gauss
μ = 1.08, σ = 0.17
HPD
μ = 1.07, σ = 0.17 (+0.17-0.15)
Prior
x = 1.00 , σ = 0.30
Steps
CC_Coh_C

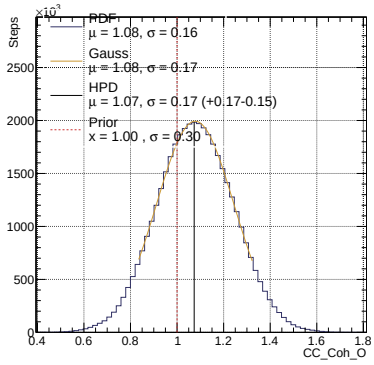
PDF
μ = 1.08, σ = 0.16
Gauss
μ = 1.08, σ = 0.17
HPD
μ = 1.07, σ = 0.17 (+0.17-0.15)
Prior
x = 1.00 , σ = 0.30
Steps
CC_Coh_O

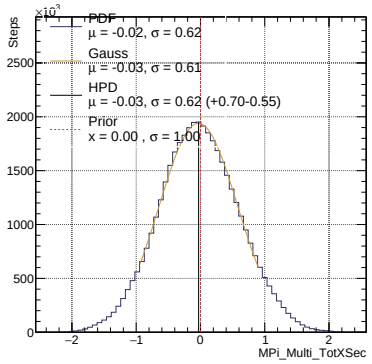
PDF
μ = -0.02, σ = 0.62
Gauss
μ = -0.03, σ = 0.61
HPD
μ = -0.03, σ = 0.62 (+0.70-0.55)
Prior
x = 0.00 , σ = 1.00
Steps
MPi_Multi_TotXSec

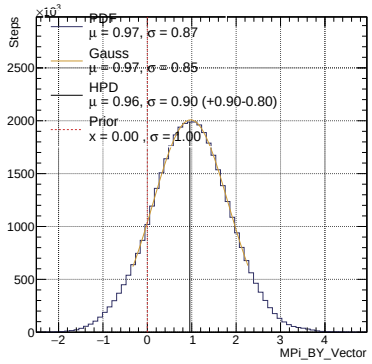
PDF
μ = 0.97, σ = 0.87
Gauss
μ = 0.97, σ = 0.85
HPD
μ = 0.96, σ = 0.90 (+0.90-0.80)
Prior
x = 0.00 , σ = 1.00
Steps
MPi_BY_Vector

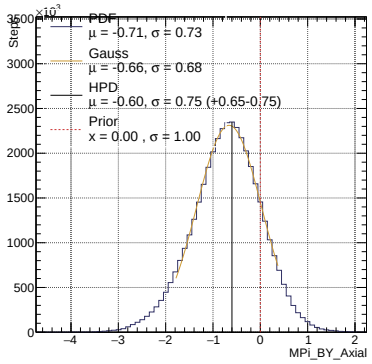
PDF
μ = -0.71, σ = 0.73
Gauss
μ = -0.66, σ = 0.68
HPD
μ = -0.60, σ = 0.75 (+0.65-0.75)
Prior
x = 0.00 , σ = 1.00
Steps
MPi_BY_Axial

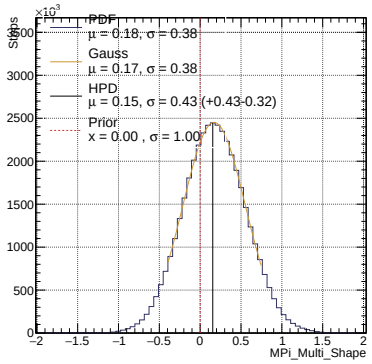
PDF
μ = 0.18, σ = 0.38
Gauss
μ = 0.17, σ = 0.38
HPD
μ = 0.15, σ = 0.43 (+0.43-0.32)
Prior
x = 0.00 , σ = 1.00
Steps
MPi_Multi_Shape

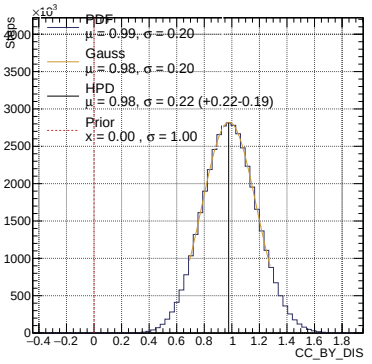
PDF
μ = 0.99, σ = 0.20
Gauss
μ = 0.98, σ = 0.20
HPD
μ = 0.98, σ = 0.22 (+0.22-0.19)
Prior
x = 0.00 , σ = 1.00
Steps
CC_BY_DIS

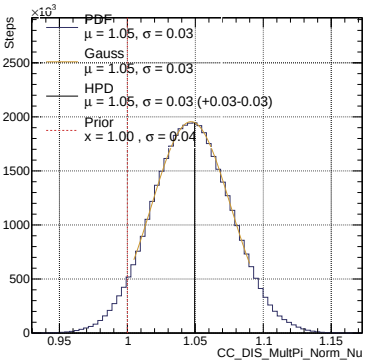
PDF
μ = 1.05, σ = 0.03
Gauss
μ = 1.05, σ = 0.03
HPD
μ = 1.05, σ = 0.03 (+0.03-0.03)
Prior
x = 1.00 , σ = 0.04
Steps
CC_DIS_MultPi_Norm_Nu

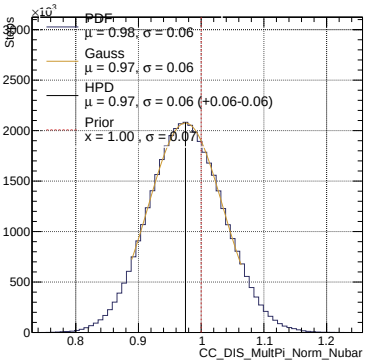
PDF
μ = 0.98, σ = 0.06
Gauss
μ = 0.97, σ = 0.06
HPD
μ = 0.97, σ = 0.06 (+0.06-0.06)
Prior
x = 1.00 , σ = 0.07
Steps
CC_DIS_MultPi_Norm_Nubar

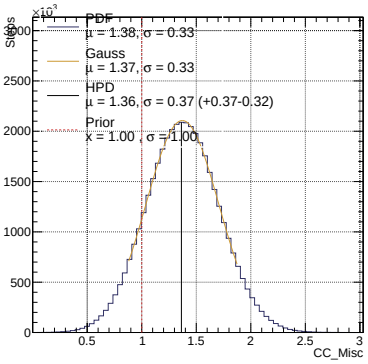
PDF
μ = 1.38, σ = 0.33
Gauss
μ = 1.37, σ = 0.33
HPD
μ = 1.36, σ = 0.37 (+0.37-0.32)
Prior
x = 1.00 , σ = 1.00
Steps
CC_Misc

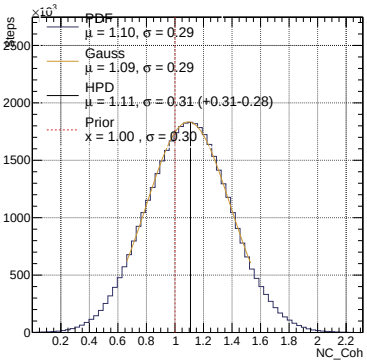
PDF
μ = 1.10, σ = 0.29
Gauss
μ = 1.09, σ = 0.29
HPD
μ = 1.11, σ = 0.31 (+0.31-0.28)
Prior
x = 1.00 , σ = 0.30
Steps
NC_Coh

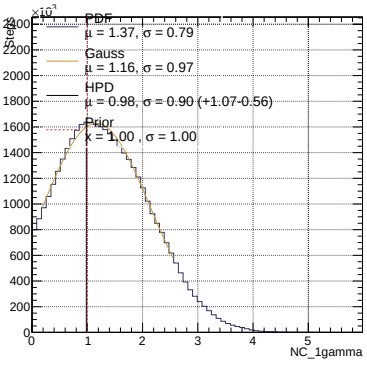
PDF
μ = 1.37, σ = 0.79
Gauss
μ = 1.16, σ = 0.97
HPD
μ = 0.98, σ = 0.90 (+1.07-0.56)
Prior
x = 1.00 , σ = 1.00
Steps
NC_1gamma

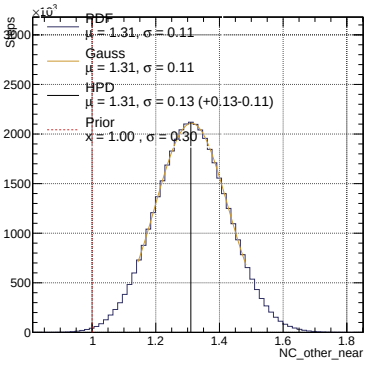
PDF
μ = 1.31, σ = 0.11
Gauss
μ = 1.31, σ = 0.11
HPD
μ = 1.31, σ = 0.13 (+0.13-0.11)
Prior
x = 1.00 , σ = 0.30
Steps
NC_other_near

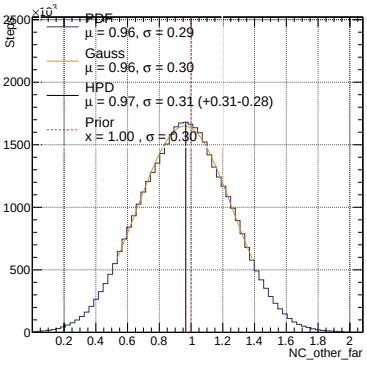
PDF
μ = 0.96, σ = 0.29
Gauss
μ = 0.96, σ = 0.30
HPD
μ = 0.97, σ = 0.31 (+0.31-0.28)
Prior
x = 1.00 , σ = 0.30
Steps
NC_other_far

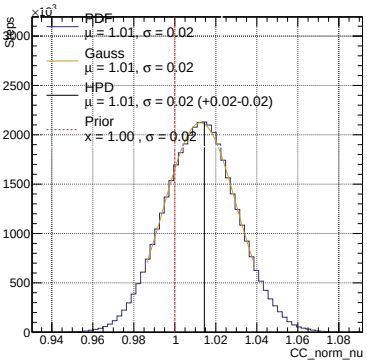
PDF
μ = 1.01, σ = 0.02
Gauss
μ = 1.01, σ = 0.02
HPD
μ = 1.01, σ = 0.02 (+0.02-0.02)
Prior
x = 1.00 , σ = 0.02
Steps
CC_norm_nu

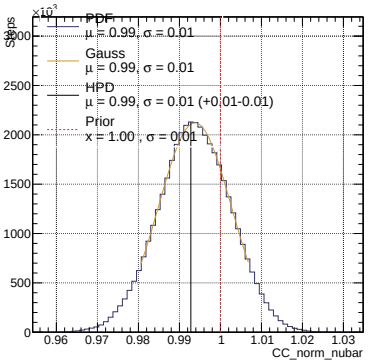
PDF
μ = 0.99, σ = 0.01
Gauss
μ = 0.99, σ = 0.01
HPD
μ = 0.99, σ = 0.01 (+0.01-0.01)
Prior
x = 1.00 , σ = 0.01
Steps
CC_norm_nubar

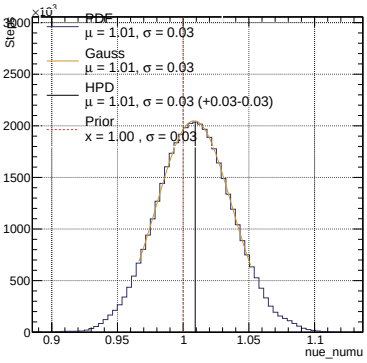
PDF
μ = 1.01, σ = 0.03
Gauss
μ = 1.01, σ = 0.03
HPD
μ = 1.01, σ = 0.03 (+0.03-0.03)
Prior
x = 1.00 , σ = 0.03
Steps
nue_numu

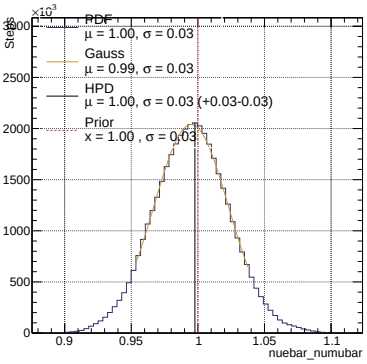
PDF
μ = 1.00, σ = 0.03
Gauss
μ = 0.99, σ = 0.03
HPD
μ = 1.00, σ = 0.03 (+0.03-0.03)
Prior
x = 1.00 , σ = 0.03
Steps
nuebar_numubar

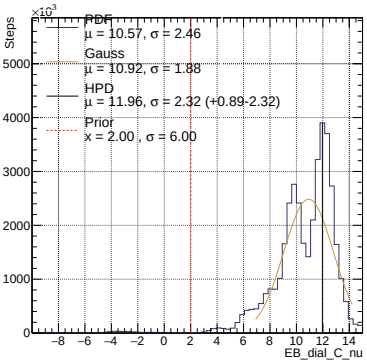
PDF
μ = 10.57, σ = 2.46
Gauss
μ = 10.92, σ = 1.88
HPD
μ = 11.96, σ = 2.32 (+0.89-2.32)
Prior
x = 2.00 , σ = 6.00
Steps
EB_dial_C_nu

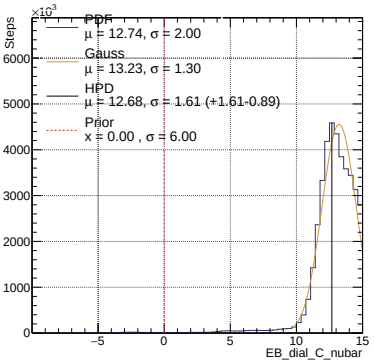
PDF
μ = 12.74, σ = 2.00
Gauss
μ = 13.23, σ = 1.30
HPD
μ = 12.68, σ = 1.61 (+1.61-0.89)
Prior
x = 0.00 , σ = 6.00
Steps
EB_dial_C_nubar

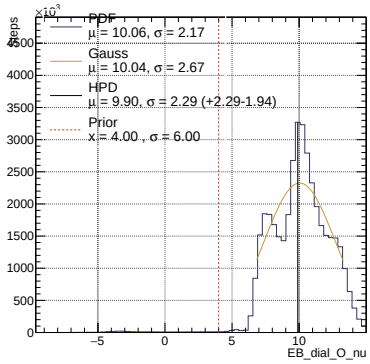
PDF
μ = 10.06, σ = 2.17
Gauss
μ = 10.04, σ = 2.67
HPD
μ = 9.90, σ = 2.29 (+2.29-1.94)
Prior
x = 4.00 , σ = 6.00
Steps
EB_dial_O_nu

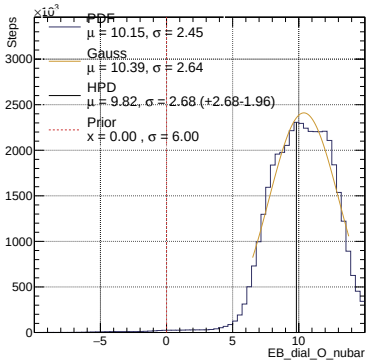
PDF
μ = 10.15, σ = 2.45
Gauss
μ = 10.39, σ = 2.64
HPD
μ = 9.82, σ = 2.68 (+2.68-1.96)
Prior
x = 0.00 , σ = 6.00
Steps
EB_dial_O_nubar

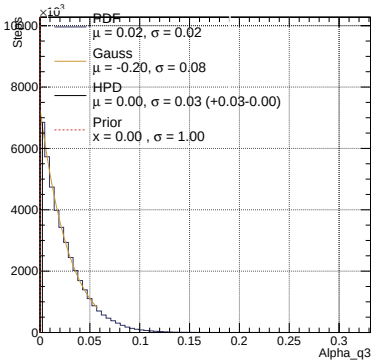
PDF
μ = 0.02, σ = 0.02
Gauss
μ = -0.20, σ = 0.08
HPD
μ = 0.00, σ = 0.03 (+0.03-0.00)
Prior
x = 0.00 , σ = 1.00
Steps
Alpha_q3

B.2 SK Detector Parameters

The detailed scheme of SK detector matrix binning is shown in Table B.1.

Sample	MC component	Reconstructed neutrino energy range [MeV]	Bin number
FHC 1Re	Oscillated ν_e CC	0 – 350	0
		350 – 800	1
		800 – 1250	2
	ν_μ CC	0 – 350	3
		350 – 800	4
		800 – 1250	5
	Intrinsic ν_e CC	0 – 350	6
		350 – 800	7
		800 – 1250	8
	NC	0 – 350	9
		350 – 800	10
		800 – 1250	11
FHC 1Rμ	ν_μ CCQE-like	0 – 400	12
		400 – 1100	13
		$\geq$ 1100	14
	ν_μ CC non-QE-like	All	15
	ν_eCC	All	16
	NC	All	17
RHC 1Re	Oscillated ν_e CC	0 – 350	18
		350 – 800	19
		800 – 1250	20
	ν_μ CC	0 – 350	21
		350 – 800	22
		800 – 1250	23
	Intrinsic ν_e CC	0 – 350	24
		350 – 800	25
		800 – 1250	26
	NC	0 – 350	27
		350 – 800	28
		800 – 1250	29
RHC 1Rμ	ν_μ CCQE-like	0 – 400	30
		400 – 1100	31
		$\geq$ 1100	32
	ν_μ CC non-QE-like	All	33
	ν_eCC	All	34
	NC	All	35
FHC ν_e CC1π^+	Oscillated ν_e CC	350 – 800	36
		800 – 1250	37
	ν_μ CC	350 – 800	38
		800 – 1250	39
	Intrinsic ν_e CC	350 – 800	40
		800 – 1250	41
	NC	350 – 800	42
		800 – 1250	43
FHC ν_μ CC1π^+	ν_μCC1π^+	0 – 800	44
		800 – 2000	45
		$\geq$ 2000	46
	ν_μ CCQE-like	0 – 800	47
		800 – 2000	48
		$\geq$ 2000	49
	ν_μ CC-other	0 – 800	50
		800 – 2000	51
		$\geq$ 2000	52
	NC	0 – 1500	53
		1500 – 2500	54
		$\geq$ 2500	55
	ν_eCC	All	56

TABLE B.1: SK detector uncertainty covariance matrix E_{rec} binning.

Note that the SK detector parameter's posteriors are labelled as "FD Det *i*", where the index "i" is the bin number mentioned in Table B.1. Additionally, the energy scale parameter, which is not mentioned in the table is also shown but with the label "momentum scale".

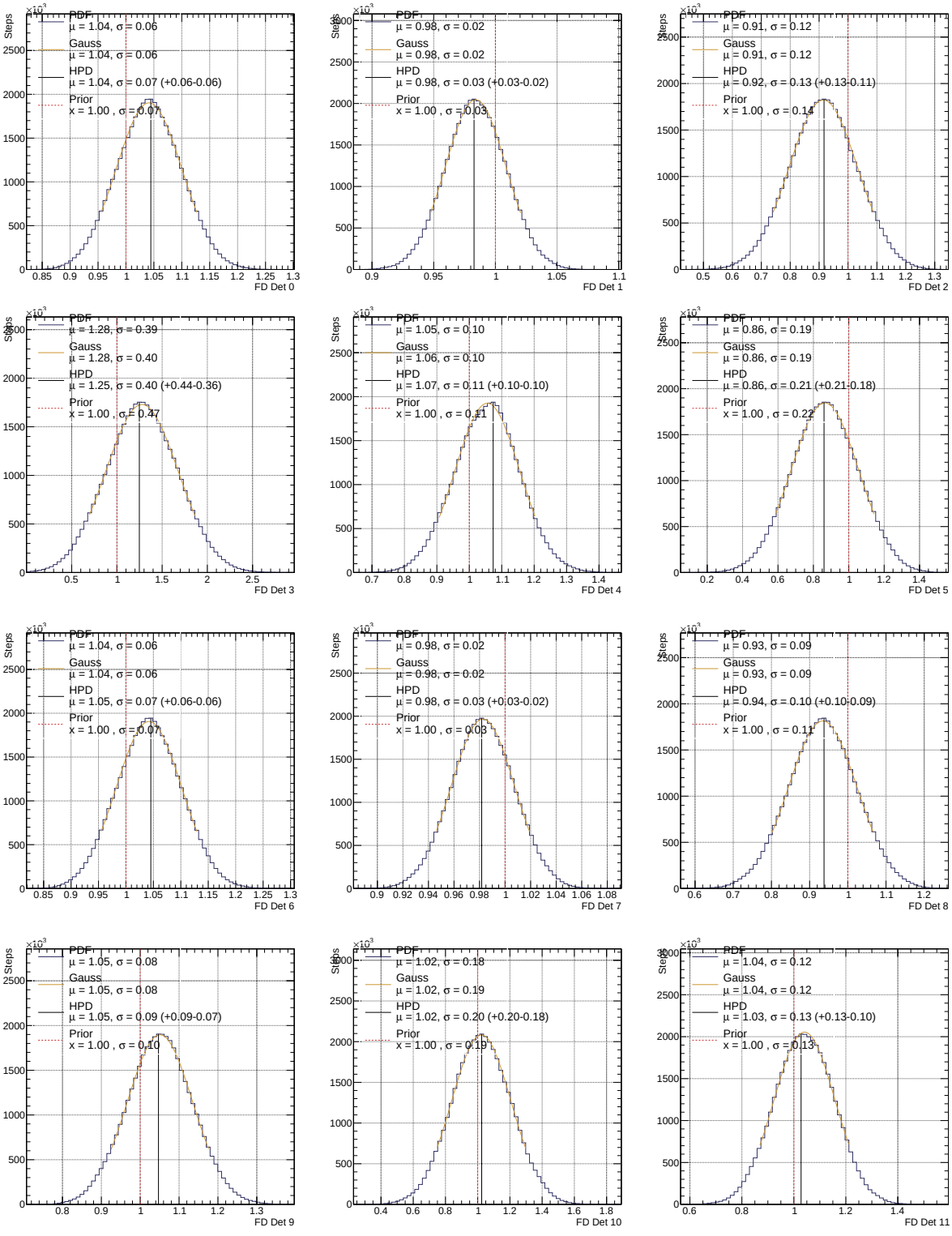
PDF
μ = 1.04, σ = 0.06
Gauss
μ = 1.04, σ = 0.06
HPD
μ = 1.04, σ = 0.07 (+0.06-0.06)
Prior
x = 1.00 , σ = 0.07
FD Det 0
PDF
μ = 0.98, σ = 0.02
Gauss
μ = 0.98, σ = 0.02
HPD
μ = 0.98, σ = 0.03 (+0.03-0.02)
Prior
x = 1.00 , σ = 0.03
FD Det 1
PDF
μ = 0.91, σ = 0.12
Gauss
μ = 0.91, σ = 0.12
HPD
μ = 0.92, σ = 0.13 (+0.13-0.11)
Prior
x = 1.00 , σ = 0.14
FD Det 2
PDF
μ = 1.28, σ = 0.39
Gauss
μ = 1.28, σ = 0.40
HPD
μ = 1.25, σ = 0.40 (+0.44-0.36)
Prior
x = 1.00 , σ = 0.47
FD Det 3
PDF
μ = 1.05, σ = 0.10
Gauss
μ = 1.06, σ = 0.10
HPD
μ = 1.07, σ = 0.11 (+0.10-0.10)
Prior
x = 1.00 , σ = 0.11
FD Det 4
PDF
μ = 0.86, σ = 0.19
Gauss
μ = 0.86, σ = 0.19
HPD
μ = 0.86, σ = 0.21 (+0.21-0.18)
Prior
x = 1.00 , σ = 0.22
FD Det 5
PDF
μ = 1.04, σ = 0.06
Gauss
μ = 1.04, σ = 0.06
HPD
μ = 1.05, σ = 0.07 (+0.06-0.06)
Prior
x = 1.00 , σ = 0.07
FD Det 6
PDF
μ = 0.98, σ = 0.02
Gauss
μ = 0.98, σ = 0.02
HPD
μ = 0.98, σ = 0.03 (+0.03-0.02)
Prior
x = 1.00 , σ = 0.03
FD Det 7
PDF
μ = 0.93, σ = 0.09
Gauss
μ = 0.93, σ = 0.09
HPD
μ = 0.94, σ = 0.10 (+0.10-0.09)
Prior
x = 1.00 , σ = 0.11
FD Det 8
PDF
μ = 1.05, σ = 0.08
Gauss
μ = 1.05, σ = 0.08
HPD
μ = 1.05, σ = 0.09 (+0.09-0.07)
Prior
x = 1.00 , σ = 0.10
FD Det 9
PDF
μ = 1.02, σ = 0.18
Gauss
μ = 1.02, σ = 0.19
HPD
μ = 1.02, σ = 0.20 (+0.20-0.18)
Prior
x = 1.00 , σ = 0.19
FD Det 10
PDF
μ = 1.04, σ = 0.12
Gauss
μ = 1.04, σ = 0.12
HPD
μ = 1.03, σ = 0.13 (+0.13-0.10)
Prior
x = 1.00 , σ = 0.13
FD Det 11

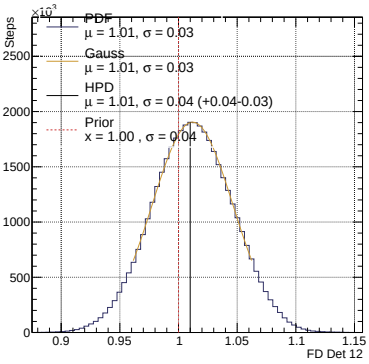
PDF
μ = 1.01, σ = 0.03
Gauss
μ = 1.01, σ = 0.03
HPD
μ = 1.01, σ = 0.04 (+0.04-0.03)
Prior
x = 1.00 , σ = 0.04
Steps
FD Det 12

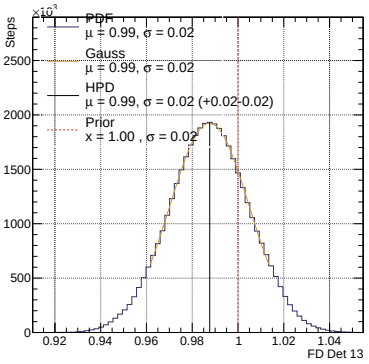
PDF
μ = 0.99, σ = 0.02
Gauss
μ = 0.99, σ = 0.02
HPD
μ = 0.99, σ = 0.02 (+0.02-0.02)
Prior
x = 1.00 , σ = 0.02
Steps
FD Det 13

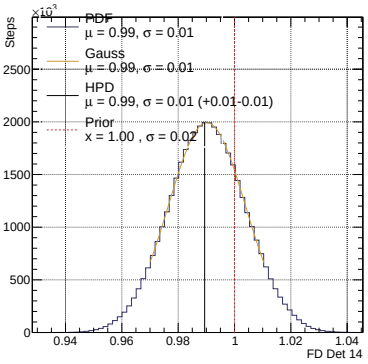
PDF
μ = 0.99, σ = 0.01
Gauss
μ = 0.99, σ = 0.01
HPD
μ = 0.99, σ = 0.01 (+0.01-0.01)
Prior
x = 1.00 , σ = 0.02
Steps
FD Det 14

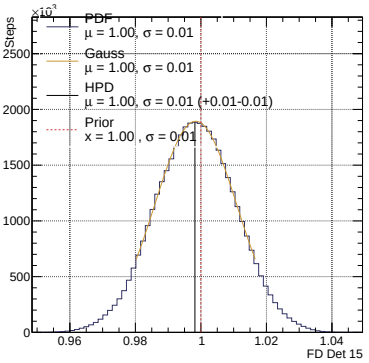
PDF
μ = 1.00, σ = 0.01
Gauss
μ = 1.00, σ = 0.01
HPD
μ = 1.00, σ = 0.01 (+0.01-0.01)
Prior
x = 1.00 , σ = 0.01
Steps
FD Det 15

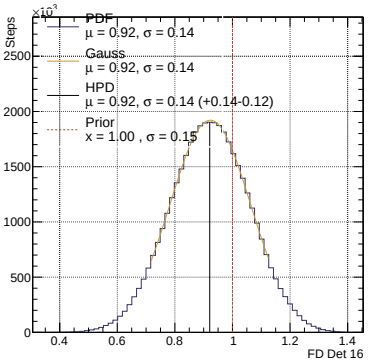
PDF
μ = 0.92, σ = 0.14
Gauss
μ = 0.92, σ = 0.14
HPD
μ = 0.92, σ = 0.14 (+0.14-0.12)
Prior
x = 1.00 , σ = 0.15
Steps
FD Det 16

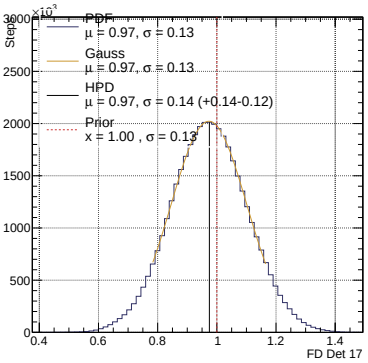
PDF
μ = 0.97, σ = 0.13
Gauss
μ = 0.97, σ = 0.13
HPD
μ = 0.97, σ = 0.14 (+0.14-0.12)
Prior
x = 1.00 , σ = 0.13
Steps
FD Det 17

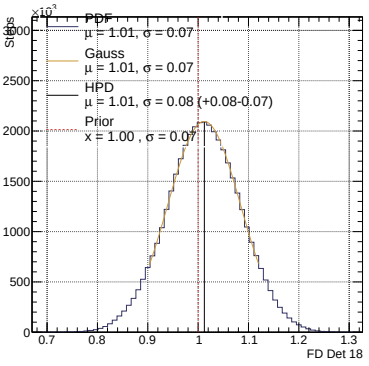
PDF
μ = 1.01, σ = 0.07
Gauss
μ = 1.01, σ = 0.07
HPD
μ = 1.01, σ = 0.08 (+0.08-0.07)
Prior
x = 1.00 , σ = 0.07
Steps
FD Det 18

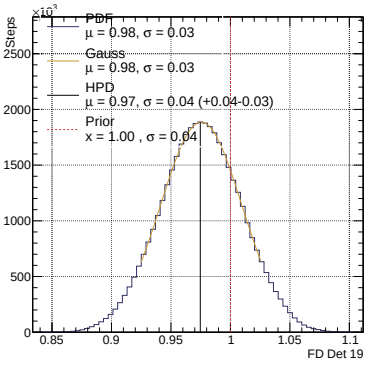
PDF
μ = 0.98, σ = 0.03
Gauss
μ = 0.98, σ = 0.03
HPD
μ = 0.97, σ = 0.04 (+0.04-0.03)
Prior
x = 1.00 , σ = 0.04
Steps
FD Det 19

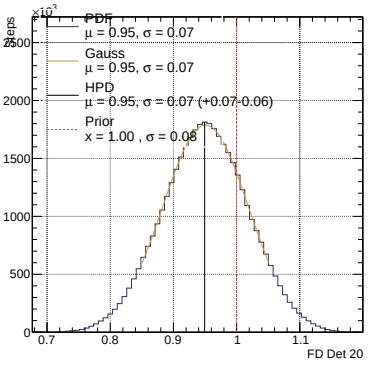
PDF
μ = 0.95, σ = 0.07
Gauss
μ = 0.95, σ = 0.07
HPD
μ = 0.95, σ = 0.07 (+0.07-0.06)
Prior
x = 1.00 , σ = 0.08
Steps
FD Det 20

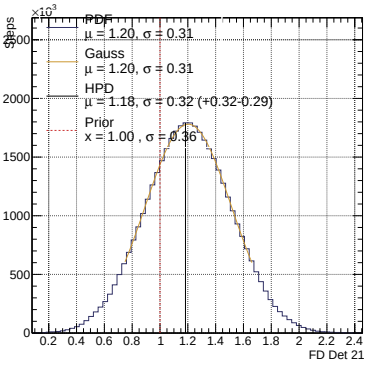
PDF
μ = 1.20, σ = 0.31
Gauss
μ = 1.20, σ = 0.31
HPD
μ = 1.18, σ = 0.32 (+0.32-0.29)
Prior
x = 1.00 , σ = 0.36
Steps
FD Det 21

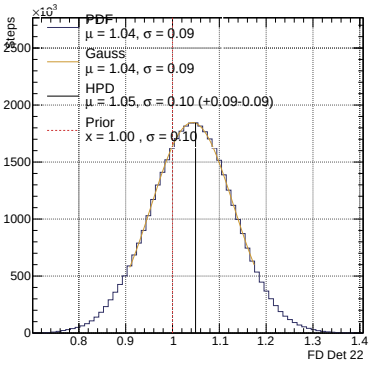
PDF
μ = 1.04, σ = 0.09
Gauss
μ = 1.04, σ = 0.09
HPD
μ = 1.05, σ = 0.10 (+0.09-0.09)
Prior
x = 1.00 , σ = 0.10
Steps
FD Det 22

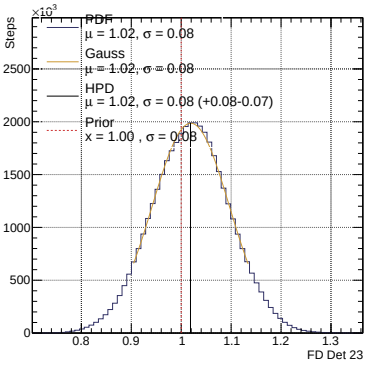
PDF
μ = 1.02, σ = 0.08
Gauss
μ = 1.02, σ = 0.08
HPD
μ = 1.02, σ = 0.08 (+0.08-0.07)
Prior
x = 1.00 , σ = 0.08
Steps
FD Det 23

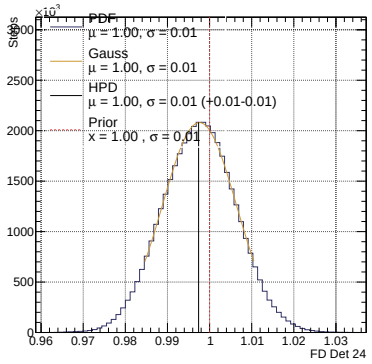
PDF
μ = 1.00, σ = 0.01
Gauss
μ = 1.00, σ = 0.01
HPD
μ = 1.00, σ = 0.01 (+0.01-0.01)
Prior
x = 1.00 , σ = 0.01
Steps
FD Det 24

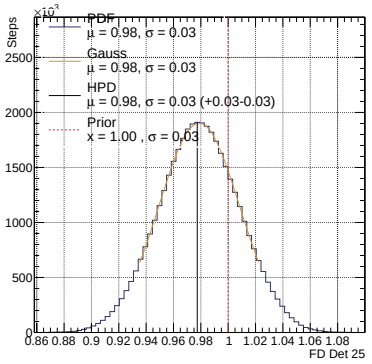
PDF
μ = 0.98, σ = 0.03
Gauss
μ = 0.98, σ = 0.03
HPD
μ = 0.98, σ = 0.03 (+0.03-0.03)
Prior
x = 1.00 , σ = 0.03
Steps
FD Det 25

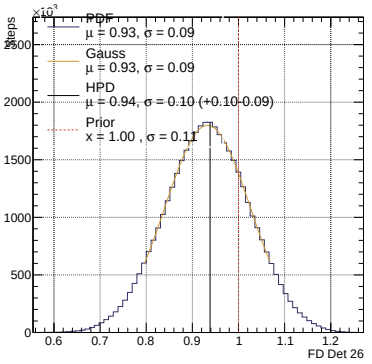
PDF
μ = 0.93, σ = 0.09
Gauss
μ = 0.93, σ = 0.09
HPD
μ = 0.94, σ = 0.10 (+0.10-0.09)
Prior
x = 1.00 , σ = 0.11
Steps
FD Det 26

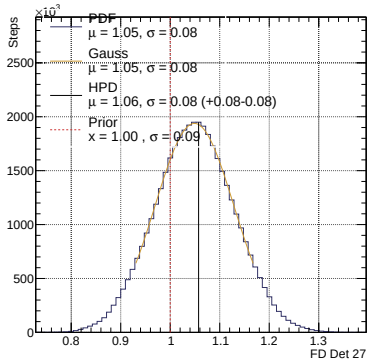
PDF
μ = 1.05, σ = 0.08
Gauss
μ = 1.05, σ = 0.08
HPD
μ = 1.06, σ = 0.08 (+0.08-0.08)
Prior
x = 1.00 , σ = 0.09
Steps
FD Det 27

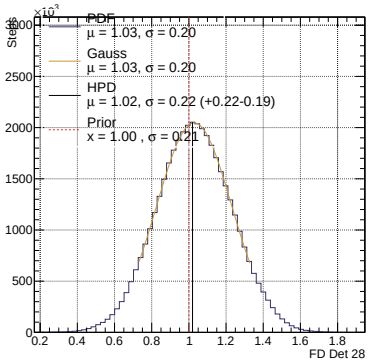
PDF
μ = 1.03, σ = 0.20
Gauss
μ = 1.03, σ = 0.20
HPD
μ = 1.02, σ = 0.22 (+0.22-0.19)
Prior
x = 1.00 , σ = 0.21
Steps
FD Det 28

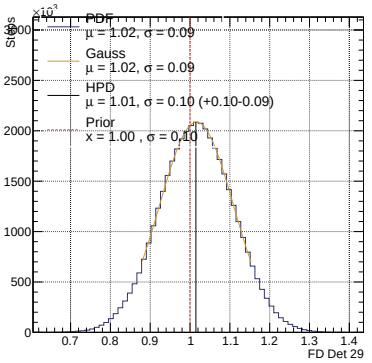
PDF
μ = 1.02, σ = 0.09
Gauss
μ = 1.02, σ = 0.09
HPD
μ = 1.01, σ = 0.10 (+0.10-0.09)
Prior
x = 1.00 , σ = 0.10
Steps
FD Det 29

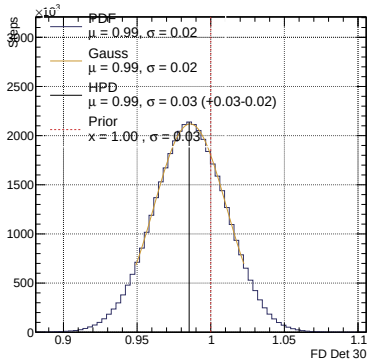
PDF
μ = 0.99, σ = 0.02
Gauss
μ = 0.99, σ = 0.02
HPD
μ = 0.99, σ = 0.03 (+0.03-0.02)
Prior
x = 1.00 , σ = 0.03
Steps
FD Det 30

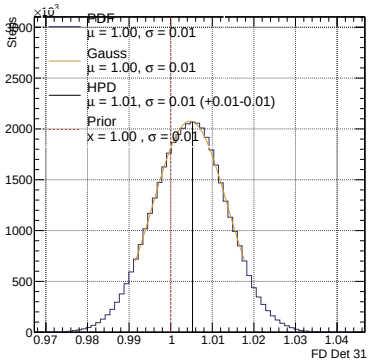
PDF
μ = 1.00, σ = 0.01
Gauss
μ = 1.00, σ = 0.01
HPD
μ = 1.01, σ = 0.01 (+0.01-0.01)
Prior
x = 1.00 , σ = 0.01
Steps
FD Det 31

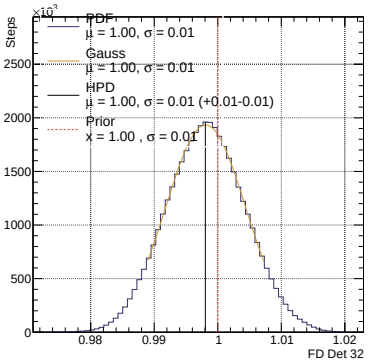
PDF
μ = 1.00, σ = 0.01
Gauss
μ = 1.00, σ = 0.01
HPD
μ = 1.00, σ = 0.01 (+0.01-0.01)
Prior
x = 1.00 , σ = 0.01
Steps
FD Det 32

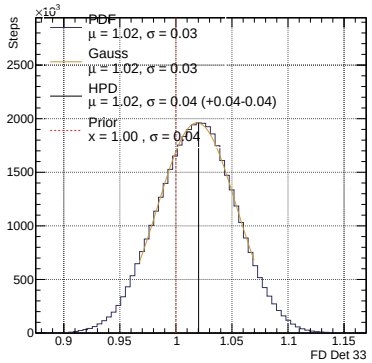
PDF
μ = 1.02, σ = 0.03
Gauss
μ = 1.02, σ = 0.03
HPD
μ = 1.02, σ = 0.04 (+0.04-0.04)
Prior
x = 1.00 , σ = 0.04
Steps
FD Det 33

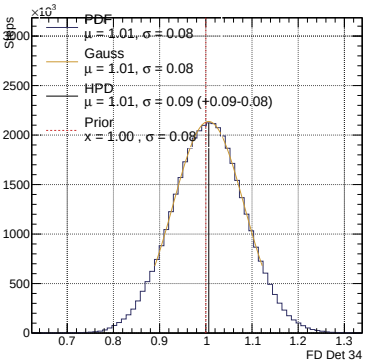
PDF
μ = 1.01, σ = 0.08
Gauss
μ = 1.01, σ = 0.08
HPD
μ = 1.01, σ = 0.09 (+0.09-0.08)
Prior
x = 1.00 , σ = 0.09
Steps
FD Det 34

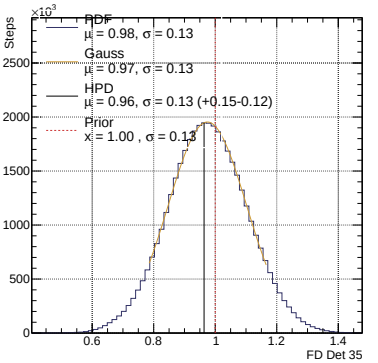
PDF
μ = 0.98, σ = 0.13
Gauss
μ = 0.97, σ = 0.13
HPD
μ = 0.96, σ = 0.13 (+0.15-0.12)
Prior
x = 1.00 , σ = 0.13
Steps
FD Det 35

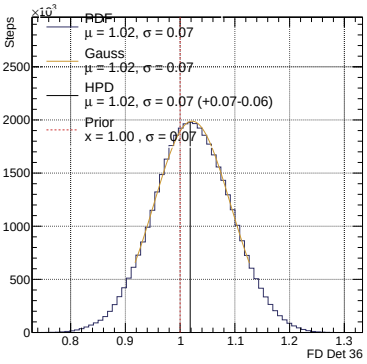
PDF
μ = 1.02, σ = 0.07
Gauss
μ = 1.02, σ = 0.07
HPD
μ = 1.02, σ = 0.07 (+0.07-0.06)
Prior
x = 1.00 , σ = 0.07
Steps
FD Det 36

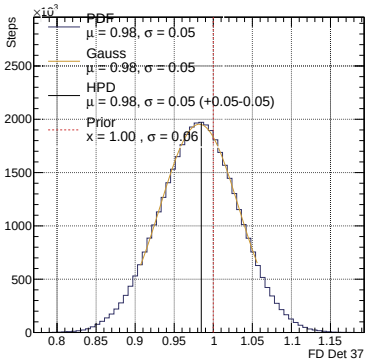
PDF
μ = 0.98, σ = 0.05
Gauss
μ = 0.98, σ = 0.05
HPD
μ = 0.98, σ = 0.05 (+0.05-0.05)
Prior
x = 1.00 , σ = 0.06
Steps
FD Det 37

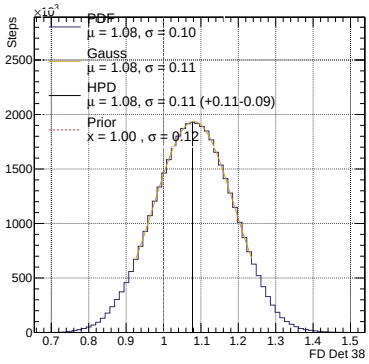
PDF
μ = 1.08, σ = 0.10
Gauss
μ = 1.08, σ = 0.11
HPD
μ = 1.08, σ = 0.11 (+0.11-0.09)
Prior
x = 1.00 , σ = 0.12
Steps
FD Det 38

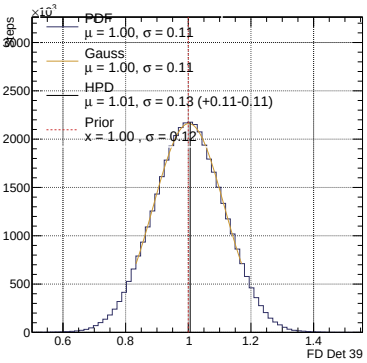
PDF
μ = 1.00, σ = 0.11
Gauss
μ = 1.00, σ = 0.11
HPD
μ = 1.01, σ = 0.13 (+0.11-0.11)
Prior
x = 1.00 , σ = 0.12
Steps
FD Det 39

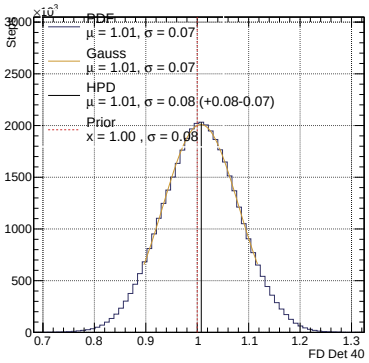
PDF
μ = 1.01, σ = 0.07
Gauss
μ = 1.01, σ = 0.07
HPD
μ = 1.01, σ = 0.08 (+0.08-0.07)
Prior
x = 1.00 , σ = 0.08
Steps
FD Det 40

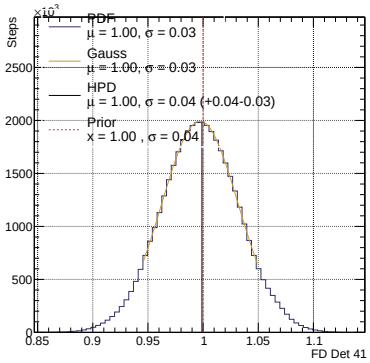
PDF
μ = 1.00, σ = 0.03
Gauss
μ = 1.00, σ = 0.03
HPD
μ = 1.00, σ = 0.04 (+0.04-0.03)
Prior
x = 1.00 , σ = 0.04
Steps
FD Det 41

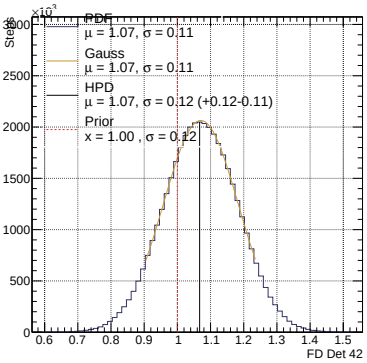
PDF
μ = 1.07, σ = 0.11
Gauss
μ = 1.07, σ = 0.11
HPD
μ = 1.07, σ = 0.12 (+0.12-0.11)
Prior
x = 1.00 , σ = 0.12
Steps
FD Det 42

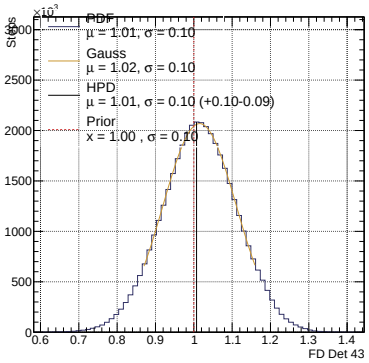
PDF
μ = 1.01, σ = 0.10
Gauss
μ = 1.02, σ = 0.10
HPD
μ = 1.01, σ = 0.10 (+0.10-0.09)
Prior
x = 1.00 , σ = 0.10
Steps
FD Det 43

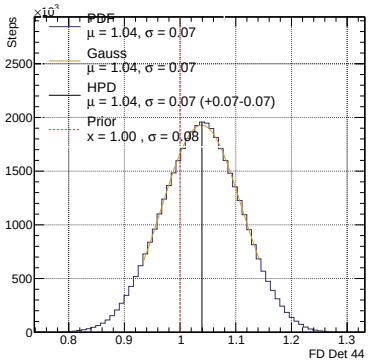
PDF
μ = 1.04, σ = 0.07
Gauss
μ = 1.04, σ = 0.07
HPD
μ = 1.04, σ = 0.07 (+0.07-0.07)
Prior
x = 1.00 , σ = 0.08
Steps
FD Det 44

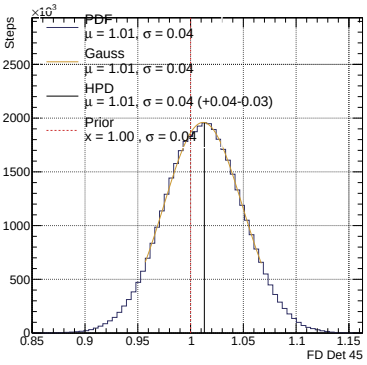
PDF
μ = 1.01, σ = 0.04
Gauss
μ = 1.01, σ = 0.04
HPD
μ = 1.01, σ = 0.04 (+0.04-0.03)
Prior
x = 1.00 , σ = 0.04
Steps
FD Det 45

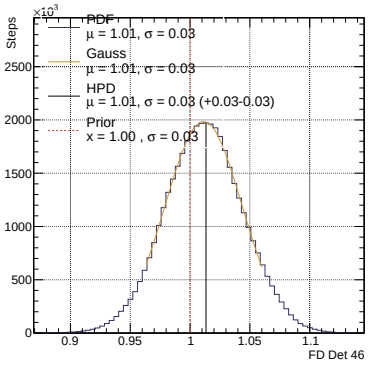
PDF
μ = 1.01, σ = 0.03
Gauss
μ = 1.01, σ = 0.03
HPD
μ = 1.01, σ = 0.03 (+0.03-0.03)
Prior
x = 1.00 , σ = 0.03
Steps
FD Det 46

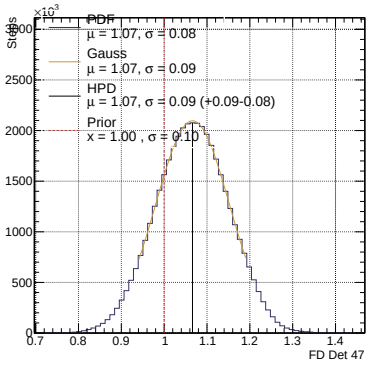
PDF
μ = 1.07, σ = 0.08
Gauss
μ = 1.07, σ = 0.09
HPD
μ = 1.07, σ = 0.09 (+0.09-0.08)
Prior
x = 1.00 , σ = 0.10
Steps
FD Det 47

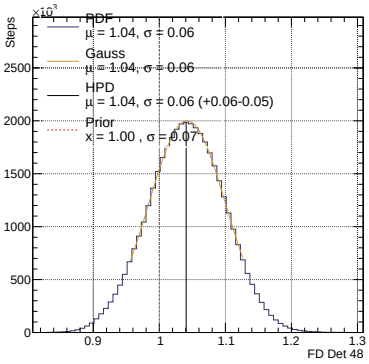
PDF
μ = 1.04, σ = 0.06
Gauss
μ = 1.04, σ = 0.06
HPD
μ = 1.04, σ = 0.06 (+0.06-0.05)
Prior
x = 1.00 , σ = 0.07
Steps
FD Det 48

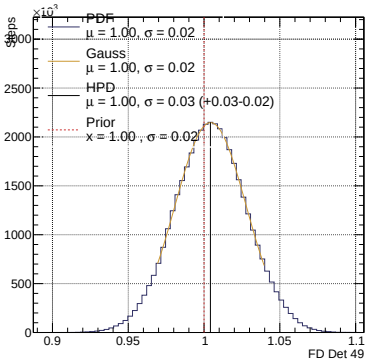
PDF
μ = 1.00, σ = 0.02
Gauss
μ = 1.00, σ = 0.02
HPD
μ = 1.00, σ = 0.03 (+0.03-0.02)
Prior
x = 1.00 , σ = 0.02
Steps
FD Det 49

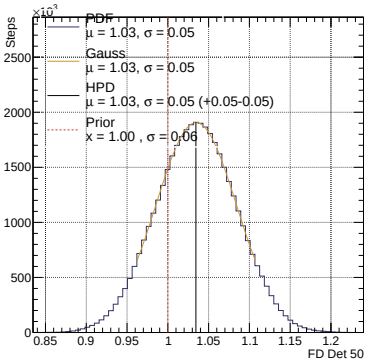
PDF
μ = 1.03, σ = 0.05
Gauss
μ = 1.03, σ = 0.05
HPD
μ = 1.03, σ = 0.05 (+0.05-0.05)
Prior
x = 1.00 , σ = 0.06
Steps
FD Det 50

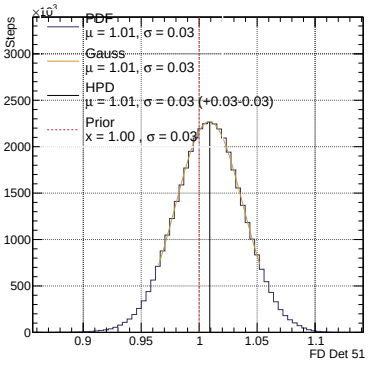
PDF
μ = 1.01, σ = 0.03
Gauss
μ = 1.01, σ = 0.03
HPD
μ = 1.01, σ = 0.03 (+0.03-0.03)
Prior
x = 1.00 , σ = 0.03
Steps
FD Det 51

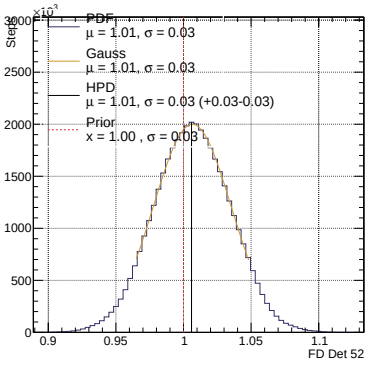
PDF
μ = 1.01, σ = 0.03
Gauss
μ = 1.01, σ = 0.03
HPD
μ = 1.01, σ = 0.03 (+0.03-0.03)
Prior
x = 1.00 , σ = 0.03
Steps
FD Det 52

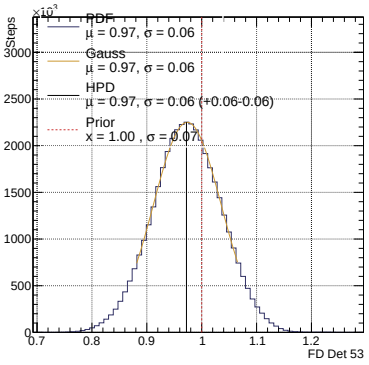
PDF
μ = 0.97, σ = 0.06
Gauss
μ = 0.97, σ = 0.06
HPD
μ = 0.97, σ = 0.06 (+0.06-0.06)
Prior
x = 1.00 , σ = 0.07
Steps
FD Det 53

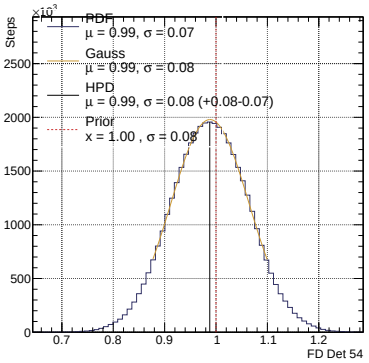
PDF
μ = 0.99, σ = 0.07
Gauss
μ = 0.99, σ = 0.08
HPD
μ = 0.99, σ = 0.08 (+0.08-0.07)
Prior
x = 1.00 , σ = 0.08
Steps
FD Det 54

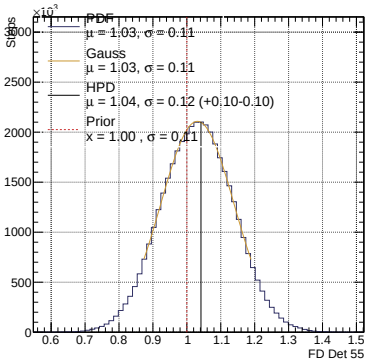
PDF
μ = 1.03, σ = 0.11
Gauss
μ = 1.03, σ = 0.11
HPD
μ = 1.04, σ = 0.12 (+0.10-0.10)
Prior
x = 1.00 , σ = 0.11
Steps
FD Det 55

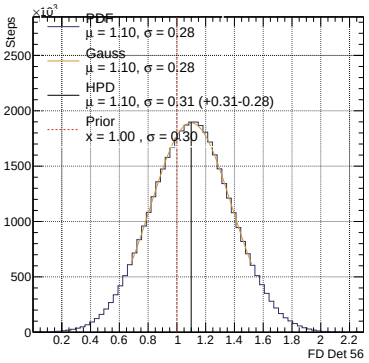
PDF
μ = 1.10, σ = 0.28
Gauss
μ = 1.10, σ = 0.28
HPD
μ = 1.10, σ = 0.31 (+0.31-0.28)
Prior
x = 1.00 , σ = 0.30
Steps
FD Det 56

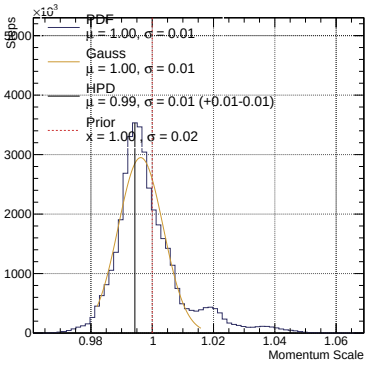
PDF
μ = 1.00, σ = 0.01
Gauss
μ = 1.00, σ = 0.01
HPD
μ = 0.99, σ = 0.01 (+0.01-0.01)
Prior
x = 1.00 , σ = 0.02
Steps
Momentum Scale

B.3 Flux Parameters

The posterior distributions of all the 100 (50 for ND and 50 for FD) flux parameters are shown in this section. Table B.2 summarises each of these 50 parameters split by the neutrino flavour and neutrino energy range.

Index	Beam mode	ν flavour	ν energy (GeV)
0	FHC	ν_μ	0.0–0.4
1			0.4–0.5
2			0.5–0.6
3			0.6–0.7
4			0.7–1.0
5			1.0–1.5
6			1.5–2.5
7			2.5–3.5
8			3.5–5.0
9			5.0–7.0
10			7.0–30.0
11		$\bar{\nu}_\mu$	0.0–0.7
12			0.7–1.0
13			1.0–1.5
14			1.5–2.5
15			2.5–30.0
16		ν_e	0.0–0.5
17			0.5–0.7
18			0.7–0.8
19			0.8–1.5
20			1.5–2.5
21			2.5–4.0
22			4.0–30.0
23		$\bar{\nu}_e$	0.0–2.5
24			2.5–30.0
25	RHC	ν_μ	0.0–0.7
26			0.7–1.0
27			1.0–1.5
28			1.5–2.5
29			2.5–30.0
30		$\bar{\nu}_\mu$	0.0–0.4
31			0.4–0.5
32			0.5–0.6
33			0.6–0.7
34			0.7–1.0
35			1.0–1.5
36			1.5–2.5
37			2.5–3.5
38			3.5–5.0
39			5.0–7.0
40			7.0–30.0
41		ν_e	0.0–2.5
42			2.5–30.0
43		$\bar{\nu}_e$	0.0–0.5
44			0.5–0.7
45			0.7–0.8
46			0.8–1.5
47			1.5–2.5
48			2.5–4.0
49			4.0–30.0

TABLE B.2: The flux parameters broken down by the neutrino flavour and energy

The posterior distributions of these 100 parameters are labelled as "b_i" where i ranges from 0–99. The ND flux parameters range from b_0–b_{49} and those of SK range from b_{50}–b_{99}.

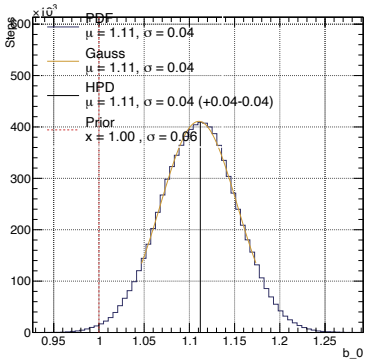
PDF
μ = 1.11, σ = 0.04
Gauss
μ = 1.11, σ = 0.04
HPD
μ = 1.11, σ = 0.04 (+0.04-0.04)
Prior
x = 1.00 , σ = 0.06
Steps
b_0

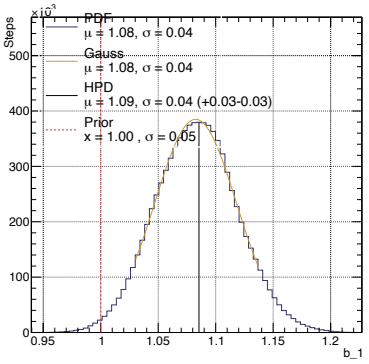
PDF
μ = 1.08, σ = 0.04
Gauss
μ = 1.08, σ = 0.04
HPD
μ = 1.09, σ = 0.04 (+0.03-0.03)
Prior
x = 1.00 , σ = 0.05
Steps
b_1

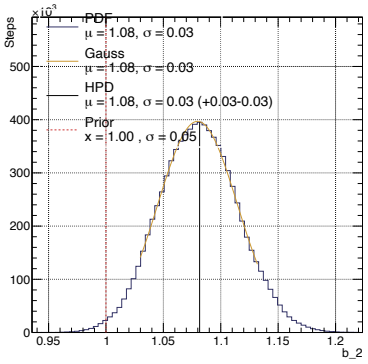
PDF
μ = 1.08, σ = 0.03
Gauss
μ = 1.08, σ = 0.03
HPD
μ = 1.08, σ = 0.03 (+0.03-0.03)
Prior
x = 1.00 , σ = 0.05
Steps
b_2

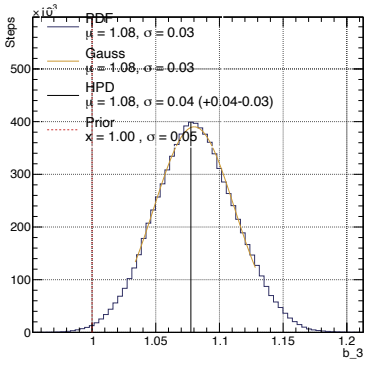
PDF
μ = 1.08, σ = 0.03
Gauss
μ = 1.08, σ = 0.03
HPD
μ = 1.08, σ = 0.04 (+0.04-0.03)
Prior
x = 1.00 , σ = 0.05
Steps
b_3

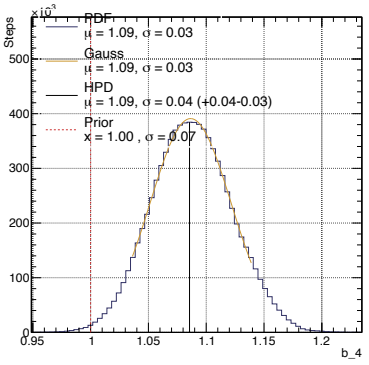
PDF
μ = 1.09, σ = 0.03
Gauss
μ = 1.09, σ = 0.03
HPD
μ = 1.09, σ = 0.04 (+0.04-0.03)
Prior
x = 1.00 , σ = 0.07
Steps
b_4

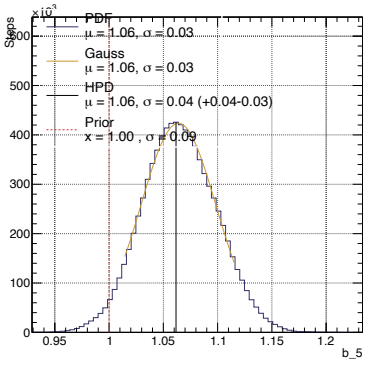
PDF
μ = 1.06, σ = 0.03
Gauss
μ = 1.06, σ = 0.03
HPD
μ = 1.06, σ = 0.04 (+0.04-0.03)
Prior
x = 1.00 , σ = 0.09
Steps
b_5

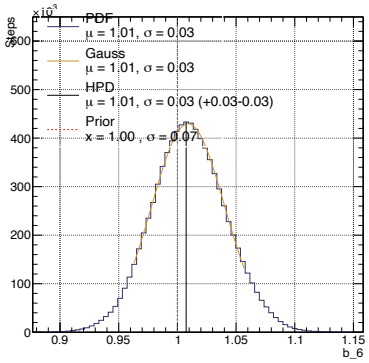
PDF
μ = 1.01, σ = 0.03
Gauss
μ = 1.01, σ = 0.03
HPD
μ = 1.01, σ = 0.03 (+0.03-0.03)
Prior
x = 1.00 , σ = 0.07
Steps
b_6

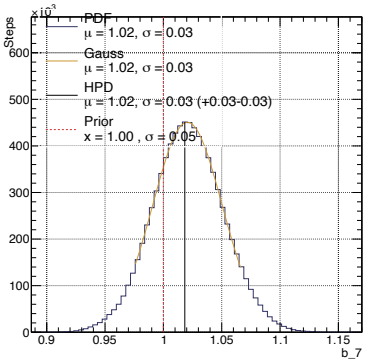
PDF
μ = 1.02, σ = 0.03
Gauss
μ = 1.02, σ = 0.03
HPD
μ = 1.02, σ = 0.03 (+0.03-0.03)
Prior
x = 1.00 , σ = 0.05
Steps
b_7

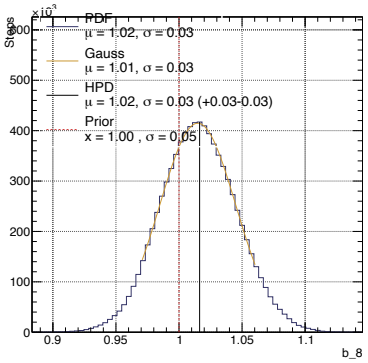
PDF
μ = 1.02, σ = 0.03
Gauss
μ = 1.01, σ = 0.03
HPD
μ = 1.02, σ = 0.03 (+0.03-0.03)
Prior
x = 1.00 , σ = 0.05
Steps
b_8

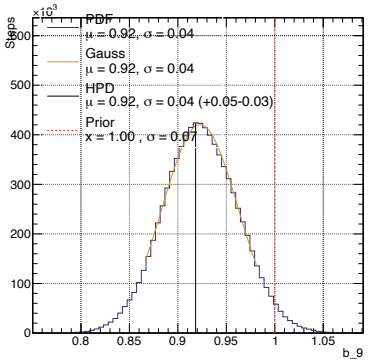
PDF
μ = 0.92, σ = 0.04
Gauss
μ = 0.92, σ = 0.04
HPD
μ = 0.92, σ = 0.04 (+0.05-0.03)
Prior
x = 1.00 , σ = 0.07
Steps
b_9

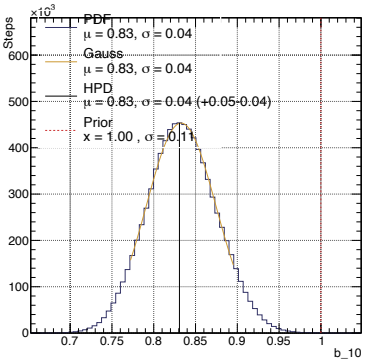
PDF
μ = 0.83, σ = 0.04
Gauss
μ = 0.83, σ = 0.04
HPD
μ = 0.83, σ = 0.04 (+0.05-0.04)
Prior
x = 1.00 , σ = 0.11
Steps
b_10

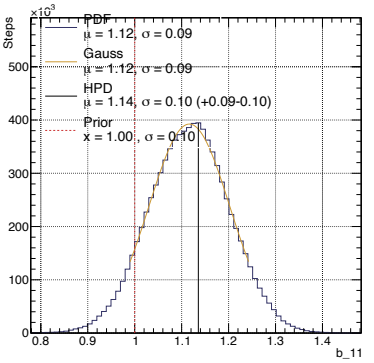
PDF
μ = 1.12, σ = 0.09
Gauss
μ = 1.12, σ = 0.09
HPD
μ = 1.14, σ = 0.10 (+0.09-0.10)
Prior
x = 1.00 , σ = 0.10
Steps
b_11

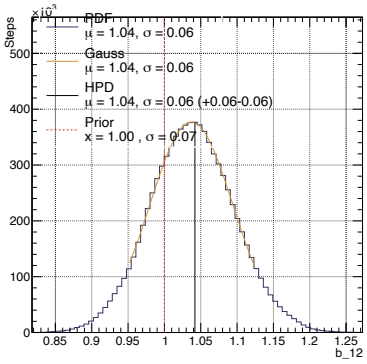
PDF
μ = 1.04, σ = 0.06
Gauss
μ = 1.04, σ = 0.06
HPD
μ = 1.04, σ = 0.06 (+0.06-0.06)
Prior
x = 1.00 , σ = 0.07
Steps
b_12

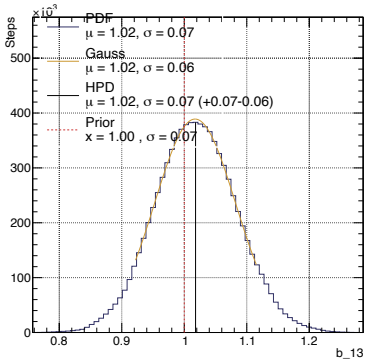
PDF
μ = 1.02, σ = 0.07
Gauss
μ = 1.02, σ = 0.06
HPD
μ = 1.02, σ = 0.07 (+0.07-0.06)
Prior
x = 1.00 , σ = 0.07
Steps
b_13

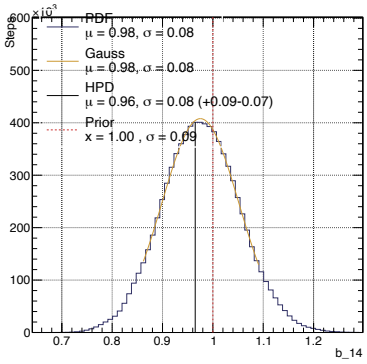
PDF
μ = 0.98, σ = 0.08
Gauss
μ = 0.98, σ = 0.08
HPD
μ = 0.96, σ = 0.08 (+0.09-0.07)
Prior
x = 1.00 , σ = 0.09
Steps
b_14

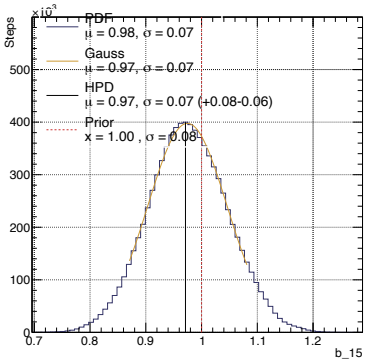
PDF
μ = 0.98, σ = 0.07
Gauss
μ = 0.97, σ = 0.07
HPD
μ = 0.97, σ = 0.07 (+0.08-0.06)
Prior
x = 1.00 , σ = 0.08
Steps
b_15

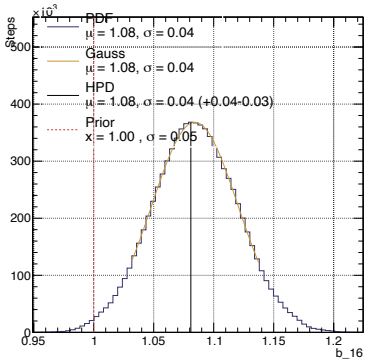
PDF
μ = 1.08, σ = 0.04
Gauss
μ = 1.08, σ = 0.04
HPD
μ = 1.08, σ = 0.04 (+0.04-0.03)
Prior
x = 1.00 , σ = 0.05
Steps
b_16

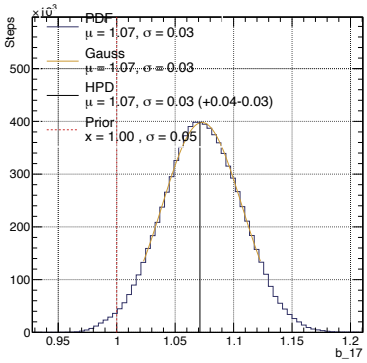
PDF
μ = 1.07, σ = 0.03
Gauss
μ = 1.07, σ = 0.03
HPD
μ = 1.07, σ = 0.03 (+0.04-0.03)
Prior
x = 1.00 , σ = 0.05
Steps
b_17

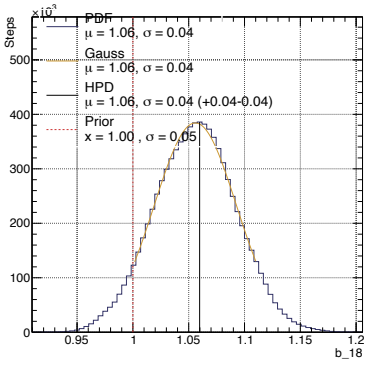
PDF
μ = 1.06, σ = 0.04
Gauss
μ = 1.06, σ = 0.04
HPD
μ = 1.06, σ = 0.04 (+0.04-0.04)
Prior
x = 1.00 , σ = 0.05
Steps
b_18

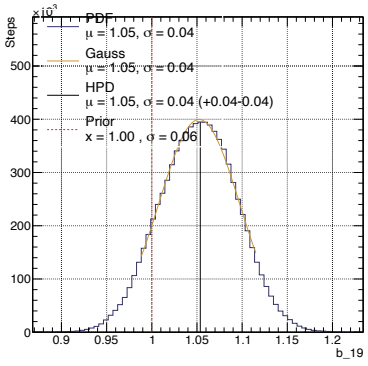
PDF
μ = 1.05, σ = 0.04
Gauss
μ = 1.05, σ = 0.04
HPD
μ = 1.05, σ = 0.04 (+0.04-0.04)
Prior
x = 1.00 , σ = 0.06
Steps
b_19

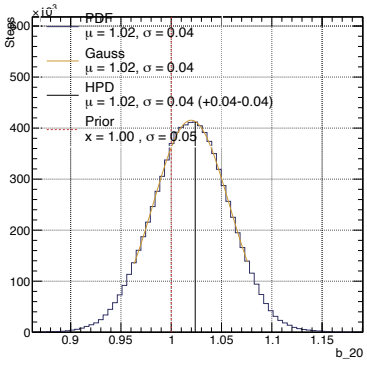
PDF
μ = 1.02, σ = 0.04
Gauss
μ = 1.02, σ = 0.04
HPD
μ = 1.02, σ = 0.04 (+0.04-0.04)
Prior
x = 1.00 , σ = 0.05
Steps
b_20

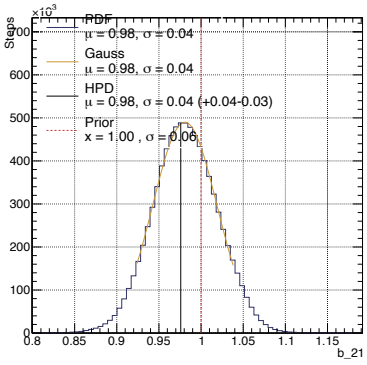
PDF
μ = 0.98, σ = 0.04
Gauss
μ = 0.98, σ = 0.04
HPD
μ = 0.98, σ = 0.04 (+0.04-0.03)
Prior
x = 1.00 , σ = 0.06
Steps
b_21

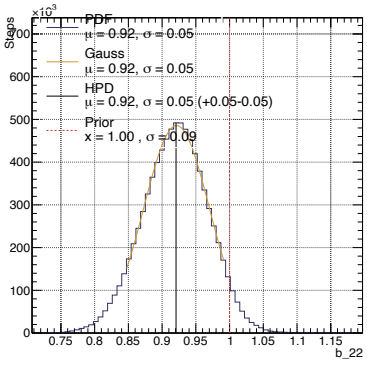
PDF
μ = 0.92, σ = 0.05
Gauss
μ = 0.92, σ = 0.05
HPD
μ = 0.92, σ = 0.05 (+0.05-0.05)
Prior
x = 1.00 , σ = 0.09
Steps
b_22

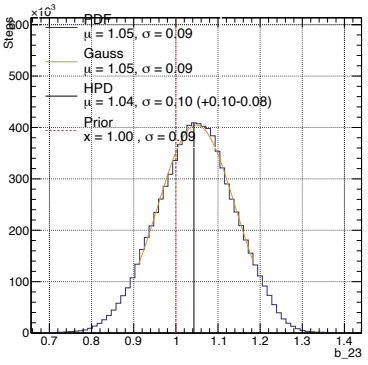
PDF
μ = 1.05, σ = 0.09
Gauss
μ = 1.05, σ = 0.09
HPD
μ = 1.04, σ = 0.10 (+0.10-0.08)
Prior
x = 1.00 , σ = 0.09
Steps
b_23

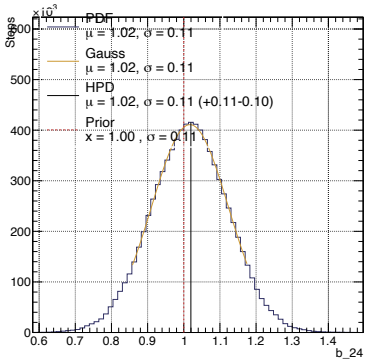
PDF
μ = 1.02, σ = 0.11
Gauss
μ = 1.02, σ = 0.11
HPD
μ = 1.02, σ = 0.11 (+0.11-0.10)
Prior
x = 1.00 , σ = 0.11
Steps
b_24

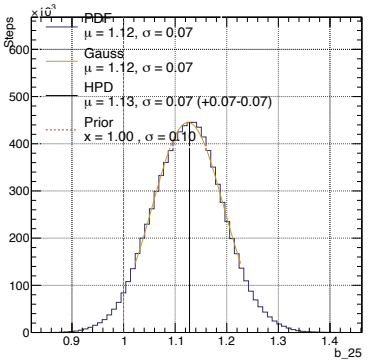
PDF
μ = 1.12, σ = 0.07
Gauss
μ = 1.12, σ = 0.07
HPD
μ = 1.13, σ = 0.07 (+0.07-0.07)
Prior
x = 1.00 , σ = 0.10
Steps
b_25

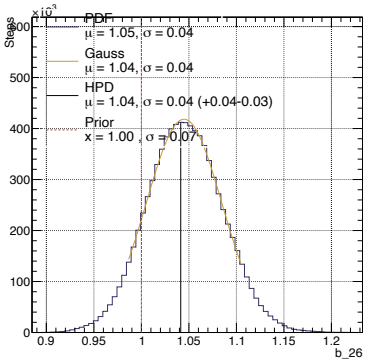
PDF
μ = 1.05, σ = 0.04
Gauss
μ = 1.04, σ = 0.04
HPD
μ = 1.04, σ = 0.04 (+0.04-0.03)
Prior
x = 1.00 , σ = 0.07
Steps
b_26

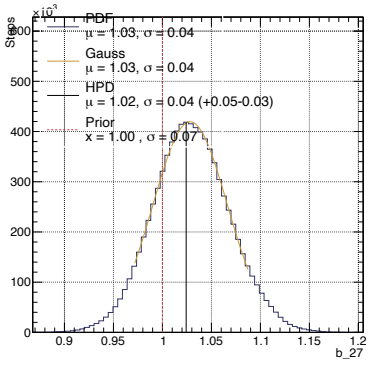
PDF
μ = 1.03, σ = 0.04
Gauss
μ = 1.03, σ = 0.04
HPD
μ = 1.02, σ = 0.04 (+0.05-0.03)
Prior
x = 1.00 , σ = 0.07
Steps
b_27

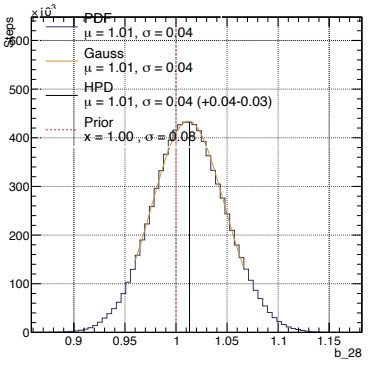
PDF
μ = 1.01, σ = 0.04
Gauss
μ = 1.01, σ = 0.04
HPD
μ = 1.01, σ = 0.04 (+0.04-0.03)
Prior
x = 1.00 , σ = 0.08
Steps
b_28

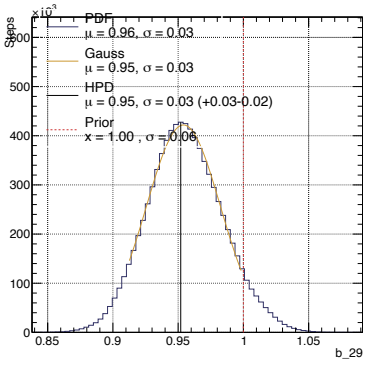
PDF
μ = 0.96, σ = 0.03
Gauss
μ = 0.95, σ = 0.03
HPD
μ = 0.95, σ = 0.03 (+0.03-0.02)
Prior
x = 1.00 , σ = 0.06
Steps
b_29

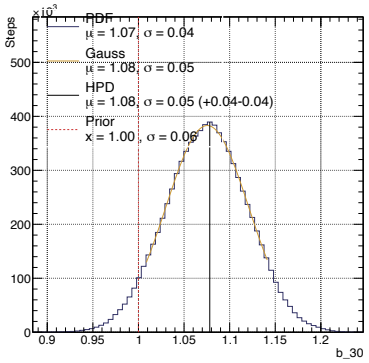
PDF
μ = 1.07, σ = 0.04
Gauss
μ = 1.08, σ = 0.05
HPD
μ = 1.08, σ = 0.05 (+0.04-0.04)
Prior
x = 1.00 , σ = 0.06
Steps
b_30

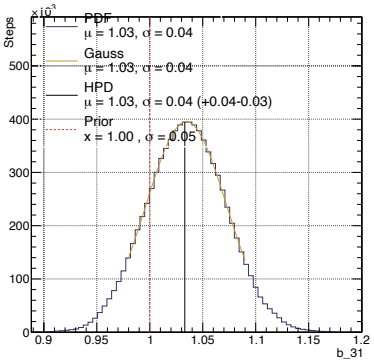
PDF
μ = 1.03, σ = 0.04
Gauss
μ = 1.03, σ = 0.04
HPD
μ = 1.03, σ = 0.04 (+0.04-0.03)
Prior
x = 1.00 , σ = 0.05
Steps
b_31

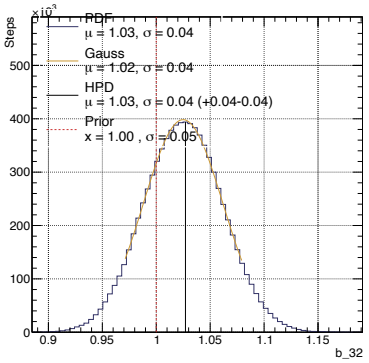
PDF
μ = 1.03, σ = 0.04
Gauss
μ = 1.02, σ = 0.04
HPD
μ = 1.03, σ = 0.04 (+0.04-0.04)
Prior
x = 1.00 , σ = 0.05
Steps
b_32

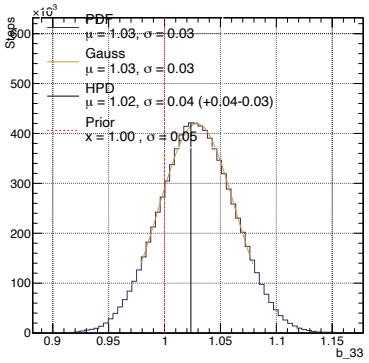
PDF
μ = 1.03, σ = 0.03
Gauss
μ = 1.03, σ = 0.03
HPD
μ = 1.02, σ = 0.04 (+0.04-0.03)
Prior
x = 1.00 , σ = 0.05
Steps
b_33

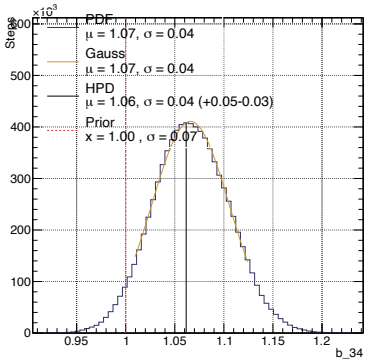
PDF
μ = 1.07, σ = 0.04
Gauss
μ = 1.07, σ = 0.04
HPD
μ = 1.06, σ = 0.04 (+0.05-0.03)
Prior
x = 1.00 , σ = 0.07
Steps
b_34

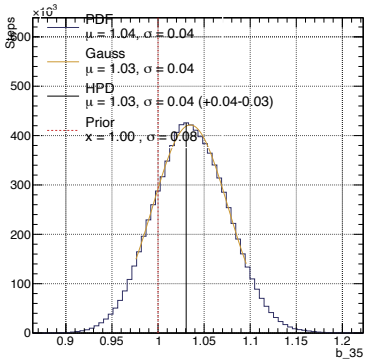
PDF
μ = 1.04, σ = 0.04
Gauss
μ = 1.03, σ = 0.04
HPD
μ = 1.03, σ = 0.04 (+0.04-0.03)
Prior
x = 1.00 , σ = 0.08
Steps
b_35

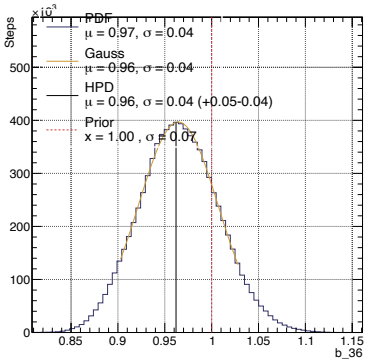
PDF
μ = 0.97, σ = 0.04
Gauss
μ = 0.96, σ = 0.04
HPD
μ = 0.96, σ = 0.04 (+0.05-0.04)
Prior
x = 1.00 , σ = 0.07
Steps
b_36

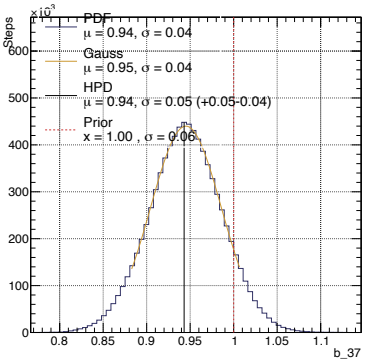
PDF
μ = 0.94, σ = 0.04
Gauss
μ = 0.95, σ = 0.04
HPD
μ = 0.94, σ = 0.05 (+0.05-0.04)
Prior
x = 1.00 , σ = 0.06
Steps
b_37

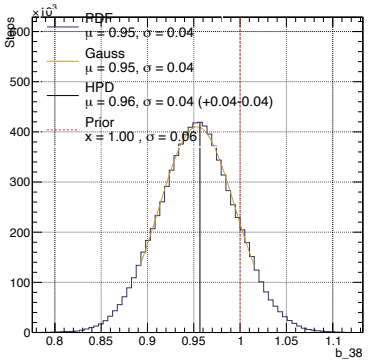
PDF
μ = 0.95, σ = 0.04
Gauss
μ = 0.95, σ = 0.04
HPD
μ = 0.96, σ = 0.04 (+0.04-0.04)
Prior
x = 1.00 , σ = 0.06
Steps
b_38

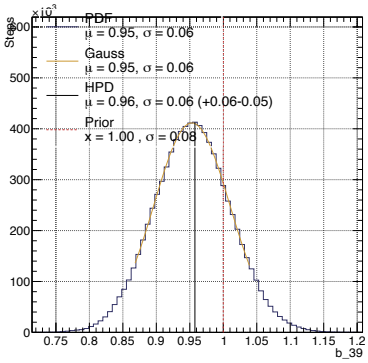
PDF
μ = 0.95, σ = 0.06
Gauss
μ = 0.95, σ = 0.06
HPD
μ = 0.96, σ = 0.06 (+0.06-0.05)
Prior
x = 1.00 , σ = 0.08
Steps
b_39

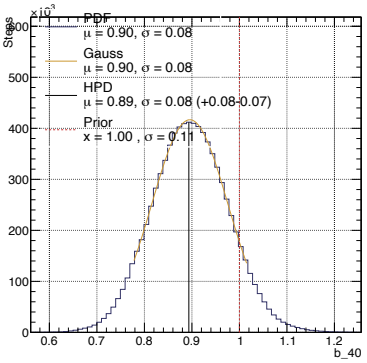
PDF
μ = 0.90, σ = 0.08
Gauss
μ = 0.90, σ = 0.08
HPD
μ = 0.89, σ = 0.08 (+0.08-0.07)
Prior
x = 1.00 , σ = 0.11
Steps
b_40

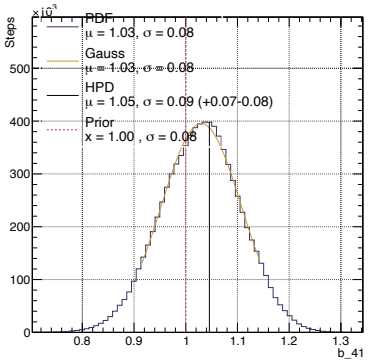
PDF
μ = 1.03, σ = 0.08
Gauss
μ = 1.03, σ = 0.08
HPD
μ = 1.05, σ = 0.09 (+0.07-0.08)
Prior
x = 1.00 , σ = 0.08
Steps
b_41

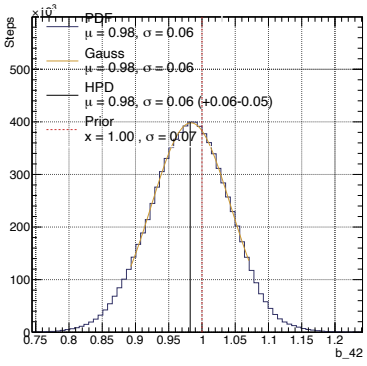
PDF
μ = 0.98, σ = 0.06
Gauss
μ = 0.98, σ = 0.06
HPD
μ = 0.98, σ = 0.06 (+0.06-0.05)
Prior
x = 1.00 , σ = 0.07
Steps
b_42

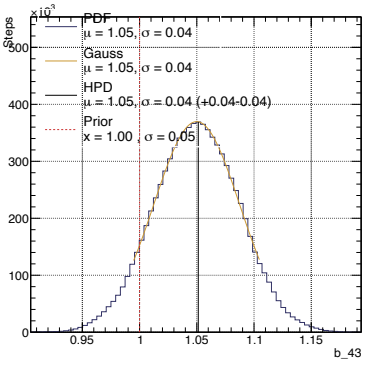
PDF
μ = 1.05, σ = 0.04
Gauss
μ = 1.05, σ = 0.04
HPD
μ = 1.05, σ = 0.04 (+0.04-0.04)
Prior
x = 1.00 , σ = 0.05
Steps
b_43

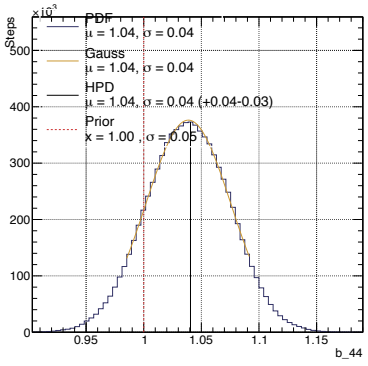
PDF
μ = 1.04, σ = 0.04
Gauss
μ = 1.04, σ = 0.04
HPD
μ = 1.04, σ = 0.04 (+0.04-0.03)
Prior
x = 1.00 , σ = 0.05
Steps
b_44

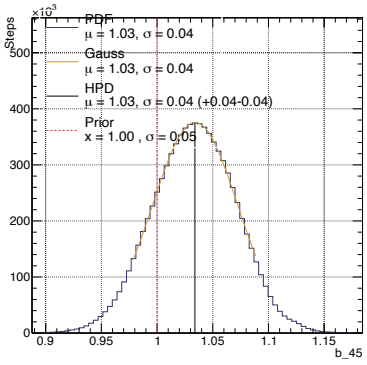
PDF
μ = 1.03, σ = 0.04
Gauss
μ = 1.03, σ = 0.04
HPD
μ = 1.03, σ = 0.04 (+0.04-0.04)
Prior
x = 1.00 , σ = 0.05
Steps
b_45

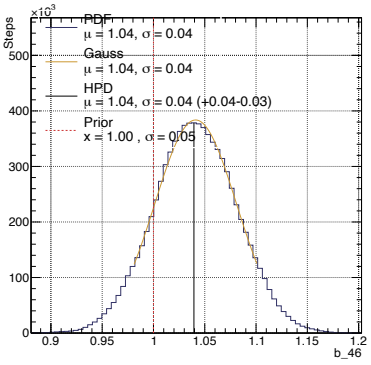
PDF
μ = 1.04, σ = 0.04
Gauss
μ = 1.04, σ = 0.04
HPD
μ = 1.04, σ = 0.04 (+0.04-0.03)
Prior
x = 1.00 , σ = 0.05
Steps
b_46

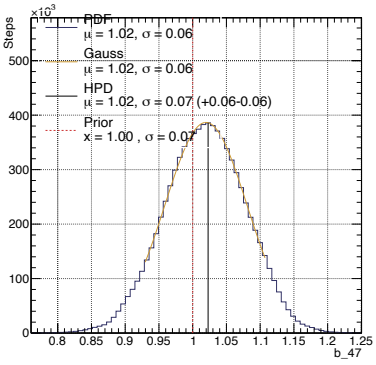
PDF
μ = 1.02, σ = 0.06
Gauss
μ = 1.02, σ = 0.06
HPD
μ = 1.02, σ = 0.07 (+0.06-0.06)
Prior
x = 1.00 , σ = 0.07
Steps
b_47

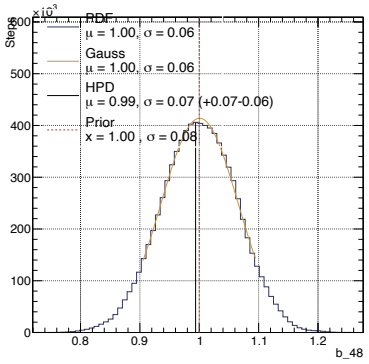
PDF
μ = 1.00, σ = 0.06
Gauss
μ = 1.00, σ = 0.06
HPD
μ = 0.99, σ = 0.07 (+0.07-0.06)
Prior
x = 1.00 , σ = 0.08
Steps
b_48

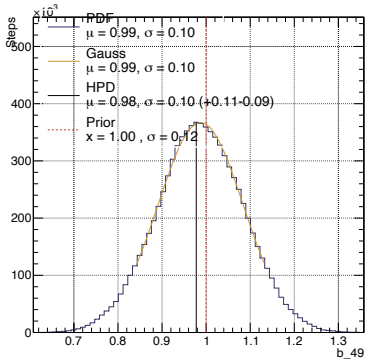
PDF
μ = 0.99, σ = 0.10
Gauss
μ = 0.99, σ = 0.10
HPD
μ = 0.98, σ = 0.10 (+0.11-0.09)
Prior
x = 1.00 , σ = 0.12
Steps
b_49

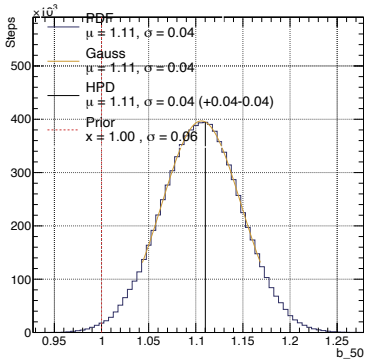
PDF
μ = 1.11, σ = 0.04
Gauss
μ = 1.11, σ = 0.04
HPD
μ = 1.11, σ = 0.04 (+0.04-0.04)
Prior
x = 1.00 , σ = 0.06
Steps
b_50

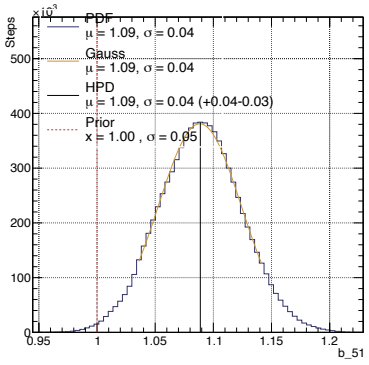
PDF
μ = 1.09, σ = 0.04
Gauss
μ = 1.09, σ = 0.04
HPD
μ = 1.09, σ = 0.04 (+0.04-0.03)
Prior
x = 1.00 , σ = 0.05
Steps
b_51

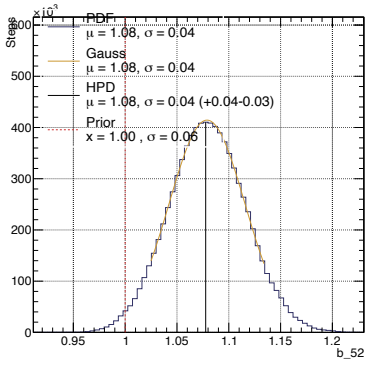
PDF
μ = 1.08, σ = 0.04
Gauss
μ = 1.08, σ = 0.04
HPD
μ = 1.08, σ = 0.04 (+0.04-0.03)
Prior
x = 1.00 , σ = 0.06
Steps
b_52

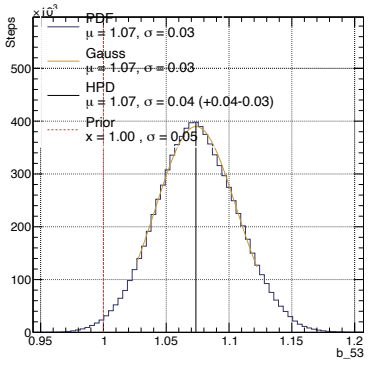
PDF
μ = 1.07, σ = 0.03
Gauss
μ = 1.07, σ = 0.03
HPD
μ = 1.07, σ = 0.04 (+0.04-0.03)
Prior
x = 1.00 , σ = 0.05
Steps
b_53

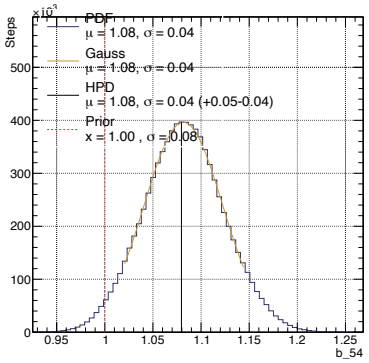
PDF
μ = 1.08, σ = 0.04
Gauss
μ = 1.08, σ = 0.04
HPD
μ = 1.08, σ = 0.04 (+0.05-0.04)
Prior
x = 1.00 , σ = 0.08
Steps
b_54

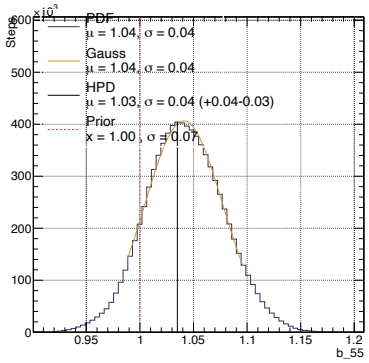
PDF
μ = 1.04, σ = 0.04
Gauss
μ = 1.04, σ = 0.04
HPD
μ = 1.03, σ = 0.04 (+0.04-0.03)
Prior
x = 1.00 , σ = 0.07
Steps
b_55

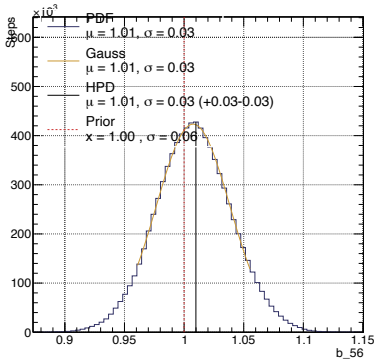
PDF
μ = 1.01, σ = 0.03
Gauss
μ = 1.01, σ = 0.03
HPD
μ = 1.01, σ = 0.03 (+0.03-0.03)
Prior
x = 1.00 , σ = 0.06
Steps
b_56

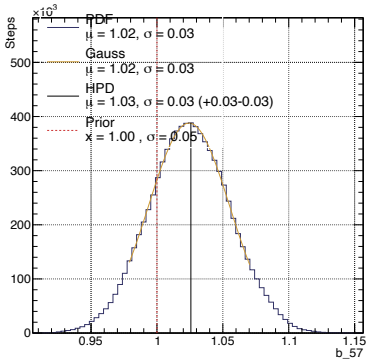
PDF
μ = 1.02, σ = 0.03
Gauss
μ = 1.02, σ = 0.03
HPD
μ = 1.03, σ = 0.03 (+0.03-0.03)
Prior
x = 1.00 , σ = 0.05
Steps
b_57

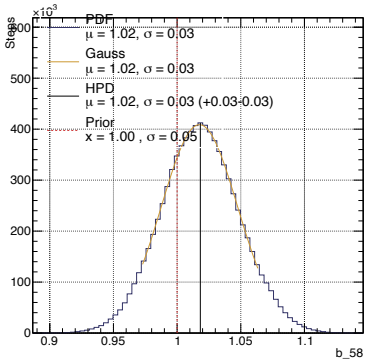
PDF
μ = 1.02, σ = 0.03
Gauss
μ = 1.02, σ = 0.03
HPD
μ = 1.02, σ = 0.03 (+0.03-0.03)
Prior
x = 1.00 , σ = 0.05
Steps
b_58

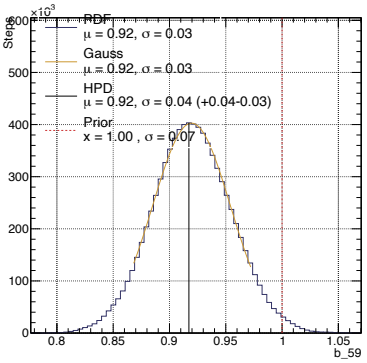
PDF
μ = 0.92, σ = 0.03
Gauss
μ = 0.92, σ = 0.03
HPD
μ = 0.92, σ = 0.04 (+0.04-0.03)
Prior
x = 1.00 , σ = 0.07
Steps
b_59

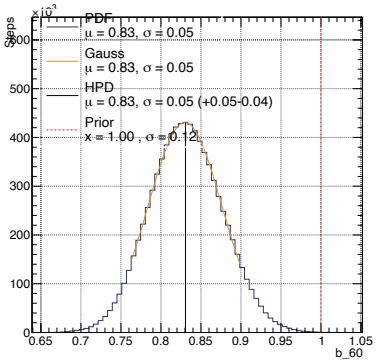
PDF
μ = 0.83, σ = 0.05
Gauss
μ = 0.83, σ = 0.05
HPD
μ = 0.83, σ = 0.05 (+0.05-0.04)
Prior
x = 1.00 , σ = 0.12
Steps
b_60

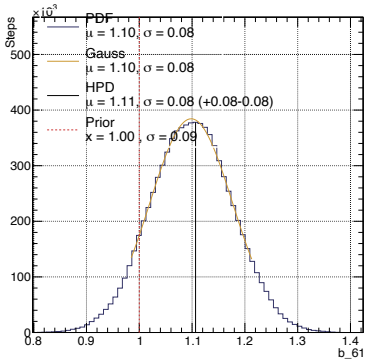
PDF
μ = 1.10, σ = 0.08
Gauss
μ = 1.10, σ = 0.08
HPD
μ = 1.11, σ = 0.08 (+0.08-0.08)
Prior
x = 1.00 , σ = 0.09
Steps
b_61

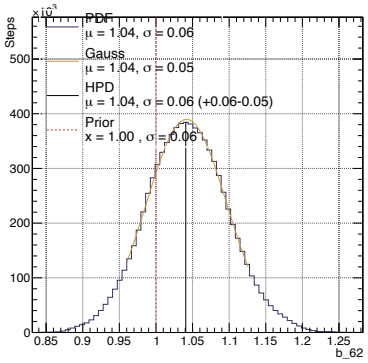
PDF
μ = 1.04, σ = 0.06
Gauss
μ = 1.04, σ = 0.05
HPD
μ = 1.04, σ = 0.06 (+0.06-0.05)
Prior
x = 1.00 , σ = 0.06
Steps
b_62

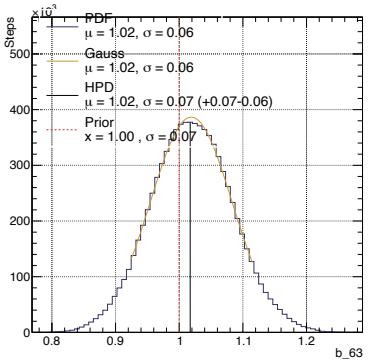
PDF
μ = 1.02, σ = 0.06
Gauss
μ = 1.02, σ = 0.06
HPD
μ = 1.02, σ = 0.07 (+0.07-0.06)
Prior
x = 1.00 , σ = 0.07
Steps
b_63

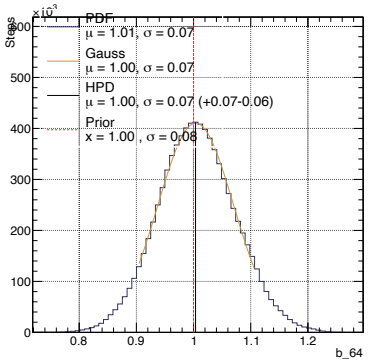
PDF
μ = 1.01, σ = 0.07
Gauss
μ = 1.00, σ = 0.07
HPD
μ = 1.00, σ = 0.07 (+0.07-0.06)
Prior
x = 1.00 , σ = 0.08
Steps
b_64

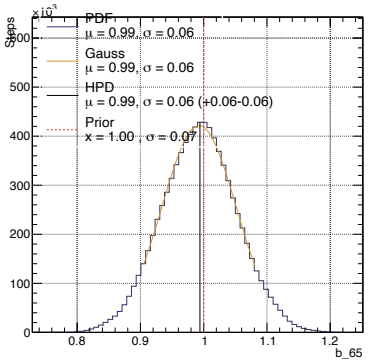
PDF
μ = 0.99, σ = 0.06
Gauss
μ = 0.99, σ = 0.06
HPD
μ = 0.99, σ = 0.06 (+0.06-0.06)
Prior
x = 1.00 , σ = 0.07
Steps
b_65

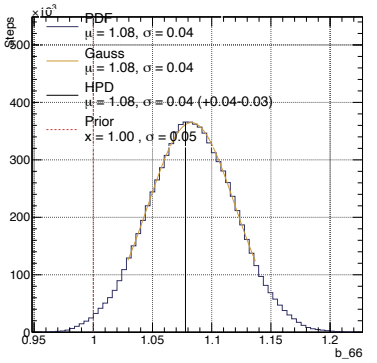
PDF
μ = 1.08, σ = 0.04
Gauss
μ = 1.08, σ = 0.04
HPD
μ = 1.08, σ = 0.04 (+0.04-0.03)
Prior
x = 1.00 , σ = 0.05
Steps
b_66

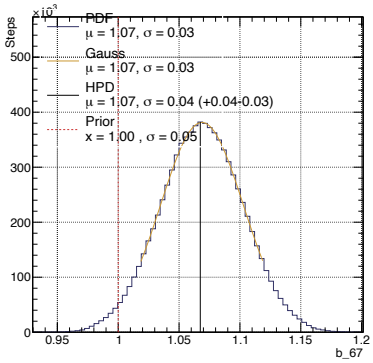
PDF
μ = 1.07, σ = 0.03
Gauss
μ = 1.07, σ = 0.03
HPD
μ = 1.07, σ = 0.04 (+0.04-0.03)
Prior
x = 1.00 , σ = 0.05
Steps
b_67

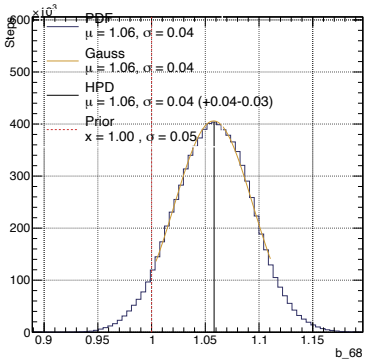
PDF
μ = 1.06, σ = 0.04
Gauss
μ = 1.06, σ = 0.04
HPD
μ = 1.06, σ = 0.04 (+0.04-0.03)
Prior
x = 1.00 , σ = 0.05
Steps
b_68

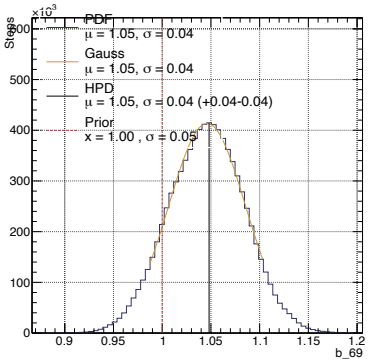
PDF
μ = 1.05, σ = 0.04
Gauss
μ = 1.05, σ = 0.04
HPD
μ = 1.05, σ = 0.04 (+0.04-0.04)
Prior
x = 1.00 , σ = 0.05
Steps
b_69

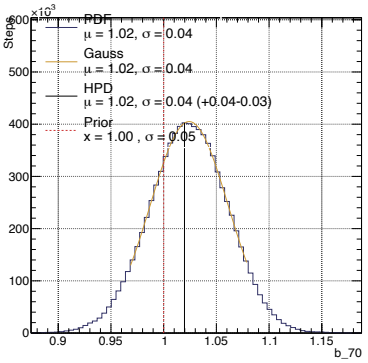
PDF
μ = 1.02, σ = 0.04
Gauss
μ = 1.02, σ = 0.04
HPD
μ = 1.02, σ = 0.04 (+0.04-0.03)
Prior
x = 1.00 , σ = 0.05
Steps
b_70

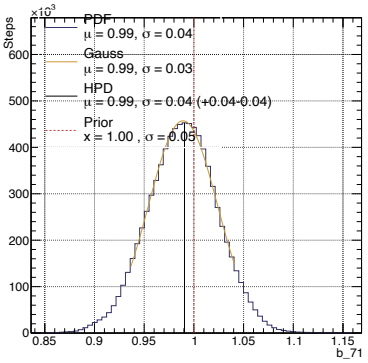
PDF
μ = 0.99, σ = 0.04
Gauss
μ = 0.99, σ = 0.03
HPD
μ = 0.99, σ = 0.04 (+0.04-0.04)
Prior
x = 1.00 , σ = 0.05
Steps
b_71

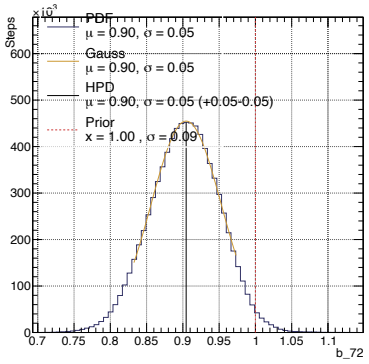
PDF
μ = 0.90, σ = 0.05
Gauss
μ = 0.90, σ = 0.05
HPD
μ = 0.90, σ = 0.05 (+0.05-0.05)
Prior
x = 1.00 , σ = 0.09
Steps
b_72

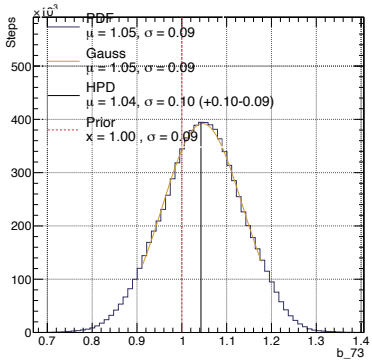
PDF
μ = 1.05, σ = 0.09
Gauss
μ = 1.05, σ = 0.09
HPD
μ = 1.04, σ = 0.10 (+0.10-0.09)
Prior
x = 1.00 , σ = 0.09
Steps
b_73

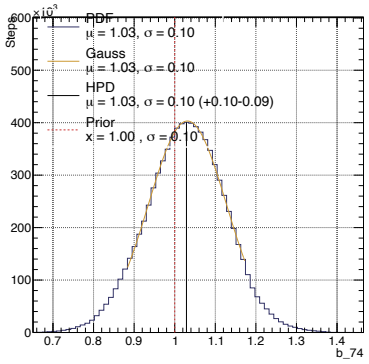
PDF
μ = 1.03, σ = 0.10
Gauss
μ = 1.03, σ = 0.10
HPD
μ = 1.03, σ = 0.10 (+0.10-0.09)
Prior
x = 1.00 , σ = 0.10
Steps
b_74

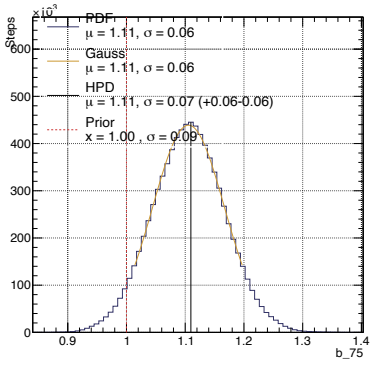
PDF
μ = 1.11, σ = 0.06
Gauss
μ = 1.11, σ = 0.06
HPD
μ = 1.11, σ = 0.07 (+0.06-0.06)
Prior
x = 1.00 , σ = 0.09
Steps
b_75

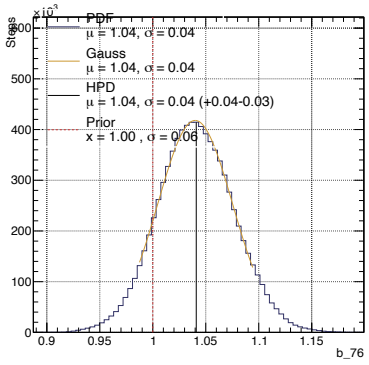
PDF
μ = 1.04, σ = 0.04
Gauss
μ = 1.04, σ = 0.04
HPD
μ = 1.04, σ = 0.04 (+0.04-0.03)
Prior
x = 1.00 , σ = 0.06
Steps
b_76

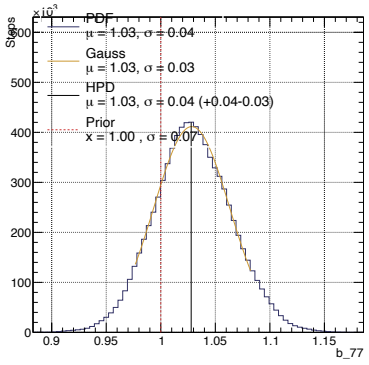
PDF
μ = 1.03, σ = 0.04
Gauss
μ = 1.03, σ = 0.03
HPD
μ = 1.03, σ = 0.04 (+0.04-0.03)
Prior
x = 1.00 , σ = 0.07
Steps
b_77

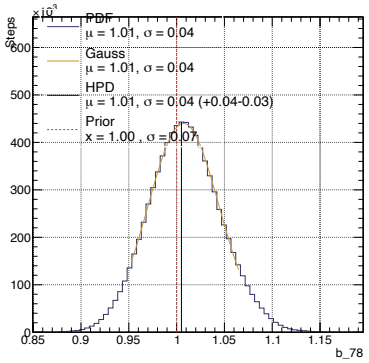
PDF
μ = 1.01, σ = 0.04
Gauss
μ = 1.01, σ = 0.04
HPD
μ = 1.01, σ = 0.04 (+0.04-0.03)
Prior
x = 1.00 , σ = 0.07
Steps
b_78

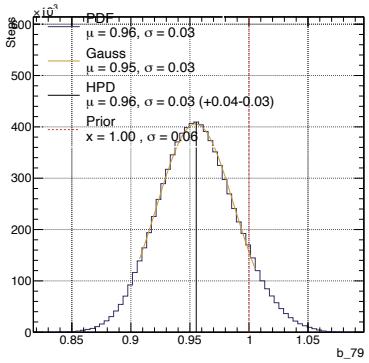
PDF
μ = 0.96, σ = 0.03
Gauss
μ = 0.95, σ = 0.03
HPD
μ = 0.96, σ = 0.03 (+0.04-0.03)
Prior
x = 1.00 , σ = 0.06
Steps
b_79

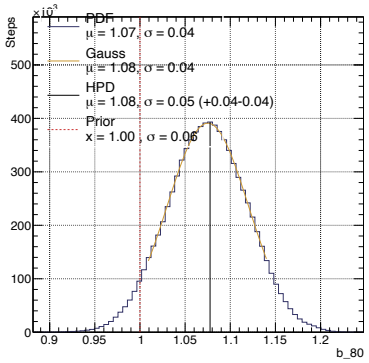
PDF
μ = 1.07, σ = 0.04
Gauss
μ = 1.08, σ = 0.04
HPD
μ = 1.08, σ = 0.05 (+0.04-0.04)
Prior
x = 1.00 , σ = 0.06
Steps
b_80

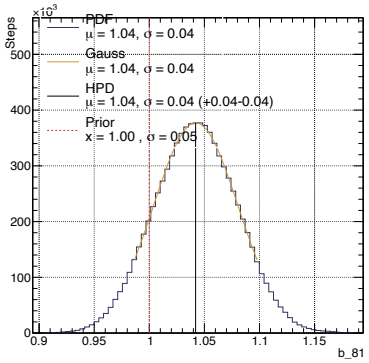
PDF
μ = 1.04, σ = 0.04
Gauss
μ = 1.04, σ = 0.04
HPD
μ = 1.04, σ = 0.04 (+0.04-0.04)
Prior
x = 1.00 , σ = 0.05
Steps
b_81

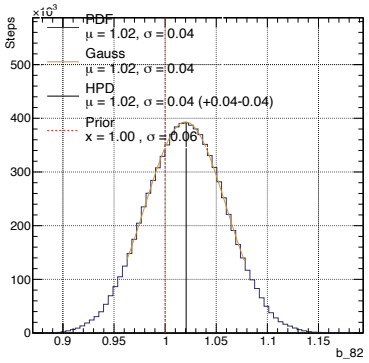
PDF
μ = 1.02, σ = 0.04
Gauss
μ = 1.02, σ = 0.04
HPD
μ = 1.02, σ = 0.04 (+0.04-0.04)
Prior
x = 1.00 , σ = 0.06
Steps
b_82

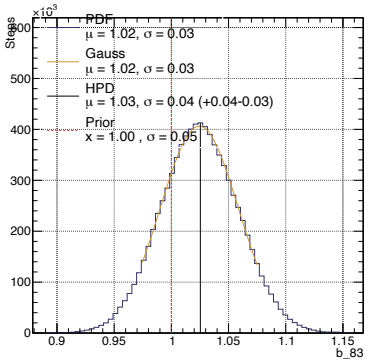
PDF
μ = 1.02, σ = 0.03
Gauss
μ = 1.02, σ = 0.03
HPD
μ = 1.03, σ = 0.04 (+0.04-0.03)
Prior
x = 1.00 , σ = 0.05
Steps
b_83

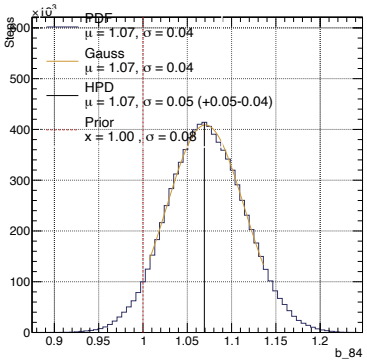
PDF
μ = 1.07, σ = 0.04
Gauss
μ = 1.07, σ = 0.04
HPD
μ = 1.07, σ = 0.05 (+0.05-0.04)
Prior
x = 1.00 , σ = 0.08
Steps
b_84

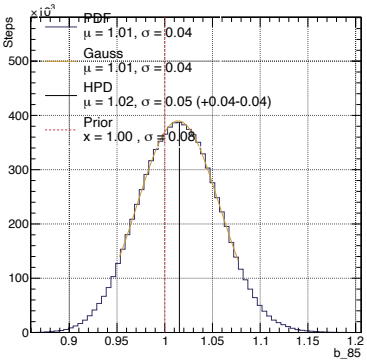
PDF
μ = 1.01, σ = 0.04
Gauss
μ = 1.01, σ = 0.04
HPD
μ = 1.02, σ = 0.05 (+0.04-0.04)
Prior
x = 1.00 , σ = 0.08
Steps
b_85

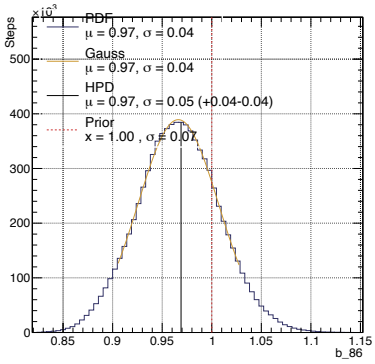
PDF
μ = 0.97, σ = 0.04
Gauss
μ = 0.97, σ = 0.04
HPD
μ = 0.97, σ = 0.05 (+0.04-0.04)
Prior
x = 1.00 , σ = 0.07
Steps
b_86

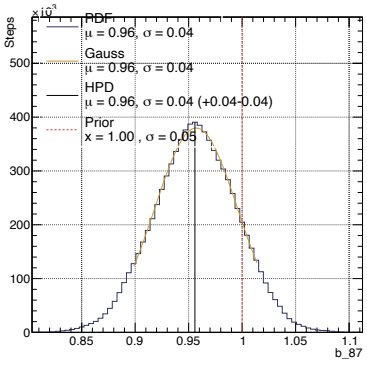
PDF
μ = 0.96, σ = 0.04
Gauss
μ = 0.96, σ = 0.04
HPD
μ = 0.96, σ = 0.04 (+0.04-0.04)
Prior
x = 1.00 , σ = 0.05
Steps
b_87

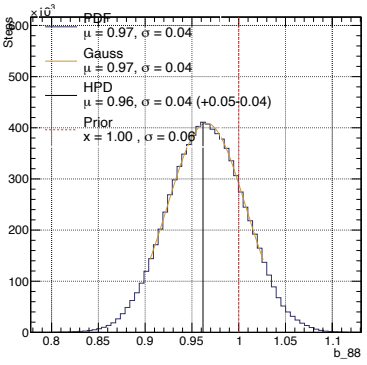
PDF
μ = 0.97, σ = 0.04
Gauss
μ = 0.97, σ = 0.04
HPD
μ = 0.96, σ = 0.04 (+0.05-0.04)
Prior
x = 1.00 , σ = 0.06
Steps
b_88

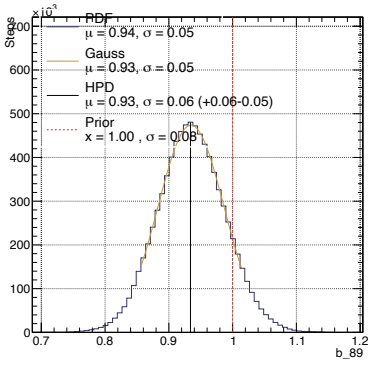
PDF
μ = 0.94, σ = 0.05
Gauss
μ = 0.93, σ = 0.05
HPD
μ = 0.93, σ = 0.06 (+0.06-0.05)
Prior
x = 1.00 , σ = 0.08
Steps
b_89

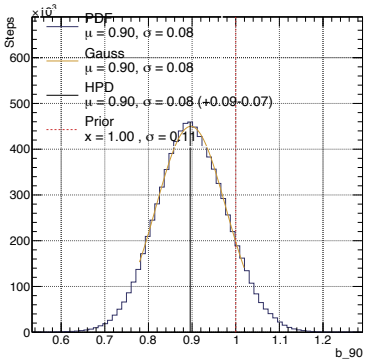
PDF
μ = 0.90, σ = 0.08
Gauss
μ = 0.90, σ = 0.08
HPD
μ = 0.90, σ = 0.08 (+0.09-0.07)
Prior
x = 1.00 , σ = 0.11
Steps
b_90

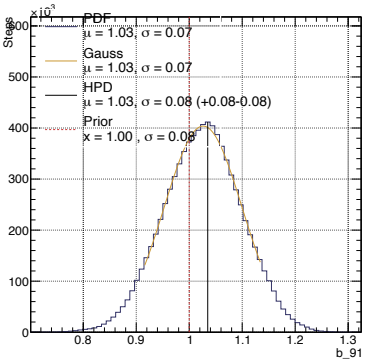
PDF
μ = 1.03, σ = 0.07
Gauss
μ = 1.03, σ = 0.07
HPD
μ = 1.03, σ = 0.08 (+0.08-0.08)
Prior
x = 1.00 , σ = 0.08
Steps
b_91

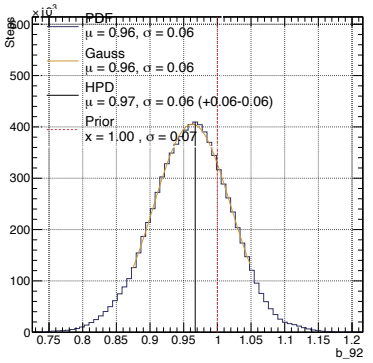
PDF
μ = 0.96, σ = 0.06
Gauss
μ = 0.96, σ = 0.06
HPD
μ = 0.97, σ = 0.06 (+0.06-0.06)
Prior
x = 1.00 , σ = 0.07
Steps
b_92

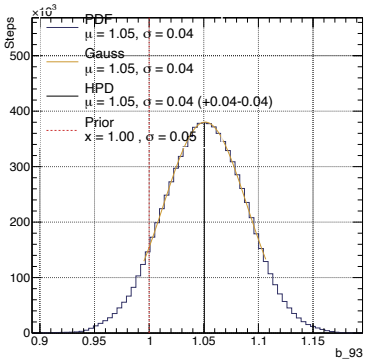
PDF
μ = 1.05, σ = 0.04
Gauss
μ = 1.05, σ = 0.04
HPD
μ = 1.05, σ = 0.04 (+0.04-0.04)
Prior
x = 1.00 , σ = 0.05
Steps
b_93

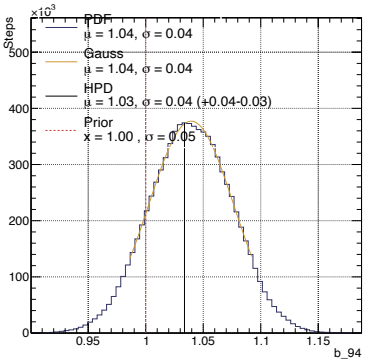
PDF
μ = 1.04, σ = 0.04
Gauss
μ = 1.04, σ = 0.04
HPD
μ = 1.03, σ = 0.04 (+0.04-0.03)
Prior
x = 1.00 , σ = 0.05
Steps
b_94

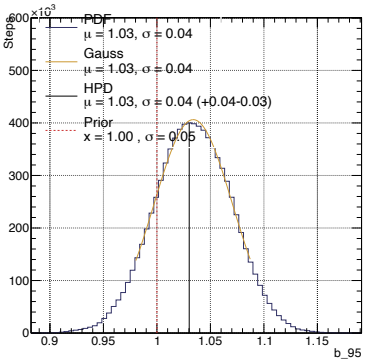
PDF
μ = 1.03, σ = 0.04
Gauss
μ = 1.03, σ = 0.04
HPD
μ = 1.03, σ = 0.04 (+0.04-0.03)
Prior
x = 1.00 , σ = 0.05
Steps
b_95

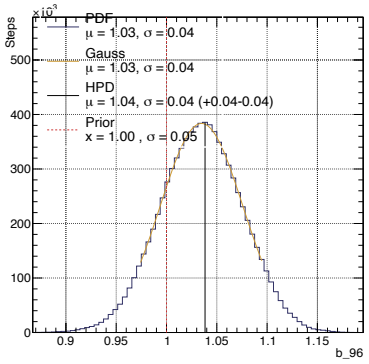
x10³
Steps
PDF
μ = 1.03, σ = 0.04
Gauss
μ = 1.03, σ = 0.04
HPD
μ = 1.04, σ = 0.04 (+0.04-0.04)
Prior
x = 1.00 , σ = 0.05
b_96

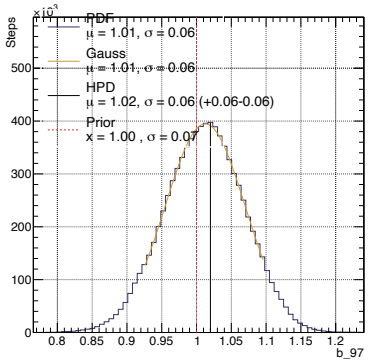
x10³
Steps
PDF
μ = 1.01, σ = 0.06
Gauss
μ = 1.01, σ = 0.06
HPD
μ = 1.02, σ = 0.06 (+0.06-0.06)
Prior
x = 1.00 , σ = 0.07
b_97

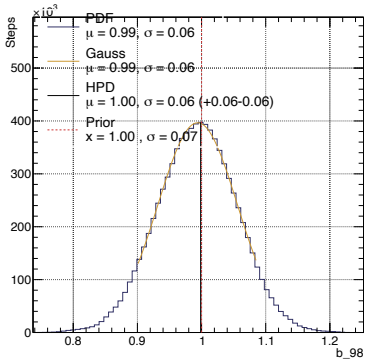
x10³
Steps
PDF
μ = 0.99, σ = 0.06
Gauss
μ = 0.99, σ = 0.06
HPD
μ = 1.00, σ = 0.06 (+0.06-0.06)
Prior
x = 1.00 , σ = 0.07
b_98

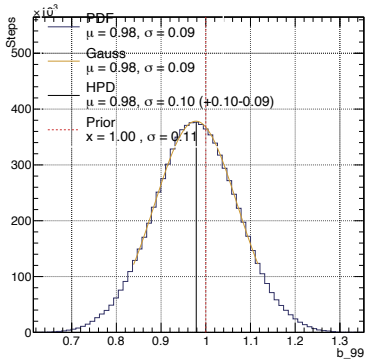
x10³
Steps
PDF
μ = 0.98, σ = 0.09
Gauss
μ = 0.98, σ = 0.09
HPD
μ = 0.98, σ = 0.10 (+0.10-0.09)
Prior
x = 1.00 , σ = 0.11
b_99

Glossary

1. **2p2h** Two Particles Two Holes - An interaction that results in the ejection of two nucleons because of correlations between them.
2. **AKGY** Andreopoulos-Gallagher- Kehayias-Yan model describes multi-π kinematics and multiplicities at low W.
3. **BANFF** Beam And ND280 Flux measurement task Force - ND280's frequentist fitter that uses gradient descent algorithm.
4. **BY** Bodek-Yang - Authors whose corrections affect DIS cross-sections at low Q^2.
5. **CC** Charged Current - Weak interaction mediated by charged vector boson $W^{\pm}$.
6. **CCQE** Charged Current Quasi-Elastic - Weak interaction of neutrino that produces a charged lepton and a nucleon in the final state.
7. **CEX** Charge Exchange - A final state interaction that converts $\pi^{\pm}$ to π^0.
8. **COH** Coherent - Interactions where the neutrino interacts with the nucleus as a whole.
9. **CP** Charged-Parity symmetry.
10. **DIS** Deep Inelastic Scattering - An interaction with a very high 4-momentum (Q^2) transfer that probes the quark structure of the nucleon.
11. **FC** Fully Contained - Events at Super-Kamiokande with little or no outer detector activity.
12. **FD** Far Detector - which for T2K is the Super-Kamiokande detector.
13. **FHC** Forward Horn Current - neutrino beam mode
14. **FSI** Final State Interactions - secondary interactions taking place inside the nucleus.
15. **FV** Fiducial Volume of the detector.
16. **GPU** Graphics Processing Unit.
17. **HPD** Highest Posterior Density - It is the maximum of a posterior distribution.
18. **IH** Inverted Hierarchy.
19. **INGRID** Interactive Neutrino GRID - T2K's on-axis detector
20. **J-PARC** Japan Proton Accelerator Research Complex - The research facility that produces T2K's (anti)neutrino beam and also houses the near detectors
21. **LLH** Log Likelihood.
22. **LO** Lower Octant of θ_{23}.

23. **MCMC** Markov Chain Monte Carlo - a statistical method for sampling from a probability distribution.
24. **NC** Neutral Current - Weak interaction mediated by neutral vector boson Z^0.
25. **ND** Near Detector - In this thesis, this abbreviation is mostly used for the ND280 off-axis detector.
26. **NH** Normal Hierarchy.
27. **PID** Particle IDentification.
28. **POT** Protons On Target - A unit that measures the accumulated data.
29. **RES** RESonant process where a resonance is produced as an intermediate state.
30. **RC** Reactor Constraint - constraint on $\sin^2\theta_{13}$ from reactor neutrino experiments.
31. **RHC** Reverse Horn Current - antineutrino beam mode.
32. **SF** Spectral Function - An advanced model that incorporates the shell structure of the nucleus.
33. **SI** Secondary Interactions - The interactions that particles undergo after exiting the nucleus and within the detector.
34. **SK** Super-Kamiokande detector.
35. **SPP** Single Pion Production - Processes where a single pion is produced.
36. **T2K** Tokai-to-Kamioka long baseline neutrino experiment in Japan.
37. **UO** Upper Octant of θ_{23}.

Bibliography

[1] Andrei D Sakharov. Violation of CP invariance, C asymmetry, and baryon asymmetry of the universe. *Soviet Physics Uspekhi* 34.5 (May 1991), pp. 392393. ISSN: 0038-5670. DOI: 10.1070/pu1991v034n05abeh002497 (cit. on pp. 1, 11).

[2] K. Abe et al. The T2K experiment. *Nuclear Instruments and Methods in Physics Research Section A: Accelerators, Spectrometers, Detectors and Associated Equipment* 659.1 (Dec. 2011), pp. 106135. ISSN: 0168-9002. DOI: 10.1016/j.nima.2011.06.067 (cit. on pp. 1, 19).

[3] K. Abe et al. Indication of Electron Neutrino Appearance from an Accelerator-produced Off-axis Muon Neutrino Beam. *Phys. Rev. Lett.* 107 (2011), p. 041801. DOI: 10.1103/PhysRevLett.107.041801. arXiv: 1106.2822 [hep-ex] (cit. on pp. 1, 10).

[4] K. Abe et al. Observation of Electron Neutrino Appearance in a Muon Neutrino Beam. *Phys. Rev. Lett.* 112 (2014), p. 061802. DOI: 10.1103/PhysRevLett.112.061802. arXiv: 1311.4750 [hep-ex] (cit. on p. 1).

[5] K. Abe et al. Measurements of neutrino oscillation parameters from the T2K experiment using 3.6×10^{21} protons on target. *The European Physical Journal C* 83.9 (Sept. 2023). ISSN: 1434-6052. DOI: 10.1140/epjc/s10052-023-11819-x (cit. on pp. 1, 105).

[6] S. L. Glashow. Partial Symmetries of Weak Interactions. *Nucl. Phys.* 22 (1961), pp. 579–588. DOI: 10.1016/0029-5582(61)90469-2 (cit. on p. 5).

[7] Steven Weinberg. A Model of Leptons. *Phys. Rev. Lett.* 19 (1967), pp. 1264–1266. DOI: 10.1103/PhysRevLett.19.1264 (cit. on p. 5).

[8] Abdus Salam. Weak and Electromagnetic Interactions. *Conf. Proc. C* 680519 (1968), pp. 367 –377. DOI: 10.1142/9789812795915_0034 (cit. on p. 5).

[9] D. Galbraith and C. Burgard. Standard Model of Physics (cit. on p. 6).

[10] C. L. Cowan et al. Detection of the Free Neutrino: a Confirmation. *Science* 124.3212 (July 1956), pp. 103104. ISSN: 1095-9203. DOI: 10.1126/science.124.3212.103 (cit. on p. 6).

[11] Raymond Davis, Don S. Harmer, and Kenneth C. Hoffman. Search for Neutrinos from the Sun. *Physical Review Letters* 20.21 (May 1968), pp. 12051209. ISSN: 0031-9007. DOI: 10.1103/PhysRevLett.20.1205 (cit. on p. 6).

[12] B. Pontecorvo. Mesonium and anti-mesonium. *Sov. Phys. JETP* 6 (1957), p. 429 (cit. on p. 7).

[13] B. Pontecorvo. Inverse beta processes and nonconservation of lepton charge. *Zh. Eksp. Teor. Fiz.* 34 (1957), p. 247 (cit. on p. 7).

[14] B. Pontecorvo. Neutrino Experiments and the Problem of Conservation of Leptonic Charge. *Zh. Eksp. Teor. Fiz.* 53 (1967), pp. 1717–1725 (cit. on p. 7).

[15] V. Gribov and B. Pontecorvo. Neutrino astronomy and lepton charge. *Physics Letters B* 28.7 (Jan. 1969), pp. 493496. ISSN: 0370-2693. DOI: 10.1016/0370-2693(69)90525-5 (cit. on p. 7).

[16] Ziro Maki, Masami Nakagawa, and Shoichi Sakata. Remarks on the Unified Model of Elementary Particles. *Progress of Theoretical Physics* 28.5 (Nov. 1962), pp. 870880. ISSN: 0033-068X. DOI: 10.1143/ptp.28.870 (cit. on p. 7).

[17] Carlo Giunti and Chung W. Kim. *Fundamentals of Neutrino Physics and Astrophysics*. Oxford University Press, Mar. 2007. ISBN: 9780198508717. DOI: 10.1093/acprof:oso/9780198508717.001.0001 (cit. on p. 8).

[18] Boris Kayser. Neutrino Oscillation Physics. 2013. arXiv: 1206.4325 [hep-ph] (cit. on p. 8).

[19] Samoil Bilenky. *Introduction to the Physics of Massive and Mixed Neutrinos*. Springer Berlin Heidelberg, 2010. ISBN: 9783642140433. DOI: 10.1007/978-3-642-14043-3 (cit. on p. 8).

[20] Y. Fukuda et al. Evidence for Oscillation of Atmospheric Neutrinos. *Physical Review Letters* 81.8 (Aug. 1998), pp. 15621567. ISSN: 1079-7114. DOI: 10.1103/PhysRevLett.81.1562 (cit. on p. 8).

[21] L. Wolfenstein. Neutrino oscillations in matter. *Physical Review D* 17.9 (May 1978). ISSN: 0556-2821. DOI: 10.1103/PhysRevD.17.2369 (cit. on p. 8).

[22] Q. R. Ahmad et al. Direct Evidence for Neutrino Flavor Transformation from Neutral-Current Interactions in the Sudbury Neutrino Observatory. *Physical Review Letters* 89.1 (June 2002). ISSN: 1079-7114. DOI: 10.1103/PhysRevLett.89.011301 (cit. on p. 9).

[23] S Adrián-Martínez et al. Letter of intent for KM3NeT 2.0. *Journal of Physics G: Nuclear and Particle Physics* 43.8 (June 2016), p. 084001. DOI: 10.1088/0954-3899/43/8/084001 (cit. on p. 10).

[24] F. P. An et al. Observation of electron-antineutrino disappearance at Daya Bay. *Phys. Rev. Lett.* 108 (2012), p. 171803. DOI: 10.1103/PhysRevLett.108.171803. arXiv: 1203.1669 [hep-ex] (cit. on p. 10).

[25] J. K. Ahn et al. Observation of Reactor Electron Antineutrinos Disappearance in the RENO Experiment. *Phys. Rev. Lett.* 108 (19 May 2012), pp. 191802. DOI: 10.1103/PhysRevLett.108.191802. URL: https://link.aps.org/doi/10.1103/PhysRevLett.108.191802 (cit. on p. 10).

[26] C. Jarlskog. Matrix Representation of Symmetries in Flavor Space, Invariant Functions of Mass Matrices and Applications. *Physical Review Letters* 55.10 (Sept. 1985), pp. 1039–1042. ISSN: 0031-9007. DOI: 10.1103/PhysRevLett.55.1039 (cit. on p. 10).

[27] Ivan Esteban et al. The fate of hints: updated global analysis of three-flavor neutrino oscillations. *Journal of High Energy Physics* 2020.9 (Sept. 2020). ISSN: 1029-8479. DOI: 10.1007/jhep09(2020)178. URL: http://dx.doi.org/10.1007/JHEP09(2020)178 (cit. on p. 11).

[28] J. A. Formaggio and G. P. Zeller. From eV to EeV: Neutrino cross sections across energy scales. *Reviews of Modern Physics* 84.3 (Sept. 2012), pp. 1307–1341. DOI: 10.1103/revmodphys.84.1307 (cit. on p. 12).

[29] L. Alvarez-Ruso et al. NuSTEC White Paper: Status and challenges of neutrinonucleus scattering. *Progress in Particle and Nuclear Physics* 100 (May 2018), pp. 168. ISSN: 0146-6410. DOI: 10.1016/j.ppnp.2018.01.006 (cit. on pp. 13, 17).

[30] C.H. Llewellyn Smith. Neutrino reactions at accelerator energies. *Physics Reports* 3.5 (June 1972), pp. 261379. ISSN: 0370-1573. DOI: 10.1016/0370-1573(72)90010-5 (cit. on p. 13).

[31] G. D. Megias et al. New evaluation of the axial nucleon form factor from electron- and neutrino-scattering data and impact on neutrino-nucleus cross sections. *Physical Review C* 101.2 (Feb. 2020). ISSN: 2469-9993. DOI: 10.1103/PhysRevC.101.025501 (cit. on p. 13).

[32] Yoshinari Hayato and Luke Pickering. The NEUT neutrino interaction simulation program library. *The European Physical Journal Special Topics* 230.24 (Oct. 2021), pp. 44694481. ISSN: 1951-6401. DOI: 10.1140/epjs/s11734-021-00287-7. URL: http://dx.doi.org/10.1140/epjs/s11734-021-00287-7 (cit. on p. 13).

[33] Toru Sato, D. Uno, and T. S. H. Lee. Dynamical model of weak pion production reactions. *Phys. Rev. C* 67 (2003), p. 065201. DOI: 10.1103/PhysRevC.67.065201. arXiv: nucl-th/0303050 (cit. on p. 14).

[34] Dieter Rein and Lalit M. Sehgal. Neutrino Excitation of Baryon Resonances and Single Pion Production. *Annals Phys.* 133 (1981), pp. 79–153. DOI: 10.1016/0003-4916(81)90242-6 (cit. on p. 14).

[35] Krzysztof M. Graczyk and Jan T. Sobczyk. Erratum: Form factors in the quark resonance model [Phys. Rev. D 77, 053001 (2008)]. *Phys. Rev. D* 79 (7 Apr. 2009), p. 079903. DOI: 10.1103/PhysRevD.79.079903 (cit. on p. 14).

[36] Callum Wilkinson et al. Reanalysis of bubble chamber measurements of muon-neutrino induced single pion production. *Physical Review D* 90.11 (Dec. 2014). ISSN: 1550-2368. DOI: 10.1103/PhysRevD.90.112017 (cit. on p. 14).

[37] G. M. Radecky et al. Study of Single Pion Production by Weak Charged Currents in Low-energy Neutrino *d* Interactions. *Physical Review D* 25.5 (Mar. 1982), pp. 11611173. ISSN: 0556-2821. DOI: 10.1103/PhysRevD.25.1161 (cit. on p. 15).

[38] T. Kitagaki et al. Charged-current exclusive pion production in neutrino-deuterium interactions. *Physical Review D* 34.9 (Nov. 1986), pp. 25542565. ISSN: 0556-2821. DOI: 10.1103/PhysRevD.34.2554 (cit. on p. 15).

[39] K. Abe et al. Measurements of the ν_μ and $\overline{\nu}_\mu$-induced coherent charged pion production cross sections on ^{12}C by the T2K experiment. *Phys. Rev. D* 108 (9 Nov. 2023), p. 092009. DOI: 10.1103/PhysRevD.108.092009 (cit. on p. 15).

[40] Christian Bierlich et al. A comprehensive guide to the physics and usage of PYTHIA 8.3. 2022. arXiv: 2203.11601 [hep-ph] (cit. on p. 16).

[41] T. Yang et al. A hadronization model for the MINOS experiment. *AIP Conf. Proc.* 967.1 (2007). Ed. by Geralyn P. Zeller, Jorge G. Morfin, and Flavio Cavanna, pp. 269–275. DOI: 10.1063/1.2834490 (cit. on p. 16).

[42] A Bodek and U. K. Yang. Higher twist, xi(omega) scaling, and effective LO PDFs for lepton scattering in the few GeV region. *J. Phys. G* 29 (2003). Ed. by K. Long and R. Edgecock, pp. 1899–1906. DOI: 10.1088/0954-3899/29/8/369. arXiv: hep-ex/0210024 (cit. on p. 16).

[43] R. Anni, G. Co, and P. Pellegrino. Nuclear charge density distributions from elastic electron scattering data. *Nucl. Phys. A* 584 (1995), pp. 35–59. DOI: 10.1016/0375-9474(94)00508-K. arXiv: nucl-th/9410023 (cit. on p. 17).

[44] L. L. Salcedo et al. Computer Simulation of Inclusive Pion Nuclear Reactions. *Nucl. Phys. A* 484 (1988), pp. 557–592. DOI: 10.1016/0375-9474(88)90310-7 (cit. on p. 17).

[45] P. A. Zyla et al. Review of Particle Physics. *PTEP* 2020.8 (2020), p. 083C01. DOI: 10.1093/ptep/ptaa104 (cit. on p. 17).

[46] S. Fukuda et al. The Super-Kamiokande detector. *Nuclear Instruments and Methods in Physics Research Section A: Accelerators, Spectrometers, Detectors and Associated Equipment* 501.2 (2003), pp. 418–462. ISSN: 0168-9002. DOI: https://doi.org/10.1016/S0168-9002(03)00425-X (cit. on pp. 19, 25, 27).

[47] Susumu Igarashi et al. Accelerator design for 1.3-MW beam power operation of the J-PARC Main Ring. *Progress of Theoretical and Experimental Physics* 2021 (Feb. 2021). DOI: 10.1093/ptep/ptab011 (cit. on p. 20).

[48] K. Abe et al. T2K Neutrino Flux Prediction. *Phys. Rev. D* 87 (1 Jan. 2013), p. 012001. DOI: 10.1103/PhysRevD.87.012001 (cit. on pp. 21, 23).

[49] Edward T. Atkin. Neutrino Oscillation Analysis at the T2K experiment including studies of new uncertainties on interactions involving additional final state hadrons. PhD thesis. 2022. URL: \href{https://t2k.org/docs/thesis/131}{T2KThesis131} (cit. on p. 22).

[50] K. Abe et al. First gadolinium loading to Super-Kamiokande. *Nucl. Instrum. Meth. A* 1027 (2022), p. 166248. DOI: 10.1016/j.nima.2021.166248. arXiv: 2109.00360 [physics.ins-det] (cit. on p. 25).

[51] K. Abe et al. Second gadolinium loading to Super-Kamiokande. *Nucl. Instrum. Meth. A* 1065 (2024), p. 169480. DOI: 10.1016/j.nima.2024.169480. arXiv: 2403.07796 [physics.ins-det] (cit. on p. 25).

[52] K. Abe et al. Constraint on the matter–antimatter symmetry-violating phase in neutrino oscillations. *Nature* 580.7803 (2020). [Erratum: Nature 583, E16 (2020)], pp. 339–344. DOI: 10.1038/s41586-020-2177-0. arXiv: 1910.03887 [hep-ex] (cit. on p. 26).

[53] Shimpei Tobayama. An analysis of the oscillation of atmospheric neutrinos. PhD thesis. University of British Columbia, 2016. DOI: http://dx.doi.org/10.14288/1.0340615. URL: https://open.library.ubc.ca/collections/ubctheses/24/items/1.0340615 (cit. on p. 28).

[54] M Jiang et al. Atmospheric neutrino oscillation analysis with improved event reconstruction in Super-Kamiokande IV. *Progress of Theoretical and Experimental Physics* 2019.5 (May 2019), 053F01. ISSN: 2050-3911. DOI: 10.1093/ptep/ptz015. eprint: https://academic.oup.com/ptep/article-pdf/2019/5/053F01/28638877/ptz015.pdf. URL: https://doi.org/10.1093/ptep/ptz015 (cit. on p. 28).

[55] John F. Beacom and Mark R. Vagins. GADZOOKS! Anti-neutrino spectroscopy with large water Cherenkov detectors. *Phys. Rev. Lett.* 93 (2004), p. 171101. DOI: 10.1103/PhysRevLett.93.171101. arXiv: hep-ph/0309300 (cit. on p. 28).

[56] F and James. MINUIT: Function Minimization and Error Analysis Reference Manual (1998). CERN Program Library Long Writeups. URL: https://cds.cern.ch/record/2296388 (cit. on p. 29).

[57] Joe Walsh. Constraining the T2K neutrino oscillation parameter results using data from the off-axis near detector, ND280: Implementation of a nucleon removal energy systematic uncertainty treatment in the BANFF fit. English. PhD thesis. Lancaster University, 2022. DOI: 10.17635/lancaster/thesis/1604 (cit. on p. 29).

[58] Lucile Mellet. From T2K to Hyper-Kamiokande : neutrino oscillation analysis and preparation of the time synchronization system. PhD thesis. 2023. URL: \href{https://t2k.org/docs/thesis/141}{T2KThesis141} (cit. on p. 29).

[59] The MaCh3 Collaboration. mach3-software/MaCh3: v1.0.0-beta. 2024. DOI: 10.5281/ZENODO.10949376 (cit. on pp. 29, 55).

[60] Claudio Giganti. T2K experiment status and plans. Talk at Neutrino 2024 Conference. 2024 (cit. on pp. 29, 110, 121).

[61] Lucile Mellet et al. P-Theta 2023 Run 1-11 Joint-fit Analysis Note. T2K Technical note 461. 2023 (cit. on p. 29).

[62] Henry Wallace et al. P-Theta 2023 Run 1-11 Joint-fit Analysis Note. T2K Technical note 462. 2023 (cit. on p. 29).

[63] Edward Atkin et al. OA2023: Physics Analysis Summary. T2K Technical note 463. 2023 (cit. on pp. 29, 112).

[64] Kamil Skwarczynski. Neutrino Oscillation Measurements at T2K. *PoS* ICHEP2022 (2022), p. 606. DOI: 10.22323/1.414.0606 (cit. on pp. 30, 121).

[65] IX. On the problem of the most efficient tests of statistical hypotheses. *Philosophical Transactions of the Royal Society of London. Series A, Containing Papers of a Mathematical or Physical Character* 231.694-706 (Feb. 1933), pp. 289–337. DOI: 10.1098/rsta.1933.0009 (cit. on pp. 35, 56).

[66] Trevor Towstego. Study of Neutrino Oscillations with Enhanced Selection of Electron Neutrino Interactions. PhD thesis. 2022 (cit. on pp. 37, 38).

[67] S. S. Wilks. The Large-Sample Distribution of the Likelihood Ratio for Testing Composite Hypotheses. *Annals Math. Statist.* 9.1 (1938), pp. 60–62. DOI: 10.1214/aoms/1177732360 (cit. on p. 56).

[68] Roger J. Barlow and Christine Beeston. Fitting using finite Monte Carlo samples. *Comput. Phys. Commun.* 77 (1993), pp. 219–228. DOI: 10.1016/0010-4655(93)90005-W (cit. on p. 57).

[69] A. Markov. An Example of Statistical Investigation of the Text Eugene Onegin Concerning the Connection of Samples in Chains. *Science in Context* 19 (Dec. 2006), pp. 591 –600. DOI: 10.1017/S0269889706001074 (cit. on p. 58).

[70] W. K. Hastings. Monte Carlo Sampling Methods Using Markov Chains and Their Applications. *Biometrika* 57 (1970), pp. 97–109. DOI: 10.1093/biomet/57.1.97 (cit. on p. 59).

[71] Seung-Seop Jin, Heekun Ju, and Hyung-Jo Jung. Adaptive Markov chain Monte Carlo algorithms for Bayesian inference: recent advances and comparative study. *Structure and Infrastructure Engineering* (June 2019). DOI: 10.1080/15732479.2019.1628077 (cit. on p. 60).

[72] I. Asimov. *The Complete Stories Volume 1*. Doubleday, 1990. URL: https://books.google.pl/books?id=SYc-zwEACAAJ (cit. on p. 60).

[73] Kamil Skwarczynski. Constraining neutrino cross-section and flux models using T2K Near Detector with proton information in Markov chain Monte Carlo framework. PhD thesis. 2023 (cit. on pp. 60, 77, 100).

[74] A. Gelman et al. *Bayesian Data Analysis, Third Edition*. Chapman & Hall/CRC Texts in Statistical Science. Taylor & Francis, 2013. ISBN: 9781439840955. URL: https://books.google.pl/books?id=ZXL6AQAAQBAJ (cit. on pp. 65, 66).

[75] Aki Vehtari et al. Rank-Normalization, Folding, and Localization: An Improved R for Assessing Convergence of MCMC (with Discussion). *Bayesian Analysis* 16.2 (June 2021). ISSN: 1936-0975. DOI: 10.1214/20-ba1221. URL: http://dx.doi.org/10.1214/20-BA1221 (cit. on pp. 65, 66).

[76] N Abgrall et al. NA61/SHINE facility at the CERN SPS: beams and detector system. *Journal of Instrumentation* 9.06 (June 2014), P06005. DOI: 10.1088/1748-0221/9/06/P06005. URL: https://dx.doi.org/10.1088/1748-0221/9/06/P06005 (cit. on p. 69).

[77] N. Abgrall et al. Measurements of $\pi^{\pm}$, $K^{\pm}$ and proton double differential yields from the surface of the T2K replica target for incoming 31 GeV/c protons with the NA61/SHINE spectrometer at the CERN SPS. *Eur. Phys. J. C* 79.2 (2019), p. 100. DOI: 10.1140/epjc/s10052-019-6583-0. arXiv: 1808.04927 [hep-ex] (cit. on p. 69).

[78] N. Abgrall et al. Measurements of $\pi^{\pm}$ differential yields from the surface of the T2K replica target for incoming 31 GeV/c protons with the NA61/SHINE spectrometer at the CERN SPS. *Eur. Phys. J. C* 76.11 (2016), p. 617. DOI: 10.1140/epjc/s10052-016-4440-y. arXiv: 1603.06774 [hep-ex] (cit. on p. 69).

[79] T. Golan, J. T. Sobczyk, and J. Zmuda. NuWro: the Wroclaw Monte Carlo Generator of Neutrino Interactions. *Nucl. Phys. B Proc. Suppl.* 229-232 (2012). Ed. by George S. Tzanakos, pp. 499–499. DOI: 10.1016/j.nuclphysbps.2012.09.136 (cit. on p. 71).

[80] J. Chakrani et al. Parametrized uncertainties in the spectral function model of neutrino charged-current quasielastic interactions for oscillation analyses. *Phys. Rev. D* 109.7 (2024), p. 072006. DOI: 10.1103/PhysRevD.109.072006. arXiv: 2308.01838 [hep-ex] (cit. on p. 71).

[81] Artur M. Ankowski and Jan T. Sobczyk. Construction of spectral functions for medium-mass nuclei. *Phys. Rev. C* 77 (2008), p. 044311. DOI: 10.1103/PhysRevC.77.044311. arXiv: 0711.2031 [nucl-th] (cit. on p. 71).

[82] S. Dolan et al. Electron-nucleus scattering in the NEUT event generator. *23rd International Workshop on Neutrinos from Accelerators*. Jan. 2023. arXiv: 2301.09195 [hep-ex] (cit. on p. 71).

[83] M. Kabirnezhad. Single pion production in neutrino-nucleon interactions. *Physical Review D* 97.1 (Jan. 2018). ISSN: 2470-0029. DOI: 10.1103/physrevd.97.013002. URL: http://dx.doi.org/10.1103/PhysRevD.97.013002 (cit. on p. 72).

[84] G. M. Radecky et al. Study of Single Pion Production by Weak Charged Currents in Low-energy Neutrino *d* Interactions. *Phys. Rev. D* 25 (1982). [Erratum: Phys.Rev.D 26, 3297 (1982)], pp. 1161–1173. DOI: 10.1103/PhysRevD.25.1161 (cit. on p. 72).

[85] T. Kitagaki et al. Charged Current Exclusive Pion Production in Neutrino Deuterium Interactions. *Phys. Rev. D* 34 (1986), pp. 2554–2565. DOI: 10.1103/PhysRevD.34.2554 (cit. on p. 72).

[86] Dieter Rein and Lalit M Sehgal. Neutrino-excitation of baryon resonances and single pion production. *Annals of Physics* 133.1 (1981), pp. 79–153. ISSN: 0003-4916. DOI: https://doi.org/10.1016/0003-4916(81)90242-6 (cit. on p. 72).

[87] C. Bronner et al. NIWG model and uncertainties for 2021 oscillation analysis. T2K Technical note 414. 2021 (cit. on pp. 73, 74, 99, 100).

[88] J. Nieves, I. Ruiz Simo, and M. J. Vicente Vacas. The nucleon axial mass and the MiniBooNE Quasielastic Neutrino-Nucleus Scattering problem. *Phys. Lett. B* 707 (2012), 72 –75. DOI: 10.1016/j.physletb.2011.11.061. arXiv: 1106.5374 [hep-ph] (cit. on p. 73).

[89] K. Abe et al. Atmospheric neutrino oscillation analysis with external constraints in Super-Kamiokande I-IV. *Phys. Rev. D* 97 (7 Apr. 2018), p. 072001. DOI: 10.1103/PhysRevD.97.072001. URL: https://link.aps.org/doi/10.1103/PhysRevD.97.072001 (cit. on p. 79).

[90] K. Abe et al. Calibration of the Super-Kamiokande detector. *Nuclear Instruments and Methods in Physics Research Section A: Accelerators, Spectrometers, Detectors and Associated Equipment* 737 (Feb. 2014), pp. 253272. ISSN: 0168-9002. DOI: 10.1016/j.nima.2013.11.081. URL: http://dx.doi.org/10.1016/j.nima.2013.11.081 (cit. on p. 89).

[91] M. Tanabashi et al. Review of Particle Physics. *Phys. Rev. D* 98.3 (2018), p. 030001. DOI: 10.1103/PhysRevD.98.030001 (cit. on p. 106).

[92] Andrew Gelman, Xiao-Li Meng, and Hal Stern. Posterior predictive assessment of model fitness via realized discrepancies. *Statistica sinica* (1996), pp. 733–760 (cit. on p. 106).

[93] Andrew Gelman et al. Diagnostic Checks for Discrete Data Regression Models Using Posterior Predictive Simulations. *Journal of the Royal Statistical Society Series C* 49 (Feb. 2000), pp. 247–268. DOI: 10.1111/1467-9876.00190 (cit. on p. 106).

[94] Harold Jeffreys. *Theory of Probability*. Oxford, England: Clarendon Press, 1939 (cit. on p. 109).

[95] K. Abe et al. First joint oscillation analysis of Super-Kamiokande atmospheric and T2K accelerator neutrino data (May 2024). arXiv: 2405.12488 [hep-ex] (cit. on p. 113).

[96] L. Berns et al. T2K+SK atmospheric joint analysis: model updates for the data fit . T2K Technical note 456. 2023 (cit. on p. 113).

[97] Tomas Nosek. T2K+NOvA Joint Neutrino Oscillation Analysis. 2024 (cit. on p. 122).

[98] Super-Kamiokande and T2K collaborations. First joint oscillation analysis of Super-Kamiokande atmospheric and T2K accelerator neutrino data. 2024. arXiv: 2405.12488 [hep-ex] (cit. on p. 122).

[99] Hyper-Kamiokande Proto-Collaboration. Hyper-Kamiokande Design Report. 2018 . arXiv: 1805.04163 [physics.ins-det] (cit. on p. 122).